FLOW IN RECIPROCATING ENGINE CYLINDERS AND CURVED DUCTS

MICHAEL YIANNESKIS

B.Sc.(Tech.), A.U.M.I.S.T., M.Sc.(Eng.), D.I.C.

Thesis submitted for the degree of

Doctor of Philosophy

in the University of London

Imperial College of Science and Technology

(Department of Mechanical Engineering)

April 1982

To all those who, in one way or another,

helped the realisation of this thesis.

ABSTRACT

Detailed measurements of the mean and turbulence velocity components, by laser Doppler anemometry, in the cylinders of two model reciprocating engines are reported. One engine operated without compression in an intake and return stroke cycle and the other operated with compression in a four-stroke cycle. The effects of a pipe inlet and of a simulated valve inlet, of a plane piston and of a cylindrical-bowl piston, of swirl (for swirl numbers of 0.0, 0.45 and 1.2), of engine speed variation (between 100 and 300 r.p.m.) and of compression (with a compression ratio of 3.7) on the flow patterns were investigated in axisymmetric configurations. With a valve inlet, a system of ring vortices is present during intake and most of the indrawn air is recirculated in the primary vortex behind the valve; the length of this recirculation region increases with swirl. With an asymmetrical valve inlet, the flow structure is similar, but the vortices vary in size and intensity around the periphery of the cylinder. Swirl patterns with the axisymmetric valve geometry are shown to be characterised by a solid-body-rotation region near the axis with uniform swirl profiles near the cylinder wall. Mean and turbulence velocities were found to scale with engine speed and under compressing conditions they decayed to low and uniform levels near TDC of compression.

Similar measurements are reported for laminar and turbulent developing flows in a strongly curved, square cross-sectioned duct, relevant to those encountered in the intakes and manifolds of internal combustion engines. For turbulent flow, measurements of cross-correlations, turbulence kinetic energy and wall pressures are also reported. Secondary flows of the first kind are present in both flows and are more pronounced

in the laminar flow (0.6 as opposed to 0.4 of the bulk flow velocity, V_c), mainly due to the thicker boundary layers at the bend inlet. In turbulent flow, the values of the kinetic energy of turbulence do not exceed 0.0014 V_c^2 over most of the duct cross-section.

The measurements of this thesis are suitable for the assessment of numerical techniques and turbulence models employed for the calculation of the flows.

ACKNOWLEDGEMENTS

It gives me pleasure to acknowledge the assistance of a number of people during the course of the research and the preparation of this thesis.

Professor J.H. Whitelaw has provided me with constant supervision, encouragement and valuable advice and criticism, for which I am greatly indebted.

I am obliged, for the time and knowledge generously given, to Dr. Alan Morse, who introduced me to laser Doppler anemometry, and to Dr. Alex Taylor who helped to consolidate many practical and theoretical aspects of the work.

My thanks go to Mr. Dinos Arcoumanis, Mr. Ali Bicen, Dr. Richard Johns, Dr. Nick Vlachos and Dr. Paul Watkins for numerous discussions and valuable advice.

I have benefitted from association with many colleagues and in particular Dr. D. Crabb, Professor D.F.G. Durão, Ms. M. Founti, Dr. R. Issa, Mr. Z. Khan and Dr. Y. Levy.

I am grateful to Messrs. R. Church, N. Frost, J. Laker and O. Vis for their help with, and construction of, the experimental apparatus.

The preparation of this thesis was expedited by the excellent and speedy typing of Ms. S. Crofton and the execution of the diagrams by Mr. R. Potter.

I am indebted to the Science Research Council and the NASA Lewis Research Center for financial support provided for this work.

CONTENTS

		Page
ABSTRACT		iii
ACKNOWLEDGEMENTS		v
CONTENTS		vi
LIST OF TABLES		xi
LIST OF FIGURES		xii
NOMENCLATURE		xx
CHAPTER 1:	INTRODUCTION	1
1.1	The flow configurations	1
1.2	Literature survey	6
1.2.1	In-cylinder flow	6
	Experiments	6
	Calculations	13
	Summary of findings	18
1.2.2	Curved duct	19
	Experiments	20
	Calculations	23
	Summary of findings	26
1.3	The present contribution	27
1.4	Thesis outline	29
CHAPTER 2:	FLOW IN RECIPROCATING ENGINE CYLINDERS	44
2.1	Introduction	44

			Page
2.2	Description of the flow configurations		46
	2.2.1	Non-compressing engine	46
		Cylinder and piston head arrangements	49
	2.2.2	Compressing engine	50
2.3	Measurement systems and techniques		53
	2.3.1	Laser Doppler anemometer optical systems	53
		Off-axis collection system	55
		Seeding	56
		Beam orientation, displacement and alignment	56
	2.3.2	Laser Doppler anemometer signal processing systems, measurement procedures and data reduction	58
		Frequency counter/keyboard programmed system	58
		Frequency counter/PDP 8/e mini-computer system	60
		Spectrum analyser/PDP 8/e mini-computer system	62
		Frequency counter/Apple microprocessor system	63
	2.3.3	Pressure measurement system	65
	2.3.4	Measurement uncertainties	65
		Positional errors	65
		Asymmetry	66
		Engine speed	67
		Frequency shift	68
		Doppler broadening	69
		Crank-angle broadening	71

			Page
		Count ambiguity and finite time resolution	74
		Bias effects	75
		Continuity check	78
2.4	Results with model non-compressing engine		79
	2.4.1	Introduction	79
	2.4.2	Pipe inlet	81
	2.4.3	Valve inlet with plane and cylindrical-bowl pistons	82
	2.4.4.	Valve inlet with swirl	84
		Profiles at 36^{o} ATDC	86
		Profiles at 90^{o} ATDC	89
		Profiles at 144^{o} ATDC	93
		Profiles at 270^{o} ATDC	95
	2.4.5	Engine speed variation	98
2.5	Results with model compressing engine		99
	2.5.1	Preliminary tests	99
	2.5.2	Operating valve with compression	100
2.6	Discussion		102
	2.6.1	Influence of flow and geometrical conditions on the in-cylinder fluid motion	103
		Influence of cylinder geometry	103
		Influence of swirl	106
		Effect of engine speed	107
		Influence of compression with an operating valve	108

			Page
		The significance of the "rolled-up" vortex	109
		Flow in production engines	111
	2.6.2	Calculation of the flow in reciprocating engine cylinders	112
2.7	Summary		116
APPENDIX 2.1	The flow characteristics of a piston-cylinder assembly with an off-centre, open port		118
APPENDIX 2.2	Mean and r.m.s. velocity profiles for pipe and valve inlet configurations in the non-compressing engine without swirl		127
APPENDIX 2.3	Listing of PDP 8/e mini-computer program sampling data from the frequency counter and spectrum analyser and storing data on magnetic tape		138
APPENDIX 2.4	Listing of main-frame computer program decoding and processing data stored on magnetic tape		149
CHAPTER 3:	FLOW IN CURVED DUCTS		207
3.1	Preamble		207
3.2	Bend flow configuration		208
3.3	Measurement system and technique		210
	3.3.1	Optical system	210
	3.3.2	Signal processing system	212
	3.3.3	Measurement uncertainties	212
3.4	Flow visualisation		216
3.5	Wall pressure measurements		218
3.6	Velocity results		219
	3.6.1	Laminar flow results	221
	3.6.2	Turbulent flow results	222

		Page
3.7	Discussion	225
	Influence of inlet boundary layer thickness	225
	Effect of Reynolds number	228
	Influence of curvature	229
	Effect of duct cross-sectional shape and bend deflection angle	232
	Effects on the turbulence structure	235
	Calculation of the flow in curved ducts	237
3.8	Summary	239
APPENDIX 3.1	Turbulent flow in a square-to-round transition	242
CHAPTER 4:	CONCLUDING REMARKS	290
REFERENCES		295

LIST OF TABLES

Table No.		Page(s)
1.1	Experimental investigations of the flow in reciprocating engine cylinders	31-35
1.2	Theoretical investigations of the flow in reciprocating engine cylinders	36-38
1.3	Experimental investigations of the flow in curved ducts	39-40
1.4	Theoretical investigations of the flow in curved ducts	41-43
2.1	In-cylinder flow configurations and variables measured	45
2.2	Model non-compressing engine characteristics	48
2.3	Model compressing engine characteristics	52
2.4	Principal characteristics of optical systems	54
3.1	Characteristics of the optical arrangements	211
3.2	Estimates of measurement uncertainties	214
3.3	Measurement stations and variables in bend flow	220

LIST OF FIGURES

Fig. No.		Page(s)
2.1	Valve inlet: cross-section of cylinder head arrangement with valve positioning attachment	154
2.2	Compressing engine valve lift diagram	155
2.3	Laser Doppler anemometer optical system	
	(a) Schematic diagram	156
	(b) Photograph	157
2.4	Schematic diagram of optical arrangement for inlet profile (z = 0.5 mm) measurements	158
2.5	Laser Doppler anemometer signal processing	
	(a) Frequency counter/keyboard programmed system	159
	(b) Frequency counter/PDP 8/e mini-computer system	160
2.6	Variation of count rate and mean velocity with crank angle	161
2.7(a)	Spectrum analyser/PDP 8/e mini-computer signal processing system	162
2.7(b)	Profiles measured at $\theta = 90^{o}$, z = 20 mm with spectrum analyser	163
	(i) Axial mean velocity component with 256 step scan	
	(ii) Axial r.m.s. velocity component with 256 step scan	

Fig. No.		Page(s)
	(iii) Axial mean velocity component with 128 step scan	164
	(iv) Axial r.m.s. velocity component with 128 step scan	164
2.8	Pipe inlet: stream function contours	
	(a) 36 degrees	165
	(b) 90 degrees	165
	(c) 144 degrees	166
	(d) 270 degrees	166
2.9	Pipe inlet: axial component profiles at $z' = 0.5$ mm	
	(a) Mean velocity	167
	(b) R.m.s. velocity	167
2.10	Pipe inlet: comparison of mean velocity profiles in the pipe and near the inlet	168
2.11	Valve inlet, no swirl: stream function contours	
	(a) 36 degrees	169
	(b) 90 degrees	169
	(c) 144 degrees	170
	(d) 270 degrees	170
2.12	Valve inlet, no swirl: axial component profiles at $z = 0.5$ mm	
	(a) 36 degrees	171
	(b) 90 degrees	171
	(c) 144 degrees	172
	(d) 270 degrees	172

Fig. No.		Page(s)
2.13	Valve inlet: profiles of axial velocity at $\theta = 36^{o}$	
	(a) 15 degree vanes	173
	(i) mean velocity and (ii) r.m.s. component	
	(b) 30 degree vanes	173
	(i) mean velocity and (ii) r.m.s. component	
2.14	Valve inlet: profiles of radial velocity at $\theta = 36^{o}$, 30 degree vanes	174
	(i) mean velocity and (ii) r.m.s. component	
2.15	Valve inlet: profiles of swirl velocity at $\theta = 36^{o}$	
	(a) 15 degree vanes	175
	(i) mean velocity and (ii) r.m.s. component	
	(b) 30 degree vanes	175
	(i) mean velocity and (ii) r.m.s. component	
2.16	Valve inlet: stream function contours at $\theta = 36^{o}$	
	(a) 15 degree vanes	176
	(b) 30 degree vanes	176
2.17	Valve inlet: profiles of axial velocity at $\theta = 90^{o}$	
	(a) 15 degree vanes	177
	(i) mean velocity and (ii) r.m.s. component	
	(b) 30 degree vanes	178
	(i) mean velocity and (ii) r.m.s. component	
2.18	Valve inlet: profiles of radial velocity at $\theta = 90^{o}$, 30 degree vanes	179
	(i) mean velocity and (ii) r.m.s. component	

Fig. No.		Page(s)
2.19	Valve inlet: profiles of swirl velocity at $\theta = 90^{o}$	
	(a) 15 degree vanes	180
	(i) mean velocity and (ii) r.m.s. component	
	(b) 30 degree vanes	181
	(i) mean velocity and (ii) r.m.s. component	
2.20	Valve inlet: stream function contours at $\theta = 90^{o}$	
	(a) 15 degree vanes	182
	(b) 30 degree vanes	182
2.21	Valve inlet: profiles of axial velocity at $\theta = 144^{o}$	
	(a) 15 degree vanes	183
	(i) mean velocity and (ii) r.m.s. component	
	(b) 30 degree vanes	184
	(i) mean velocity and (ii) r.m.s. component	
2.22	Valve inlet: profiles of radial velocity at $\theta = 144^{o}$, 30 degree vanes	185
	(i) mean velocity and (ii) r.m.s. component	
2.23	Valve inlet: profiles of swirl velocity at $\theta = 144^{o}$	
	(a) 15 degree vanes	186
	(i) mean velocity and (ii) r.m.s. component	
	(b) 30 degree vanes	187
	(i) mean velocity and (ii) r.m.s. component	

Fig. No.		Page(s)
2.24	Valve inlet: stream function contours at $\theta = 144^{o}$	
	(a) 15 degree vanes	188
	(b) 30 degree vanes	188
2.25	Valve inlet: profiles of axial velocity at $\theta = 270^{o}$	
	(a) 15 degree vanes	189
	(i) mean velocity and (ii) r.m.s. component	
	(b) 30 degree vanes	190
	(i) mean velocity and (ii) r.m.s. component	
2.26	Valve inlet: profiles of radial velocity at $\theta = 270^{o}$, 30 degree vanes	191
	(i) mean velocity and (ii) r.m.s. component	
2.27	Valve inlet: profiles of swirl velocity at $\theta = 270^{o}$	
	(a) 15 degree vanes	192
	(i) mean velocity and (ii) r.m.s. component	
	(b) 30 degree vanes	193
	(i) mean velocity and (ii) r.m.s. component	
2.28	Valve inlet: stream function contours at $\theta = 270^{o}$	
	(a) 15 degree vanes	194
	(b) 30 degree vanes	194
2.29	Profiles of mean and r.m.s. axial velocity at 90 degrees	
	(a) 100 r.p.m., 335 r.p.m.	

Fig. No.		Page(s)
	(b) 300 r.p.m.	196
2.30	Stream function contours at 90 degrees, 100 r.p.m.	197
2.31	Axial component profiles at 100, 200 and 300 r.p.m.	198
	(i) mean velocities at $\theta = 270^{o}$, z = 20mm	
	(ii) r.m.s. component at $\theta = 270^{o}$, z = 20mm	
	(iii) mean velocities at $\theta = 144^{o}$, z = 60mm	
	(iv) r.m.s. component at $\theta = 144^{o}$, z = 60mm	
2.32	Swirl component profiles at 100, 200 and 300 r.p.m.	
	(a) $\theta = 90^{o}$, z = 20mm	199
	(i) mean velocity and (ii) r.m.s. component	
	(b) $\theta = 144^{o}$, z = 20 and 60mm	200
	(i) mean velocity and (ii) r.m.s. component	
2.33	Comparison of stream function contours with orifice inlet at 90 degrees	201
	(i) 10 and (ii) 200 r.p.m.	
2.34	Comparison of axial component profiles in the two model engine cylinders without compression	202
	(i) mean velocity and (ii) r.m.s. component	
2.35	Compressing engine: axial mean velocity and r.m.s. component profiles	
	(a) $\theta = 90^{o}$	203
	(b) $\theta = 144^{o}$	203
	(c) $\theta = 270^{o}$	204
	(d) $\theta = 342^{o}$	204

Fig. No.		Page(s)
	(e) $\theta = 378^{o}$	205
	(f) $\theta = 450^{o}$	205
	(g) $\theta = 540^{o}$	206
	(h) $\theta = 630^{o}$	206
3.1	Dimensions of bend and coordinate definition sketch	264
3.2	Plan view of water tunnel	265
3.3	(i) Schematic diagram of laser Doppler anemometer optical system	266
	(ii) Photograph of the optical system	267
	(iii) Photograph of the bend showing intersection volume	267
3.4	Block diagram of laser Doppler anemometer signal processing arrangement	268
3.5(a)	Flow visualisation at Re = 790	
	(i) wires located at $\theta = 0^{o}$	269
	(ii) wires located at $\theta = 45^{o}$	269
	(iii) wires located at $\theta = 71^{o}$	270
	(iv) wires located at $\theta = 90^{o}$	270
3.5(b)	Flow visualisation at Re = 1275	
	(i) wires located at $\theta = 0^{o}$	271
	(ii) wires located at $\theta = 45^{o}$	271
	(iii) wires located at $\theta = 71^{o}$	272
	(iv) wires located at $\theta = 90^{o}$	272
3.5(c)	Visualisation of secondary flow near top side wall at Re = 1275	273

Fig. No.		Page(s)
3.5(d)	Visualisation of helical secondary flow near inner wall at Re ≃ 3000	273
3.6	Turbulent flow: wall static pressure measurements (i) streamwise distribution (ii) radial distribution	274
3.7	Laminar flow: isotachs of U/V_c	275
3.8	Laminar flow: profiles of U/V_c	276
3.9	Laminar flow: profiles of V/V_c	277
3.10	Laminar flow: isotachs of V/V_c	278
3.11	Laminar flow: profiles of W/V_c at $X_H = 2.50$	279
3.12	Turbulent flow: profiles of $\tilde{U}/V_c$ at the symmetry plane near the bend inlet	280
3.13	Turbulent flow: profiles of $\tilde{U}/V_c$	281
3.14	Turbulent flow: isotachs of $\tilde{U}/V_c$	282
3.15	Turbulent flow: profiles of $\tilde{V}/V_c$	283
3.16	Turbulent flow: isotachs of $\tilde{V}/V_c$	284
3.17	Turbulent flow: profiles of $\tilde{W}/V_c$ at $X_H = 2.50$	285
3.18	Turbulent flow: contours of $-\overline{uv}/V_c^2$ (x1000)	286
3.19	Turbulent flow: contours of $\tilde{u}/V_c$ (x100)	287
3.20	Turbulent flow: contours of $\tilde{v}/V_c$ (x100)	288
3.21	Turbulent flow: contours of $\overline{uw}/V_c^2$ (x1000) at $X_H = 2.50$	289
3.22	Turbulent flow: contours of $\tilde{w}/V_c^2$ (x100) at $X_H = 2.50$	289
3.23	Turbulent flow: contours of k/V_c^2 (x1000) at $X_H = 2.50$	289

NOMENCLATURE

Roman characters

c	Clearance length in model compressing engine, equation (2.4)
C_p	Static pressure coefficient $\equiv \frac{p - p_{ref}}{\frac{1}{2}\rho V_c^2}$
D_H	Hydraulic diameter of curved duct, equation (3.1)
De	Dean number, equation (3.2)
$f_{1,2,3}$	Focal length of anemometer lenses
f_τ	Counter clock frequency, equation (2.15)
$\tilde{f}(\theta)$	R.m.s. of the frequency fluctuations at a crank angle θ
$\bar{F}(\theta)$	Mean frequency at a crank angle θ
h	Manometer fluid height in bend wall pressure measurements
k	· Turbulent kinetic energy $\equiv \frac{1}{2}(\tilde{u}^2 + \tilde{v}^2 + \tilde{w}^2)$ · Anemometer transfer constant $\equiv \frac{2\pi}{\lambda/2\sin\phi}$ $(\text{rad}\cdot\text{m}^{-1})$, equation (3.4)
ℓ	· Crankpin length in model compressing engine, equation (2.4) · Typical large eddy size, equation (3.5)
L	Connecting rod length in model compressing engine, equation (2.4)
N_{ph}	Number of zero crossings counted, equation (2.15)
$N(\theta)$	Count rate (number of Doppler signals per unit time) at a crank-angle θ
p	Wall pressure in curved duct
p_{ref}	Reference value of p, at $\theta = 0^o$, $r^* = 0$, $z^* = 0$

r	Radial coordinate direction in engine cylinder and curved duct
r_i	Radius of curvature bend inner (suction) surface
r_o	Radius of curvature of bend outer (pressure) surface
r^*	Normalised radial coordinate $\equiv \frac{r - r_o}{r_i - r_o}$
R	· Engine cylinder radius (Chapter 2) · Correlation coefficient $\equiv \frac{\overline{uv}}{\tilde{u}\tilde{v}}$ (Chapter 3)
R_c	Mean radius of curvature of bend $\equiv 0.5\ (r_i + r_o)$
Re	Reynolds number $\equiv \frac{V_{p\ max}\ 2R}{\nu}$, $\frac{V_c\ D_H}{\nu}$
R_r	Radius ratio $= \frac{R_c}{D_H}$
$R_{1,2}$	Inner and outer radii of cylinder head annular port
S	· Model engine stroke length, equations (2.1), (2.2), (2.3) · Swirl number, equation (2.19)
$\tilde{u}$	R.m.s. of velocity fluctuations in axial/streamwise direction
$\tilde{u}(\theta)$	Value of $\tilde{u}$ at a crank angle θ
$\overline{uv}$	Cross-correlation between $\tilde{u}$ and $\tilde{v}$
$\overline{uw}$	Cross-correlation between $\tilde{u}$ and $\tilde{w}$
U	Velocity in axial (z) direction (Chapter 2) or in streamwise (X_H, θ) direction (Chapter 3)
$\bar{U}$	Mean velocity in axial (Chapter 2)/streamwise (Chapter 3) direction
$\bar{U}(\theta)$	Value of $\bar{U}$ at a crank angle θ
$\tilde{v}$	R.m.s. of velocity fluctuations in radial (r) direction
$\overline{vw}$	Cross-correlation between $\tilde{v}$ and $\tilde{w}$

V	Velocity in radial (r) direction
$\bar{V}$	Mean velocity in radial (r) direction
V_c	Bulk mean velocity
V_p	Instantaneous piston velocity
$\bar{V}_p$	Mean piston velocity
$V_{p_{max}}$	Maximum piston velocity
$\tilde{w}$	R.m.s. of velocity fluctuations in circumferential direction (Chapter 2) and in spanwise (z) direction (Chapter 3)
W	Velocity in circumferential (Chapter 2)/spanwise (Chapter 3) direction
$\bar{W}$	Mean velocity in circumferential (Chapter 2)/ spanwise (Chapter 3) direction
X	Streamwise direction coordinate in bend tangents
X_H	Streamwise distance along bend tangents, expressed in hydraulic diameters
z	Axial (Chapter 2)/spanwise (Chapter 3) coordinate direction
$z_{\frac{1}{2}}$	Half-width of curved duct
z^*	Normalised spanwise coordinate $\equiv \frac{z}{z_{\frac{1}{2}}}$

Greek characters

α	Angle of crankshaft rotation in model compressing engine, equations (2.4) and (2.5)
α_1	Anisotropy coefficient $\equiv \frac{-\overline{uv}}{1.5(\tilde{u}^2 + \tilde{v}^2)}$
δ	· Distance of the piston from the cylinder head, equation (2.4) · Boundary layer thickness (Chapter 3)

$\Delta\theta$	Crank-angle interval
ΔR	Throat opening in annual port inlet on cylinder head = $R_2 - R_1$
ε	Isotropic rate of dissipation of turbulent kinetic energy
ε_r	Relative timing error in the frequency measured by counter, equation (2.15)
η	Kolmogorov length microscale
θ	· Crank angle · Streamwise coordinate direction in curved duct
λ	Wavelength of laser light
μ	Dynamic viscosity of fluid
ν	Kinematic viscosity of fluid
$\bar{\nu}_D$	Mean Doppler frequency
$\tilde{\nu}_D$	R.m.s. of Doppler frequency fluctuations
ρ	Density of fluid
σ	Standard deviation of scattering volume dimension, equations (2.9) and (2.10)
σ_b	R.m.s. due to broadening contributions, equations (2.7) and (2.8)
σ_D	Total measured r.m.s. of fluctuations, equation (2.7)
σ_v	R.m.s. of fluctuations due to the flow turbulence
$\sigma_{F,g,l,T}$	R.m.s. broadening contributions due to finite transit time, velocity gradient, finite instrument bandwidth and small scale fluctuations within the control volume respectively
σ_3	Scattering volume dimension near the Kolmogorov micro-scale, equations (2.9) and (3.4)

τ_i	Mean time between particle arrivals at the scattering volume
τ_s	Mean time between Doppler signals contributing to a measurement
τ_t	Time-scale of turbulence
ϕ	· Half-angle of beam intersection at scattering volume, equation (2.11), Table 3.2 · Angle of measured inlet component orientation to the cylinder axis (Chapter 2) · Angle of flow direction to the cylinder head (Chapter 2) · Representation of fluid mechanical quantities such as $\bar{U}$, $\tilde{u}$ etc. (Chapter 3)
ψ	Stream function
ω	Angular speed of engine crankshaft (Chapter 2)
ω_e	Rotational speed of the engine
ω_f	Rotational speed of swirling flow in engine, assuming solid-body rotation

Operator

<....>	Time-averaged quantity

Subscripts

e	Quantity contributing to measured value due to errors
h	High
l	Low
m	Quantity measured

Superscript

*	Normalised coordinate (Chapter 3)

Abbreviations

A,B	After and Before, used in conjunction with BDC, etc.
BDC	Bottom dead centre
EVC	Exhaust valve closing
EVO	Exhaust valve opening
IVC	Inlet valve closing
IVO	Inlet valve opening
TDC	Top dead centre

CHAPTER ONE

INTRODUCTION

1.1 The flow configurations

This thesis describes investigations of reciprocated and of strongly curved flows. The main part of the work is concerned with the velocity characteristics of the flows which were quantified by laser Doppler anemometry. Flow visualisation was also used to acquire qualitative knowledge of the flow in a curved duct, in which wall pressure measurements were also obtained.

The in-cylinder aerodynamic characteristics of reciprocating internal combustion engines are important to the engine performance and efficiency (Blumberg et al, 1979) and are currently intensively researched because of the increasingly stringent requirements for fuel economy and control of exhaust emissions. In-cylinder conditions, the unsteady nature of the flow and its highly complicated structure pose, however, significant problems for measurement as well as analysis. Most of the information on internal combustion engines to date has been obtained on specific engines through trial-and-error procedures and by global measurements in which the engine was treated as a "black box" and its inputs and outputs monitored for different running conditions (Obert, 1968). Empirical methods have resulted in highly refined engines but new requirements have still to be met.

The cost of an engine development programme along the above lines is considerable and calculation methods have been developed which show promise for predicting the in-cylinder processes more economically with considerable detail and accuracy. They are not, however, totally predictive and require inputs which include inlet and outlet conditions

and assumptions for the turbulence structure (see e.g. Gosman et al, 1978 a). Experimentation is thus inevitably required to ascertain the degree of validity of the methods and provide the necessary inputs.

A detailed investigation of all the factors affecting the in-cylinder flow and combustion is, however, a very lengthy task. These factors can be broadly classified into intake-, compression-, and combustion-related effects on the in-cylinder processes, and take part in that order during the cycle. The present contribution, as an initial investigation, is consequently directed towards gaining better understanding of the intake-generated flow structure and related processes.

The intake flow is important in determining the mixing process prior to combustion, as the requirements of enhanced mixing, prevention of the deposition of unburnt fuel on the walls etc. demand vigorous highly turbulent air motion. Small scale high intensity turbulence is normally required in spark ignition engines (Ma, 1975) as the fuel and air are premixed, and large scale turbulent motion in compression ignition engines in order to distribute the fuel jet. As both the mean motion and the turbulence affect the engine performance, they are promoted by the means described below.

During the induction stroke the descending piston draws in air through the inlet port and valve which constitutes a restriction to the flow and causes a high velocity annular jet. The resulting flow structure in the cylinder is complex and can be usefully resolved into axial, radial and tangential velocity components. The axial component is produced by the motion of the piston and the radial by the deflection of the flow at the port and the asymmetry of the cylinder head. The tangential velocity, swirl, is important, particularly in

Diesel engines where it must persist until the injection of the fuel in order to carry fuel particles away from their point of entry, and is produced primarily by the flow entering through, for example, a combination of a masked valve and a directed port or a helical port (see e.g. Fitzgeorge and Allison, 1963).

The structure described above is used during compression and combustion. In Diesel engines, if a bowl exists on the piston crown, a strong rotation about the cylinder axis is produced in the bowl near TDC of compression; a vigorous radial motion of the gas in the space between the piston and cylinder head is also observed, termed squish (see e.g. Dicksee, 1940). In spark ignition engines disc-type chambers are normally used, and turbulence generators are often incorporated in the inlet passages (Ma, 1975).

In order to describe the in-cylinder flow, it is therefore important to quantify the mean and turbulence structure, and to examine the influences of relevant parameters such as inlet geometry, piston geometry and swirl.

The second configuration examined is that of a square duct of strong curvature, referred to hereafter as the "bend", relevant to those encountered in the manifolds of reciprocating internal combustion engines and in the intake ducts of aircraft gas turbine engines. Manifolds are generally of complex shape, often with transition from round to oval or near-rectangular cross-section. In addition, they involve bends, of varying curvature and deflection angle, to redirect the flow (see e.g. Annand, 1969). The positioning of the turbines on the aircraft, dictated by aerodynamic and other requirements, frequently requires the use of curved passages also, to intake the air to the turbine. Bends of various centreline and cross-sectional shapes are

again employed for this purpose. A uniform flow is required at the compressor face for efficient turbine operation. The flows through bends, though, are dominated by pressure-gradient induced cross-stream flows which involve significant pressure losses and a major redistribution of the flow downstream of the bend; in order to minimise these losses, an understanding of the secondary flow development is essential. The present investigation of a square-sectioned, 90-degree bend is intended to allow the quantification of the important flow characteristics influencing the pressure-driven secondary flows for a simplified geometry. Thus, understanding will be improved and an accurate basis provided for the development and testing of relevant calculation methods.

Secondary flows are generated in bends as in order to turn the flow a higher pressure is required along the outer wall surface than along the inner one. Low-momentum fluid from the boundary layer is acted upon by the cross-stream pressure gradient and is swept along the side walls towards the low static pressure region on the inside of the bend. The movement and accumulation of the momentum defficient fluid near the inner wall sets up two secondary flow cells (see e.g. Nippert, 1929). It is convenient to distinguish between the "core" flow - the region of larger streamwise velocity - moving slowly towards the outer wall, and the boundary layer/secondary flow rushing towards the inner surface and resulting in a helical motion in the inside of the bend. These pressure-driven flows are known as secondary flows of the first kind (Prandtl, 1926), and are an inviscid, rotational flow phenomenon. Although the mechanism is an inviscid one, there must be non-uniform velocity distributions at the bend inlet for the generation of the secondary flow, which is thus related to the inlet boundary layer thickness. In rectangular bends of high aspect ratio the secon-

dary flows are confined to regions close to the side walls and the core flow is nearly two-dimensional. In intake ducts, aspect ratios close to unity are normally employed and the flows are predominantly three-dimensional.

The turbulence structure is also affected by the curvature, as low energy particles accumulate near the inner wall and energy transfer and dissipation are reduced (Miller, 1978). Conversely, fluid particles near the outer wall have a higher momentum and the flow is stabilised near the inner convex surface with a corresponding decrease in shear stress while it is destabilised near the concave surface with an increase in shear stress.

For the bend flow investigation, it is important to determine, therefore, the magnitude of the pressure gradient, the streamwise and cross-stream velocities, the turbulence structure and the influence of the inlet boundary layer thickness.

The motivation for the choice of the flows investigated is threefold. Firstly, the applications of the two flow regimes in engine systems are practically and fluid mechanically diverse and cover a range of flow processes. In-cylinder flow is characterised by high shear and turbulence which are generated at intake with the intention of persisting until the ignition of the fuel/air mixture. In curved ducts, pressure-induced flows hinder the objective of redirecting the flow with minimal losses and disturbance. Secondly, they are both internal flows, presenting the problem of access for measurement which calls for the application of laser Doppler anemometry with its characteristic advantages. Thirdly, as both types of flow have applications in internal combustion engines, they are currently researched with interest due to the energy crisis. Finally, although

calculations are not presented for either flow in this thesis, the ability to calculate the flows is an important part of the background to the motivation for the work.

The remainder of this chapter is divided into three sections. In the following section previous work, both experimental and theoretical, is reviewed in order to outline the current knowledge of the flows and identify relevant parameters and variables of interest. The present objectives and contribution are formulated in the light of previous work in section 1.3 and the chapter concludes with an outline of the remainder of the thesis. In order to avoid repetition, topics of relevance to both flows are expressed in the in-cylinder flow investigation part and are only referred to in the bend flow part.

1.2 Literature survey

1.2.1 In-cylinder flow

Most previous studies, both experimental and theoretical, have focussed on specific aspects of the flow such as the intake and related structure, squish, swirl, fuel sprays and combustion. The body of literature dealing with the last two subjects has been omitted from this review which concentrates on the flow processes relevant to the intake and, to a lesser extent, the compression stroke.

Experiments

The most relevant experimental investigations are listed in Table 1.1 and consist mainly of:

(1) steady flow or "blowing" tests to determine intake port characteristics with pressure probes;

(2) rotating vane anemometer tests in steady flow conditions to determine the intake generated swirl patterns;

(3) visualisation of in-cylinder flow to obtain qualitative information;

(4) hot-wire anemometer, or

(5) laser Doppler anemometer measurements to describe the mean and turbulence flow fields. Some measurements by spark discharge or ionization techniques have also been reported.

The earliest studies of in-cylinder air motion were made in the manner of (1) above, to assess the pressure drop performance of intake ports. Tanaka (1929) for example, examined suction valves of conical seats with results which showed discontinuities in the coefficient of discharge through the valve as the valve lift was varied. Dennison et al (1953), Wood et al (1942), Kastner et al (1963) and Annand (1969) have produced similar experimental data and verified the existence of four modes of flow through the port at different valve lifts. For small lifts the flow boundaries remain close to the wall of the valve passage and as the lift increases a vena contracta is formed by the valve head diverting the flow. In the third mode, occurring in slightly higher lifts, the flow breaks away from both the valve head and seat. For larger valve lifts there is no more breakaway of the flow. An important consequence of these findings is that the prescription of appropriate inlet conditions in calculation methods is made very difficult.

Flow visualisation and rotating vane anemometer measurements have shown that the flow in Diesel engine cylinders is characterised by a spiral swirling motion, approximating solid-body rotation (Fitzgeorge and Allison, 1963). However, the rotating vane anemometer cannot give information on the offset of the swirl core or the deviation of the flow from solid-body rotation (Willis et al, 1966). Hot-wire anemometry has been used extensively for quantitative investigations

(Molchanov, 1953; Semenov, 1958; James, 1972; Dent and Derham, 1974; Tindal et al, 1974; Witze, 1977; and others) but, although qualitative trends as described below have been established, no detailed descriptions of the flow field are available.

The intake flow is known to be characterised by large spatial gradients which reflect a jet-like structure (Semenov, 1958). The intake mean structure depends on the inlet geometry: e.g. with directed ports there is only one centre of swirl rotation (Fitzgeorge and Allison, 1963) and swirl produced with a masked valve can have one or two swirl centres depending on the mask orientation, with solid-body rotation near the swirl centre and potential flow in the wall regions (Willis et al, 1966). During compression mean velocities decay (Semenov, 1958), but the swirl rotation persists until the end of compression (Tindal et al, 1974), and as TDC is approached swirl velocities in the piston bowl increase rapidly (Horvatin and Hussmann, 1969). A double toroidal motion is set up in the piston bowl near TDC as a result of the strong squish motion (Dicksee, 1940) which is not always present in firing runs, and reverse squish is often present during expansion (Alcock and Scott, 1962). Both mean and turbulence velocities have been observed to increase linearly with engine speed (e.g. James and Lucas, 1975; Lancaster, 1976; Witze, 1977; Wakisaka et al, 1979).

Profiles of mean velocity are both useful and interesting because they describe not only the mean motion, but can also be used to deduce the streamline patterns in cylinders of axisymmetric geometries and thus evaluate the structure, size and intensity of the intake vortices which determine the in-cylinder mixing. In addition, the high

mean velocity gradients during intake are the main source of turbulence (Semenov, 1958) and there is a strong correlation observed between mean and turbulent velocities during the cycle (Lancaster, 1976); thus mean and r.m.s. velocity profiles can provide a good description of both the mean and the turbulence structure and are essential as detailed data are lacking.

Turbulence as well as mean velocities were found to decay continuously during compression after IVC (Inlet Valve Closing) until TDC (e.g. Dent and Salama,1975 a, b; James, 1972; Lancaster, 1976): turbulence is found to become uniform reaching a low level at TDC. Other measurements have shown constant turbulence during the whole of the cycle (Witze, 1976), or significant residual turbulence during compression at higher speeds (Cole and Swords, 1979). Turbulence measured during intake was anisotropic with high turbulence energy frequencies, which shifted towards lower frequencies during compression becoming increasingly isotropic (Lancaster, 1976). The energy containing eddies during intake were found to be in the 1-3 kHz frequency range and the macro length scale to be of the order of 1.8 - 2.2 mm (Semenov, 1958).

The response of the hot-wire allows high frequency resolution and, therefore, the measurement of flow characteristics (length scales, etc.) not easily obtained with other methods. However, the probe is obtrusive and its calibration depends on pressure and temperature, which vary over the cycle, and results can be in error (Asanuma and Obokata, 1972; Witze, 1976 b). The major advantages and shortcomings of the technique for in-cylinder applications are outlined by Horvatin and Hussmann (1969). The inability of the hot-wire to resolve the flow direction can, with significant effort, be overcome by, for example,

employing the spark trace method to detect the direction (Wakisaka et al, 1979), but its interference with the flow and calibration problems cast serious doubt on its use.

Witze (1978) made a comparative study between hot-wire anemometry and laser Doppler anemometry in-cylinder measurements in an engine modified for optical access. This study is useful as it provides a direct comparison of the two techniques for in-cylinder work. The laser Doppler and hot-wire results are in very good agreement until the middle of the compression stroke, but large discrepancies are found after that, especially in the turbulent velocities. The differences were attributed to the temperature sensitivity of the hot-wire anemometer, as results at different hot-wire operating temperatures varied significantly. In a similar critical comparison (Witze, 1980), it is concluded that the laser Doppler technique is far superior to the hot-wire method, primarily due to its inherent accuracy and secondarily because a hot-wire probe cannot be used purposefully (especially in a combusting engine) due to its inherent limitations (probe interference, lack of directional sensitivity, calibration problems) that cannot be overcome. Two difficulties are identified in the application of laser Doppler anemometry namely:

(1) gaining in-cylinder optical access in two orthogonal directions for the measurement of all three velocity components; and
(2) obtaining high data rates in order firstly to enable turbulence time-scale and power spectra measurements and secondly to make the data acquisition process faster and less laborious.

The suitability of laser Doppler anemometry for in-cylinder measurements was demonstrated by Melling and Whitelaw (1976a) in a model non-compressing engine and a motored Diesel engine. Although measure-

ments in real engines are desirable, the use of model engines has many advantages as in-cylinder conditions are less hostile than those of real engines and the experiments can be performed in configurations which are experimentally and conceptually simpler. The suitability of model engines for in-cylinder measurements is anticipated, as measurements in motored engines with and without compression show similarities until IVC (see e.g. Morse and Whitelaw, 1981) and as motored and firing runs give identical results up to the point of ignition (Asanuma and Obokata, 1979; Rask, 1979).

There are four important advantages in the use of model engines. First, the two difficulties associated with the application of laser Doppler anemometry (Witze, 1980) are minimised: in purpose-designed engines optical access is readily provided and higher and more constant data rates can be achieved throughout the cycle. Secondly, difficulties associated with the engine operation (leakage past the piston rings, optical window wear and contamination etc. (see e.g. Morse and Whitelaw, 1981) are also minimised; as a result of the easier operation measurement time is reduced. Thirdly, although the use of model engines does not obviate the need for measurement in real, firing engines, it facilitates the development of measurement systems and techniques for real engines in more favourable conditions. Finally, as present computer sizes limit most calculation methods to simpler-than-practice geometries (Gosman et al, 1979), the validation of such methods can be better achieved in purpose-built arrangements of simple geometry. The measurement of inlet conditions - which are very desirable for intake port design and calculation purposes - is only possible in model engines, although still with difficulty: this difficulty is manifested by the pronounced lack of inlet data on reciprocated flows.

Gosman et al (1978 b) measured the velocities in the axisymmetric model engine of Melling and Whitelaw (1976a) with an orifice and a pipe inlet which they compared with corresponding calculations. The same non-compressing engine was adapted for most of the work reported in the second chapter and in the relevant work reported in the literature (see e.g. Yianneskis, 1977 and Morse, Whitelaw and Yianneskis, 1979 a, b, c and 1980 a, b). Various other workers have used laser anemometry to measure in motored or firing real engines (Rask, 1978, 1979; Asanuma and Obokata, 1979; Cole and Swords, 1979; Morse and Whitelaw, 1981; Wigley et al, 1981).

Most laser Doppler systems have employed backscatter operation and the main measurement problems identified were the excessive spurious light scattered back into the optical system, the adjustment of the seeding particle generation, the contamination of the window, and the data rate which was not high enough to enable the separation of cycle-to-cycle variation from turbulence intensity as ensemble-averages had to be used (see e.g. Rask, 1978, 1979). Doppler signals have been processed by frequency counting, filterbanks and photon correlation methods. Frequency counters require the simplest means of data processing, while photon correlation techniques in particular require considerable effort to retrieve the desired information and cannot be justified simply on the suggested basis of the ability to obtain data over the cycle without artificial seeding (Cole and Swords, 1979).

Recent studies in motored and firing engines have reaffirmed previous findings and, although the accuracy and detail of measurements has been improved, only small regions of the flow are examined. Model engines have been employed for flow visualisation by Ekchian and Hoult (1979) and Namazian et al (1980) and for flow measurement by Bicen et

al (1980), Gany et al (1980) and Arcoumanis et al (1981 a, b, c, 1982) and are discussed in section 2.6 in relation to the results presented in this thesis.

Calculations

Exact solutions of the partial differential equations for the conservation of mass and momentum can only be achieved for simplified flow cases and other solution methods have to be employed. The earliest theoretical engine studies were thermodynamic in character and the equations solved were "zero-dimensional", i.e. spatial variations within the cylinder were ignored and only temporal (i.e. time or equivalently crank-angle) variations were considered. They were followed by one-dimensional models in which the three-dimensional forms of the partial differential equations were reduced to one-dimensional forms, by ignoring, or making assumptions about, the variations in two of the coordinate directions. Later multi-dimensional models were used to solve the equations in their two-dimensional (axisymmetric) or full three-dimensional forms. Many zero-dimensional models employed the "zonal" method, which is a rather crude approximation, while full-field modelling (in two or three dimensions) and large eddy simulation (in three dimensions) account better for the flow processes (Reynolds, 1978). The last method in particular is well suited to in-cylinder flows but present computer sizes prohibit its use.

Full-field modelling solutions are considered in this subsection, in which finite difference formulations for the equations for the conservation of mass and momentum in their laminar flow form or Reynolds-averaged form are solved, together with boundary conditions and turbulence models accounting for the velocity-fluctuation correla-

lations which appear in the equations. A comprehensive listing of relevant work is given in Table 1.2 and extensive surveys of zero- and one-dimensional models are given by Watkins (1977) and of multi-dimensional models by Johns (1980).

In-cylinder flow calculations must provide time-varying solutions, accommodate complex geometries and deal with a flowspace which is swept during the cycle. In the first attempt at multi-dimensional prediction made by Watkins (1973), the coordinate frame expanded and contracted with the piston motion to account for the swept flowspace. The compression and expansion strokes of an axi-symmetric engine were calculated with laminar flow assumed. A motored four-stroke cycle was subsequently computed with a varying-in-area annular opening simulating a centrally-located valve (Gosman and Watkins, 1976 b). The prediction code was assessed by comparisons of laminar and turbulent non-compressing cycle calculations with corresponding measurements (Watkins, 1977) and, although the major flow features were predicted, weaker motions (such as corner vortices) were not. Discrepancies were attributed mainly to errors arising from uncertainties in the inlet conditions specified.

Most calculations made to date have been performed for two-dimensional (axisymmetric) geometries. This is dictated at present by the considerable computational time and storage costs involved in the calculation methods, which are the result of the representation of a complex flow (recirculating, unsteady and involving steep gradients and complex geometries). In addition, the conceptual simplicity of two-dimensional configurations facilitates both the understanding of the flow and the evaluation of calculation methods. Although some three-dimensional calculations have been made (e.g. Griffin et al, 1978), the assumptions that need to be made to simplify the problem

and thus reduce the calculation costs make the results not very relevant to engine practice.

Predictions in which laminar flow was assumed have been reported by various authors (e.g. Boni et al, 1976; Chong et al, 1976; Griffin et al, 1976; Diwakar et al, 1976) and generally indicate the existence of a single vortex formed during intake and persisting until TDC of compression, with a nearly one-dimensional structure during expansion and a vortex of reverse rotation during the exhaust stroke. The approximations made in the calculations restrict severely though the usefulness of the results.

Chong et al (1976) used a 10 x 5 computational grid and their method of "masking" part of the grid to simulate a bowl on the piston head resulted in a time-varying bowl depth. Boni et al (1976) produced a good representation of a cylinder geometry with a prechamber but also employed a coarse grid. The discrepancy in the size of the vortex predicted by Boni et al in comparison to that present in the flow visualisation of Tabaczynski et al (1970) is attributed to the numerical errors arising from the coarseness of the grid; however, the vortex of Tabaczynski et al bears no direct relation to the intake-generated vortices (see discussion in section 2.6). The inviscid calculations of Diwakar et al (1976) made use of a coarse grid and are in agreement with the three-dimensional inviscid calculations of Griffin et al (1978), but very different to the viscous calculations of Griffin et al (1976) who employed a similar technique. The valve representation in the four-stroke simulation of Griffin et al (1976) was made by only one grid point on the cylinder head, and resulted in the prediction of a nearly one-dimensional flow structure for most of the flow space.

Ramos et al (1979) calculated the flow in an axisymmetric engine cylinder with a centrally located valve opening and closing

instantaneously. The calculations were later extended (Ramos et al, 1980) to include swirl and a valve representation by an annual orifice of varying area (cf. Gosman and Watkins, 1976 b). With the annular "valve" two eddies are present until the end of compression, while there is only one with the "sudden-valve" idealisation. The differences indicate the inappropriateness of the "sudden-valve" and the authors' claim of obtaining the same trends with both valve representations is not substantiated by the results presented.

The discrepancies in the solutions obtained seem to stem partly from the existence of regions of steep gradients of velocity during intake, which require significant grid refinement to take account of the gradients and to reduce numerical (truncation) errors also, and partly from the crude representation of complex geometries. Gosman and Johns (1978) accounted for these problems by employing a combination of curvilinear-orthogonal and rectilinear grid systems, which were refined in regions of steep gradients, to accommodate cylinder and piston bowl geometries in predicting the velocity and turbulence fields of the compression and expansion strokes. Their results showed a strong influence of both swirl level and bowl shape on the TDC flow structure, which consisted of several vortices at high swirl levels. In similar calculations of the flow in a two-dimensional idealisation of the "Howerd" engine geometry (Gosman et al, 1979) complex prechamber geometries were also incorporated successfully. Recent calculations by Johns (1980), discussed further in section 2.6, in configurations similar to those investigated in this thesis, have yielded reasonable quantitative agreement with experimental results.

The problem of the representation of turbulence was dealt with by Gosman and Watkins (1976 a) with the incorporation of the

"k-ε" model (Jones and Launder, 1972) in the prediction code. Calculations of the flow showed that the solution was strongly influenced by the radial velocities prescribed at the inlet plane (Gosman et al, 1978 a). These velocities affected the spread and subsequent decay of the indrawn jet and therefore the associated turbulence structure predictions were poor. Gosman et al identified also the need for models taking into account contributions from all turbulent scales present in the flow, which they accounted for by their method of "statistical flux modelling".

Calculation results show clearly that most of the turbulence (and the problem of its prediction) is generated at the shear layers of the intake jet (Ramos et al, 1979). Thus the calculation of turbulence reintroduces the problem of grid refinement as it is linked with the mean motion and corresponding gradients. Although validation of the calculation methods is rather scarce, the difficulties in the accurate prediction of the mean flow due to numerical and inlet condition uncertainties are evident and the turbulence models used cannot be easily assessed.

Combustion-related work by Syed and Bracco (1979) showed that the "k-ε" model was far superior in the calculation of the turbulence structure and flame propogation than the constant diffusivity assumption of Gupta et al (1978). Recent work to incorporate combustion in the flow field modelling by Ahmadi-Befrui et al (1981) showed the suitability of the use of the dissipation-control hypothesis with the employment of the "k-ε" model. More complicated turbulence models, such as the Reynolds-stress models (Launder, Reece and Rodi, 1975) have not found much use in engine flow predictions, as the increase in computational cost due to the extra number of equations to

be solved is considerable.

In conclusion, two-dimensional calculations can represent accurately cylinder geometries and predict the qualitative flow features, but are limited at present due to uncertainties in the inlet conditions prescribed and the numerical errors introduced mainly by the coarseness of the grids employed.

Summary of findings

The most important findings of the preceding survey are outlined in this sub-section.

(1) Experimental data on in-cylinder flows have indicated qualitative trends but are in general limited in not having sufficient detail of description of the flow processes, in that they do not quantify the influence of geometrical and other parameters on the flow, and in their accuracy of measurement.

(2) Laser Doppler anemometry has been shown to be the most suitable technique for in-cylinder measurements of the mean and turbulence velocities.

(3) Measurements obtained in firing runs and in motored runs with compression were identical up to the point of ignition, and mean velocities measured in motored compressing and non-compressing cycles were very similar up to the closure of the intake valve, while r.m.s. velocities were lower under compressing conditions.

(4) During intake the flow is determined to a large degree by the geometry of the port, which induces an annular jet; a significant amount of turbulence is generated at the edges of the incoming jet.

(5) The solution of the finite difference formulation of the conservation equations is the most viable method for in-cylinder flow calculations at present. The investigation of axisymmetric config-

urations is suggested at present by the computer size limitations, its conceptual simplicity and the similarities with fully three-dimensional flows. Flexibility of representations of cylinder and piston head geometry can be allowed for, as shown by the codes of Gosman et al (1978 b) and Boni et al (1976). The representation of turbulence has been achieved with the use of the "k-ε" model to date and the use of more advanced turbulence models is not deemed necessary.

(6) Qualitative agreement with experiment has been achieved with the above calculation methods; uncertainties due to e.g. inlet conditions exist and validation of the calculations is required. Experimental data for direct detailed quantitative comparisons are very scarce; such comparisons have been carried out only by Watkins (1977) and Johns (1980).

(7) In view of (3) and (6) above, and of present computer sizes restricting calculations to simple geometries only, measurements in model axisymmetric engines are at present of importance to in-cylinder flow studies, as they can promote the understanding of the physical processes in conceptually simple arrangements and they can provide the only means of experimental verification of the current flow predictions.

(8) The main parameters of importance for the intake flow processes identified are the cylinder geometry, swirl and engine speed; mean and r.m.s. velocities are appropriate variables for the description of the flow.

1.2.2 Curved duct

An extensive survey of work related to bend flows has been provided by Humphrey (1977) and, in order to avoid repetition, the

present survey refers only to more recent studies or to those omitted from Humphrey's work. The most widely researched applications of curved flows are those related to aircraft intakes, turbine blade passages and blood vessels. It is useful to distinguish between two- and three-dimensional investigations as the nature of the flow depends on the duct geometry; two-dimensional experimental studies are considered briefly at the end of the following sub-section. All experimental bend flow studies cited are listed in Table 1.3.

Experiments

The occurrence of secondary flows in bends motivated measurements of the mean flow and of the streamwise (longitudinal) pressure gradient. Total and wall static pressures were mainly measured in early investigations (see e.g. Ward-Smith, 1971). An extensive study of this nature was carried out by Nippert (1929), for a number of flow parameters. The effects of the secondary flows could not be quantified in Nippert's work as cross-stream velocities were not measured, but they can be assessed from flow visualisation and the presented isotachs of streamwise velocities at the exit planes of bends of 90^{o} and 180^{o} deflection angles. The generation of secondary flow was found to increase with the upstream tangent length (and the associated different inlet boundary thicknesses) and the bend flow became more three-dimensional as the aspect ratio was reduced.

The measurement of the cross-stream velocities was made possible with the development of the hot-wire and the laser Doppler anemometer. Humphrey et al (1977, 1981) made detailed laser Doppler measurements of fully-developed laminar and turbulent flows in a square duct. The flow development was similar in both regimes, but flow visualisation revealed a region of recirculation near the inlet in the

laminar case. The use of laser Doppler anemometry allowed the measurement of the flow development within the bend (as opposed to only that in the exit plane measured in most studies) which is important for the understanding of the secondary flow generation. The investigation of similar developing flows is additionally interesting because of the different growth of the boundary layers in the laminar and turbulent flow regimes and the associated considerably different inlet velocity distributions. The results of Humphrey et al are discussed further in section 3.7.

Developing laminar flows in curved pipes of 180^{o} deflection angles have been measured by Agrawal et al (1978). Streamwise and cross-stream velocities were measured, although the latter are presented for different flow conditions and positions to the former. A weak secondary flow of the first kind was found just downstream of the inlet, and as the boundary layers became thicker further downstream an additional pair of vortices was present near the inner wall. Apart from the three aforementioned studies, no investigations of quantitative detail have been reported for three-dimensional curved flow regimes. There are no reported measurements of the third velocity component (in the spanwise direction), which are quite necessary to the flow description, especially in regions where more vortices are present. For example, Cheng et al (1979) showed the existence of instabilities, in the form of Görtler-like vortices, along the outer wall of the exit of 180^{o} rectangular bends, with fully developed laminar flow entering the bend.

Developing flows in ducts relevant to aircraft intakes have been reported only for round cross-section S-ducts (Bansod and Bradshaw, 1972), and for two-dimensional flow in the symmetry plane of an S-duct of large aspect ratio (Butz, 1979). Bansod and Bradshaw found a low

pressure region in the duct exit which they attributed to the existence of secondary flows generated by the duct curvature in the first bend and intensified by vortex stretching in the second bend. Butz's investigation showed that in the absence of secondary flow interference, a near-potential flow structure is present in the centre of the duct.

The physiological aspect of curved flows has been examined by Choi et al (1979), Lin and Tarbell (1980) and Mullin and Greated (1980 a, b), who studied the flow in curved pipes with and without oscillation as occurring in the arterial blood vessels. Choi et al's results indicate that secondary flows have a stabilising effect on the flow development in curved tubes; it is also suggested that several pairs of vortices are present in developing flow, in contrast with one pair normally found in fully-developed flow. Mullin and Greated examined both developing and fully-developed flow and found that the inlet velocity distribution determined the secondary flow generation and the extent of the effects of curvature on the flow.

The secondary flow losses in relation to the flow in turbo-machinery blade cascades have been investigated in two rectangular bends by Bruun (1979). The measurements presented indicate a direct relationship between the decrease in total pressure and the turbulence in the exit plane. Smaller secondary flows were measured in the bend with the thinner inlet boundary layers, although the secondary flow development was similar in both bends. Weak inward flows were measured near the outer wall at the bend exits, with a Görtler-vortex pattern present in a 1.5 aspect ratio bend. Bruun's results show the importance of the pressure losses and of the effect of the pressure gradient and centripetal forces on the flow, and show that turbulence has only a minor role in the flow development. However, Humphrey's (1977) results have shown that with fully-developed flow at the bend inlet, although

the turbulence levels did not exceed 0.14 of the bulk velocity, Reynolds-stress driven secondary flows (Melling, 1975) were present in the bend.

It is important thus to quantify the turbulence structure in developing flows and to determine its effect on the overall flow development. Contours of the mean and r.m.s. streamwise velocity components would indicate the presence of stress-driven secondary flows. The measurement of turbulence levels allows the estimation of the kinetic energy of turbulence and thus the evaluation of the role of turbulence in the flow. The magnitude of the turbulence parameters is expected to be smaller in developing than in fully developed flows (Bruun, 1979), and the measurement of such parameters in more detail than is necessary in fully-developed flows would be indicated in order to resolve the turbulence structure adequately.

The effects of curvature on the two-dimensional turbulent boundary layer structure are well understood. Mildly curved flows have been examined by Hoffmann and Bradshaw (1978) and Ramaprian and Shivaprasad (1978). The results of the latter, however, were obtained in a duct of 2.5 aspect ratio, too small to ensure two-dimensionality, and their results exhibited significant errors, both consistent and random. Hoffmann and Bradshaw (1978) found that concave surface curvature generally increased turbulent mixing, and led to the appearance of spanwise variations, associated with the Taylor-Görtler vortex pattern. Their data define the turbulence structure in detail and suggest useful parameters for the evaluation of curvature effects.

Calculations

The vast majority of recent theoretical studies has employed the numerical solution of the finite difference forms of the mass and

momentum conservation equations and are discussed in this section. Some analytical solutions have also been obtained, as e.g. by Singh (1974), Yao and Berger (1978) and Hunt and Joubert (1979). Analytical solutions are, on the whole, restricted to flows with very small curvature effects and are not very relevant to the flow case studied. All the investigations and their major findings are listed in Table 1.4.

Various solution procedures have been employed for the calculation of bend flows, in view of the fact that recirculations may or may not be present in the flow. Forward marching techniques, which make use of a previously calculated inviscid pressure field, have been employed in the prediction of developing flows by Eiseman et al (1978), Levy et al (1980) and Towne and Anderson (1981). A similar parabolic technique was used by Leschziner and Rodi (1979), using a guessed pressure field stored in all three dimensions while the variable fields were stored in two dimensions. Although a single-pass calculation is performed through the field for velocity, the pressure field is elliptic (i.e. influences the upstream flow)and is swept through a number of times in an iterative fashion, in order to account for the upstream influences. However, Humphrey et al (1977, 1981) suggest the need for fully-elliptic procedures in their calculation of fully-developed strongly curved flows, especially as their flow visualisation revealed a recirculation region at the bend inlet.

Humphrey (1978) extended the procedure of Humphrey et al (1977) to developing pipe flows, subsequently including heat transfer in the calculations (Yee and Humphrey, 1979). Although the results show the flow fields to be highly elliptic in strongly curved bends, it is suggested that a semi-elliptic procedure (in which only pressure is stored in three dimensions) would be appropriate if no streamwise flow

recirculation exists. Yee and Humphrey compared elliptic and parabolic solutions of the same numerical procedure and found significantly better agreement of the former with experimental data.

All the investigations show qualitative agreement with the limited experimental data available, but quantitative comparisons are poor. Discrepancies are larger in regions near the side and inner walls where steep gradients are present. This limitation of calculations, similar to that encountered in in-cylinder ones, points to the need for grid refinement which could be economically achieved by the use of parabolic procedures. Moreover, deviations of the flows calculated from the potential flow structure assumed for the pressure field specified initially in single-pass calculations (Eiseman et al, 1980) inevitably result in quantitative discrepancies with experimental data. Better agreement with such data has been achieved in the calculations of Leschziner and Rodi (1979) and Humphrey et al (1977, 1981). The latter calculated also the decay of the flow downstream of the bend which is important in practice in determining the extent of the bend influence to the supply duct in intakes.

De Vriend (1981) used a numerical solution of the Navier-Stokes equations but reformulated the radial and vertical (spanwise) momentum equations and the equation of continuity for the secondary flow in terms of a stream function in order to reduce the number of equations to be solved. The method was validated by comparisons of the results with other numerical, analytical and experimental data but it has not yet been widely tested.

The calculation of the turbulence structure was made by Humphrey et al (1981) by the use of the "k-ε" model. Their work indicated that turbulence modelling errors are not as important as numerical errors in view of the small contributions of the turbulence

structure to the flow development. Stress-transport models have not been used in the calculation of turbulent bend flows, as simpler turbulence representations are expected to be appropriate, especially in developing flows where turbulence generation is weaker; such flows provide an appropriate testing ground for turbulence models due to their low turbulence content.

The validation of models such as that based on k and ε, suggests the need for the measurement of the kinetic energy of turbulence and its constituent turbulence levels. A knowledge of the magnitudes of the cross-correlations arising in the averaged form of the equations can furnish an appraisal of the need of their modelling.

Summary of findings

The following is a summary of the most important findings of the preceding survey of bend flows.

(1) Pressure-driven secondary flows are present in curved duct flows, and their generation and magnitude is strongly related to the inlet boundary layer thickness.

(2) The pressure gradients present in a bend are important to the flow development, while turbulence has only a minor role. Knowledge of the mean velocity components is desirable in order to describe the flow patterns and of turbulence quantities such as the kinetic energy of turbulence and its constituent normal stresses in order to quantify the effects of turbulence in comparison with those of the pressure induced motions.

(3) Flow visualisation of bend flows is useful as recirculation regions, however small, may be present.

(4) Detailed investigations of three-dimensional bend flows have been

reported by Humphrey et al (1977, 1981) and Agrawal et al (1978). There are no detailed data on developing laminar and turbulent flows in curved square ducts. The measurement of the flow within and downstream of the bend is important in order to determine the generation and decay of the secondary flows.

(5) Calculations of the flow employing the numerical solution of the conservation equations have shown that the major flow features can be predicted but discrepancies with experimental data exist and are primarily attributed to numerical errors which were found to be larger than turbulence modelling errors.

1.3 The present contribution

It is clear from the preceding section that the information available to assist understanding of the flows in the cylinders of reciprocating engines and in bends is far from complete. In both cases, previous investigations have been lacking in detail and, at least as important, the quantitative influence of flow and geometrical boundary conditions has not been determined. These deficiencies occur largely because of the absence of instrumentation to allow them to be removed.

In the case of reciprocating engines, the preliminary work of Melling and Whitelaw (1976a) and Gosman et al (1978b) has shown that laser Doppler anemometry can, with careful application, allow the determination of the velocity characteristics of in-cylinder flows. Thus, one major purpose of the present work was to develop laser Doppler anemometry for use in piston-cylinder flows and to determine the influence of variations in relevant geometrical and flow conditions. The complete task is a long one and involves a step-by-step process from determining the influence of idealised inlet arrangements in the absence

of compression and combustion to the variation of fuel injection parameters in combusting Diesel engines. The present objectives were restricted to the investigation of the flow in relation to the intake process, and in particular to examine the influences of a pipe and of a stationary valve inlet, of a flat and of a bowl piston head geometry, of swirl and of engine speed on the flow patterns in a motored, two-stroke cycle without compression, and of an operating valve inlet in a motored four-stroke cycle with compression.

Within this scope, the research was conducted to provide measurements which would explain the differences in the flow patterns and aid their interpretation for design purposes. At the same time the measurements can allow the appraisal and improvement of calculation methods and care was taken, for example by measuring close to the inlet arrangements, to provide data appropriate for this purpose. The in-cylinder measurements in all but one configuration were made in axi-symmetric arrangements and this choice was made mainly to simplify the task of understanding the measured flow patterns. This point is illustrated by the complexity of the flow measured in asymmetrical arrangements such as that presented in Appendix 2.1. At the same time, of course, the required number of measurements is reduced and calculation requirements are satisfied which, at the present time, are concerned mainly with axisymmetric arrangements.

In view of the previous measurements of Humphrey et al (1977, 1981), there was less need for instrumentation development in the bend flows but changes were still necessary to improve the conduct of the measurements and they are reported in section 3.3. It can be appreciated from the work of Nippert (1929) and Mullin and Greated (1980 a, b) that secondary flows are strongly dependent on the boundary layer thickness at the bend inlet and the present purpose was to determine the flow

patterns in developing flow with inlet boundary layers which were thin in comparison with the fully developed flows of Humphrey et al.

1.4 Thesis outline

The remainder of this thesis is divided into three chapters. The following two chapters present the work related to each of the two configurations examined. The last chapter provides a summary of the more important conclusions and suggestions for future work.

Chapter two deals with the work on reciprocating engine flows. After a brief introduction, the engines and the laser Doppler anemometer systems are described in detail in sections 2.2 and 2.3 respectively. Measurement uncertainties are analysed in detail in sub-section 2.3.5. The results obtained in the model non-compressing engine are presented in section 2.4 in order of complexity of flow configuration examined. The measurements made in the model compressing engine are included under section 2.5. A discussion follows in section 2.6 of the effects of the geometrical parameters, swirl, engine speed and compression on the flow, and of the importance of the results for real engines. The discussion is concluded with an appraisal of the significance of the results for calculation methods. The chapter is closed with a summary of the main findings.

The investigation of bend flows is presented in chapter three. An introduction to the work is followed by a description of the bend rig, instrumentation and measurement procedures in sections 3.2 and 3.3. The results of the flow visualisation, and measurements of wall pressures, of the laminar and turbulent flow velocities and of the Reynolds stresses are presented in sections 3.4 through to 3.6. The results are discussed primarily with respect to the effects of inlet

boundary layer thickness, Reynolds number, curvature and turbulence in section 3.7 and considered in relation to relevant flow calculations. In the last section, the most important conclusions of the chapter are listed.

In the final chapter the main conclusions of the thesis are stated and recommendations are made for future work on the flow configurations examined and for the techniques employed for the investigation of the flows.

TABLE 1.1

EXPERIMENTAL INVESTIGATIONS OF THE FLOW IN RECIPROCATING ENGINE CYLINDERS

Author(s);Year	Flow Configuration	Technique	Findings
Tanaka; 1929	Steady flow through suction valves of conical seats	Pressure probes	Discontinuities found in the variation of the coefficient of discharge with valve lift
Alcock; 1934	Motored engine	Rotating vane anemometer	Swirl ratio of 10 found necessary for optimum engine performance
Lee; 1939	Motored 4-stroke engine	Photography of flow visualisation with feathers	Intake air motion observed to persist through compression and to be suppressed during expansion with non-shrouded intake valves
Dicksee; 1940	Motored Diesel engine with toroidal bowl piston	Visualisation of flow on cylinder surfaces with aluminium paint	Double toroidal motion suggested to be present in bowl, with a spiral flow pattern found to exist in the flow space
Molchanov; 1953	Motored disc-chamber engine	Hot-wire anemometry	Highest velocities recorded at 60^{o} AIVO; increase in turbulence levels near TDC of compression stroke
Semenov; 1958	Motored disc-chamber engine	Hot-wire anemometry	Mean and turbulence velocities decayed during the start of compression;velocity gradients during intake found to be the major source of turbulence
Alcock & Scott; 1962	Motored Diesel engine with toroidal piston bowl	High speed photography of flow visualisation with cotton tufts	No evidence of squish found prior to TDC, but significant reverse squish observed after TDC
Fitzgeorge & Allison; 1963	Steady flow through cylinder head assemblies	Rotating vane anemometer and flow visualisation	Influence of port shape on in-cylinder flow and swirl determined; spiral solid-body rotation type of swirling motion observed
Kastner et al; 1963	Flow through stationary and reciprocating valves and in a piston/cylinder assembly	Pressure probes	Different flow regimes through the ports encountered for different valve lifts; effects of inlet parameters on cylinder volumetric efficiency evaluated
Willis et al; 1966	Model engine simulating intake stroke with water as the medium	Photography of flow visualisation with lucite beads	Solid-body rotation observed near the cylinder centre and potential flow in the outer regions in the cross-stream planes
Annand; 1969	Steady flow through intake valves	Pitot probes and manometers	Three types of flow at different lifts were observed and bi-stable flow at low lifts

TABLE 1.1 (cont.)

Author(s);Year	Flow Configuration	Technique	Findings
Horvatin & Hussmann; 1969	Motored Diesel engine	Hot-wire anemometry with probes plunging into holes on the piston	Velocity increased approximately linearly with speed; swirl increased in the piston bowl at TDC of compression, with near-solid-body type of rotation
El-Khafaji et al; 1971	Motored Petter Diesel engine	Hot-wire anemometry with probe mounted on traversing mechanism	Development of hot-wire anemometry for in-cylinder work. A circuit providing automatic gas temperature compensation was incorporated in the normal constant temperature operation
Arnold et al; 1972	Motored engine with hemispherical cylinder head and flat piston crown	Hot-wire anemometry with both moving and fixed probes	Mean velocities decayed during compression and remained low during expansion with some increase in the exhaust stroke
Asanuma & Obokata; 1972	Flat-top piston engine with air entering tangentially through side valve	Hot-wire anemometry and high speed photography of high voltage spark discharge	Swirl decayed more at low speeds and swirl ratios were very high; no pressure or temperature corrections made to the hot-wire calibration
James; 1972	Spark-ignition engine with flat and piston bowl geometry	Hot-wire anemometry	No indication of squish at low compression ratios but some reverse squish present; mean velocity varied linearly with engine speed. Turbulence decreased by 50% from IVC to TDC at 1450 rpm but was nearly constant at 700 rpm
Huebner & McDonald; 1972	Motored model Diesel engine with two-valve cylinder head	Hot-wire anemometry, paddle-wheel anemometer and flow visualisation with a grid of tufts	Non-solid-body rotation found in most geometries; no effects of engine speed noted, apart from near the piston crown; angular momentum decreased with decreasing compression ratio
Ohigashi et al; 1972	Firing 4-stroke Diesel engine	Electric spark discharge	Intake flow was different in motored and firing runs, but the swirl motion near TDC was the same in both
Asanuma & Obokata; 1973	Swirling water flow inside a rotating cylinder, impulsively stopped at start of observation	Photography of the movement of aluminium powder in water	Recirculations observed near the cylinder wall/piston corners
Dent & Derham; 1974	Motored Diesel engine	Hot-wire anemometry; probes attached to the piston and penetrating holes on the cylinder head	Swirl increased linearly with engine speed; solid-body rotation present for most of intake and compression strokes; swirl increased by 25% with masked valve

TABLE 1.1 (cont.)

Author(s);Year	Flow Configuration	Technique	Findings
Tindal et al; 1974	Motored Diesel engine with flat and part spherical recess piston crowns	Hot-wire anemometry with probe following the piston motion	Velocities were higher at TDC with the bowl piston geometry
Dent & Salama; 1975a, b	Spark-ignition engines with wedge and "Heron" combustion chambers	Hot-wire anemometry	Mean and turbulent velocities decayed until IVC, but with the wedge chamber they increased until 20^{0} BTDC and then they decayed at TDC with both chambers
James & Lucas; 1975	Motored spark-ignition engine with squish and disc-type chambers	Hot-wire anemometry	Most turbulence energy contained in frequencies below 700 Hz; low frequency fluctuations (below 200 Hz) increased linearly with speed
Woods & Ghirlando; 1975	Motored engine with both flat and bowl piston crowns	Hot-wire anemometry and flow visualisation	Squish was negligible with flat piston, but significant with bowl piston; reverse squish present in both cases
Lancaster; 1976	Motored engine with disc chamber and valves with and without shroud	Hot-wire anemometry; tri-axial probe for simultaneous 3-component measurement	Mean and turbulence velocities increased linearly with speed; turbulence decayed after IVC; cycle-to-cycle variations up to 35% were measured
Melling & Whitelaw; 1976a	Motored Diesel engine and model non-compressing engine	Laser Doppler anemometry	Development and testing of in-cylinder measuring systems; frequency counting found appropriate for signal processing and backscatter optics found suitable for Diesel engine
Witze; 1976 a,b,c	Motored Wisconsin L-head engine	Hot-wire anemometry	Mean velocities were maximum at 110^{0} ATDC of intake and 20^{0} BTDC of compression; turbulence intensity was virtually constant
Morse; 1977	Motored model non-compressing engine	Laser Doppler anemometry	Crank-angle broadening effects quantified; values obtained with 1^{0} and 10^{0} crank-angle windows were different by 2% in the mean and 10% in the r.m.s. values in general
Witze; 1977	Motored Wisconsin L-head engine	Hot-wire anemometry	Mean and turbulence velocities shown to vary linearly with engine speed; turbulence structure near cylinder head found to be inhomogenous
Gosman et al; 1978b	Axisymmetric motored non-compressing engine	Laser Doppler anemometry	Vortical nature of flow observed with orifice and pipe inlets; the jet trajectory was the determining factor in the resulting vortex structure

TABLE 1.1 (cont.)

Author(s);Year	Flow Configuration	Technique	Findings
Hoult & Wong; 1978	Axisymmetric water model simulating intake process	Flow visualisation; photography of polystyrene beads in water	Ring vortex generated at intake found to break up for bore-to-stroke ratios greater than one and the vortex stability depended on valve location and engine speed
Ishikawa & Daily; 1978	Square cross-sectioned model engine	High speed Schlieren cinematography	Appreciable effects of turbulence found, attributed to the rolled-up vortex and wall turbulence
Rask; 1978	Motored L-head engine with high swirl chamber	Laser Doppler anemometry	In-cylinder flow was of highly vortical nature, with turbulence velocities distributed uniformly during compression
Wigley & Hawkins; 1978	Steady flow through directed and helical ports	Laser Doppler anemometry	Helical port produced ordered flow approaching solid-body rotation; directed port found to produce higher velocities and two main recirculation zones
Witze; 1978	Motored Wisconsin L-head engine	Hot-wire anemometry and laser Doppler anemometry	Comparison of the two measurement techniques; hot-wire results inaccurate near and after TDC due to their temperature dependence
Asanuma & Obokata; 1979	Motored and firing Honda engine	Laser Doppler anemometry	Differences observed in the squish velocities and the flow through the nozzle between motored and firing tests during the expansion stroke
Cole & Swords; 1979	Motored engine	Laser Doppler anemometry	Linear dependence of mean and turbulence velocities on engine speed; local flow structure existed near spark plug; significant residual turbulence at high speeds
Davies & Kent; 1979	Steady flow through axi-symmetric ports; motored PROCO research engine	Angular momentum flux swirl meter spark discharge/time of flight method	Swirl found approximately proportional to engine speed influences of inlet configurations on swirl determined
Ekchian & Hoult; 1979	Water analogue model engine simulating intake process	Flow visualisation; photography of polystyrene beads in water	Small geometric changes influenced flow significantly; bi-stable intake jet observed at low lifts; linear dependence of velocity on engine speed
Rask; 1979	Motored and firing L-head "Onan" engine	Laser Doppler anemometry	Flow field of highly vortical nature observed; mean and r.m.s. velocities scaled with engine speed
Wakisaka et al; 1979	Motored Diesel engine	Hot-wire anemometry; oil-film and smoke-wire visualisation; spark discharge method	Strong turbulence of low frequency content measured; length scales independent of speed but mean and r.m.s. velocities increased with engine speed

TABLE 1.1 (cont)

Author(s);Year	Flow Configuration	Technique	Findings
Gany et al; 1980	Motored axisymmetric model with and without compression	Laser Doppler anemometry	Similarities found in intake flow patterns with moving and stationary valves; cycle-to-cycle variations considered to be not important
Namazian et al; 1980	Square cross-sectioned firing spark ignition engine	Schlieren photography and high-speed cinematography	Cylinder head/wall corner vortex found to be present in all four strokes
Williams & Tindal; 1980	Motored direct injection Diesel engine with toroidal, re-entrant and simplified re-entrant bowl configurations	Hot-wire anemometry with both fixed and moving probes	The existence of toroidal air motion in toroidal bowls was verified; in the re-entrant bowls the air motion divided into two streams and swirl levels were higher, persisting longer during expansion.
Morse & Whitelaw; 1981	Motored Petter Diesel engine with and without compression	Laser Doppler anemometry	Similarities found in intake flow with and without compression; swirl structured into solid-body rotation as TDC is approached; swirl centre moving during the cycle
Wigley et al; 1981	Motored and firing Diesel engine	Laser Doppler anemometry	Swirl velocities similar in motored and firing runs prior to injection; swirl was always less after ignition than found in the motored runs

TABLE 1.2

THEORETICAL INVESTIGATIONS OF THE FLOW IN RECIPROCATING ENGINE CYLINDERS

Author(s);Year	Flow Configuration	Type of Solution	Findings
Watkins; 1973	Piston reciprocating within a cylinder; compression and expansion strokes	Numerical solution of the conservation equations of mass, momentum and energy	The formation of an annular vortex was calculated as the piston approached TDC and the flow reverted to a nearly one-dimensional behaviour during expansion
Boni et al; 1976	Axisymmetric model of a divided chamber, stratified-charge engine	Numerical method of Hirt et al (1974) used to solve conservation equations for 5 species, energy and momentum in two directions	The method allowed geometrical flexibility; spatially oscillating solution was obtained, presumably of numerical origin
Chong et al; 1976	Laminar flow in an axisymmetric engine with a flat and a cylindrical bowl piston	Numerical solution of the conservation equations of mass, momentum and energy	Effect of engine speed and compression ratio on the flow examined; flat-top piston results in agreement with Watkins (1973) for speeds below 100 rpm with a one-dimensional flow present at higher speeds
Diwakar et al; 1976	4-stroke engine simulation with only axial inlet motion specified at intake	Inviscid solution with Griffin et al (1976) method	Single vortex calculated to be formed during intake persisting until TDC of compression, being suppressed during expansion and a second vortex formed during exhaust
Gosman & Watkins; 1976a	As in Watkins (1973)	Numerical method of Watkins (1973) with the incorporation of a turbulence model by two additional equations for the kinetic energy of turbulence (k) and its rate of dissipation (ε)	Effects of engine speed, compression ratio and bore/stroke ratio on the in-cylinder heat transfer rates was investigated
Gosman & Watkins; 1976b	4-stroke cycle simulation with a disc-shaped chamber and a single centrally located valve represented by an annular opening of varying area		Strong recirculation found to develop soon after the start of intake which remained during compression, with one-dimensional flow during expansion and a sink-flow structure during exhaust. Turbulence was high during intake, diminishing during compression and increasing again during exhaust
Griffin et al; 1976	Two-dimensional piston-cylinder arrangement	Numerical solution of the conservation equations for mass, momentum, and thermal energy	No turbulence modelling was included in the calculation; the flow predicted was nearly one-dimensional; numerical instabilities are apparent in the solution
Watkins; 1977	Laminar and turbulent flow in a 2-stroke cycle without compression with a pipe inlet; compression/expansion strokes with compression	Method of Watkins (1973) and Gosman and Watkins (1976a,b)	Comparison with non-compressing measurements showed the major features were predicted but weaker motions were not; discrepancies attributed to inlet condition uncertainties

TABLE 1.2 (cont.)

Author(s);Year	Flow Configuration	Type of Solution	Findings
Boni; 1978	Simulation of a Honda CVCC prechamber engine	Numerical method of Boni et al (1976) with an improved differencing scheme	Turbulence representation was not included; the structure at TDC of compression calculated consisted of a single vortex in both the prechamber and the main chamber
Gosman & Johns; 1978	Compression and expansion strokes in an axisymmetric engine cylinder	Method of Gosman & Watkins (1976 a) with the incorporation of curvilinear orthogonal grids	Effect of piston bowl geometry and swirl ratio on the flow investigated; TDC flow structure calculated was complex and affected by both parameters
Gosman et al; 1978a	Axisymmetric flow in an engine cylinder with an orifice and a pipe inlet without compression	Numerical method of Gosman & Watkins (1976a)	Comparisons with experimental data showed that most of the qualitative features of the flow were predicted
Griffin et al; 1978	Three-dimensional inviscid flow in a cylinder with diametrically opposed valves	Numerical method of Griffin et al (1976) with an artificial viscosity term introduced to avoid numerical instabilities	A recirculation was calculated to be generated during intake, which persisted until the TDC of the compression stroke
Gosman et al; 1979	Plane two-dimensional representation of the "Howerd" prechamber engine cylinder; compression and expansion strokes predicted	Method of Gosman & Watkins (1976 a) with the incorporation of curvilinear orthogonal grids	During compression a large eddy was calculated to be present in the prechamber with a small one in the main chamber; the trends were reversed during expansion
Ramos et al; 1979	Axisymmetric laminar and turbulent 4-stroke cycle in a disc-type chamber with an "instantaneous" intake/exhaust process	Numerical solution of the conservation equations for mass, momentum and energy with k-ε model for turbulent flow representation	In laminar flow a large vortex is formed during intake, which decays during compression and expansion; in turbulent flow the turbulence generated at the shear layers during intake is convected and diffused during the cycle
Syed & Bracco; 1979	Divided chamber stratified charge engine simulation	Numerical solution of conservation equations for mass, momentum, energy and species with "k-ε" turbulence model	Computations divided into 3 stages with different condition assumed for each stage; "k-ε" model found appropriate for the prediction of combustion processes but the results were sensitive to the initial conditions for k and ε specified
Johns; 1980	Compression and expansion stroke predictions in axisymmetric geometries with and without piston bowls;	Numerical method of Gosman & Watkins (1976a) with the incorporation of curvilinear/orthogonal grids to represent complex geometries	Non-compressing 2-stroke cycle predictions in agreement with experimental data of Morse et al (1979b) 4-stroke cycle predictions in reasonable agreement with the data of Witze (1976c)

TABLE 1.2 (cont.)

Author(s);Year	Flow Configuration	Type of Solution	Findings
	(cont.) 4-stroke predictions with operating valve; 2-stroke cycle predictions without compression		
Ramos et al; 1980	2- and 4-stroke configuration of Ramos et al (1979) with the incorporation of swirl and an annular valve of varying area	Numerical method of Ramos et al (1979)	Two eddies calculated to be formed during intake: one in the cylinder head/wall corner persisting up to TDC of compression and one behind the infinitely thin valve used to simulate intake; valve representation was unrealistic and 2-stroke results show poor agreement with the experiment
Ahmadi-Befrui et al; 1981	Idealised homogeneous-charge spark-ignited engine geometry: disc-type chamber with centrally-located spark plug and inlet/exhaust valve	Numerical method of Gosman & Watkins (1976 a) with a dissipation-control combustion model	Results were obtained for a range of engine speeds and showed correct trends; the flame front did not provoke significant increase in the turbulence levels of the unburnt gases

TABLE 1.3

EXPERIMENTAL INVESTIGATIONS OF THE FLOW IN CURVED DUCTS

[For additional investigations see Humphrey (1977)]

Author(s);Year	Flow Configuration	Technique	Findings
Nippert; 1929	Circular and rectangular ducts of various aspect ratios, inlet tangent lengths deflection angles and curvatures	Static and total pressure measurement; flow visualisation	Effects of inlet tangent length, curvature, inner and outer wall radius variation, cross-sectional shape etc. on the streamwise isotachs and static pressure distribution determined
Bansod & Bradshaw; 1972	Round cross-section S-shaped ducts ($22.5^{o}/22.5^{o}$ with and without spacers)	Static and total pressure, surface shear stress and yaw angle measurements	Region of low total pressure in the exit plane attributed to the existence of a pair of contra-rotating vortices generated by the duct curvature
Humphrey et al; 1977	90^{o} square duct of 2.3 radius ratio; laminar fully developed inlet flow	Laser Doppler anemometry and flow visualisation	Velocity maximum found to migrate towards the outer wall; secondary velocities up to 0.65 of the bulk were measured; small recirculation observed at the outer wall near the inlet
Agrawal et al; 1978	Round cross-section ducts of 20 and 7 radius ratios, 180^{o} deflection angle; thin inlet boundary layers; laminar flow	Laser Doppler anemometry	Secondary flows of the first kind measured upstream, with an additional vortex structure generated near the inner wall downstream
Hoffmann & Bradshaw; 1978	Rectangular duct of 6.0 aspect ratio, radius ratio of 20 and thin inlet boundary layers	Hot-wire anemometry	Effects of curvature on turbulence structure parameters determined for two-dimensional flow, along the convex and concave curved walls
Ramaprian & Shivaprasad; 1978	Rectangular duct of 2.5 aspect ratio, radius ratio of 25 and thin inlet boundary layers	Hot-wire anemometry	Curvature effects found to be more significant in the outer region of the boundary layer; convex curvature suppressed the diffusion of turbulent energy from the wall
Bruun; 1979	Rectangular ducts of 2.0 and 1.5 aspect ratios, 120^{o} deflection angle, 3.0 radius ratio, with thin and thick inlet boundary layers	Pressure probes, static pressure measurement and flow visualisation	Core flow adjustment to the pressure field completed by the first 15^{o} in the bends; secondary velocity maxima of 0.25 of the bulk found at the bend exits; weak inwards flow existed near the outer wall; turbulence kinetic energy at exit was only a few percent of the total pressure losses

TABLE 1.3 (cont.)

Author(s);Year	Flow Configuration	Technique	Findings
Butz; 1979	Rectangular S-ducts (30^{o}-45^{o} and 45^{o}-45^{o}) of 5.6 aspect ratio, 5.0 radius ratio and turbulent thin inlet boundary layers	Hot-film anemometry and laser Doppler anemometry	Potential-like flow measured at the duct symmetry plane; concave and convex wall curvatures found to accelerate and retard the growth of the boundary layers respectively
Cheng et al; 1979	Rectangular ducts of aspect ratios 1-12 with 5.0 and 40.0 radius ratios, and fully developed laminar flow at the inlets	Flow visualisation	Additional vortex pairs observed to appear near the outer wall of the ducts; their presence and number depended on the aspect ratio and curvature; the vortices are generated by Dean's hydrodynamic instability
Choi et al; 1979	Curved pipe of 180^{o} deflection angle, 7.0 radius ratio; laminar developing flow	Electrochemical limiting current method for the measurement of wall shear rates	Presence of several vortex pairs suggested; potential vortex flow formed in upstream core; wall shear stress enhanced by the secondary motion; inner wall shear decreased downstream, while outer-wall shear increased.
Hunt & Joubert; 1979	Rectangular duct of 13.2 aspect ratio and 100 radius ratio; developing turbulent flow	Pressure probes and hot-wire anemometry	Taylor-Görtler vortex pattern found to occur in the central flow region; streamline curvature effects shown to be determined by the central region flow structure only; suggested that flows with small curvature are "shear-dominated"
Lin & Tarbell; 1980	Helical curved tube coil; laminar fully developed periodic flow	Flow rate-pressure drop measurements (differential pressure transducer)	Resonance between the axial and secondary flows postulated to exist at intermediate pulsating frequencies
Mullin & Greated; 1980 a, b	Curved pipe of 180^{o} deflection angle and 7.0 radius ratio; laminar developing and fully developed periodic flow	Laser Doppler anemometry	Inlet vorticity found to determine the extent of upstream influence of curvature and secondary flow generation; for low frequencies the flow is quasi-steady and for some frequencies both viscous and inertial effects are important
Humphrey et al; 1981	Square duct of 90^{o} deflection angle, 2.3 radius ratio fully developed turbulent flow	Laser Doppler anemometry	Secondary velocities up to 0.28 of the bulk measured; stress-driven secondary flows insignificant in comparison. Core flow is located near mean radius until 71^{o} and thereafter moves towards outer wall

TABLE 1.4

THEORETICAL INVESTIGATIONS OF THE FLOW IN CURVED DUCTS

[For additional investigations see Humphrey (1977)]

Author(s);Year	Flow Configuration	Type of Solution	Findings
Singh; 1974	Inlet flow in a curved pipe	Analytical method of matched asymptotic expansions	The geometry and the nature of the entry condition found to influence the initial flow development appreciably; pressure distribution not significantly influenced by secondary flow during the initial development of the motion
Humphrey et al; 1977	Laminar fully-developed flow in a 90^{o} square duct of 2.3 radius ratio	Fully-elliptic solution of finite difference formulation of the Navier-Stokes equations in cylindrical coordinates	Results in reasonable agreement with measurements; observed recirculation near the inlet predicted
Eiseman et al; 1978	Laminar and turbulent flow in S-shaped ducts of circular, elliptic and super-elliptic cross-sections	Parabolic 3-dimensional solution of finite difference equations with technique of McDonald & Briley (1975)	Secondary flow in S-ducts found to reverse its direction after the first bend
Humphrey; 1978	Laminar flow in curved 90^{o} pipes and annuli of strong curvature	Elliptic solution of the Navier-Stokes equations in finite difference form	Flow reversal calculated at the outer wall of a curved pipe of radius ratio of 1.0 between 9^{o} and 21^{o} of deflection; secondary flows up to 80% of the bulk velocity calculated at 45^{o} after the bend entry. Two pairs of vortices predicted in the annular flow calculations
Singh et al; 1978	Oscillatory flow in a curved pipe inlet	As in Singh (1974)	Oscillation of the flow found to cause the flow to behave in a near-inviscid manner at first with thin boundary layers, with secondary flow effects becoming pronounced later
Yao & Berger; 1978	Fully-developed laminar flow in a heated curved pipe	Analytical solution of governing equations of motion and energy	Solutions presented for horizontal and vertical curved pipes, taking account of buoyancy and centrifugal forces; both effects found to introduce secondary flows of the first kind
Hunt & Joubert; 1979	Rectangular duct of 13.2 aspect ratio and 7.0 radius ratio; developing turbulent flow	Analytical solution of momentum energy and Reynolds-stress equations	A conservative reorientation of turbulent energy components is suggested as the significant mechanism by which streamline curvature effects are manifested

TABLE 1.4 (cont.)

Author(s);Year	Flow Configuration	Type of Solution	Findings
Leschziner & Rodi; 1979	Turbulent flow in rectangular 180^0 curved channels of mild and strong curvature	Parabolic numerical solution of the 3-D finite difference equations of continuity and momentum with k-ε model of turbulence	Model predicted the gradual formation and decay of transverse surface slope and secondary motion and the redistribution of streamwise velocities reasonably
Moore & Moore; 1979 a,b	Compressible flow in a rectangular 90^0 elbow; 2-D inviscid and 3-D viscous turbulent flow	Numerical solution of parabolic conservation equations with an elliptic pressure correction; turbulence "mixing length" type of model	Secondary flows predicted in good agreement with measurements;use of a simple turbulence model justified
Yee & Humphrey; 1979	Laminar flow (and heat transfer) in 90^0 rectangular bends	Numerical solution procedure of Humphrey et al (1977)	Effect of inlet velocity conditions, duct geometry and wall temperature to the flow and heat transfer calculated; secondary flows were found to enhance heat transfer on the outer bend wall. Heat transfer favoured by aspect ratio of unity and strong curvature
Levy et al; 1980	Turbulent flow in an S-shaped pipe	Forward marching numerical technique of Briley & McDonald (1977)	Vortex movement in the duct predicted in reasonable agreement with measurements
Lin & Tarbell; 1980	Helical curved tube coil; laminar fully-developed periodic flow	Numerical solution of the finite difference form of the Navier-Stokes and continuity equations	Dean-type vortices were predicted,but no Lyne-type ones due to the flow oscillation were present; calculations restricted to slow flows. High shear stresses at outer wall predicted, and indications of resonant frequencies between axial and transverse flows
Mullin & Greated; 1980b	Helical curved tube coil; laminar fully-developed oscillatory flow	Numerical solution of linearized Navier-Stokes equations using finite Hankel integral transforms	Two- or four-vortex system of Lyne-type found to appear depending on the values of the frequency and amplitude parameters of the flow oscillation
De Vriend; 1981	Laminar flow in coiled rectangular channels	Numerical solution of Navier-Stokes equations	The transverse transport of main-flow momentum by the secondary flow shown to be the principal cause of streamwise velocity redistribution; wall regions very important for channel flow
Humphrey et al; 1981	Turbulent fully-developed flow in a square bend	Numerical solution procedure of Humphrey et al (1977) with k-ε model of turbulence	Mean velocity results considered not strongly dependent on the turbulence model employed; numerical errors stated to be of greater importance

TABLE 1.4 (cont.)

Author(s);Year	Flow Configuration	Type of Solution	Findings
Humphrey & Pourahmadi;1981	Turbulent developing two-dimensional curved channel flow	Numerical solution of Navier-Stokes equations with k-ε model incorporates an expression for coefficient including streamwise curvature and wall pressure fluctuation effects	Discrepancies of the predictions with experiments attributed to GÖrtler vortices on the outer wall; the model overpredicted the kinetic energy near the inner wall
Towne & Anderson; 1981	Laminar developing flow in a round-section S-duct	Numerical solution of Navier-Stokes equations by forward marching with a predetermined "inviscid" pressure field.	Qualitative agreement obtained with experimental data; the secondary flow generated at the first bend found to be intensified in the second bend

CHAPTER TWO

FLOW IN RECIPROCATING ENGINE CYLINDERS

2.1 Introduction

The experimental investigations of in-cylinder flows outlined in section 1.3 are presented in this chapter. Laser Doppler anemometry was employed to quantify the mean and turbulence flow structure in two motored model engines, one of which operated without compression in a two-stroke cycle and one with compression in a four-stroke cycle. The major part of the work was made without compression; a detailed description of the intake stroke was obtained for a range of parameters. The effects of cylinder and piston head geometry on the flow patterns were examined progressing from an idealised pipe inlet to a more practical valve geometry with a combination of plane and cylindrical-bowl piston heads and the influences of swirl and engine speed on the flow were also determined. The study with compression was made with an axisymmetric disc-chamber geometry with an operating valve. Thus a comparative study has been made of the effects of cylinder and piston head geometry and of related flow conditions to determine their influence on the in-cylinder flow and, in particular, on the intake-related processes.

The model engines employed are described in the following section. The laser Doppler anemometer, which made use of one optical system with minor alterations and a variety of signal processing systems, is described in section 2.3 and associated measurement uncertainties are discussed. As there was little previous application of the technique to in-cylinder flows, there was scope for development and improvement of measurement systems, which are described in detail. The results obtained in the non-compressing engine are presented in section 2.4 and those obtained in the compressing engine in section 2.5.

The measurements obtained are presented in temporal and spatial detail such as to give an extensive yet concise description of the flow. A listing of the configurations investigated and of the components measured in each is given in Table 2.1.

TABLE 2.1

IN-CYLINDER FLOW CONFIGURATIONS AND VARIABLES MEASURED

Flow configuration \ Variable measured	$\bar{U}$	$\bar{V}$	$\bar{W}$	$\tilde{u}$	$\tilde{v}$	$\tilde{w}$	Inlet	
							$\bar{U}$	$\tilde{u}$
Model non-compressing engine (200 r.p.m.)								
Pipe inlet, plane piston	X			X			X	X
Valve inlet, plane piston, no swirl	X			X			X	X
" " , cylindrical-bowl piston, no swirl	X			X				
" " , plane piston, 15° swirl vanes	X		X	X		X		
" " , " " , 30° " "	X	X	X	X	X	X		
" " , " " , " " " , 100 and 300 r.p.m.	X		X	X		X		
Offset valve, plane piston, no swirl	X		X	X		X		
Model compressing engine (200 r.p.m.)								
Valve inlet, plane piston, no swirl	X			X				

Axial components were measured in all configurations and swirl components where relevant. The high swirl configuration was measured in significant detail and is presented at length as it was considered to be the case most relevant to practice as well as to calculations. In the two plane piston configurations without swirl, velocities near the inlet were also measured in order to describe the flow near the port and obtain inlet data relevant for calculations of the flow. For economy of presentation,

measurements in a configuration with an asymmetric inlet are reported in Appendix 2.1. The results are discussed in section 2.6 and related to previously obtained data, and their implications for numerical methods and turbulence modelling are considered. The chapter closes with a summary of the most important conclusions.

2.2 Description of the flow configurations

The two engines employed for the measurements were purpose-designed to maximise optical access to the flow space and their modular construction allowed the variation of geometrical and flow conditions. The non-compressing engine is described in the following sub-section. The design of the second engine, which was made more robust to withstand compression, was based on experience gained with the first and the engine is described in sub-section 2.2.2.

2.2.1 Non-compressing engine

The engine cylinder was precision-bored from Perspex to allow optical access, with a wall thickness of 3.5 mm, and was mounted with its axis horizontal. The clearance between the cylinder and the piston, of $0.1^{+0.05}_{0}$mm was sealed by polythene piston rings located sufficiently far from the piston head, so as not to wipe the part of the cylinder where optical access was required. Contact was limited by using eight PTFE studs, located four at each end of the piston, thus eliminating the need for lubrication and minimising friction.

The piston was driven in simple harmonic motion by a drive shaft connected to a cross-head and moving on pairs of orthogonal slide bars. The engine was motored by a geared electric motor allowing variable speed control, from 0-350 r.p.m. All the measurements presented in this chapter, with the exception of some of those presented in sub-section 2.4.5, were made at an engine speed of 200 r.p.m. The peak Reynolds

number was determined by the peak piston velocity, cylinder diameter and kinematic viscosity of air at $20^{o}C$ and 1 bar, as $Re = 3.18 \times 10^{3}$. The fluid velocities encountered, which were frequently ten times the peak piston velocity, and the shearing nature of the flow ensured that turbulent diffusion was much greater than laminar diffusion except in the immediate vicinity of the walls.†

The engine operated on a two-stroke cycle, intake and exhaust only, as a consequence of the continuously open port and there was no compression. A constant stroke length was used, although variation of the stroke was possible in the assembly. The engine characteristics are tabulated in Table 2.2.

As the piston was driven in simple harmonic motion (as is shown in sub-section 2.3.4), the piston velocity at a crank angle θ is given by

$$V_p = \frac{S\omega\sin\theta}{2} \qquad (2.1)$$

Where S is the stroke and ω the angular speed of the crankshaft. Thus the peak piston speed (at 90^{o} and 270^{o} crank angles) is

$$V_{p\ max} = \frac{S\omega}{2} \qquad (2.2)$$

At an engine speed of 200 r.p.m, $V_{p\ max} = 0.628$ m/s.

---

†Data on the transition to turbulence in such a configuration are not available, but the flow in a smooth pipe (cf. cylinder) becomes turbulent at a Reynolds number of 2,300 - based on the pipe diameter - (Schlichting, 1955), while a jet flow undergoes transition at a Reynolds number of around 50 based on the diameter (or the annular gap width in the case of the valve) of the jet outlet (Sato and Sakao, 1964); corresponding Reynolds numbers with the valve and pipe inlets used are approximately 1,000 and 8,000 respectively.

TABLE 2.2

MODEL NON-COMPRESSING ENGINE CHARACTERISTICS

Bore, mm	: 75	
Stroke, mm	: 60	
Clearance length, mm	: 30	
Bore-to-stroke ratio	: 1.25	
$\frac{\text{Swept volume + clearance volume}}{\text{clearance volume}}$	: 3	
Engine speed, r.p.m.	: 200	
Cylindrical-bowl diameter, mm	: 43	
depth, mm	: 21.5	
Valve lip diameter, mm	: 33.65	
annular aperture width, mm	: 4	
port length, mm	: ~7.5	(varying in different configurations)
seat angle	: 60^{o}	
Valve-to-cylinder diameter ratio	: 0.45	
Pipe inlet diameter, mm	: 18.75	
length, m	: 1.82	
Pipe-to-cylinder diameter ratio	: 0.25	

The mean piston speed through the cycle is

$$\bar{V}_p = \frac{1}{\pi} \int_0^{\pi} V_p d\theta = \frac{S\omega}{\pi} \qquad (2.3)$$

and at 200 r.p.m. $\bar{V}_p$ is 0.4 $^m/s$.

Cylinder and piston head arrangements

The modular design of the engine allowed the incorporation of various types of cylinder and piston heads. The piston was made from duraluminium with a Perspex crown which could be removed and interchanged. Two piston head configurations were used; one was flat to simulate a disc-type of chamber and the other had a cylindrical-bowl. The cylindrical-bowl was bored centrally in the Perspex piston head and had a depth which could be adjusted by a simple screw arrangement; the bowl depth was set equal to the bowl radius. The curved surface of the bowl was well polished to allow optical access inside the bowl without significant signal deterioration.

Two cylinder head arrangements were employed with the inlet located on the axis and one with an offset port. A long horizontal straight pipe inlet centrally located on the cylinder head was used first for geometrical simplicity. The air entered and left the cylinder through the pipe, a part of which was made from Perspex to allow measurements in the pipe. A jet of quasi-uniform velocity approximately sixteen times that of the piston was drawn into the cylinder. The second configuration consisted of a fixed metal valve inlet, centrally located on the cylinder head. The valve was held by a spring and set in a position by a detachable micrometer. The valve was located flush with the cylinder head to allow optical access for inlet profile measurements and the valve arrangement is shown in Fig. 2.1. The indrawn jet at the entry

plane had a velocity slightly less than ten times that of the piston.

Swirl was imposed on the entering flow by the incorporation of vanes upstream of the valve port and located radially around the valve stem. For the two sets of swirling flow measurements, swirl vanes inclined at 15^{o} and 30^{o} to the cylinder axis respectively were used.

The effect of asymmetrical inlet flow was examined with a cylinder head arrangement in which an identical valve geometry was employed, but offset by 8 mm from the cylinder axis as shown in Fig. 1 in Appendix 2.1. As the lack of symmetry required measurements in more than one diametrical plane, the head could be rotated and the optical axis aligned with diametrical markings (lines AB, CD, EF and GH on the figure).

In all cases the cylinder head was connected to a polythene bag in which the air was mixed with the seeding particles (see section 2.3.1). All cylinder/piston head geometries are shown in outline in the figures which present the results.

2.2.2 Compressing engine

On the basis of the experience gained with the non-compressing engine, a similar motored engine was designed to operate on a four-stroke cycle with moderate compression ratios. Similarity between the two engine geometries was maintained to enable direct comparison of the results.

The engine cylinder was made of Perspex with 12.58 mm wall thickness. It was fitted with a duraluminium cylinder head, which had a centrally located valve operated by a double cam mechanism coupled to the engine shaft. The motor could provide engine speeds up to 1,500 r.p.m. and was coupled through a pulley system,which allowed for speed variation, to a slider-crank chain to which the piston was attached by means of a connecting rod.

The flat piston head was fabricated from Perspex to allow optical access in future incorporation of piston bowls and to avoid thermal stressing of the Perspex part of the cylinder. The clearance between the piston and cylinder was 0.1 mm. The non-swept part of the cylinder and the rear of the piston was made of metal. Sealing on the piston end was achieved with a pair of PTFE rings, used also as guides for the sliding motion of the piston and bearing most of the wear, and three rings constructed of graphite reinforced plastic. The PTFE rings were reinforced by a set of phosphor bronze rings, of slightly larger clearance, in case of PTFE wear. The plastic rings were shaped so that their tips were pressed towards the cylinder wall during compression and thus leakage was minimised. A simple gravity-fed silicone oil lubricator was installed on the metal part of the cylinder to minimise friction and wear. Cooling water coils were wound around the metal part to maintain outside wall temperatures below 40^{o}C. For all the measurements reported, the engine speed was constant at 200 r.p.m.

The valve was used to intake and exhaust the air and fitted flush onto the cylinder head. The two cams were set into position by measuring the valve lift by means of a dial gauge and rotating the crankshaft until the gating circuit indicated the required crank-angle position. The resulting valve lift diagram is shown in Fig. 2.2. The engine characteristics are given in the following table. No swirl vanes were used for the compressing engine measurements reported.

The distance of the piston from the cylinder head, δ , is determined by

$$\delta = c + \ell\,(1 - \cos\alpha) + L\left(1-\sqrt{1-\left(\frac{\ell}{L}\sin\alpha\right)^2}\right) \qquad (2.4)$$

where c is the clearance length, ℓ the crankpin length - equal to the half-stroke (47 mm) -, L the connecting rod length (132 mm) and α the

angle of the crankshaft rotation, where $\alpha = \omega t$. Thus the piston velocity is

$$V_p = \omega \ell \left(\sin\alpha + \frac{\ell}{2} \frac{\sin 2\alpha}{\sqrt{L^2-(\ell\sin\alpha)^2}}\right) \qquad (2.5)$$

However, the piston reciprocated in approximately simple harmonic motion, as shown in sub-section 2.3.4. The mean piston velocity of the engine, assuming simple harmonic motion, is found by (2.3) to be 0.627 $^{m}/s$. Other variations of piston speed within a cycle were eliminated because of the inertia of the flywheel.

TABLE 2.3

MODEL COMPRESSING ENGINE CHARACTERISTICS

Bore, mm	:	75
Stroke, mm	:	94
Compression ratio	:	3.7
Valve diameter, mm	:	33.65
seat angle, degrees	:	60
lift (maximum), mm	:	7
dimensionless lift	:	0.20
"Intake" valve opening at	:	2^{o} BTDC
closing at	:	48^{o} ABDC
"Exhaust" valve opening at	:	48^{o} BBDC
closing at	:	2^{o} ATDC

2.3 Measurement systems and techniques

2.3.1 Laser Doppler anemometer optical systems

The optical arrangement used for the measurements presented in 2.4.2 and 2.4.3 is shown in Fig. 2.3(a). The beam from a Spectra Physics model 120 Helium-Neon laser (5mW at a wavelength λ = 632.8nm) was focussed by a plano-convex lens of focal length f_1 = 127 mm on to a diffraction grating. The bleached radial grating (manufactured by Optical Measuring Tools Ltd.) had 18,000 lines at a mean radius of 62mm, which split the incident beam, diffracting approximately half of the laser power into the first order beams. The grating was rotated at 2500 r.p.m. to produce a frequency shift between the first order beams. The two beams were allowed through a mask and subsequently focussed by a bi-convex lens of focal length 150mm to intersect in the scattering volume within the cylinder. Forward-scattered light was collected through a lens of focal length f_2 = 100mm and focussed on to a pinhole of 0.55mm diameter at the front of the housing of an RCA model 4836 photomultiplier (PM1 in Fig. 2.3(a)). The principal characteristic of the system (see Durst et al, 1976 , pp. 125-129) are given in Table 2.4, column (1).

To provide a continuous check on the applied frequency shift and therefore compensate for any drift in the speed of the rotating grating, a small proportion of the light in the incident beams was removed by means of a thin sheet of glass. The resulting beams were focussed onto a ground glass screen, from which scattered light was collected through a lens of focal length f_3 = 75mm and focussed on to the aperture of an EMI 9558B photomultiplier (PM2). The resulting signal was processed with a Cambridge Consultants CC01 frequency tracker, which gave an analogue voltage output proportional to the

modulation frequency.

A second type of grating, Technische Physische Dienst tno-th model H, was employed for the measurements of sub-sections 2.4.4, 2.4.5, 2.5.1 and 2.5.2. The grating had 16384 lines and its smaller diameter (35mm) and thickness provided an improvement in signal quality and ease of manipulation and alignment. It was driven by a Siemens 1AD-20 motor with a fixed speed control and its rotational speed was monitored by means of a digital counter (TSA model 6636/2) counting the time for a preset number of revolutions of the motor shaft. The grating was housed in an optical unit identical to that described by Taylor (1981) (see p.32), which allowed for beam rotation and elimination of spherical aberration. The characteristics of the modified system calculated according to Oldengarm et al (1976), are given in Table 2.4, column (2). The optical unit is shown in section in a similar system in Fig. 3.3(i) and in the photograph of Fig. 2.3(b).

TABLE 2.4

PRINCIPAL CHARACTERISTICS OF OPTICAL SYSTEMS

	(1)	(2)
Half-angle of intersection between beams, degrees	4.5	4.0
Fringe spacing, μm	4.0	4.53
Diameter of scattering volume at $1/e^2$ intensity, μm	58	150
Length of scattering volume at $1/e^2$ intensity, mm	0.73	1.9
No. of stationary fringes in scattering volume	14.5	33
Magnification of collecting optics	3.07	3.07
Frequency-to-velocity conversion factor, ms^{-1}/MHz	4.03	4.53
Frequency shift, MHz	±1.5	±1.84

Off-axis collection system

The inlet velocity profiles presented in sub-sections 2.4.2 and 2.4.3 were measured 0.5mm away from the actual inlet plane, with one of the beams parallel to and almost grazing the cylinder head as shown in Fig. 2.4. The optical axis was tilted so that the component measured was at an angle to the axial direction equal to the half-angle of beam intersection. This orientation necessitated off-axis light collection on the other side of the cylinder. The light was collected at 6^{o} to the optical axis and the loss in intensity was approximately 5% of the forward scattered light (see Vlachos, 1977). Measured mean and rms values are negligibly affected by such a small angle of off-axis collection. Signal quality was reduced by flare, caused by the reflection of the beams from the cylinder head on to the pinhole, and careful masking of the collected light was necessary.

As the optical axis was tilted by 4.5^{o} to the normal to the cylinder axis, the components measured along a diameter 0.5mm from the inlet plane in points located symmetrically about the cylinder axis are given by(assuming perfect symmetry) $V_1 = \bar{U}\cos\phi + \bar{V}\sin\phi$ and $V_2 = \bar{U}\cos\phi - \bar{V}\sin\phi$ so that $\frac{V_1 + V_2}{2} = \bar{U}\cos\phi = 0.996\bar{U}$ and $\frac{V_1 - V_2}{2} = \bar{V}\sin\phi = 0.078\bar{V}$ for $\phi = 4.5^{o}$. For the pipe inlet radial velocities were very small near the inlet. The contribution of the radial component was eliminated by the two measurements, but as the radial velocities were smaller than the axial ones, and only 7% of $\bar{V}$ was measured, errors from asymmetries (of the order of 3% of $\bar{V}_p$) exaggerated measurement errors and thus radial velocities were not calculated. In all other axial component in-cylinder measurements made the optical axis was located sufficiently far from the cylinder head (5mm or more), so that normal forward scatter operation (as shown in

Fig. 2.3(a)) was employed.

Seeding

Most of the measurements were made with the indrawn air seeded with silicone oil particles of 1μm mean diameter. The particles were generated in a blast atomiser (see Melling and Whitelaw, 1973). The seeded jet from the atomiser was inserted in a polythene bag from which the seeded air was drawn and into which it was exhausted, or by simply positioning the seeded jet near the inlet so that it did not affect the intake flow.

Corn oil particles were also tried for seeding the flow. It was found that although higher seeding and therefore higher data rates could be obtained (mainly due to the lower viscosity of corn oil) and corn oil particles were good scatterers, the cylinder walls had to be cleaned much more often than with the silicone particles. Two lubricator type atomisers (Norgen L04-200-MPQD and L11-200-MLRD) were also used, but they were not as efficient or consistent in producing a jet of uniformly sized particles.

The half-angle of intersection of the beams was matched to the mean diameter of the scattering particles in both optical systems employed (see Durst et al, 1976, p. 126).

Beam orientation, displacement and alignment

The optical arrangement could be traversed across a horizontal and a vertical diameter and parallel to the axis of the cylinder. Measurements were obtained on a horizontal diameter with the light beams in the horizontal plane to provide the axial velocity and in the vertical plane to provide the circumferential velocity. To obtain

measurements of the radial velocity components, the beams were in the vertical plane and traversed across a vertical diameter.

For the axial component measurements, no refraction correction due to the wall thickness was necessary and the anemometer was simply aligned with respect to the two inner wall surfaces. Refraction effects were present when the beams were orientated in the vertical plane for the swirl component measurements in the non-compressing engine but as the cylinder wall was thin the required corrections made were small (see e.g. Bicen and Whitelaw, 1981).

In the radial component measurements,once the beams were moved along the vertical diameter off the horizontal diametrical plane, their intersection was not on that diameter anymore due to asymmetric refraction of the beams at the curved surfaces. A geometrical calculation showed however that the beams intersect,when traversed vertically, so that the bisector of their angle of intersection, and consequently the velocity component measured, always lies in the radial direction, although not on the same diameter. Thus any asymmetries present in the flow would be more evident in the radial component measurements of sub-section 2.4.4. Corrections to the control volume position can readily be made, but are not necessary as the thin walls cause negligible displacement (see Bicen and Whitelaw, 1981). Radial components could be measured to within 2.5mm of the cylinder wall, but not without loss of signal quality in the near-wall regions. The collecting optics were moved to collect the scattered light which was refracted by the opposite curved surface of the cylinder also.

The optical axis was aligned once it was established that the traversing mechanism was translating in one direction parallel to the cylinder axis and two perpendicular radial directions. The laser beam was set for grazing incidence on the cylinder head and the optical

components were successively inserted and aligned progressively from the laser to the photomultiplier end. The angle of intersection of the beams was measured, once the transmitting focussing lens was aligned, by projecting the beams on to a distant screen and measuring the distances with a steel tape.

The coordinate origin inside the cylinder was found in the axial direction for the zeroth order beam grazing on the cylinder head. In the radial direction, the location of the wall was found by visual observation of the coincidence of the control volume on the inner wall surfaces; the mid-point between the two walls was set to coincide with the cylinder axis and the corresponding compound table wheel set to zero.

2.3.2 Signal processing systems, measurement procedures and data reduction

In this sub-section the frequency counting system used to process the Doppler signals and the three data acquisition systems employed during the course of the measurements are described. A test of a spectrum analyser based processor for in-cylinder measurements is also presented. The measurement procedures and data reduction methods are described and the signal duty cycles, data rates and signal-to-noise ratios encountered are also discussed.

Frequency counter/keyboard programmed system

The measurements presented in sub-sections 2.4.2 and 2.4.3 were made with the processing system described below. Signals from particles crossing the fringe system were amplified and band-pass filtered (Harwell amplifier model 91-2151-2/6) to remove low frequency pedestal and high frequency electronic noise. The signals were then passed to channel A of a Hewlett Packard model 1740A oscilloscope to be displayed,

and to the input of a Hewlett Packard model 5360A computing counter with model 5375A keyboard to program the instrument. The instrument specifications and the program routine, devised by N.S. Vlachos, are given by Durao (1976). The triggering mechanism of the oscilloscope was used to accept Doppler signals above a certain threshold, and for each accepted burst, an arming pulse was sent from the oscilloscope to the computing counter via a gating circuit, which ensured that only signals from the desired part of the engine cycle were processed. The system is shown in Fig. 2.5 (a).

The gate was opened and closed after a preset number of pulses were received from an optical shaft encoder (Digitech model DR1034) coupled to the engine drive shaft. The encoder produced 1000 pulses per revolution with a marker pulse to monitor the engine speed. Setting the gate opening angle (i.e. the number of pulses following the marker pulse which was aligned with the arrival of the piston at TDC) and the gate interval $\Delta\theta$ in the circuit, enabled only pulses received from signals in the region between $\theta - \frac{\Delta\theta}{2}$ and $\theta + \frac{\Delta\theta}{2}$ (θ being the crank angle of interest) to pass and arm the computing counter. For each pulse so obtained, a d.c. logic signal was returned from the counter to channel B of the oscilloscope to display the part of the signal whose frequency was measured and to verify that the measurement was carried out properly.

The counter was programmed to receive a sample size of 100 signals and display the mean frequency $\bar{F}(\theta)$ and the normalised r.m.s. of the frequency fluctuations $\tilde{f}(\theta)/\bar{F}(\theta)$. This sample is rather small for turbulent flow measurements and so several sets of samples, typically five, were taken.[†] Data obtained in regions of low turbulence

[†] A statistical calculation shows that for a confidence level of 95% and a standard deviation normalised with the mean piston velocity of, say, 1.0, the r.m.s. values obtained from sample sizes of 128 and 512 can be subject to errors of not more than 17.32 and 8.66% respectively.

intensity ($\tilde{u}$ (θ)/$\bar{U}$ (θ) < 0.1) generally showed reproducibility to within ±2% of the mean velocity and ±5% for the r.m.s. component: the latter figure increased approximately five-fold for regions of very high turbulence intensity (~1.0). The sets of data were averaged to obtain the overall mean and r.m.s. components.

Signal-to-noise ratios obtained in the cylinder flow were generally of the order of 28dB (25:1) to 26dB (20:1), although the high flow velocities encountered in mid-stroke with the pipe inlet arrangement (maximum total frequency ~5MHz) gave rise to lower signal-to-noise ratios (~5:1). The amplifier had a flat response up to about 2MHz and a 3dB point (i.e. voltage reduction by a factor of $\sqrt{2}$) at about 4MHz. The applied frequency shift was therefore reduced to decrease the total frequency of the signals to below 3MHz and thus prevent erroneous measurements at locations where the velocity was high.

Data acquisition rates also varied through the engine cycle but were typically of the order of 1 or 2 s (i.e. 1 per 3 or 6 engine cycles) for a crank-angle interval of 1 degree. Measurements could, with care, be obtained to within 1mm of the cylinder wall.

Frequency counter/PDP 8/e mini-computer system

The time required for the acquisition of sufficient data to provide the mean and r.m.s. of the measured frequencies in some parts of the cycle motivated the development of a more efficient data processing system. The system described below was developed to enable the acquisition and storage of the frequencies of signals from all parts of the cycle without "gate" limitations. The measurements presented in sub-sections 2.4.4, 2.4.5 and in Appendix 2.1 were obtained with this

system.

The arming pulse of the oscilloscope was sent to the measured time input of the counter. The start and stop information of the arming pulses, allowed by the approximately 3ms response of the counter, which permitted a maximum of 100 samples per revolution of the crankshaft, was sent to the "gating" circuit. The Doppler frequency from the counter and the encoder pulse at which the signal occurred were read through corresponding digital buffers and interfaces to the memory of a Digital PDP 8/e mini-computer.

When the frequencies and crank-angle locations, corresponding to 8,000 signals, had been recorded in the memory of the computer, the information was passed through an interface and a format unit and written on a magnetic tape recorder (Racal model 7000). This process was successively repeated until sufficient measurements had been obtained at each measurement station. The processing system is shown schematically in Fig. 2.5(b).

The computer interfacing hardware system was designed and the software programmed in PAL III, to read the frequency of the Doppler signal, the crank-angle pulse and the time from the TDC marker pulse at which it occurred,and write them on the magnetic tape. Upon validation of a frequency signal and reception of an arming pulse, the corresponding crank-angle information was "frozen" in the hardware, so that the small delay, due to the software reading and storing crank-angle information only after the frequency was read, did not introduce a "lag" in the frequency-crank-angle pairing. The machine language control program is listed in Appendix 2.3.

Once the measurements were completed, the magnetic tape was decoded on a CDC 6400 main-frame computer, programmed in FORTRAN IV, which divided the signal information into prescribed crank-angle

intervals, and evaluated the mean and r.m.s. velocities and (as desired) the probability distributions, skewness, kurtosis and stream function for the crank-angle(s) of interest. The program is listed in Appendix 2.4.

A 10 degree crank-angle window was used for the processing of the results, in accordance with the suggestions of Morse (1977). Typical sample sizes for this crank-angle interval were in the range 150-800, depending on the point in the cycle and the location inside the cylinder. The cyclic variation of sample size is shown for two measurement points (z = 10mm, r = 20mm and 25mm) in Fig. 2.6: the results refer to the axial velocity component in the 15 degree swirl vane configuration.

The count rate corresponds fairly closely with the variation of mean velocity; at r = 25mm, the number of signals received during the high velocity part of the intake stroke is about 75% greater than during the exhaust stroke, where the velocities are relatively low. At r = 20mm, the count rate is signficantly more uniform, as the variation of mean velocity over the cycle is only slight. In both cases, the number of counts lessens at locations corresponding to TDC and BDC, as the piston is momentarily stationary. The data rate over the whole cycle was typically 50/s (15 per revolution) for signal-to-noise ratios of the order of 25:1 (28dB), thus requiring a measurement time at each point of the order of 150s.

Spectrum analyser/PDP 8/e mini-computer system

In motored production engines, the deterioration of the signal-to-noise ratio due to the operating conditions and the use of back-scatter optics dictated by the limited optical access, restricts the

use of frequency counting with acceptable data rates, for at least some parts of the cycle. Spectrum analysis on the other hand permits frequency measurements with significantly lower signal-to-noise ratios. In order to enable in-cylinder measurements in the above conditions, and because of the opportunity to utilise the high signal-to-noise ratios in the model engines for comparison and development, a Hewlett Packard spectrum analyser (model 8553B/8552B/141T) was interfaced to the PDP 8/e mini-computer. The instrument was software controlled and scanned.

The system is shown in Fig. 2.7(a) and the software control and FORTRAN decoding and calculating programs are given in Appendices 2.3 and 2.4 with the corresponding ones for the frequency counter system. A detailed description is given by Crabb et al (1979). Sample results obtained in the non-compressing model engine are shown in Fig. 2.7(b), at $\theta = 90^{o}$ and z = 20mm. They indicate the effect of step size and bandwidth on the measured mean and r.m.s. velocities. Best agreement with the frequency counter results is achieved with the system's maximum resolution, 256 steps with 10kHz bandwidth, although the 30kHz results are also in close agreement. The results indicate that an accurate description of the flow can be obtained with significantly lower signal-to-noise ratios from the frequency analyser. The signal-to-noise ratios encountered in the two model engines were sufficiently high in all measurements to allow the use of the frequency counter and there was therefore no need to employ the frequency analyser system.

Frequency counter/Apple microprocessor system

The frequency counter/PDP 8/e mini-computer system enabled measurements to be made over the whole cycle but required the careful

setting of a trigger level appropriate for all the signals within the cycle (see section 2.3.4), as there was no signal validation incorporated in the counter. The second drawback was that the time elapsing between storing the data on tape and decoding them on the main-frame computer meant that on-line information as to the quality of the data or the flow description could not be obtained, and more measurements had to be made at a later stage in flow regions of interest. Thirdly, the even larger variation of signal amplitude and quality expected in the compressing engine would mean more laborious checks on the setting of the discrimination level.

To overcome the above deficiencies in the compressing engine measurements (sub-section 2.5.2) the counter was interfaced to a microprocessor (Apple II) to permit on-line data reduction at specific crank-angle windows. The interfacing system has been described in detail by Bicen et al (1980). In brief, the binary-coded decimal frequency output from the counter was interfaced to the microprocessor which was controlled by a 6502 machine language code with a software dependent maximum sampling rate of 5Hz corresponding to a 200ms time interval. The data reduction was programmed in BASIC and calculated mean and r.m.s. values. Wide-band filtering was carried out by accepting frequency values within three standard deviations in order to reject noise-induced erroneous counts. Approximately 99% of the counted frequencies were validated. The gating circuit opened every 600ms (one four-stroke cycle) and remained opened for 8ms (corresponding to a 10 degree window) so that a maximum of one measurement per cycle was possible due to the 200 ms sampling time of the microprocessor.

2.3.3 Pressure measurement system

In order to provide a check on the compressing engine cylinder pressures and ensure there was no leakage past the piston rings, a piezoelectric pressure transducer (Kistler 6121A1) was mounted on the cylinder, installed flush with the inner wall surface. The transducer signal was amplified by a charge amplifier (Kistler 5007) and the amplifier voltage output displayed on an oscilloscope. The transducer was calibrated on a dead weight calibrating machine, yielding 0.99V per bar, before being installed each time.

The pressure traces indicated a peak cycle pressure of 4.7 ± 0.2 bars. The difference between the measured value and the calculated one of 5.8 bars corresponding to the compression ratio of 3.7 is attributed to the intake valve closing 48^{o} ABDC and possible heat losses through the walls.

2.3.4 Measurement uncertainties

In this section, uncertainties affecting the quality of the in-cylinder measurements are discussed. Where possible, estimates of the systematic errors (accuracy)† and random errors (precision)† are given.

Positional errors

The optical system was traversed by means of a compound table of 0.05mm accuracy. The precision in location between positions separated by 10mm and 5mm is thus 0.5% and 1% respectively. The random error

---

†For definitions, see B.S. 1042: Part 1: 1964, p. 67.

in the setting of the control volume, which was made by visual observation, was of the order of the control volume size, ±0.1 mm. Both errors are negligible relative to the separation between measurement locations.

The location of the TDC on the engine crankshaft was found by means of a dial gauge, which located the end of the piston travel and by means of the "gating" circuit which was set at zero degrees crank-angle and 0.36 degrees interval: the encoder was rotated until the "gating" circuit indicated that the shaft encoder's TDC marker pulse was on when the piston was at the end of its travel. The error in the crank-angle setting was determined to be less than 0.36 degrees in the two-stroke and 0.72 degrees in the four-stroke cycle.

Asymmetry

The symmetry of the flow was checked in all the configurations measured. Near the axis, on the edge of the indrawn jet and in the re-circulation zone near the wall in the pipe inlet geometry, maximum asymmetries of 2%, 12% and 5% respectively, expressed as fractions of local mean velocity, were observed. With the valve inlet, the maximum asymmetries were 2% near the axis and 8% near the edge of the indrawn jet. The poorer symmetry in the former case is attributed to the difficulties involved in ensuring that the pipe was mounted at exactly 90^{o} to the cylinder head. Asymmetries of the radial components amounted to 3% of the local axial velocity near the axis and 10% close to the edge of the jet. For the circumferential component these values were 2% and 5% respectively. In the immediate vicinity of the exit plane, the effect of the swirl vanes could be detected in the flow, and local wakes existed, particularly for the 15 degree swirl vanes. The position of occurrence of zero circumferential velocity did not normally deviate from the

axis by more than 1mm. Asymmetries in the operating valve and on either side of the symmetry plane in the offset valve configurations were the same as for the stationary centrally located valve.

Engine speed

Unsteadiness in the engine speed results from the fluctuating torque requirement over the cycle, as the piston velocity and the resulting sliding friction vary from zero to a maximum. The cyclic torque fluctuations were, however, smoothed by the flywheels of the engines, as mentioned in sub-section 2.2.2. Short term variations were less than ±0.5% and longer term drifts in engine speed did not normally exceed ±1%. Any greater variations were compensated in the non-compressing engine by altering the motor speed control. The mean velocity error is insignificant; the r.m.s. level attributable to speed fluctuations can be found by equation (2.6) below. If the measured r.m.s. level is $(\tilde{v}_D/\bar{v}_D)_m$ and the r.m.s. due to various error sources is $(\tilde{v}_D/\bar{v}_D)_e$, then the corrected turbulence intensity is

$$\frac{\tilde{u}}{\bar{U}} = \left[\left(\frac{\tilde{v}_D}{\bar{v}_D}\right)_m^2 - \left(\frac{\tilde{v}_D}{\bar{v}_D}\right)_e^2\right]^{1/2} \qquad (2.6)$$

For an r.m.s. fluctuation of the engine speed $\left(\frac{\tilde{v}_D}{\bar{v}_D}\right)_e$ of about 1% the error in $\frac{\tilde{u}}{\bar{U}}$ is negligible in comparison to the levels measured in the cylinder (e.g. for measured r.m.s. levels, $\left(\frac{\tilde{v}_D}{\bar{v}_D}\right)_m$, of 0.25, the error is 0.1%).

Checks on the variation of piston speeds throughout the cycle were made for both engines to confirm that sinusoidal variations in piston speed were obtained. In the case of the compressing engine in particular, it was possible that significant retardation and accelera-

tion of the piston before and after TDC of compression respectively could occur. Pairs of values of the crank-angle and the time elapsed from TDC (or the beginning of the cycle) were obtained for both engines' cycles, using the PDP 8/e mini-computer system. A sinusoidal piston speed variation yields a linear relation between crank-angle and time, and this was the case for both engines, so that $d\theta/dt$ = constant in both cases throughout the cycle (measured to 1.5% precision in the two-stroke engine and to 3% precision in the four-stroke engine).

Frequency shift

The frequency shift applied between the first order beams with both gratings used (1.5 and 1.84 MHz respectively) was much larger than the Doppler frequencies corresponding to the mean piston speeds (≈100 - 125kHz), but a shift of this size was generally necessary to resolve the directional ambiguity in regions of high reverse velocities and turbulence intensities.

Both gratings were rotated by d.c. motors with feedback controls. The rotational speed and therefore the frequency shift of the Optical Measuring Tools grating had an r.m.s. variation of about 0.3% and an extreme fluctuation of ±1%. The maximum variation is not important as most of the mean velocity profiles are characterised by regions where the velocity is much greater than that of the piston (whether positive or negative). However, as the net mass flux at any axial location must equal the mass of fluid drawn in by the piston (for the axisymmetric non-compressing flows), an error of ±1% in the frequency shift will cause discrepancies (e.g. ±9.6% at mid-stroke) in the measured mass flux. The influence of variations in frequency shift on measured r.m.s. values has been shown by Melling (1977) to be negligible; even in regions of low turbulence intensity the errors involved do not exceed 2%.

The stability of the Technische Physische Dienst grating frequency shift was significantly better, with 0.1% long term stability and 0.2% r.m.s. variation (short term stability) at a rotational speed of 3360 r.p.m.

Doppler broadening

Broadening of the measured Doppler frequency spectrum can occur because of the mean velocity gradient, the finite time that particles take to cross the control volume, the small scale velocity fluctuations within the control volume, the finite instrument bandwidth, Brownian motion and the laser linewidth. The last two contributions have negligible effect (see Durst et al, 1976). The total measured mean square of fluctuations (σ_D^2) is the sum of the actual flow (σ_v^2) and broadening contributions:

$$\sigma_D^2 = \sigma_v^2 + \sigma_b^2 \qquad (2.7)$$

where

$$\sigma_b^2 = \sigma_g^2 + \sigma_F^2 + \sigma_T^2 + \sigma_I^2 \qquad (2.8)$$

and the r.h.s. terms corresponding to the effects in the order mentioned. Finite transit time broadening and instrument bandwidth errors are important in frequency tracking or spectrum analysis but not in frequency counting systems, and are considered in sub-section 3.3.3.

Velocity gradient broadening occurs when a finite-size scattering volume is placed across a mean velocity gradient in the flow. The variation of velocity is proportional to the gradient and to the dimension of the volume parallel to the gradient. If the profile is nearly linear, broadening effects will average out over the control volume.

Gradient broadening affects mainly the r.m.s. levels, and its contribution on the mean <U> and r.m.s. $(\tilde{\nu}_D/\bar{\nu}_D)_g$ velocities can be estimated by

$$<U> = U_o + \frac{\sigma^2}{2}\left(\frac{\partial^2 U}{\partial r^2}\right)_o \qquad (2.9)$$

and

$$\left(\frac{\tilde{\nu}_D}{\bar{\nu}_D}\right)_g = \left| \frac{\sigma}{\bar{U}} \frac{\partial \bar{U}}{\partial r} \right| \qquad (2.10)$$

where U_o is the true velocity at the centre of the control volume and σ the standard deviation of the control volume dimension parallel to the velocity gradient. The uncertainty on the measured mean velocity values was calculated to be below 3 percent in most regions, with a maximum of 10 percent in regions of highly non-linear gradients. Sample calculations by Melling (1977) and Arcoumanis and Vlachos (1980) have shown that the broadening effects on the r.m.s. values are negligible, compared to the measured r.m.s. levels, apart from the peaks in the r.m.s. profiles (corresponding to steep velocity gradients) where the values are overestimated by up to about 15 percent.

Broadening from velocity fluctuations in small scales (of the size of the control volume) has been expressed by George and Lumley (1973) as

$$\sigma_T^2 \approx \frac{2}{15}\,\sigma_3^2\left(\frac{4\pi \sin\phi}{\lambda}\right)^2 \frac{\varepsilon}{\nu} \qquad (2.11)$$

where σ_3 is a scattering volume dimension near the Kolmogorov microscale. For most in-cylinder measurements, the Kolmogorov microscales are in the region of a few hundred μm (e.g. 0.2 - 0.5mm in the work of Dent and Salama, 1975a,b), which are close to the control volume dimen-

sions employed for the present work. An accurate calculation of the broadening effect is difficult, but Melling (1975) has estimated it to be of the order of mean velocity gradient broadening. His result is confirmed in a similar calculation in section 3.3.

Finally, vibration of optical components due to transmission of vibration from the motor or from imbalances of the reciprocating parts can introduce broadening effects ("microphony", see Bradshaw, 1971). Checks were made with both engines with the motors both on and off and the pistons both connected and disconnected. The r.m.s. in the core of a jet inserted in the cylinder was measured in all cases; no r.m.s. contribution was indicated from component vibration in the non-compressing engine, while in the compressing engine, the induced r.m.s. was almost 0.025 $\bar{V}_p$, or about 1 percent of the levels normally encountered.

Crank-angle broadening

In cyclic flows with moderate data rates, it is necessary to measure frequencies over a finite crank-angle interval, $\Delta\theta$, so that all measurements in the interval $\theta-(\Delta\theta/2)$ to $\theta+(\Delta\theta/2)$ will contribute to a value attributed to the crank-angle θ. In analogy to the spatial mean velocity gradient broadening, temporal (crank-angle) velocity gradient broadening is present in reciprocating flows.

The r.m.s. levels are affected more than the mean velocity by crank-angle broadening. The broadening of the r.m.s. levels is given by Melling (1977) as

$$\left(\frac{\tilde{\nu}_D}{\bar{\nu}_D}\right) = \frac{\Delta\theta}{\sqrt{12}} \left|\cot\theta\right| \qquad (2.12)$$

and it is thus greater in the regions of large temporal gradients in

the cycle, i.e. at crank-angles of 36^0 and 144^0 as opposed to 90^0 and 270^0 in the results presented. A detailed analysis of crank-angle broadening effects is given by Morse (1977); they are well described for intervals up to 20 degrees by the equations

$$\bar{U}_m(\theta) = \bar{U}(\theta) + \frac{\Delta\theta^2}{12} \frac{\partial \bar{U}(\theta)}{\partial\theta} \left\{ \frac{1}{N(\theta)} \frac{\partial N(\theta)}{\partial\theta} \right\} \qquad (2.13)$$

and

$$\tilde{u}_m(\theta) = \left(\bar{u}^2(\theta) + \frac{\Delta\theta^2}{12} \left\{ \frac{\partial \bar{U}(\theta)}{\partial\theta} \right\}^2 \right)^{1/2} \qquad (2.14)$$

where the suffix m denotes measured quantities and $N(\theta)$ the count rate (the number of Doppler signals per unit time) at a crank-angle θ. Fig.1 in Appendix 2.2 demonstrates the influence of crank-angle broadening in the pipe-inlet arrangement, by comparing present results obtained at 36^0 ATDC, with a 1 degree interval, with those of Melling (1977), who employed an interval of 10 degrees. The mean velocities are only slightly affected, but the r.m.s. levels are overestimated as $\partial\bar{U}(\theta)/\partial\theta$ is large. In contrast, measurements reported by Yianneskis (1977) at 144^0 ATDC show significantly less broadening effects. This is a consequence of the fact that the variation of the velocity with crank-angle is less rapid over the second half of the intake stroke; the fluid in the cylinder is already moving as the piston decelerates, whereas in the early part of the stroke, the cylinder is filled with stagnant air which quickly accelerates as the jet flow enters.

For crank-angle intervals of less than 10 degrees, Morse showed theoretically and experimentally that the effect on the mean values was negligible, while the r.m.s. values were overestimated only in regions of steep temporal gradients. Nevertheless, he suggested a window of 10 degrees as a compromise between loss of accuracy and an adequate data

rate. Morse's analysis was of a general form. and most of his experimental results were taken in the inlet pipe described earlier (sub-section 2.2.1) at 1.25 cylinder diameters upstream of the cylinder head. In the pipe centreline, the variation of velocity is sinusoidal, following the simple harmonic motion of the piston. This variation is both simple and convenient for analysis as in-cylinder variations differ from point to point.

Rask (1981) has compared window, smooth-ensembled[†] and cycle-by-cycle data reduction techniques with data obtained in the L-head engine (see sub-section 1.2.1) at 300 r.p.m. Window-ensembled values differed from smooth-ensembled ones only in the early part of the intake stroke and for small crank-angle windows. Rask concluded that due to the simplicity of the window method and the difficulty of obtaining high data rates, a 5 degree window was acceptable in describing the flow. Rask noted discrepancies between his findings and the results of Morse et al (1979a) presented here in Fig. 1 in Appendix 2.2. Although the comparison of crank-angle windows of 1 and 10 degrees here refers to different data sets, Morse (1977) has reported similar results for 1 and 10 degree windows which he also compared to Melling's 10 degree window results, showing larger differences between the values obtained with the two windows than those of Rask. The discrepancy between the values obtained by Morse and Rask for different crank-angle windows cannot be easily assessed, as different configurations were used and different

---

[†]Smooth-ensemble averages are obtained by arithmetically averaging the data which are divided in 1 degree windows and then fitting a mean velocity curve to the average window values using a smoothing technique. Window-averages are ensemble averages of the data obtained in a prescribed crank-angle window.

components were measured: Rask measured the radial and swirl components in the clearance volume of his L-head engine, while Morse measured axial velocities all over the flowspace in the pipe inlet configuration. A confirmation of the magnitude of broadening effects has been obtained by the recent measurements of Arcoumanis et al (1981b) in the model compressing engine: during the first 30 degrees of the intake stroke r.m.s. values obtained with windows of 1.5 and 20 degrees are different by about 50%, in a flow with smaller gradients than those present with a pipe inlet.

Sample data from the valve inlet measurements were processed with 1 and 10 degree crank-angle windows and, in accordance with the analysis of Morse, showed maximum differences in the mean and in the r.m.s. velocity values to be in general about 3% and 15% respectively, with higher mean and lower r.m.s. values corresponding to the 1 degree interval. Differences of this order are only found at points near the axis and the jet edge, i.e. the parts of the cycle where the variation of mean velocity and count rate are large.

Count ambiguity and finite time resolution

All counting systems have an inherent error of ±1 clock count ambiguity as the gate can open or close missing one pulse from the gated pulse train provided by the crystal stabilised oscillator. The Hewlett Packard model 5360A counter has a 10MHz clock, but the instrument uses a stretching technique to increase the effective clock frequency by a factor of 1000, reducing the ambiguity error by the same factor.

In a system employing a counter with a clock frequency f_τ and measuring Doppler frequency ν_D by timing N_{ph} zero crossings, the relative

timing error is given by Durst et al (1976) as

$$\varepsilon_r = \frac{\nu_D}{N_{ph} f_\tau} \tag{2.15}$$

For ν_D = 2MHz and f_τ = 10MHz, the error for the count of 10 crossings is ε_r = 0.02, which by stretching becomes 0.002%.

In fixed gate counting systems with a large frequency variation in the Doppler bursts encountered, as in the case of the present work, the gate time is normally matched to the high velocity, $(\nu_D)_h$, signals to ensure that no noise is measured after the burst ends. The number of cycles counted from a burst of lower frequency, $(\nu_D)_\ell$, can be considerably less. The relative error due to count ambiguity is (see Durst et al, 1976)

$$\frac{(\nu_D)_h}{N_{ph}(\nu_D)_\ell} \tag{2.16}$$

For a frequency range 0.5 - 3.5MHz and 10 crossings the relative error in (ν_D) is 1.4 of ε_r calculated by (2.15).

Bias effects

Bias effects can occur due to the observation of more fast-moving particles, due to the integration characteristic of the photo-multiplier, due to the sampling and filtering characteristics of the instrumentation used (see sub-section 2.3.2) and due to incorrect choice of discrimination level, and can influence the accuracy of laser Doppler measurements. The effects are discussed in the literature (see e.g. Durst et al, 1981) and are only briefly mentioned here in relation to in-cylinder measurements.

In turbulent flow situations measured by individual realisation laser anemometry, the results are biased towards higher velocity values as a larger than average volume of fluid, and hence a larger than average number of scattering centres, passes through the probe volume during periods when the velocity is faster than the mean (McLaughlin and Tiederman, 1973). Various suggestions for the elimination of the velocity bias have been made. Durao and Whitelaw (1975) proposed the storing of all signals contributing to an experiment and then randomly sampling them in a closed loop until the required number of signals has been considered. Dimotakis (1976) suggested that the calculation of the ensemble-average be made by weighting the frequency measurement with the time of residence of the particle in the control volume. Other suggestions have been made by Buchhave (1975), Hoesel and Rodi (1977) and Wilson (1978).

The response of the frequency counter employed, 3 ms, allows a maximum sampling rate of 2.7 signals per cycle per 10 degree interval. The rate is reduced to 1 signal per cycle per 10 degree interval with the Apple microprocessor. This, in effect, enforces a slow sampling at regular intervals, which, although not made at random, approximates the procedure of Durao and Whitelaw and is appropriate subject to the existence of relations between the time scales as mentioned below.

Durao et al (1980) have drawn attention to the variation in the bias problem as the time scales representing the average time between particle arrivals, τ_i, the average time between samples, τ_s, and the integral time scale of turbulence, τ_t, vary in relation to each other. For example, if $\langle\tau_s\rangle < \langle\tau_i\rangle$ and $\langle\tau_i\rangle < \langle\tau_t\rangle$, the averages of the Doppler signals will be biased and the related error can only be removed by weighting each Doppler frequency with the duration of the burst

before performing the average. If, with this relationship between τ_i and τ_t, the value of τ_s is increased to be bigger than either of the remaining time scales, the bias is decreased as $<\tau_s>$ is increased. For $<\tau_i> > <\tau_t>$, the unweighted averages will always be biased.

The magnitude of the bias effect is, in general, not large. Even with the gross exaggeration of the one-dimensional correction of McLaughlin and Tiederman (1973), the bias is negligible (less than 5%) up to turbulence intensities of 15 - 20%. However, at turbulence intensities of around 30 - 40% errors in the mean velocity of around 10% could be experienced. As indicated by Durao and Whitelaw (1978), however, an opposite bias effect can occur due to the photomultiplier characteristics and the use of finite discrimination levels. It is also difficult to quantify this effect exactly, but Durao and Whitelaw suggest that it acts to mitigate the velocity bias and reduce the overall bias effect.

In the present case, the range of velocities encountered is relatively small (-2 to 4 ms^{-1}) and amplitude bias at any one location is thought to be small. The relationship of time scales in the present arrangement varies with the location of measurement but usually implies that $<\tau_i> < <\tau_t>$ and the sampling time is of the same order or larger than the integral time scale. Thus the influence of velocity bias is again reduced and, although the collective influence of bias effects cannot be exactly quantified, it is thought to be unimportant or very small in most of the flow.

A related bias effect stems from the use of a constant discrimination level throughout the cycle in unsteady flows. Since the signal amplitude can change with velocity, and the data rate can change with measurement location and velocity, the constant discrimination level employed must be chosen with utmost care, so that the lower amplitude signals are not excluded from the measurement. When measurements all

over the cycle were made with the PDP/8e mini-computer, the discrimination level was set only after test measurements had been made for the individual crank-angle windows of interest.

Continuity check

From the preceding considerations, it is expected that, in general, the main sources of error are crank-angle broadening and velocity gradient broadening in regions of steep temporal and spatial gradients respectively. In general, uncertainties are not likely to be more than around 3% in the mean and 10% in the r.m.s. velocity values (except for the lower mean and the higher intensity values).

Some confirmation of the estimated error in the mean velocities, for the axisymmetric non-compressing configurations, can be obtained by reference to the mass-continuity equation, which implies

$$\frac{\partial}{\partial z} \int_0^R \rho \bar{U} \, r \, dr = 0 \qquad (2.17)$$

so that the net mass flow rate (at any point in the cycle) is constant at each measurement station along the cylinder. However, for equation (2.17) to be valid, both flow asymmetry and temporal variations in fluid density must be negligible. In the latter context, pressure gradients exist as a consequence of the basic nature of the flow inside the cylinder. In addition, when swirl is present, radial pressure gradients are created due to the streamline curvature which gives rise to axial pressure gradients as the swirl either builds up or decays. Computations by Johns (1980) however, have shown that the resultant rates of change of density are small and affect the validity of equation (2.17) by only 1 - 2%. The effects of flow asymmetry are difficult to quantify, but, for the asymmetries encountered, they are expected to be of the same

order as the pressure effects.

The present results indicate that mass continuity is usually satisfied to within ±10%. While this is larger than the estimated error in the mean velocities, the difference may be ascribed to the difficulties associated with integrating equation (2.17) over regions of steep velocity gradient using a relatively small number of data points. A discrepancy of this order is equivalent to a uniform error of 0.10 $\bar{V}_p$ across the flow and is small compared to the measured velocities. The same accuracy can be reasonably assumed to prevail in the asymmetric as well as the compressing configurations.

One consequence of the uniformity of fluid density is that the flow field in the cylinder may be represented in terms of streamline contours with the tangent to the contours at each point indicating the local direction of the mean flow. This is exploited in the present work for all results from axisymmetric non-compressing configurations.

2.4 Results with the non-compressing engine

2.4.1 Introduction

The results are presented under headings of the in-cylinder geometry or flow parameter investigated. Measurements are shown at crank-angle locations of 36^o, 90^o and 144^o on the intake stroke and 270^o on the exhaust stroke. These angles were selected to provide a concise description of the flow development in the cylinder through the engine cycle. In all the figures, the outline of the cylinder, cylinder head and piston head is drawn in cross-section with the piston in the correct position for the crank-angle under consideration. The instantaneous magnitude and direction of the piston velocity, normalised by the mean piston speed, are indicated by an arrow on the piston head. In-

cylinder profiles of the ensemble-averaged mean and r.m.s. velocity components, normalised by the mean piston speed (0.4 m/s at 200 r.p.m.), are plotted relative to base lines drawn at the appropriate axial locations of measurement.

The results are also shown (for the axisymmetric configurations employing a plane piston head) in the form of contours of the stream function, ψ, defined by

$$\frac{\partial \psi}{\partial r} = \rho \bar{U}(\theta) r \qquad (2.18)$$

Where discrepancies in the mass balance were observed, the calculated stream function values were modified to give a constant value at the wall for each crank-angle location. The contours were drawn as smooth curves and, because of the interpolation involved, they should be considered as descriptive of the large-scale features of the flow field. The stream function values are normalised by $\pi R^2 \bar{V}_p \rho$, the product of the cross-sectional area of the cylinder, the mean piston speed and the fluid density.

For economy of presentation, the results obtained with an off-centre port have been appendicised (see Appendix 2.1) and only one configuration, that of the valve inlet with swirl, is presented in great detail because of its relevance to practice and to calculations and of the changes in the flow patterns experienced with different swirl levels. The two following sub-sections present an expansion of previous work (Yianneskis, 1977) and are used to provide an indication of the flow patterns for comparisons with more complicated arrangements. Results not reported by Yianneskis (1977) are presented here in the form of streamline contours and inlet velocity profiles. The corresponding mean and

r.m.s. velocity profiles, including those reported previously, are shown in Appendix 2.2 to enable comparisons with results obtained in the other configurations.

2.4.2 Pipe inlet

The stream function contours for the configuration with the pipe inlet are shown in Fig. 2.8 (the corresponding in-cylinder mean and r.m.s. axial velocity component profiles are shown in Appendix 2.2, Figs. 1-4). The basic flow pattern is of a high velocity jet drawn into the cylinder during the intake stroke, impinging on the piston face and spreading rapidly to meet the cylinder wall. This creates a strong vortex flow over almost the entire cylinder space which in turn gives rise to a counter-rotating vortex in the corner between the wall and the cylinder head. This second vortex has already appeared at mid-stroke and increases in size relative to the primary vortex as the piston approaches BDC. On the exhaust stroke, the flow is relatively featureless; some suggestion of the vortices generated during intake remains, but the flow is essentially one-dimensional until it accelerates upon nearing the exit.

The resulting vortex motion fills almost the whole cylinder space at 90^{o} (Fig. 2.8(b)) and the region of reverse flow near the wall extends backwards to a distance of 20mm from the cylinder head. The incoming flow spreads rapidly to join the vortex (at $z \approx 10$mm) and the jet decelerates as it approaches the piston. The clockwise-rotating vortex in the corner between the cylinder head and wall grows steadily beyond mid-stroke and extends as far as z = 30mm by 144 degrees (Fig. 2.8(c)). At this stage, the primary vortex has approached nearer to the centreline than at 90 degrees. Because of the growth of both vortices, the entering flow remains close to the axis and does not spread radially until it

reaches near the piston.

The velocities during the exhaust stroke (Fig. 2.8(d)) are fairly uniform except near the inlet where the flow accelerates as it leaves the cylinder. Otherwise the velocities are essentially equal to that of the piston. The curvature of the streamlines and the small region of forward velocity near the cylinder head at z = 5mm in the corresponding profiles (Fig. 4 in Appendix 2.2) appear to be residual influences from the corresponding reverse velocities and corner vortex of the intake stroke.

Fig. 2.9 shows profiles of axial mean and r.m.s. velocity measured at the closest possible station to the inlet plane, at z = 0.5mm. They were measured with the off-axis method described in sub-section 2.3.1. The jet edge moves nearer to the cylinder axis during the intake stroke, as a result of the development of the flow in the cylinder head/wall corner. This is consistent with the movement of the peaks in the r.m.s. profiles, which correspond to the locations of the steepest velocity gradients. The near-axis velocities are different for $\theta = 90^{o}$ and 270^{o}, although the same mass of air is crossing the section in both cases. The profile shapes are also different and, it is evident from all the profiles, that the jet spreads significantly in the first 0.5mm upon entry to the cylinder. Measurements could not be obtained beyond r =10mm because of the significant optical noise induced by the proximity of the cylinder head to the control volume. The spreading of the jet upon entry to the cylinder flowspace is evident in Fig. 2.10 by comparison of the profiles at 0.5mm with the measurements of Melling (1977) at a station in the pipe at z = 93.75mm upstream of the inlet plane.

2.4.3 Valve inlet with plane and cylindrical-bowl pistons

The stream function contours for the valve inlet with the plane piston arrangement are shown in Fig. 2.11. The presence of the bowl

makes little difference to the flow structure (see Figs. 5-8 in Appendix 2.2) and no stream function contours are shown for that configuration.

Again (Fig. 2.11) a high velocity jet is drawn into the cylinder during the intake stroke but, because of the angled entry, separate vortices are formed near the cylinder head in the corner with the wall and in the region near the centreline. Initially, both vortices are pronounced, but as the piston approaches mid-stroke, the smaller (counter-clockwise rotating) corner vortex diminishes in size whilst the larger (clockwise rotating) vortex grows appreciably to fill almost all of the space between the cylinder axis and wall. In the second half of the intake stroke, a third vortex, rotating counter-clockwise is formed at the corner between the wall and the piston head. The primary vortex fills roughly the two-thirds of the flow space nearer the cylinder head and the corner vortex is still in evidence. At both 90 and 144 degrees, the flow is approximately parallel to the axis in the region near the piston head and away from the wall, with a velocity close to that of the piston. This feature is carried through to the streamlines on the exhaust stroke.

At the early part of the stroke, $\theta = 36^{o}$ (Fig. 2.11(a)) the jet is drawn through the port mainly in the axial direction. Near the piston the flow is observed to be following the piston motion.

In mid-stroke (Fig. 2.11(b)) the jet enters the cylinder with a higher velocity than at 36 degrees and is directed towards the wall due to its stronger radial velocity component. As it reaches the wall, it is deflected away from the wall at almost the same angle it approached it. The differences in the flow patterns caused by the introduction of the bowl can only be noticed by reference to the profiles as they are too small to be shown in the contours: at $\theta = 90^{o}$ the jet is allowed to penetrate further with the bowl piston and the flow is deflected somewhat

later than with the plane piston.

At 144° ATDC (Fig. 2.11(c)) the jet enters with a smaller velocity than at 90° and is deflected rapidly by the strong reverse flow in the primary vortex, reaching the wall at a distance of about 25mm from the cylinder head. The vortex in the corner between the piston head and cylinder wall is much more pronounced than in mid-stroke. Beneath this vortex, the flow is almost undisturbed, moving with a uniform velocity close to that of the piston.

The exhaust stroke stream function contours (Fig. 2.11(d)) are relatively featureless, with uniform velocity distribution over most of the flow space and some acceleration of the fluid evident near the valve as the flow exits from the cylinder.

As with the pipe inlet, measurements were made at the z = 0.5mm station. The results are presented in Fig. 2.12 and again provide an approximation to the actual inlet profile (at z = 0mm) as the jet spreads significantly over the first 0.5mm. The peaks in the mean velocity profiles lie near the mid-radius of the annular gap and higher velocities are present at $\theta = 90^{\circ}$, as expected, and the profiles for $\theta = 36^{\circ}$ and 144° are almost identical. The r.m.s. levels in the edges of the outgoing jet during exhaust ($\theta = 270^{\circ}$, Fig. 2.12(d)) are nearly double those during intake, presumably because of the strong shear generated as the flow has to negotiate the sharp valve tip during its exit.

2.4.4 Valve inlet with swirl

Profiles of the mean and r.m.s. velocity components and corresponding streamline contours measured with the valve inlet incorporating the 15 and 30 degree swirl vanes described in sub-section 2.2.1 are presented in Figs. 2.13 - 2.28. Although data were obtained as a continuous function of crank-angle, the results are presented at the same

crank-angle locations as in the previous configurations to enable comparison. Measurements of the mean and r.m.s. components of the axial and circumferential velocities were made in both configurations and, for the flow with 30 degree vanes, they were extended to include the radial components. The data is presented below in order of crank-angle location for all configurations, and compared to the zero swirl results of the previous section.

The incorporation of swirl vanes upstream of the port results in the inflow of a swirling turbulent jet during the intake stroke. A convenient measure of the degree of swirl can be obtained from the swirl number, defined by

$$S = \frac{1}{\Delta R} \frac{\int_{R_1}^{R_2} r^2 \bar{U}\bar{W} dr}{\int_{R_1}^{R_2} r \bar{U}^2 dr} \qquad (2.19)$$

in which the density has been assumed uniform and all turbulence terms neglected. R_1 and R_2 are the inner and outer radii of the annular port and $\Delta R (=R_2-R_1)$ the throat opening. Defined in this way, the swirl number represents the ratio of the angular and axial momentum fluxes at entry to the cylinder, normalized by the width of the jet. For the 15 and 30 degree vanes used in this study, the corresponding values of S, evaluated from the nearest profiles measured to the port, and averaged over the intake stroke, are 0.45 and 1.20 (±10%) respectively.

The parameter employed to characterise swirl levels in reciprocating engine practice is the swirl ratio, defined as the ratio of the rotational speed of the air motion at TDC of compression, assuming solid body rotation, over the rotational speed of the engine. The swirl ratio for the 30 degree vane configuration can be estimated from the results of Fig. 2.27(b); "average" swirl velocity at, say, r = 25mm assuming solid

body rotation, is about 2.5 $\bar{V}_p$ or 1.0 m/s. Therefore, as $W = r\omega$ for solid body rotation, $\omega_f = 40\ s^{-1}$ is the rotational speed of the flow and $\omega_e = 2\pi f \approx 20\ s^{-1}$ is the rotational speed of the engine; a typical value of the swirl ratio at mid-stroke is thus $\omega_f/\omega_e \approx 2$. This number is of similar magnitude at $\theta = 144^0$ (near BDC). In real engines swirl ratios increase near TDC as the air enters the bowl and higher numbers are quoted; for instance, Renshaw and Wigley (1979) deduce from their measurements in a Perkins 4.237 engine swirl ratios of 5.7 at TDC at 1000 r.p.m. The corresponding swirl ratio at BDC of intake is only 2-2.5 (Renshaw, 1980). A similar increase in swirl ratios from BDC to TDC should be expected in the model engines employed for the present work, if bowl geometries and smaller clearances are used. The 30 degree swirl vanes produce therefore very realistic levels of swirl.

Profiles at 36^0 ATDC

Data obtained at $\theta = 36^0$ are shown in Figs. 2.13 (axial velocity component), 2.14 (radial velocity) and 2.15 (circumferential velocity). The streamline patterns for the two swirling flows are plotted in Fig. 2.16, which may be compared with Fig. 2.11(a) for the zero swirl case.

Comparison of Fig. 2.11(a) with Fig. 2.16(a) shows that, in this early part of the cycle, the vortex structure is much the same for S = 0 and S = 0.45. The action of the swirl in increasing the rate of spread of the indrawn jet causes a slight shortening of the secondary vortex in the corner between the wall and the cylinder head and a corresponding lengthening of the primary vortex. As a consequence of the latter, the stagnation point of the axis (indicated by the dividing streamline) moves about 3mm nearer to the piston face and the curvature of the flow in this region is increased. Further contraction of the secondary vortex occurs at S = 1.20 (Fig. 2.16(b)); also, the primary vortex is

elongated by the appearance of a third (counter-clockwise rotating) vortex near the cylinder axis. This vortex is evidenced by the presence of forward axial velocities up to a distance of 10mm from the cylinder head (Fig. 2.13(b)) and is very weak, recirculating only about 0.3% of the net mass flow rate. It presumably owes its existence to the enhanced mixing of the primary vortex with the surrounding air, and may be present for the other cases, although of too small a size and intensity to be detectable.

Fig. 2.13 and Fig. 5 in Appendix 2.2 show that, on account of the large angle of entry, the peaks in the axial velocity profiles for all three flows move only slowly outwards towards the wall, from r = 21mm at z = 3mm to about r = 25mm at z = 20mm. At a distance of 10mm from the cylinder head, the magnitudes of the peak velocities, which are initially of the order of 10 $\bar{V}_p$, have fallen by approximately 15% for the zero swirl case (Fig. 5 in Appendix 2.2), 26% for S = 0.45 (Fig. 2.13(a)) and 34% for S = 1.20 (Fig. 2.13(b)), illustrating the progressive effect of swirl on jet decay rates. Between z = 10mm and z = 20mm, the peak jet velocities in each flow configuration are roughly halved, and by z = 30mm, the profiles become almost uniform as the jet spreads onto the piston face. Near the axis however, the velocities are somewhat lower for the swirl cases due to the increased size of the primary vortex.

The jet regions of the flow are accompanied by a steep rise in the level of velocity fluctuations as shearing between the jet and the more slowly moving fluid in the cylinder generates a large amount of turbulence. At distances of about 20mm from the cylinder head, the peak r.m.s. level is typically six to eight times that on the axis and corresponds in location with the inner edge of the jet. In absolute terms, the r.m.s. levels are virtually independent of the swirl number, reaching a maximum value of the order of 3 $\bar{V}_p$ for each flow at z = 10mm. The

turbulence intensities, however, show a steady increase, the corresponding values being 0.35 for S = 0, 0.42 for S = 0.45 and 0.50 for S = 1.20. This increase has been attributed (see Morse, 1981) to the extra generation of turbulence arising from the swirling motion, which is a complicated process, the non-zero shear stress in the z - θ plane ($\overline{uw}$) acting to raise the level of $\overline{uv}$, thus leading to a higher production of axial velocity fluctuations against the mean strain rate. R.m.s. levels fall sharply at z = 30mm as the velocity profile becomes flatter; turbulence intensities away from the axis are of the order of 0.2, indicating a fairly regular flow onto the piston face.

The profiles of radial velocity shown in Fig. 2.14 for the 30 degree vane arrangement are generally consistent with the corresponding data for the axial velocity component and the streamline pattern of Fig. 2.16(b). At z = 10mm, there is little or no radial velocity until the jet region is encountered between r = 20mm and r = 27.5mm, where the velocities are positive due to the outward trajectory of the flow. The abrupt peak at r = 25mm has a magnitude of about 3 $\bar{V}_p$, which is close to the value expected, since the axial velocity of this point is 5.5 $\bar{V}_p$, and the direction of the flow is inclined at an angle of $\phi \approx 65$ degrees to the cylinder head ($\bar{U}/\bar{V} = \tan\phi$). At z = 20mm the radial velocities are everywhere close to zero, but a distinct negative region exists near the axis corresponding to the downward curvature of the primary vortex and there is a positive region near the wall due to the outward flow of the jet. At z = 30mm the velocities fall to zero near the wall as the streamlines are almost parallel beyond r = 25mm; close to the axis, negative velocities prevail as a consequence of the deflection of the flow by the primary vortex.

Away from the jet region, levels of the radial velocity fluctuations are essentially equal to those of the axial velocity. In the jet

itself, apart from the sharp peak at z = 10mm and r = 25mm, $\tilde{v}$ is only about 50% of $\tilde{u}$, which is consistent with experimental data for a steady, swirling jet exhausting into stagnant surroundings (Morse, 1981). The radial fluctuations are generally slightly larger than those in the circumferential direction, shown in Fig. 2.15(b), a finding again supported by data for the steady jet.

Measurements of the mean and r.m.s. components of the swirl velocity are presented in Fig. 2.15. At 0.5mm from the cylinder head, the mean velocity profile for S = 1.20 shows peaks in the central jet region. The maximum angular velocity for the 30 degree vane configuration is approximately 2.5 $\bar{V}_p$ (Fig. 2.15(b)) compared to about 1.0 $\bar{V}_p$ for the 15 degree vanes (Fig. 2.15(a)). This is in line with the swirl numbers quoted for the two flows. The peaks rapidly disappear, and at subsequent stations the profiles tend to uniformity beyond r~10mm as the swirl diffuses from the jet into the primary vortex. The velocities remain roughly twice as large for the higher swirl number flow. The r.m.s. levels, though initially slightly higher for S = 1.20, show no obvious differences beyond z = 20mm.

Profiles at 90^{o} ATDC

At mid-stroke, the angle of trajectory of the indrawn jet relative to the cylinder head has decreased to about 50 degrees with the result that the flow is strongly directed towards the wall. The actual point of contact moves slightly closer towards the head with increasing swirl number - from about z = 25mm for the zero swirl case (Fig. 2.11(b)) to z = 23mm at S = 0.45 (Fig. 2.20(a)) and z = 20mm at S = 1.20 (Fig. 2.20(b)). In all three flows, the primary vortex has grown considerably since $\theta = 36^{o}$, extending from the axis to within 5mm of the wall and recirculating in each case approximately 100% of the net mass flow rate. For

the swirl cases, the vortex reaches considerably nearer to the piston face, the stagnation point on the centreline being situated at about z = 56mm compared to z = 40mm in the absence of swirl; its centre of rotation has also moved perceptibly further away from the axis and the cylinder head. In the region near the wall, the addition of swirl causes suppression of the vortex which forms close to the piston face, although the slight curvature of the streamlines beyond r = 25mm suggests that a vortex of very small size and intensity may in fact be present. Due to the change in the angle of entry, the vortex in the corner between the wall and cylinder head has decreased in size since $\theta = 36^{o}$, but less so for the swirl cases. As was the case at $\theta = 36^{o}$, the weak counter-clockwise rotating vortex near the cylinder axis is only present for the higher swirl number flow.

The corresponding profiles of axial velocity are shown in Figs. 6 in Appendix 2.2 (S = 0), 2.17(a) (S = 0.45) and 2.17(b) (S = 1.20). The peak jet velocity, which is initially of the order of 14 $\bar{V}_p$, moves rapidly outward towards the wall, decreasing by about 60%, 66% and 72% respectively between z = 3mm and z = 30mm. At this latter station, the peak is located at approximately 5mm from the wall in all three flows. Beyond z = 30mm, the data for the zero swirl case show that the jet is deflected from the wall, the direction of deflection being indicated by the change in position of the maximum velocity; in contrast, for the swirl cases, the jet adheres to the wall and the velocity profiles tend to become uniform in the outer regions. For S = 1.20, the region of forward velocity corresponding to the formation of the near-axis vortex extends up to a distance of about 10mm from the cylinder head. Beyond this station, the negative velocities on the centreline are always smaller than for the lower swirl number case, although the difference gradually diminishes as the piston is approached. At z = 55mm, the

velocities remain just negative, indicating the elongation of the primary vortex to within 5mm or so of the piston face. Near the cylinder head, the negative velocities are considerably larger for the zero swirl case, the streamlines in this region being almost parallel to the axis.

R.m.s. levels are higher than at $\theta = 36^{o}$ due, of course, to the increased flow velocities occurring in mid-stroke. Again, in absolute terms, the magnitude of the velocity fluctuations shows no obvious dependence on the swirl number. The turbulence intensities however, show a progressive increase. In the jet region at z = 10mm, the peak intensities are 0.38 for S = 0, 0.41 for S = 0.45 and 0.48 for S = 1.20, roughly the same values as were obtained at $\theta = 36^{o}$. As the jet widens at z = 20mm and z = 30mm, the r.m.s. profiles show a double-peak effect, corresponding to the shear layers on either side of the point of maximum velocity, with a distinct trough in the flatter central region.

The profiles of radial velocity for the 30 degree vane arrangement (Fig. 2.18) are again consistent with the measured streamline pattern, shown in Fig. 2.20(b). Thus, at z = 10mm, the velocities are positive up to a radius of about 30mm due to the presence of the vortices and the outward flow of the jet, but become negative near the wall in the secondary vortex region. The secondary vortex does not extend as far as z = 20mm, and consequently the measured velocity is everywhere positive, the peak having decreased to about 70% of its value at z = 10mm due to the diffusion of the jet. Beyond z = 20mm, the jet has reached the wall and the flow over the whole cylinder radius is directed towards the axis, giving rise to negative radial velocities, which decrease in magnitude as the piston is approached. The trough in the profile at z = 30mm corresponds to a point where the streamlines are almost parallel

to the axis; that at z = 40mm is less easily identified with any feature of the vortex pattern, but is consistent with the relationship $\bar{U}/\bar{V} = \tan\phi$. As at $\theta = 36^{o}$, the r.m.s. levels in the jet region are about 50% of those for the axial velocity fluctuations; elsewhere they are essentially equal, except beyond z = 30mm where the profiles show distinct peaks ($\tilde{v}>\tilde{u}$) near the axis. This is a plausible effect, since the swirl velocity gradients against which radial fluctuations are produced are greatest in this region (see Fig. 2.19(b)) and there is little direct generation of $\tilde{u}$.

Profiles of swirl velocity for the 15 and 30 degree vane arrangements are shown in Figs. 2.19(a) and 2.19(b) respectively. The peaks in the initial profiles (z = 0.5mm) are about 60% higher than at $\theta = 36^{o}$, which agrees well with the corresponding increase in the axial velocities. Again, the swirl diffuses rapidly, and by z = 20mm, as the jet approaches the cylinder wall, only a very slight peak remains. The early profiles show some interference from the finite width of the swirl vanes. Beyond z = 20mm, the centre of the flow is set into a state of strong solid-body rotation with peak velocities of up to twice those in the flat region between mid-radius and the wall. The peaks are of similar magnitude in each flow; away from the axis, however, velocities are nearly twice as high for S = 1.20, so that the ratio of the angular momenta (weighted with r^2) of the two flows remains roughly the same as in the initial profile. The r.m.s. levels on the axis satisfy rotational symmetry in that $\tilde{v}$ (Fig. 2.18) and $\tilde{w}$ are very nearly equal; elsewhere, as at $\theta = 36^{o}$, $\tilde{v}$ is slightly the larger. For S = 1.20, the velocity fluctuations are somewhat greater in magnitude than for S = 0.45, particularly in the jet regions, and the increase in the level near the axis beyond z = 30mm is much more pronounced.

Profiles at 144^{o} ATDC

Streamline patterns at $\theta = 144^{o}$ are presented for the two swirling flows in Figs. 2.24(a) (S = 0.45) and 2.24(b) (S= 1.20), which may be compared with Fig. 2.11(c) for the zero swirl case. As a result of the reduction in flow velocities past mid-stroke, the trajectory angle of the jet relative to the cylinder head begins to increase, reaching a value at $\theta = 144^{o}$ of about 60 degrees for both flows. This allows the secondary vortex in the corner between the head and the cylinder wall to recover in size after the contraction experienced during the first half of the stroke. Although only slightly larger for the two swirling flows, the vortex is much stronger, recirculating about 70% of the net mass flux, as against 25% for the case with zero swirl. This is evidenced by the fact that the negative velocities recorded near the wall (Figs. 2.21(a) and 2.21(b)) are approximately five times greater with swirl than when swirl is absent (Fig. 7 in Appendix 2.2). In spite of the increase in the angle of entry, the jet reaches the wall at roughly the same downstream distances as those recorded at $\theta = 90^{o}$ - due to the increased strength of the secondary vortex and the expansion of the primary vortex, the incoming jet is subject to a sudden change in direction at about z = 12.5 mm and r = 25mm and is sharply deflected towards the wall. The primary vortex now encroaches to within 2.5mm of the wall, and is somewhat stronger for S = 0, recirculating 275% of the net mass flow rate, compared with 200% for S = 0.45 and 170% for S = 1.20. The elongation of this vortex increases with swirl number, the stagnation point on the centreline shifting from z = 55mm at S = 0 to z = 74mm at S = 0.45 and z = 81mm (within 3mm of the piston face) at S = 1.20. As expected from the trends of the data at $\theta = 90^{o}$ (Figs. 2.17(a), 2.20(a)), vortices begin to form for the lower swirl number case

both in the near-axis region close to the cylinder head and in the corner between the wall and piston face. The former is both smaller and weaker (1.5% recirculation as against 2.5%) than at S = 1.20. The latter recirculates only about 5.5% of the net mass flow rate compared to 12% for the zero swirl case and does not appear at all for S = 1.20.

Profiles of mean and r.m.s. axial velocity are presented in Fig. 2.21. These show much the same trends as those recorded in mid-stroke. For the swirling flows, the profiles at z = 30mm and z = 40mm display a region of high gradient near the wall, with the location of the peak velocity subsequently moving inwards to a radius at z = 70mm, of about 15mm for S = 0 (Fig. 7 in Appendix 2.2), 22.5mm for S = 0.45 (Fig. 2.21(b)) and 27.5mm for S = 1.20 (Fig. 2.21(c)). Hence, the stronger the swirl, the closer the adherence of the jet to the cylinder wall and the smaller the vortex between the wall and the piston face. The positive velocities on the axis again show a progressive increase throughout the cylinder length as the swirl number is increased. The r.m.s. levels are generally smaller than those prevailing in mid-stroke but larger than those at $\theta = 36^{o}$ (where the incoming jet has the same bulk velocity as at $\theta = 144^{o}$). This is,of course, attributable to the increase in mixing which has occurred inside the cylinder between these two points in the cycle.

The only significant difference between the profiles of radial velocity at $\theta = 144^{o}$ (Fig. 2.22) and those at $\theta = 90^{o}$ (Fig. 2.18) is that the transition from positive to negative velocities occurs at z = 40mm instead of z = 30mm (due to the stretching of the primary vortex). The peak velocities at z = 10mm and z = 20mm are roughly equal to those recorded at $\theta = 36^{o}$. Near the piston face, the radial velocities are positive in the region immediately adjacent to the wall, for, although no detectable vortex exists with the 30 degree vane arrangement (Fig.

2.24(b)), the streamlines do show a slight convex curvature to the axis. The behaviour of the r.m.s. level of velocity fluctuations is also similar to that observed in mid-stroke, a peak appearing on the axis beyond z = 20mm and increasing steadily in magnitude as the piston is approached.

Profiles of the mean and r.m.s. swirl velocities are presented in Fig. 2.23(a) for S = 0.45 and Fig. 2.23(b) for S = 1.20. Beyond a distance of 30mm from the cylinder head,the central region of the flow begins to rotate rapidly with peak swirl velocities of 3.5 - 4.0 $\bar{V}_p$ located about 7.5mm from the axis. The data for S = 0.45 show some loss of symmetry, the location of zero swirl drifting about the axis by ±2mm between z = 30mm and z = 70mm. Although the swirl velocities in each flow are everywhere greater at z = 70mm than at z = 30mm, this does not imply a proportionate increase in the angular momentum, as the radial distribution of $\bar{U}$ has to be taken into account in evaluating the integrated flux (see equation (2.17)). The angular momentum flux is actually constant (to within ±10%) throughout the length of the cylinder, decreasing only in the immediate vicinity of the piston.

Comparison with the corresponding profiles at $\theta = 90^{o}$ (Figs. 2.19(a) and 2.19(b)) shows that the swirl velocities, which are initially lower for $\theta = 144^{o}$, eventually (for z> 50mm) become higher than in mid-stroke. This effect is,of course, due to the fact that swirl is induced continuously during the intake stroke, causing a progressive build-up in intensity near the piston. The angular momentum fluxes are in fact slightly higher than at $\theta = 90^{o}$. The r.m.s. profiles display the same general features as in mid-stroke.

Profiles at 270^{o} ATDC

By the middle of the exhaust stroke ($\theta = 270^{o}$), the vortices

generated during intake have almost completely disappeared and the flow is more or less uniform until it nears the port and exits from the cylinder. The streamline contours for the 15 degree and 30 degree vane arrangements are shown in Figs. 2.28(a) and 2.28(b) respectively. At distances greater than 20mm from the cylinder head, the streamlines are more closely parallel and show less curvature than for the zero swirl case (Fig. 2.11(d)). This effect is difficult to account for, but is presumably connected to the decay-time of the primary vortex of the intake stroke. As in the non-swirling flow there is a large amount of undisturbed flow space near the piston as it approaches BDC (Fig. 2.11(c)), the primary vortex may persist for a small fraction of time longer once the exhaust stroke has begun, since it will not be influenced by the piston movement immediately. The curvature of the streamlines in Fig. 2.11(d) is thus thought attributable to residual effects from the intake stroke.

Profiles of the axial, radial and circumferential velocity components are shown in Figs. 2.25, 2.26 and 2.27 respectively. Between z = 20mm and the piston face, the axial velocity is almost uniformly distributed, but with slightly higher values near the wall than on the axis as, due to the inclination of the port, the outer region of the flow can exit more easily from the cylinder than the flow near the centreline. The profiles for S = 0.45 (Fig. 2.25(a)) show somewhat more scatter than those for S = 0 (Fig. 8 in Appendix 2.2) and S = 1.20 (Fig. 2.25(b)). At 10mm from the cylinder head, the flow begins to curve sharply towards the port, and the peak velocity of magnitude -2.2 $\bar{V}_p$ in each arrangement shifts to mid-radius, increasing to about -5.0 $\bar{V}_p$ at z = 3mm. The profiles of radial velocity for the higher swirl number case (Fig. 2.26) show negligible velocity until 20mm from the cylinder head. At z = 10mm,

the peak velocity is approximately -4.0 $\bar{V}_p$, which implies much sharper curvature of the streamlines beyond mid-radius than shown in Fig. 2.28(b)), and is therefore probably an overestimate. Radial velocities of this magnitude could only exist closer to the port, where the axial velocities are of the same order.

R.m.s. profiles of both axial and radial velocity fluctuations are generally uniform on the exhaust stroke with $\tilde{v}$ as a rule being slightly greater than $\tilde{u}$. Interestingly, as the flow nears the port and exits from the culinder, the jet region is not accompanied by a rise in the level of axial velocity fluctuations. The turbulence intensity ($\tilde{u}/\bar{U}$) at mid-radius at z = 3mm is only about 0.15 - in fact considerably lower than the intensities elsewhere in the cylinder. The negative radial velocities increase rapidly beyond mid-radius and this accounts for the peak in the r.m.s. level at z = 10mm and r = 25mm (Fig. 2.26). Beyond r = 25mm, $\bar{V}$ falls to zero and consequently the r.m.s. values decrease.

Profiles of the swirl component of velocity are shown in Figs. 2.27(a) (S = 0.45) and 2.27(b) (S = 1.20). Apart from the near-axis region, the swirl velocities correspond approximately with those recorded at the middle of the intake stroke (Figs. 2.19(a) and 2.19(b) respectively). Near the centreline, the strong peaks occurring at $\theta = 90^{o}$ for z >20mm have disappeared, causing a decrease in the (absolute) value of the momentum flux of approximately 20%. The r.m.s. levels are again uniform and generally of similar magnitude to those of $\tilde{u}$ and $\tilde{v}$. At z = 10mm, there is no peak in the profile corresponding to the peak in $\tilde{v}$ (Fig. 2.26), as the production of circumferential fluctuations (against the strain rate $\bar{V}/r$) due to the acceleration of the jet, though positive, is small in comparison to the rate of production of radial fluctuations

(see e.g. Morse, 1981).

2.4.5 Engine speed variation

Measurements of axial and swirl velocity components obtained with the valve inlet and the 30 degree swirl vanes at engine speeds of 100, 200, 300 and 335 r.p.m. are shown in Figs. 2.29 - 2.33. The profiles are normalised by the mean piston speed, which was 0.2, 0.4, 0.6 and 0.67 m/s for the above speeds respectively. The corresponding Reynolds numbers, based on the peak piston speed and cylinder diameter, were 1.59×10^3, 3.18×10^3, 4.77×10^3 and 5.33×10^3. For the reasons stated in sub-section 2.2.1, turbulent flow is expected to prevail in all speeds.

Fig. 2.29 shows the profiles at 90^o for 100 and 300 r.p.m. respectively and in Fig. 2.29(a) a comparison is also made between measurements at 100 r.p.m. and 335 r.p.m. at the same crank-angle and at the 20mm axial station. The latter speed represented the maximum at which the engine could be run before imbalance with related vibrations became significant. The profiles for the three speeds are in close agreement between them and with the 200 r.p.m. ones (Fig. 2.17),with the normalised values of mean velocity being a few percent higher at the three stations nearest to the piston at 100 r.p.m. and showing a tendency for the incoming jet to move closer to the cylinder wall with an increasing speed. Streamline contours plotted for the speed of 100 r.p.m., shown in Fig. 2.30, indicate no significant differences in the flow patterns to those at 200 r.p.m. (Fig. 2.20(b)). Values of the r.m.s. of the velocity fluctuations, normalised with the mean piston speed, are identical within the limits of experimental accuracy.

In Fig. 2.31, the profiles of the axial component at 20 and 60mm stations are shown for crank-angles of 270 and 144^o respectively. The

differences in the profile peaks at 144^{o} confirm that the indrawn jet tends to move slightly nearer to the wall with increasing speed. The profiles at z = 20mm for the 270^{o} on the exhaust stroke are identical as are the r.m.s. levels for both profiles. Measurements of the circumferential velocity component are shown in Fig. 2.32 and are effectively identical.

Finally, Fig. 2.33 presents streamline contours drawn from the results of Gosman et al (1978b) for speeds of 10 and 200 r.p.m. (laminar and turbulent flow respectively) with an orifice inlet. The profiles in the jet core showed differences of less than 5% but much larger differences were apparent in the region of the corner between the cylinder head and wall. It is in this region, which extends more than half way down the cylinder, where the differences between laminar and turbulent mixing would be expected to be most in evidence. This is evident in the corresponding streamline contours presented, with the vortex near the cylinder head being considerably reduced in size at the higher speed.

2.5 Results with compressing engine

2.5.1 Preliminary tests

Tests, intended as a guide for the measurements with compression, were initially carried out with the compressing engine described in subsection 2.2.2 motored at 335 r.p.m. The valve inlet cylinder head with the 30 degree swirl vanes was fitted to the engine cylinder with an adaptor, so that there was no compression. The tests demonstrated that measurements in the compressing engine could be made without any modifications in the laser Doppler anemometer.

In Fig. 2.34 profiles of the ensemble-averaged mean and r.m.s. axial velocity components measured are shown. The profiles were measured at the two stations shown, and are compared with profiles obtained in the model engine motored at the same speed, but with a 60mm stroke. The profiles are normalised in each case with the mean piston speed, which was 0.67 $^{m}/s$ for the non-compressing and 1.049 $^{m}/s$ for the compressing engine. Mass continuity was calculated to be satisfied within ±15% of the mass flow rate corresponding to the instantaneous piston speed for both engines.

The results show agreement with Ekchian and Hoult's (1979) visualisation of the effect of stroke variation (see their Fig. 15(a)). The main vortex as well as the ones in the cylinder head/wall and cylinder head/axis corners are significantly elongated, as indicated by the mean velocity profiles at both stations.

2.5.2 Operating valve with compression

Measurements of the axial mean and r.m.s. velocity component obtained in the model compressing engine motored at 200 r.p.m. are presented in Fig. 2.35, with the outline of the valve drawn for the appropriate lift from the valve-lift diagram of Fig. 2.2. The measurements were made at crank-angles of 90^{o} and 144^{o} in the intake stroke, 270^{o} and 342^{o} (18^{o} BTDC) in the compression stroke, 378^{o} (18^{o} ATDC) and 450^{o} in the expansion stroke, 540^{o} (BDC), and 630^{o} in the exhaust stroke. No swirl vanes were incorporated upstream of the valve.

Profiles at $\theta = 90^{o}$ and $z = 20mm$ are shown in Fig. 2.35(a). They indicate a structure similar to that measured with the stationary valve (see Fig. 6 in Appendix 2) with the jet located nearer the axis due to the variation in lift and consequently in the jet trajectory. The smaller negative velocities indicate a primary vortex weaker than that

with the stationary valve. Similarities with the non-compressing case are also obvious at $\theta = 144^{o}$, Fig. 2.35(b). The difference in stroke, though, results in an elongation of the primary vortex, shown by the negative velocities near the axis at z = 85mm, while in Fig. 2.11(c) the zero value streamline reached only as far as z = 55mm. Similarly the negative velocity near the cylinder wall indicates the elongation of the piston head corner vortex.

By mid-compression, $\theta = 270^{o}$, the valve is totally closed and a very weak vortex is formed behind the valve (Fig. 2.35(c)), as the faster moving fluid near the wall recirculates towards the axis after the valve closure. Velocities are quite uniform, with a maximum of 1.5 $\bar{V}_p$, and the steep gradients present in the intake stroke have been suppressed. As the piston approaches TDC at $\theta = 342^{o}$ (Fig. 2.35(d)) the velocities remain uniform and of the order of 0.75 $\bar{V}_p$, reducing near mid-radius but without any signs of recirculation. The weak vortex found at mid-stroke has been suppressed due to the further compression of the gas.

At the beginning of the expansion stroke, $\theta = 378^{o}$ (Fig. 2.35(e)) the profile at z = 20mm indicates the existence of a weak, clockwise-rotating vortex in the middle of the flow space. Velocity magnitudes have diminished near the wall, and their direction changed relative to that at 342^{o}.

By mid-expansion, $\theta = 450^{o}$, the velocities near the cylinder head are uniform, following the piston motion with magnitudes not exceeding 0.75 $\bar{V}_p$ (Fig. 2.35(f)). At BDC, $\theta = 540^{o}$, the profile of Fig. 2.35(g) shows the fluid to be rushing towards the valve which has opened to 40% of its maximum lift, and a recirculation is formed behind the valve. This profile at z = 20mm does not satisfy mass balance and this could be

due to the persistence of compression effects as well as due to averaging over a crank-angle interval in which the piston movement changes direction, with the related large spatial and temporal velocity gradients.

Fig. 2.35(h) presents profiles at mid-exhaust (630^{o}). The fluid is moving towards the open valve and there is no evidence of any vortex structure. The destruction of any vortices present in the preceding stroke soon after the piston reverses its travel is expected and confirms the findings of Bicen et al (1980).

The r.m.s. components, shown plotted on the same baselines as the mean velocities, indicate a strong correspondence between the mean and turbulence intake flow structure. There are high turbulence levels ($\sim 2.0\,\bar{V}_p$) during intake with maxima at the jet edges, and low uniform levels ($\sim 0.5\,\bar{V}_p$) during compression and expansion, increasing to about $1.0\,\bar{V}_p$ during exhaust. The trends are in agreement with previous investigations (see e.g. Lancaster, 1976) in that the intake mean and turbulence structure decay gradually and the turbulence remains constant and uniform during the second half of the compression stroke. The turbulence levels at $\theta = 378^{o}$ (Fig. 2.35(e)) are comparable to those at $\theta = 342^{o}$ (Fig. 2.35(d)), but by mid-expansion they have decayed to about 50% of the values near TDC. The increase in turbulence during the exhaust stroke is associated with the generation of turbulence when the valve opens for exhaust.

2.6 Discussion

There are two major types of deductions that can be inferred from the results of the previous two sections, one related to the in-cylinder flow knowledge obtained and its consequences for the flow in real engines and the other to the consequences for the calculation of the flow. The

two sub-sections that follow discuss these contributions respectively and underline the main conclusions.

2.6.1 Influence of flow and geometrical conditions on the in-cylinder fluid motion

Influence of cylinder geometry

The flow structure during the intake stroke and the early part of the return stroke is shown by the results to be influenced almost solely by the inlet geometry. The influence of the bowl on the piston head is very small and in general bowl shapes do not influence the flow structure until late in the compression stroke (Arcoumanis et al, 1981b). The bowl profile is of no significance; although a simple bowl shape was employed for the present results, the results of Bicen (1980) showed that the effect of a lipped cylindrical-bowl (lip diameter 50% of bowl diameter) is also insignificant in the absence of compression. Piston geometry was also not important during the intake and exhaust strokes in the measurements of Arcoumanis et al (1981b) with compression.

The pipe inlet configuration, although not directly relevant to engine practice apart from some two-stroke "scavenging" geometries, furnishes the computor of reciprocating flows with a simple test case for the prediction code development and is discussed in this context in the following sub-section. Present and previous results (Gosman et al, 1978b) obtained with orifice, pipe and valve inlets show that the trajectory of the incoming jet is the determining factor in the structuring of the resulting system of vortices.

The flow structures generated with valve inlets are characterised by an annular jet which induces two ring vortices early during intake, and a third one in the wall/piston corner later on in the stroke.

Although swirl alters this pattern with the generation of an extra, though weak, ring vortex behind the valve, the basic structure described above is maintained in all configurations. With an asymmetrical inlet (see Appendix 2.1) the above pattern persists, but with the ring vortices inclined at an angle to the cylinder centreline. The influence of stroke and clearance on the flow patterns is also small and of secondary importance (Arcoumanis et al, 1982). The flow patterns are similar to those reported here, with the vortices elongated or contracted respectively in the axial direction to accommodate the changes in geometry. The vortices are, however, of stronger intensity in the early part of intake with a longer stroke, and turbulence levels are higher with a smaller clearance due to the stronger jet impingement on the piston face. The patterns measured by the same authors with a 30 degree seat angle show considerable differences; the cylinder head/wall corner ring vortex is totally suppressed, and so is the one behind the valve. The incoming jet adheres to the cylinder head and wall surface, in contrast with the 60^{o} seat angle results of this thesis. However, a bi-stable flow is possible with a 30^{o} seat angle, with the jet either adhering to the wall or remaining detached (see e.g. Ekchian and Hoult, 1979).

The vortex structure moves during the intake stroke towards the piston, with a speed approximately equal to the mean piston speed (0.75- 1.0 $\bar{V}_p$, see e.g. Figs. 2.11 and 2.24). This can be observed for the primary vortex, the corner vortex near the piston and the stagnation point between the two. The same vortex movement can be observed in the intake stroke visualisation of Ekchian and Hoult (1979), where the main vortex moves with a speed of approximately 0.5 $\bar{V}_p$. However, the primary vortex in their study is located nearer the piston head. The reason for this is the valve lift employed; this is obvious from their Fig. 20(b)

where smaller lift causes the vortex to lie nearer the cylinder head. A larger seat angle in the same experiment causes the jet to be deflected further away from the port.

With an asymmetrical inlet (see Appendix 2.1), a circumferential component of velocity is imparted to the indrawn jet so that, as it is directed towards the cylinder wall, it spirals around the primary vortex formed behind the valve. The direction of rotation of the jet is in opposite senses above and below the plane of symmetry (Figs. 6 and 10 in Appendix 2.1). The primary vortex as well as the corner vortices all vary in size and intensity with angular position and are not present at all circumferential locations at a given axial station. The three-dimensionality of the flow is manifested in the vortices, which exhibit recirculating motions in the cross-stream planes in addition to the recirculation in the axial direction.

The motion induced in the $r - \theta$ plane by the inlet asymmetry is highly complicated; its sense of rotation sometimes opposes that of the jet and sometimes follows it. This behaviour can be explained by the realisation that it is the axial motion which primarily determines the in-cylinder flow processes: axial component magnitudes, especially near the valve, are much larger than circumferential ones. The circumferential variations of axial velocity, rather than the diffusion of angular momentum from the jet initiates the recirculating motion in the cross-stream plane.

The results of Ekchian and Hoult's (1979) visualisation reveal a vortex structure consistent with the measurements in Appendix 2.1; these authors employed an off-centre port inlet, but with a finite valve lift. The primary vortex behind the port is clearly in evidence, as is the large vortex which forms near the piston face on the side of the flow

remote from the port. However, due to the finite valve lift, the plane of rotation of the primary vortex is more inclined to the cylinder centreline than in the present case, and the vortices are of different size near the cylinder head. Similar flow visualisations made by Willis et al (1966) with a shrouded valve revealed a much stronger spiralling motion than that recorded here, but with two centres of rotation.

The extent of the in-cylinder mixing process with the off-centre valve, as evidenced by the length of the primary vortex behind the port, is intermediate between those obtained with the symmetric port without swirl (Fig. 2.11(c)) and with swirl produced by the 30^{o} vanes (Fig. 2.24 (b)). A further increase in mixing would therefore presumably occur if swirl vanes were incorporated upstream of the off-centre port arrangement.

The change in the flow patterns between 144^{o} and 270^{o} in all the configurations investigated, indicates the complete destruction of the vortex system after BDC of intake with a sink-flow-like structure during the return stroke. It has been shown (Bicen et al, 1980) that the intake-generated structure is destroyed at about 216^{o} (36^{o} ABDC). The vortices are not swept out, as has been suggested (Gosman et al, 1978a) but are destroyed by shearing between the piston-induced flow towards the port after BDC and the vortices themselves which circulate in opposite sense to the outgoing flow.

Influence of swirl

The swirling flow measurements in the non-compressing engine quantify the influence of swirl in a practically relevant range, and the mechanisms involved are important in real engines as swirl can be beneficial to thermal efficiency and to the reduction of pollutants (see Khan and Wang, 1972 and Ohigashi et al, 1972).

Previous experimental studies with swirl in motored engines

(Dent and Derham, 1974, Tindal et al, 1974 and Witze, 1977) have been concerned with off-centre valve arrangements. The results in general are concerned with the flow structure at TDC, and there is frequent mention of solid-body rotation and helical flow.

For axisymmetric flow, the present results demonstrate that solid-body rotation characterises only the near-axis region; away from the centre, there is near-uniform swirl velocity decaying to zero at the cylinder wall. The flow patterns are nearer to those described by Wigley and Hawkins (1978) and Willis et al (1966). Whether there is symmetry in the flow or not, intake-generated swirl is reorganised into near solid-body rotation by the TDC of compression. This is indicated from the comparison of 144^{o} and 270^{o} crank-angle results presented here (Figs. 2.23(b) and 2.27(b)) and is evident in the results of Morse and Whitelaw (1981) in a motored Diesel engine where the peaks present in the swirl profiles at intake are lost as TDC is approached and solid-body type motion prevails.

Arcoumanis et al (1981a) in their compressing engine measurements confirm this tendency towards solid-body rotation at TDC, which is more pronounced with smaller valve lifts, and also conclude that swirl suppresses turbulence levels during compression and has a stabilising effect on turbulence.

Effect of engine speed

The rotational speed of the engine can have a significant effect on the flow patterns if the speed range encompasses laminar and turbulent flow (Fig. 2.33). The related differences occur in those regions where diffusion is important, and therefore particularly in the region between the half width of the jet and the cylinder wall.

The present results for a speed range of 100 to 335 r.p.m. show

only minor differences which are of insufficient magnitude to influence the conclusions drawn from the results. The differences are more pronounced in the jet trajectory, and are likely to stem simply from the influence of the port, as for different flow rates through it, the valve is expected to redirect the incoming jet (cf. variation in the discharge coefficient with valve lift, sub-section 1.2.1).

The flow visualisation tests of Ekchian and Hoult (1979) obtained in a range of rotational speeds from 750 to 2500 r.p.m. show negligible influence of speed on the mean flow patterns also. Linear dependence of the mean and turbulence velocities on engine speed for a range of 500 to 2500 r.p.m. has been observed by Witze (1977) with minor differences noticeable at the lower speeds. Similarly, swirl velocity profiles and swirl ratio were found to be almost independent of speed in the off-centre valve tests of Willis et al (1966); however, the centre of rotation of the swirling flow did change position with speed, presumably due to differences in the flow through the inlet port.

Effect of compression and of an operating valve

The results obtained in the compressing engine show great similarities with those from the non-compressing one. The inlet-generated structure lasts approximately as long as the intake stroke, and is destroyed during compression. The turbulence intensities are very uniform and remain almost constant during compression.

There are two differences with the non-compressing engine results, one due to the longer stroke and the other due to the moving valve. The effect of the operating valve can be concluded to be the inclination of the jet more towards the cylinder axis than with the zero valve lift case (Fig. 2.35(a) and Fig. 6 in Appendix 2.2). This is in agreement with the results of Arcoumanis et al, 1981a, b and Gany et al, 1980. The jet

penetrates further into the flowspace and suppresses somewhat the piston/cylinder wall corner recirculation. As the intake valve closes, the profiles at $\theta = 270^{o}$ are not as uniform as in the non-compressing case, with near zero velocities close to the cylinder axis. The exhaust stroke is as uneventful as the two-stroke measurements indicated.

The present results are in agreement with the detailed measurements of Arcoumanis et al (1981a, b) who also examined piston bowl configurations, valve lift and valve seat angle effects. There are differences between the above mentioned studies and the measurements of Gany et al (1980), obtained in a motored four-stroke engine with a 45^{o} seat angle and a compression ratio of 7.0. In particular, the latter found opposing velocity directions near the wall at $\theta = 270^{o}$ at z = 1" and z = 2" stations, did not find a recirculation zone at $\theta = 450^{o}$ and measured a sudden acceleration of the flow until half radius at $\theta = 570^{o}$ and a recirculation region near the cylinder head at $\theta = 630^{o}$. Their results show large scatter, and in the corner region of the cylinder head are stated by the authors as "not believable", but no reasons are given. These measurements cannot be compared to corresponding ones by Arcoumanis et al (1981c) with a compression ratio of 7.0, as the latter concentrate on the TDC of compression region where no distinct patterns can be deduced from the results of Gany et al.

Finally, none of the measurements - with or without compression - presented in this thesis revealed the existence of the so-called "rolled-up" vortex; this is discussed in the following sub-section in view of its claimed connection with in-cylinder flow regimes.

The significance of the "rolled-up" vortex

There is frequent mention in the literature of the existence of a "rolled-up" vortex created by the scraping of the cylinder wall boundary

layer by the piston during compression and of a similar corner "sink-flow" during expansion, see e.g.Tabaczynski et al (1970), Daneshyar et al (1973), Oppenheim et al (1976), Fuller (1975) and Ishikawa and Daily (1978). The results of this thesis and related papers in the literature (e.g. Morse et al, 1979a,b, 1980a,b, Bicen et al, 1980, Arcoumanis et al, 1981a,b) cast serious doubt as to the significance or relevance of these vortices for in-cylinder flows.

The water flow experiments of Tabaczynski et al made use of a configuration with fixed pistons on either side of the fluid and a moving wall around it: there was no intake structure present in the flow. The size of the "rolled-up" vortex observed by the visualisation of Tabaczynski et al was small and Fuller confirmed that this was the case for most of the speed range of a conventional engine. The present results do not confirm the existence of such a vortex.

The "sink-flow" of Tabaczynski et al is created by the wall motion that corresponds to the intake/expansion strokes. Thus the sink-flow might well be present as part of the piston head/cylinder wall corner vortex, shown e.g. in Fig. 2.11(c). The "rolled-up" vortex on the other hand, created by the wall motion corresponding to the compression/exhaust strokes, would certainly be swamped-out by the redistribution of the intake structure during the return stroke in the two-stroke cycle and during the compression stroke in the four-stroke cycle. The present results have clearly shown that the inlet-generated structure dominates the flow until its effects are largely suppressed by mid-compression.

It is possible that the "rolled-up" vortex cannot be formed because its origin, the wall boundary layer, is drawn into the existing piston/wall clearance in the engines employed for the present work; this is unlikely though in view of the thick boundary layers found near the

piston face. Both the vortex and sink-flow appear to be of significance in idealised situations only and not in reciprocating engine practice.

The last point is further illustrated by the results of Ishikawa and Daily (1978). They made flow visualisations in a model square-sectioned motored engine of a separate single intake stroke, a separate single exhaust stroke and again separately of compression-expansion stroke cycles, which led them to conclude that the "rolled-up" vortex is important in determining the overall turbulence characteristics. The fluid motion in their experiment starts at BDC of the compression stroke, without any intake motion preceding it, and again the only fluid motion present is the "rolled-up" vortex, which appears significant in the absence of other influences. The vortex is present even in their exhaust stroke visualisation, as the fluid again starts to move from stationary.

Flow in production engines

The results have shown the suitability of the present approach for obtaining information relevant to the flow in real engines. The determination of the influence of the various parameters can be better achieved in model engines as the conceptual and experimental problems of the flow in production engines are considerably greater.

The determination of the aerodynamic characteristics of the flow allows conclusions to be drawn on the mixing processes, which are crucial to the reduction of emissions and economy of fuel; further investigations of this nature are, however, required to examine the compression and combustion-related effects closely.

The present results show that in-cylinder mixing during intake is dominated by the primary recirculation zone formed near the valve, and that the length of this recirculation region increases with swirl. The intake-generated structure is largely destroyed by mid-compression, but

it is anticipated that significant mixing is achieved by that time in spark ignition engines; in Diesel engines, however, the piston geometry is expected to determine the flow structure before ignition. The corner vortices were found to be destroyed too early to enable the removal of unburnt fuel deposits on the wall as expected (Asanuma and Obokata, 1972); and no "rolled-up" vortices are expected to be present during compression.

2.6.2 Calculation of the flow in reciprocating engine cylinders

One purpose of the present investigation is to provide information which would allow those seeking to calculate the flow characteristics to assess their methods. It has previously been shown, for example by Gosman et al (1978a), that the general features of reciprocated flows can be represented by numerical solutions of appropriate conservation equations. The present work was carried out in conjunction with calculations performed by Gosman et al (1978a, 1979) and Johns (1980). The main problems encountered in the calculation of the flow can be identified as the prescription of the inlet conditions, the representation of the steep intake gradients and the representation of the turbulence processes.

Gosman et al (1978a) predicted the non-compressing cycle with the axisymmetric pipe and valve inlets without swirl. For the pipe inlet case, the profiles measured upstream in the pipe were used to approximate the inlet conditions, with radial inlet velocities specified as zero and the turbulence parameters calculated from rough approximations to the observed profiles in steady pipe flow. A 30 x 30 non-uniform grid was employed and 15 minutes of computing time required. The jet behaviour is reasonably reproduced, in comparison with the measurements,but the secondary vortex is significantly under-predicted; the

exhaust stroke results show reasonable quantitative agreement. The turbulence intensities predicted exhibit errors, in view of the intimate connection between the mean and turbulence fields in e.g. the location of the predicted shear layers etc. Discrepancies are attributed to the fact that the "k-ε" model is prone to error in regions dominated by the normal stresses, i.e. near the piston head during intake, to inlet condition uncertainties and to the possible existence of residual vortices created during exhaust and being drawn into the cylinder during intake. However, any vortex structure present in the pipe inlet would have been revealed by the measurements in the pipe.

The predictions of Gosman et al for the valve inlet case show good qualitative agreement with the present mean velocity results. Some discrepancies are evident in the regions of the jet edges and, as suggested by the authors, the variation of the inlet jet angle during the intake stroke (which can be observed in the experimental results but was not specified in the prediction code) is the main reason for the differences. Turbulence levels are generally under-predicted, most probably because zero levels are specified at the inlet although some turbulence is expected to be generated in the valve passage.

As the present measurements have shown, the problem of inlet conditions cannot be solved without considerable effort and specially devised experiments. As the jet trajectory changes during intake, it seems appropriate to specify conditions further upstream in the valve passage where the geometry is simpler and temporal changes in velocity and turbulence can be easily accounted for. One such location is the passage around the valve stem in axisymmetric geometries where the flow in an annulus must be specified. Such inlet conditions would also account for the generation of turbulence in the valve passage, and for

the current under-predictions of in-cylinder turbulence.

Johns (1980) predicted the flow in the valve configuration with swirl and found good agreement in the mean flow calculations with the present measurements. The small vortex formed behind the valve is the only feature not strongly evident in the predicted mean flow results; this is not significant though as this vortex recirculates only 1.5% of the mass of the primary one at $\theta = 144^{o}$. The predictions are in better agreement with the experiments than those of Gosman et al (1978a). It is likely though that discrepancies will increase with swirl number in view of the use of an isotropic viscosity hypothesis for a swirling flow; the problems of the use of the "k-ε" model in swirling flows have also been identified by other authors (see e.g. Habib and Whitelaw, 1979).

The sensitivity of the calculation results to the inlet conditions specified suggests, nevertheless, that the steep intake gradient regions are the main source of calculation errors, as both the mean motion and turbulence generation are controlled by these gradients. Numerical inaccuracies, due to the insufficient number of grid nodes at these regions, appear to be more significant than those arising from turbulence models and local grid refinement in the jet region is called for. For a corresponding calculation in a three-dimensional configuration, the off-centre port measurements suggest that an equivalent number of nodes would be required in the circumferential as well as the radial and axial directions. However, as numerical limitations due to the coarseness of the grids used tend to smear the intake jet, the extra number of nodes required may present an insurmountable limitation for three-dimensional flows at present.

The above considerations apply equally to four-stroke cycle calculations. The additional complication of the moving valve has been accounted for by Johns (1980), who specified the inlet conditions from the valve

lip to the end of the valve seat during the whole cycle. The uncertainties involved in this method suggest that the use of a locally refined grid in the valve passage following the valve motion might be more appropriate.

The first four-stroke motored cycle predictions were made by Gosman and Watkins (1976b) in a cylinder with a varying-area annular opening. Although the valve representation is a crude one, the primary vortex was predicted to develop during intake and be suppressed (somewhat late) after TDC of compression, with a one-dimensional flow during expansion and a sink-flow structure during exhaust.

In a later paper, Gosman et al (1978a) presented computations of a motored cycle with a moving centrally located valve, for a compression ratio of 5.8 and bore/stroke ratio of 1.3. The corresponding parameters in this thesis are 3.7 and 1.25 respectively and a direct comparison is not possible. The two intake ring vortices, the single weak vortex at 360^{o} (TDC) and the general expansion and exhaust stroke features are however, predicted. Comparisons of the predictions with the results of Witze (1976c) in a similar engine are in reasonable agreement; however, the difficulties in calibrating the hot-wire (Witze, 1976b) make comparisons difficult. In addition, point-measurements over the cycle are not a good test of agreement with predictions, as the prescribed inlet jet trajectory is very important to the predicted flow field, and profile comparisons are preferable.

Predictions of the flow in the model compressing engine currently in progress (Arcoumanis et al, 1981d) still indicate inadequacies due to the prescription of inappropriate inlet conditions. However, as the flow "memory" of the intake events diminishes during compression, it is anticipated that results at TDC of compression will be in much better agreement with experiment than intake stroke comparisons would suggest.

However, if piston bowl geometries are involved in the calculation, the high swirl and squish velocity gradients involved would have to be adequately represented also.

2.7 Summary

The most important findings and conclusions of this chapter are summarised below.

(1) The inlet geometry is the major factor determining the in-cylinder flow structure during the intake stroke and the early part of the return stroke. Valve inlets result in the generation of an annular jet with ring vortices. In-cylinder mixing is mainly determined by the primary ring vortex formed during intake behind the valve and recirculating most of the in-drawn mass of air.

(2) With an off-centre port, the plane of rotation of the vortices is tilted with respect to the cylinder centreline, and the primary recirculation extends nearer to the piston head than in axisymmetric geometries.

(3) The imposition of practically relevant levels of swirl on the incoming flow results in significant elongation of the primary recirculation zone, the generation of a weak vortex behind the valve and the suppression of the piston head ring vortex.

(4) Engine speed variation between 100 - 335 r.p.m. has no significant effect on the flow patterns. If the speed range encompasses laminar flow (e.g. 10 r.p.m.), however, differences are evident in the regions where diffusion is important.

(5) The movement of an operating valve into the flowspace causes the incoming jet trajectory to lie nearer the axis and the jet to penetrate further into the flowspace than with a stationary valve.

(6) The flow patterns in the four-stroke cycle are similar to the ones in the non-compressing two-stroke cycle until approximately mid-compression. Mean velocities are low and uniform during the late part of the compression stroke and the expansion stroke.

(7) A sink-flow structure prevails during most of the exhaust stroke in both compressing and non-compressing cycles.

(8) High turbulence levels are generated at the shear layers of the in-drawn jet during intake, and they decay during the return stroke, especially under compressing conditions.

(9) The "rolled-up" vortex and corner "sink-flow" mentioned in the literature were shown to be of no significance in engine practice but only in idealised situations where no inlet-generated or other flow structures exist.

(10) Calculations of the flow have yielded promising results and are in good agreement with the present measurements. Discrepancies of calculations with experiments appear to originate primarily from numerical errors and grid size limitations and secondarily from the specification of inappropriate inlet conditions, while turbulence modelling errors are not as significant. The difficulties in the measurement as well as calculation of the inlet conditions suggest their specification further upstream in the valve passage. As the intake-generated flow structure is suppressed during compression, future predictions near TDC of compression should be in better agreement with experimental data.

APPENDIX 2.1

ENGINEERING SCIENCES DIVISION

THE FLOW CHARACTERISTICS OF A PISTON–CYLINDER ASSEMBLY WITH AN OFF-CENTRE, OPEN PORT

A. P. MORSE, BSc, MSc, PhD
Professor J. H. WHITELAW, BSc, PhD, CEng, MIMechE
M. YIANNESKIS, BSc, MSc
Department of Mechanical Engineering, Imperial College of Science and Technology, Exhibition Road, London SW7

Laser-Doppler anemometry has been used to measure the mean and r.m.s. values of the velocity components of the flow in a reciprocating assembly containing an off-centre, open port in the cylinder head and a flat piston. The port was inclined at an angle of 60° to the head and gave rise to a three-dimensional flow with no significant compression. The rotational speed was 200 rev/min, ensuring fully turbulent flow.

The measurements were restricted to the axial and circumferential velocity components and were made on three radial planes in order to describe the flow in sufficient detail. The results are presented in the form of radial profiles and vector diagrams in both the axial and cross-stream planes. The main flow pattern on the intake stroke is of the same general shape as that previously obtained with a symmetric port, a large vortex occupying the space bounded by the indrawn jet with a much smaller vortex in the corner between the cylinder head and wall. These vortices are however no longer symmetrical about the cylinder axis, but vary in both size and intensity with circumferential position. In the cross-stream plane, the primary vortex is characterized by the presence of a stress-induced swirling motion on either side of the plane of symmetry with velocities significantly greater than the circumferential velocity of the jet. At mid-stroke, these vortices rotate counter to the jet, but at 144° ATDC, the direction of rotation reverses over part of the length of the vortex and is in the same sense as the jet motion. On the exhaust stroke, the flow patterns are relatively simple with quasi-parallel axial flow and little swirl until the port is approached, when the outgoing jet accelerates and begins to rotate in a direction opposite to its motion on the intake stroke.

1 INTRODUCTION

In three earlier papers (1, 2, 3), the characteristics of the flow in motored piston-cylinder assemblies have been quantified. The measurements were obtained partly to provide new information of the details of the flow and partly to provide data which would assist the development and refinement of calculation methods such as that of references (4) and (5). The present measurements were also obtained with an open port, but located away from the centreline of the cylinder, as shown in Fig.1, giving rise to a three-dimensional flow. As before, there was no compression or combustion.

The flow pattern for the case of the symmetric annular port and non-swirling flow has been fully described in reference (1). During the intake stroke, a jet of approximately ten times the instantaneous piston velocity was drawn into the cylinder and directed towards the wall as a consequence of its angled entry. A strong reverse flow formed in the region between the jet and the cylinder axis with a weaker vortex, of opposite sense, located in the corner between the cylinder head and wall. Past mid-stroke, the jet was deflected from the wall and a third vortex, of lesser intensity than that near the cylinder head, formed between the cylinder wall and piston face. The corner vortices appeared as continuous toroidal rings around the periphery of the cylinder wall: the primary vortex constituted a symmetrical body of revolution around the cylinder axis. All the vortices collapsed, probably due to the influence of shear, soon after the piston reached bottom dead centre and, at the mid-point of the exhaust stroke, the streamlines were almost parallel to the axis, except near the port, where the flow accelerated rapidly on leaving the cylinder.

The essential difference introduced by the off-centre location of the port is that the indrawn jet reaches the wall at an earlier stage on the GBD side (see Fig. 1) of the flow

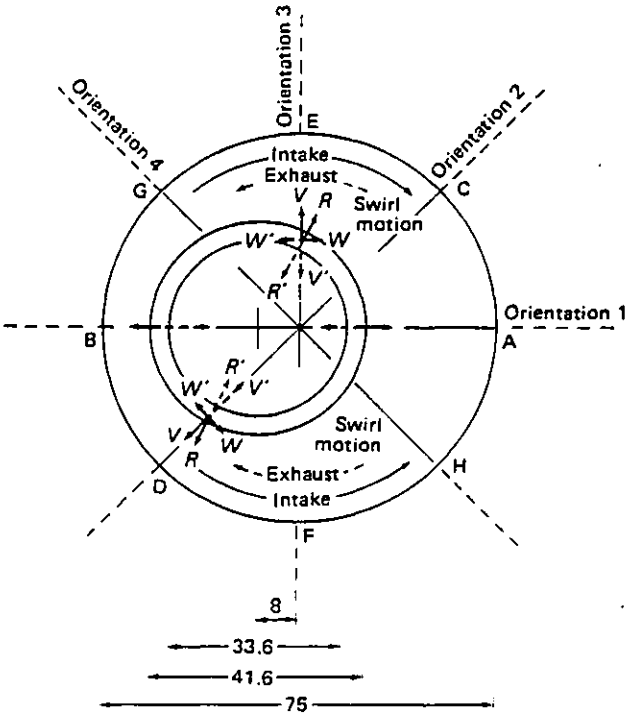


Fig. 1. Arrangement of cylinder head with off-centre valve (dimensions in mm)

©IMechE 1980
0020-3483/80/0194-0291 $02.00

than it does at corresponding points on the CAH side, with consequent implications for the axial position at which deflection occurs. As shown in Section 3, the asymmetry affects the corner vortices near the cylinder head and piston face and both now vary in size and intensity around the periphery of the wall. They exist as toroidal rings of varying cross-section which may be continuous or span only part of the circumference. Similarly, the primary vortex no longer takes the form of a symmetrical body of revolution. In addition, a swirling motion is imparted to the flow entering and leaving the cylinder. As shown in Fig. 1, the resultant mean velocity of the jet in the r–θ plane is everywhere radial to the axis of the port, so that the direction of rotation on the intake stroke is clockwise in the top half of the cylinder and counter-clockwise in the bottom half. On AB, the swirl velocities are ideally zero. Hence, two opposing circumferential jet motions exist, dividing the flow space into two regions symmetrical about AB. Given perfect alignment of the flow, this situation would prevail along the length of the cylinder. On the exhaust stroke, the rotation of the outgoing jet is in the opposite sense to that on intake, being counter-clockwise in the top half of the cylinder and clockwise in the bottom half.

The present flow is closer to a real-engine configuration than those of references (1–3), although still without the essential ingredients of compression and combustion. The three-dimensional nature of the flow poses greater problems for calculation and also for the collection and presentation of data. The number of measurements required to allow understanding of the flow is considerably greater than for two-dimensional flows and thus it was found necessary to obtain data on three radial axes, spaced 45° apart as shown in Fig. 1. This may be contrasted with measurements on a single plane for an axisymmetric flow, representing a six-fold increase in effort over the case of the symmetric port and non-swirling flow (1). This increase was found to be essential and is indicative of the effort which will be necessary to measure and understand the flow in real engine configurations. The axial and circumferential velocity components were found to be sufficient to describe the important features of the flows and, to economize of effort, the radial velocity component was not measured in the same detail and is not reported here.

The flow arrangement and instrumentation are similar to those of references (1) and (2) and are described only briefly in the following section. The results obtained are presented in Section 3 and the paper ends with a discussion and concluding remarks.

2 FLOW ARRANGEMENT AND INSTRUMENTATION

The model 'engine' was fabricated from Plexiglass and the flat-surfaced 75 mm diameter piston was driven in simple harmonic motion with a stroke of 60 mm. The ratio of swept-to-clearance volume was 2.0, and an open port arrangement, with an annular entry of 4 mm width and inclined at 60° to the flat cylinder head, ensured negligible compression. The centre of the port was located 8 mm away from the axis of the cylinder as shown in Fig. 1. The rotational speed was 200 rev/min which on the basis of previous work, suggests a fully turbulent flow.

A laser-Doppler anemometer, operating in forward-scatter mode, was used to measure two orthogonal components of mean velocity and the r.m.s. of the corresponding fluctuations. The light from a 5 mW helium–neon laser ($\lambda = 632.8$ nm) was focused onto a rotating diffraction grating which acted as a beam splitter and produced a frequency shift of ± 1.84 MHz on the first order beams. A second lens was used to eliminate spherical aberration and produce parallel beams. The first order beams were focused to intersect inside the cylinder and light scattered from atomized silicone-oil droplets in the flow was collected by a third lens and focused onto the aperture of a photo-multiplier (RCA model 4836). The half-angle of intersection of the incident light beams was 4°, giving a fringe spacing of 4.53 μm and a frequency-to-velocity conversion factor of 4.53 ms^{-1}/MHz. The length of the intersection region at the e^{-2} locations was approximately 1.9 mm and the diameter 150 μm, giving approximately thirty-three fringes in the measuring volume. The optical components were assembled on a compound table which was translated in two orthogonal planes with respect to the piston–cylinder assembly to allow measurements of the axial and circumferential velocity components. All measurements were performed on a horizontal diameter with the light beams in the horizontal plane (to provide the axial velocity) or the vertical plane (for the circumferential velocity). The port could be rotated in the cylinder head in order to permit measurements on the three radial axes shown in Fig. 1.

The Doppler signals were amplified and band-pass filtered (Harwell amplifier 91-2151-2/6) to remove low frequency pedestal and high frequency noise, and passed to an oscilloscope for display and to the input channel of a Hewlett-Packard model 5360 frequency counter. The triggering mechanism of the oscilloscope was used to accept signals above a certain threshold level and, for each corresponding burst, an arming pulse was sent from the oscilloscope to the measuring time input of the counter. The start and stop information of the arming pulses was sent to a gating circuit, which also received crank angle information from an optical encoder coupled to the drive shaft and synchronized with its rotation. The frequency measurements were processed in part within the counter, using a keyboard (Hewlett-Packard model 5265A) to program the instrument, and in part by a mini-computer (Digital PDP8e) interfaced to a digital magnetic-tape recorder (Racal model 7000). The two arrangements have been described in detail in references (1) and (2) respectively. In accordance with the procedure adopted in these earlier works, a crank-angle of $\Delta\theta = 10°$ was used to process the data, so that the mean and r.m.s. velocities at a crank angle were evaluated from signals recorded in the range $\theta - \Delta\theta/2$ to $\theta + \Delta\theta/2$.

In the two-dimensional flows of references (1) and (2), it was possible to check the precision of the measurements by integration of the mean-velocity profiles and comparison with the mass flow rate of fluid entering the cylinder (which is proportional to the instantaneous piston velocity). This suggested that the mean values are subject to uncertainties of not more than ± 3 per cent, except in regions of low velocity and high turbulence intensity. The same order of accuracy is expected to prevail in the present, asymmetric case. Likewise, measured values of r.m.s. quantities, which are always overestimated due to the effects of crank-angle broadening, are considered accurate to 10–15 per cent. Detailed analyses

©IMechE 1980

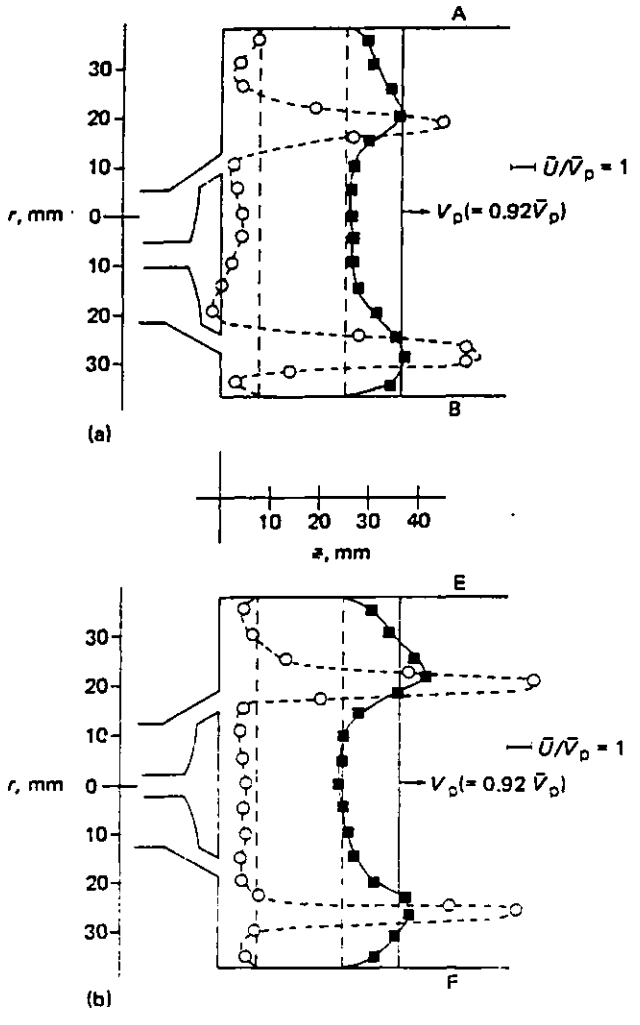


Fig. 2. Axial velocity at $\theta = 36°$
(a) orientation 1 (b) orientation 3

of the experimental uncertainties involved can be found in references (1) and (2).

3 RESULTS

In-cylinder profiles of the ensemble-averaged mean and r.m.s. velocity components and the associated velocity vector diagrams are presented in Figs. 2–12. As in the earlier works, crank angle locations of 36°, 90° and 144° on the intake stroke and 270° on the exhaust stroke have been chosen to give a concise description of the development of the flow through the cycle. In the figures, the outlines of the cylinder and port are shown in cross-section with the piston face in the correct position for the crank angle under consideration. The instantaneous magnitude and direction of the piston velocity are indicated by an arrow on the piston head. The profiles of mean and r.m.s. velocity are normalized by the average piston speed $\bar{V}_p$ (0.4 ms^{-1}) and plotted relative to base lines drawn at the appropriate axial locations. The positive swirl velocities denote a counter-clockwise rotation in the top half of the cylinder and a clockwise rotation in the bottom half.

Profiles of the mean axial velocity at $\theta = 36°$ are shown in Fig. 2. Along both orientations 1 and 3, the peaks in the profiles show only slight outward movement towards the wall between $z = 7.5$ mm and $z = 25$ mm, indicating that, in this early part of the cycle, the incoming jet is drawn mainly in the axial direction. As in the case of the symmetric port, the jet does not actually make contact with the wall at any point on the circumference, although it reaches somewhat closer at B than at A. Instead, it spreads around the primary vortex and directly onto the piston face. Because of the proximity of B to the port, the region of negative velocity at $z = 7.5$ mm corresponding to the cylinder-head vortex is considerably smaller than that at A, while the vortex is of intermediate size at E and F; it is also longer in the axial direction in the same sequence. The vortex thus takes the form of a toroidal ring, increasing continuously in cross-section from B to A. As expected, the flow is closely symmetrical about the

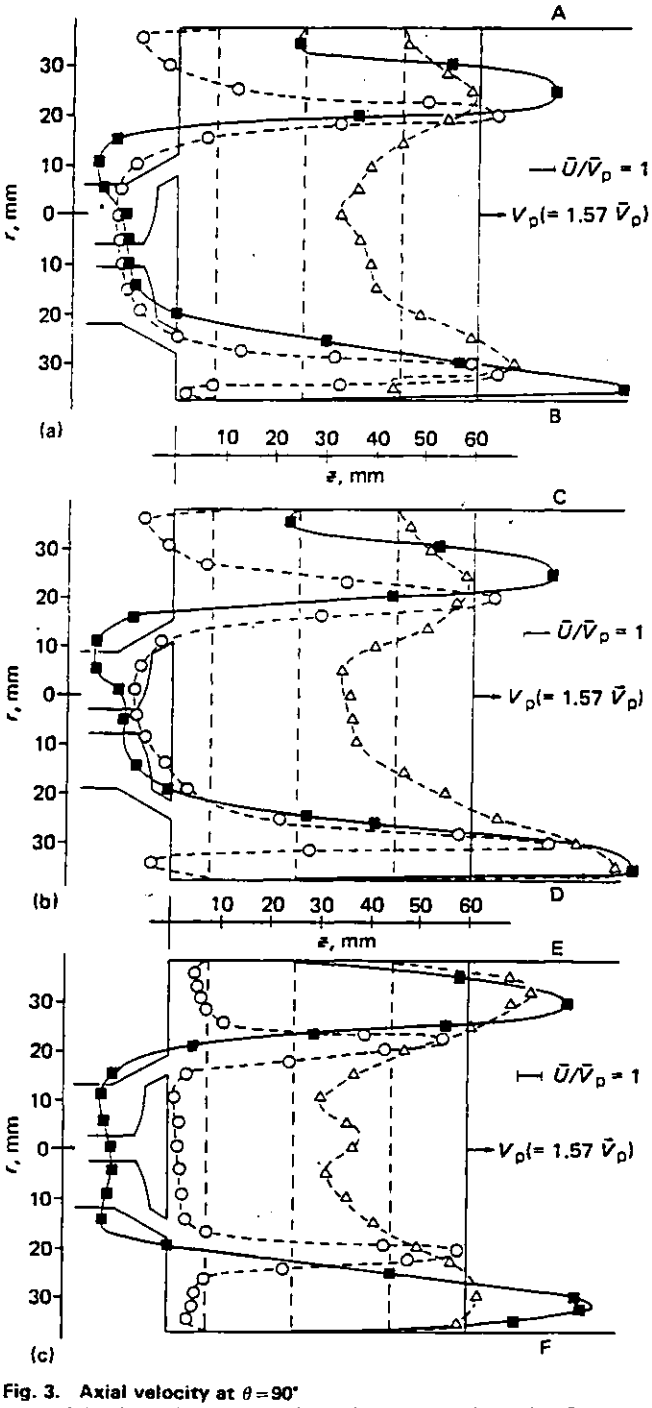


Fig. 3. Axial velocity at $\theta = 90°$
(a) orientation 1 (b) orientation 2 (c) orientation 3

©IMechE 1980

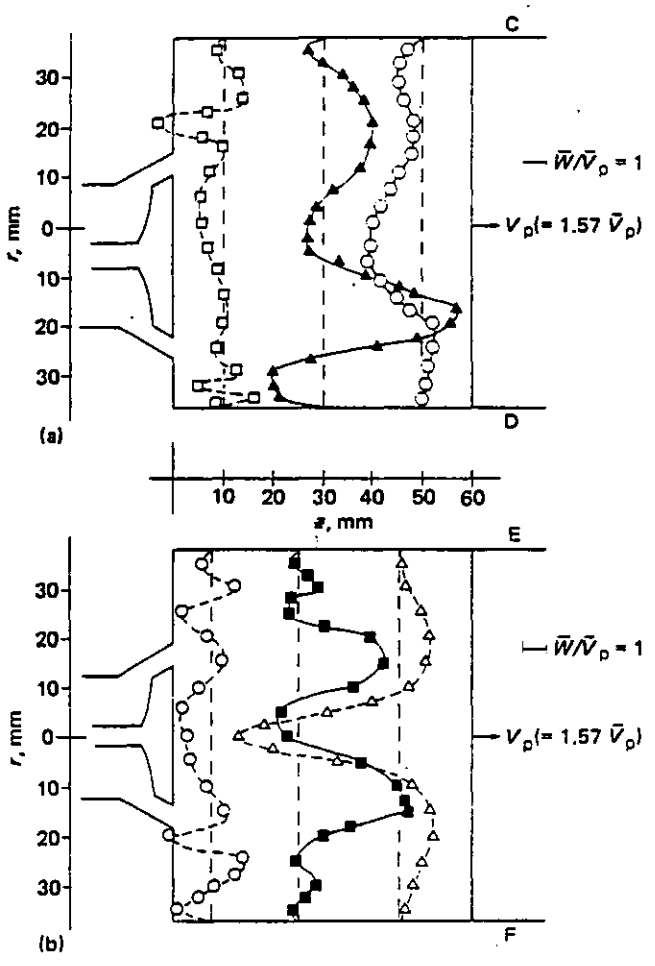


Fig. 4. Swirl velocity at $\theta = 90°$
(a) orientation 2 (b) orientation 3

cylinder axis on orientation 3, particularly at $z = 7.5$ mm. On orientation 1, the flow between the jet regions is roughly symmetrical about the centreline of the port, although the negative velocities in the primary vortex are slightly larger near B than near A. At $z = 25$ mm, the velocities gradually approach that of the piston as the flow curves sharply around the primary vortex and spreads onto the piston face. The swirl velocities at $\theta = 36°$ are too low (maximum value $\sim 0.8\ \bar{V}_p$) to permit accurate definition of the flow in the cross-stream plane.

Figures 3 and 4 show measured profiles of the mean axial and swirl components of velocity at $\theta = 90°$. By mid-stroke, the indrawn jet has reached the wall at all points on the circumference, although the point of contact varies with orientation. At $z = 25$ mm, the jet is right on the wall at location B with a maximum velocity about 2.5 mm from the surface which is 30 per cent higher than on the opposite side of the flow. The small region of negative velocity at $z = 45$ mm shows that the jet separates from the wall giving rise to a weak vortex in the corner between the wall and piston face. Separation does not however occur at any other circumferential location. At D, the jet hits the wall at $z = 25$ mm, but remains in close contact at $z = 45$ mm with a peak velocity almost three times that at C. At all points other than B and D, the jet is deflected from the wall between $z = 25$ mm and $z = 45$ mm, with the direction of its subsequent inward trajectory being denoted by the position of occurrence of the velocity maximum. Some loss of symmetry is however evident on orientation 3. In contrast to the non-swirling symmetric flow (1), velocities near the centreline of the cylinder remain negative at $z = 45$ mm, indicating that the primary vortex extends very close to the piston face. The vortex near the cylinder head shows much the same behaviour as at $\theta = 36°$, increasing continuously in size from B to A. At $z = 25$ mm, it is only

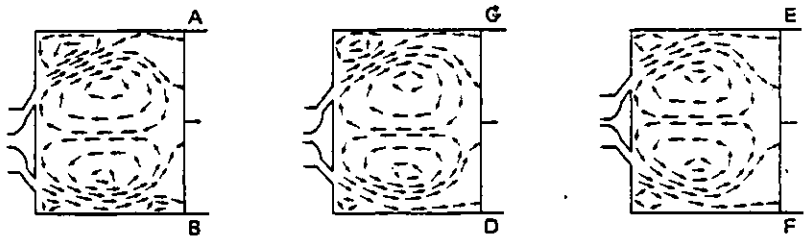


Fig. 5. Flow directions in the z-r plane at 90°

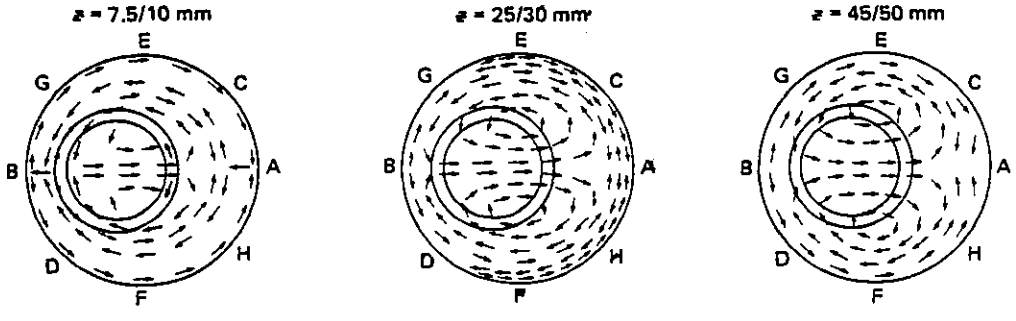


Fig. 6. Flow directions in the r-θ plane at 90°

©IMechE 1980

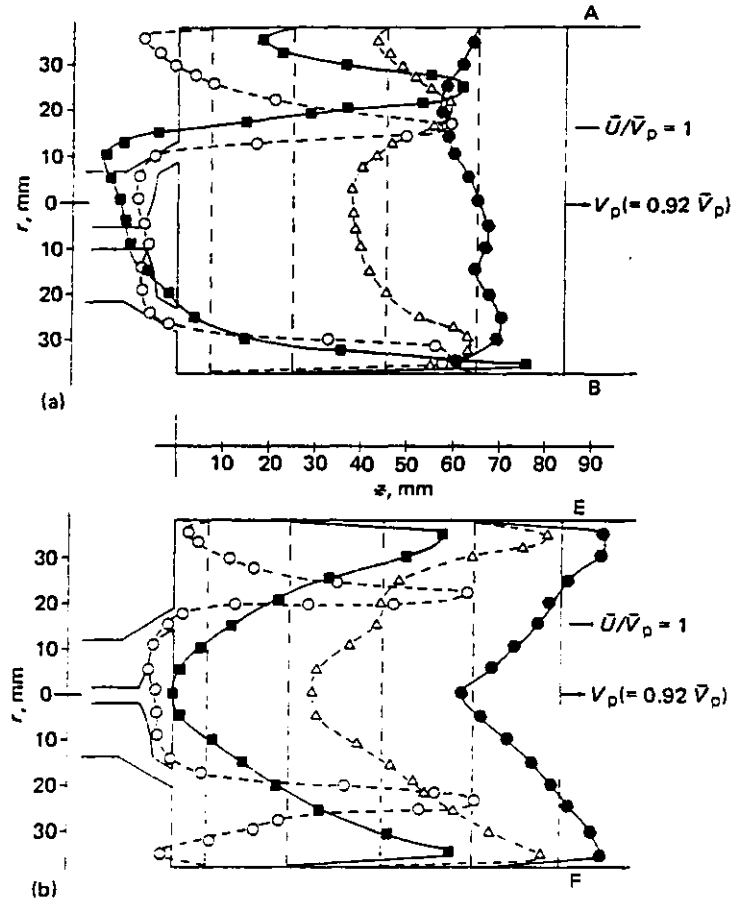


Fig. 7. Axial velocity at $\theta = 144°$
(a) orientation 1 (b) orientation 3

present at locations A and C (and H). An illustration of the flow pattern prevailing on each orientation of measurement is provided in Fig. 5.

The swirl velocity profiles (Fig. 4) are presented for orientations 2 and 3 only, since the velocities remain low ($< 1.0\ \bar{V}_p$) along the plane of symmetry AB. Due to beam interference from scratches on the cylinder surface at $z = 25$ mm and $z = 45$ mm, the measurements along orientation 2 had to be taken at slightly different axial locations. The profiles reveal a double vortex structure corresponding to the primary and wall vortices in the x–r plane and again separated by the jet region. Along both orientations, the presence of the jet at the first station of measurement is evidenced by the occurrence of strong negative velocitites approximately at the angle of trajectory, indicating that the direction of rotation is clockwise above AB and counter-clockwise below. Nearer the wall, the region of positive, then negative velocity corresponds to the formation of the cylinder-head vortex. The negative velocities near the cylinder axis indicate the presence of the primary vortex. This vortex crosses EF at $r \sim 15$ mm (where the swirl velocities are positive), but barely reaches CD. An interpretation of the flow pattern in the cross-stream plane for this and the other stations of measurement is given by the arrows of Fig. 6 which represent local flow direction. The radial velocity on the cylinder axis along AB (which equals the swirl velocity at the mid-point of EF) is negative at all three stations, so that the motion on the plane of symmetry is everywhere from B to A. This suggests that the primary vortex spirals inwards as shown, its direction of rotation being opposite to that of the jet flow. At $z = 7.5/10$ mm, the region of positive velocity adjacent to the jet is very limited, but further downstream ($z = 25/30$ mm), as the primary vortex expands, it increases considerably and the region of negative velocity near the cylinder axis becomes correspondingly small. At $z = 45$ mm, the jet suffers little deflection from the wall at E and F (see Fig. 3b) and the positive velocities of the primary vortex extend from a radius of ~ 10 mm right up to the wall. In contrast, at C ($z = 50$ mm), the deflection is more marked (see Fig. 3a) and the negative swirl velocities near the wall denote the clockwise rotation of the inward flow. At D, the primary vortex again reaches close to the wall. The contraction of the vortex on the CAH side of the flow is consistent with the flow patterns in the x–r plane, indicated by Fig. 5. As the vortex contracts, the swirl velocities near the cylinder axis become increasingly negative on both CD and EF in order to conserve angular momentum.

At mid-stroke, the vortex in the corner between the cylinder-head and wall also rotates in a direction opposite to the indrawn jet. This vortex is evidenced by a region of positive swirl velocity beyond the outer edge of the jet, followed by a region of negative velocity very close to the wall. In common with the view of the vortex in the x–r plane, it shows a continuous increase in size along the cylinder circumference from B to A; indeed, at location D ($z = 10$ mm), it is so small that the region of negative velocity is confined to within about 1.25 mm of the wall. The vortex does not cross AB, where the motion is purely

©IMechE 1980

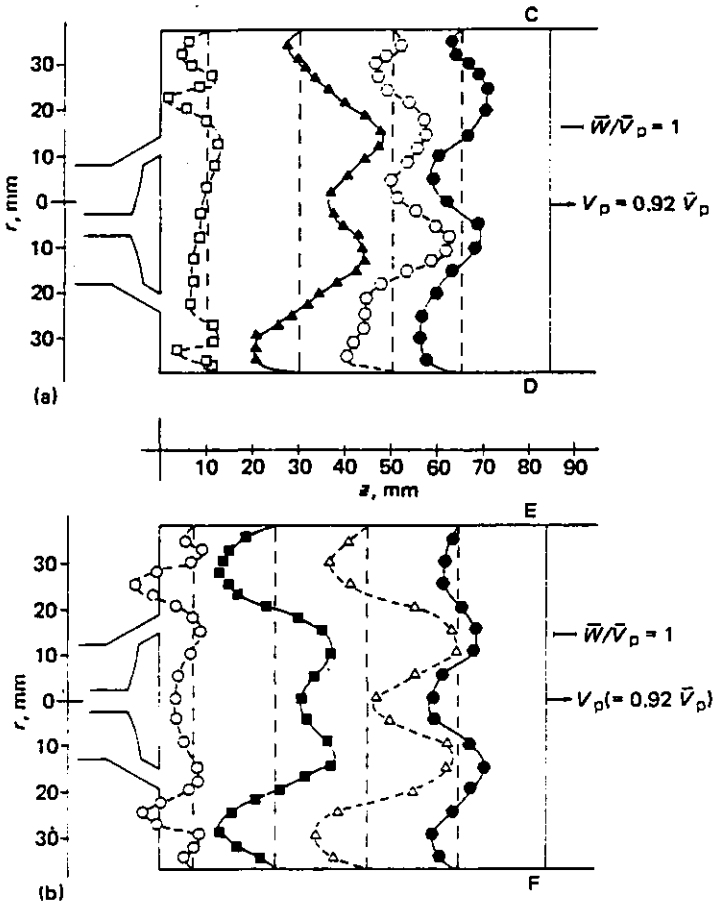


Fig. 8. Swirl velocity at $\theta = 144°$
(a) orientation 2 (b) orientation 3

radial (and axial), but divides into two symmetric zones of recirculation in the top and bottom halves of the cylinder. At $z = 25$ mm, the cylinder-head vortex just remains in existence at locations E and F, and presumably also at C, although it has disappeared at this last location by $z = 30$ mm. At $z = 45$ mm, a small vortex forms near the piston face as the jet separates from the wall at B (see Fig. 5a). Again, it exists as two recirculation zones symmetrical about AB and, although the direction of rotation is not immediately clear (the vortex does not cross CD), it is probably counter to the jet motion as with the cylinder-head vortex formed upstream.

Profiles of the mean axial velocity at $\theta = 144°$ are shown in Fig. 7 and the accompanying flow directions in Fig. 9. The cylinder-head vortex is still largest at A and is roughly of the same radial size as in mid-stroke; in the axial direction, it has however increased and extends beyond $z = 25$ mm. This vortex is not apparent at location B at $z = 7.5$ mm — it probably does exist, but only in the region between the last point of measurement ($r = 35$ mm) and the wall. It is present at E and F and also C and D (not shown), but does not reach to $z = 25$ mm on either orientation. At A, the jet reaches the wall between $z = 25$ mm and $z = 45$ mm and is sharply deflected, giving rise to a vortex near the piston face which is just in evidence at the latter station and extends beyond the cylinder axis at $z = 65$ mm. At B, the jet reaches the wall earlier — at about $z = 25$ mm — but remains in close contact and only a small piston-face vortex is formed at $z = 65$ mm. At locations E and F, the jet deflection is minor compared to that at A and the position of the maximum velocity moves only slightly inwards between $z = 25$ mm and $z = 65$ mm. The behaviour of the flow on orientation 2 is intermediate to that on orientations 1 and 3 with the piston-face vortex at C ($z = 65$ mm) extending from the wall to a radius of about 12 mm and the jet being deflected at D, but without the formation of a vortex. At $z = 65$ mm, regions of negative velocity are just in evidence between the inward trajectories of the jet flow on all three orientations, indicating that the primary vortex terminates shortly beyond this point. For the symmetric non-swirling flow (1), the primary vortex reached only as far as $z \sim 50$ mm.

The swirl velocity profiles along orientations 2 and 3 are shown in Fig. 8. At $z = 7.5/10$ mm, the flow pattern at $\theta = 144°$ is much the same as in mid-stroke with both the primary and cylinder-head vortices rotating in the opposite sense to the indrawn jet. The only significant differences

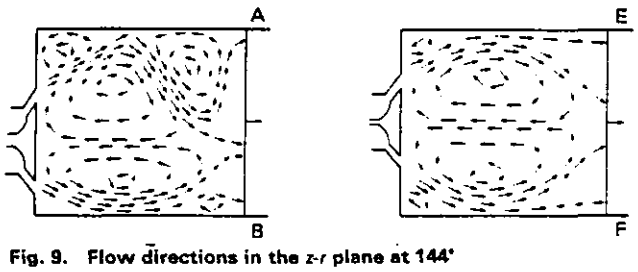


Fig. 9. Flow directions in the z-r plane at 144°

©IMechE 1980

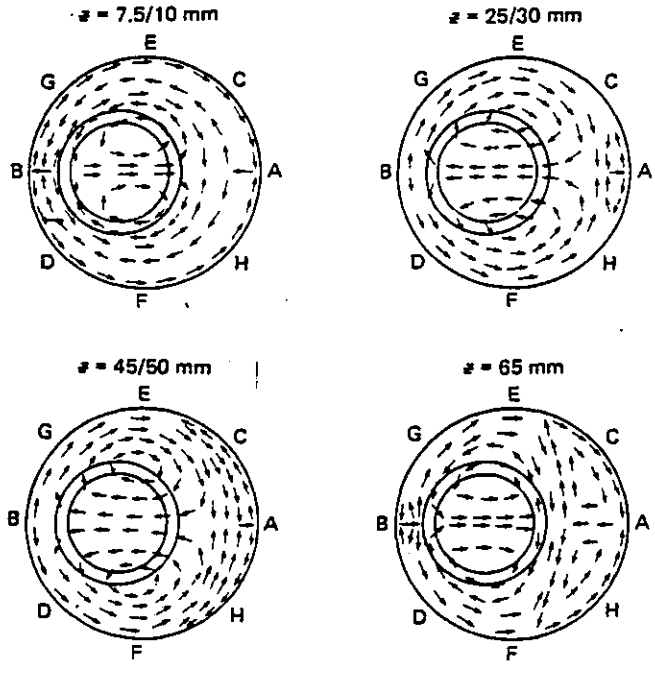


Fig. 10. Flow direction in the r-θ plane at 144°

are that positive velocities are recorded on orientation 2 in the outer region of the primary vortex, indicating that the vortex does in fact cross CD, and that the cylinder-head vortex is not well-defined at location D. Further downstream however, a significant change occurs. At $z=25$ mm and $z=45$ mm, the swirl velocity on the cylinder axis along orientation 3 (equivalent to the radial velocity at the mid-point of AB) turns positive, so that the direction of motion on the plane of symmetry becomes from A to B and not B to A as in the corresponding profiles at $\theta=90°$. This implies that the primary vortex changes direction and now rotates in the same sense as the jet flow. An interpretation of the flow patterns at all four measurement stations is given by Fig. 10. At $z=25/30$ mm, the primary vortex extends very close to the wall, where its negative swirl velocities merge with the negative velocities of the jet. At these locations, the cylinder-head vortex only exists on a part of the circumference between A and C (and H), so unfortunately it is not possible to say for certain whether this vortex also changes direction. A similar situation occurs at $z=45/50$ mm, but with the regions of negative velocity near the wall at C and D growing larger as the deflected jet spirals inward. The positive velocity very close to the wall at C denotes the formation of the piston-face vortex, which merges with the jet and the primary vortex, all of which rotate in the same sense. The decrease in the swirl velocity at the mid-point of EF between $z=25$ mm and $z=45$ mm suggests a weakening of the cross-flow from A to B, and indeed, at $z=65$ mm, the direction of motion reverses and again becomes towards A. The primary vortex, which now occupies only a very small area near the cylinder axis (but extends further along EF than along CD), thus again moves counter to the (weak) rotation of the jet. The region of positive, then negative velocity near location C corresponds to the formation of the piston-face vortex, which also opposes the jet motion, in contrast to the situation at $z=50$ mm. This vortex does not form at D, nor at E or F, where the negative swirl velocities simply indicate the spiralling motion of the incoming jet. It is however present in a limited region near location B, presumably also rotating in the opposite sense to the jet flow.

As the piston reaches BDC, the vortices generated near the cylinder-head and piston-face disappear and the primary vortex, which is very weak, expands to fill almost all of the flow space. This vortex also collapses soon after the start of the exhaust stroke, although residual effects persist for a time in the region away from the piston. By mid-stroke, the flow is lacking in feature and profiles are presented here for the mean axial and swirl velocities on orientation 2 only (Fig. 11). On orientation 3, the axial velocity distribution at $\theta=270°$ is almost uniform, indicating an approximately parallel flow, until distinct peaks appear in the profiles near the cylinder head as the flow accelerates out through the port. On orientations 1 and 2, the profiles at $z=25$ mm and $z=45$ mm are noticeably less uniform. At the latter station, the velocities are highest near the wall at A and C, but then a cross-flow (evidenced by the radial velocity measurements on the cylinder axis) occurs towards B and D, giving rise to increased velocities and a stronger jet exhaust at $z=7.5$ mm. The maximum jet velocity at $z=7.5$ mm is about 20 per cent higher at B than at A and 50 per cent at D than at C. Between the jet regions, the velocity falls to a minimum close to zero as the cylinder head is approached. The swirl velocities at $z=50$ mm are almost identically zero, but the profile at $z=30$ mm displays some trace of the primary

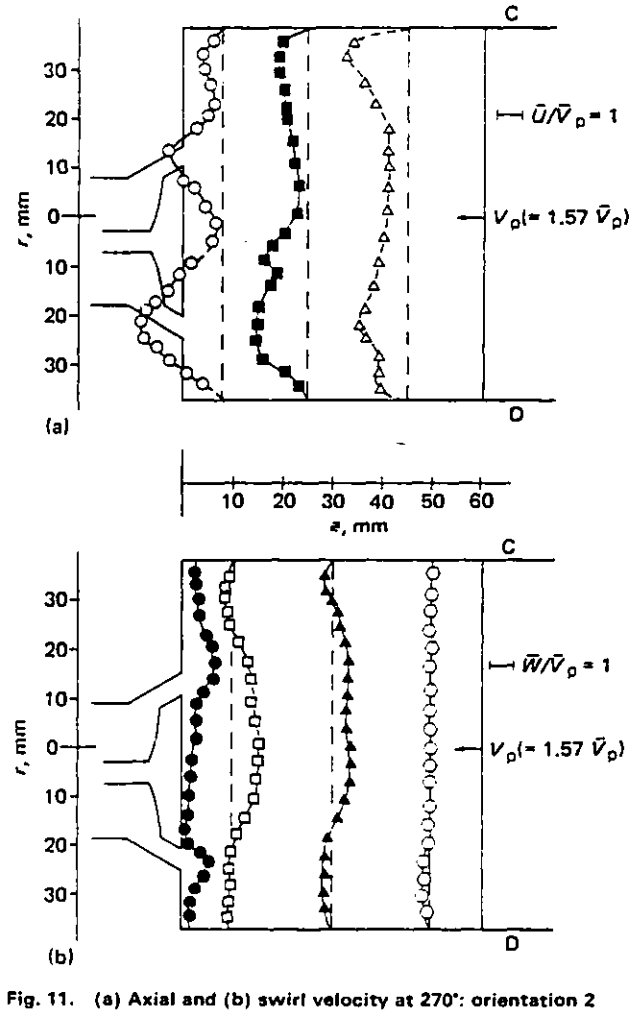


Fig. 11. (a) Axial and (b) swirl velocity at 270°: orientation 2

©IMechE 1980

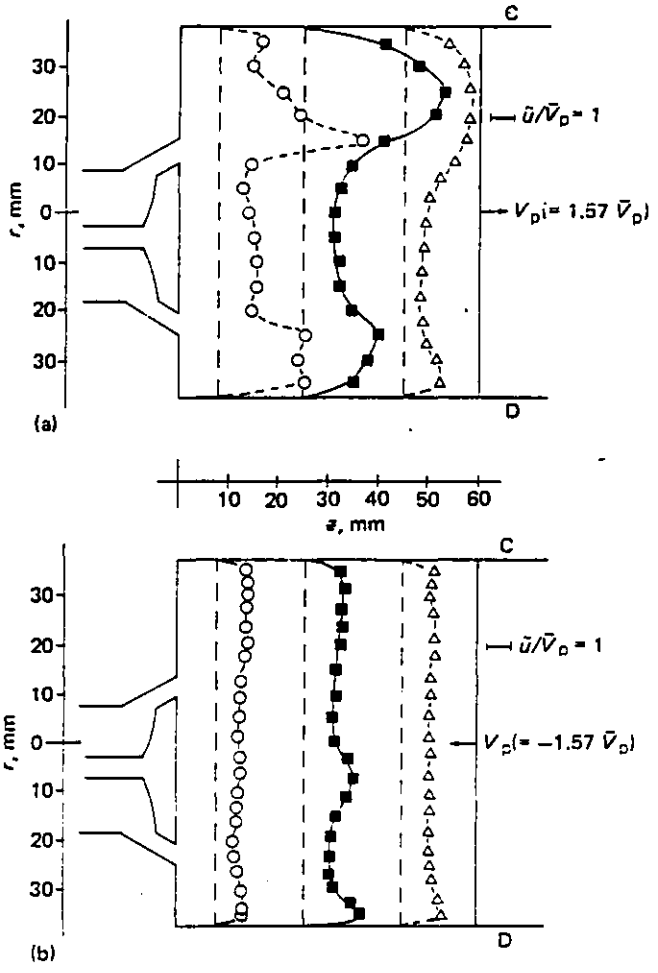


Fig. 12. R.m.s. of axial velocity at 90 and 270°: orientation 2

vortex generated during the intake stroke. At $z = 10$ mm, the flow begins to feel the presence of the port, and at $z = 2$ mm, distinct regions of positive swirl velocity appear as the jet spirals out of the cylinder, in a clockwise direction at D and counter-clockwise at C.

Root mean square profiles show the same general features as those obtained with the symmetric port arrangement (1, 2), although there is some difference in magnitudes due to the greater complexity of the stress and strain fields. Fig. 12 presents specimen results for the axial velocity fluctuations on orientation 2 at $\theta = 90°$ and $\theta = 270°$; they correspond to the mean-velocity profiles of Fig. 3b and 11a respectively. On the intake stroke, the level of fluctuations increases sharply in the shear layers adjacent to the indrawn jet as turbulence is generated against the principal strain rate $\partial\bar{U}/\partial r$. Due to the greater amount of flow space on the C side of the flow, the jet decays more rapidly, giving a peak r.m.s. level at $z = 45$ mm which is nearly twice as large as on the D side and corresponding turbulence intensity ($\tilde{u}/\bar{U}$) which is six times larger. Axial velocity fluctuations are also produced by interaction of the stress field with the circumferential strain rate $\partial\bar{U}/\partial\theta$, see reference (6), but this contribution appears to be minor, as the r.m.s. levels in the primary vortex are of much the same order of magnitude as in the symmetric case. On the exhaust stroke, the r.m.s. profiles are fairly uniform as there is little shear in either the radial or circumferential directions (see Fig. 11). As the jet accelerates on approaching the port at $z = 7.5$ mm, the profile remains uniform despite the radial shear. This is due to the positive rate of production of $\tilde{u}$ against $\partial\bar{U}/\partial r$ being cancelled by the negative rate against the strain rate $\partial\bar{U}/\partial z$.

4 DISCUSSION

The results of the previous section have led to an understanding of the effects on the in-cylinder flow introduced by the off-centre positioning of the port arrangement. The asymmetry imparts a circumferential component of velocity to the indrawn jet so that, as it is directed towards the wall, it spirals around the primary vortex formed behind the port. The direction of rotation of the jet is in opposite senses above and below the plane of symmetry. The primary vortex and the vortices formed in the corners near the cylinder head and piston face all vary in size and intensity with angular position and indeed may not be present at all circumferential locations at a given axial station. The flow within the vortices is three-dimensional with recirculating motions existing in the cross-stream planes in addition to the recirculation in the axial direction.

The motion in the r-θ plane is particularly interesting in that its sense of rotation sometimes opposes that of the jet and sometimes follows it. This behaviour can be explained with the realization that it is the *axial* motion which primarily determines the flow processes within the cylinder. This can be seen clearly from Figs. 3 and 4 where the swirl velocity of the indrawn jet at $z = 7.5$ mm is only about 12 per cent of the magnitude of the axial velocity component. The circumferential variations of axial (and to a lesser extend radial) velocity, rather than the diffusion of angular momentum from the jet, initiates the recirculating motion in the cross-stream plane. This is easily understood by examination of the production terms in the Reynolds stress transport equations for $\overline{uw}$ and $\overline{vw}$, see reference (6), which (for a steady flow) read:

$$\mathrm{PROD}_{\overline{uw}} = -\overline{u^2}\frac{\partial\bar{W}}{\partial z} - \overline{vw}\frac{\partial\bar{V}}{\partial r} - \overline{uw}\left(\frac{1}{r}\frac{\partial\bar{W}}{\partial\theta} + \frac{\bar{V}}{r}\right) - \overline{uw}\frac{\partial\bar{u}}{\partial z} - \overline{vw}\frac{\partial\bar{U}}{\partial r} - \frac{\overline{w^2}}{r}\frac{\partial\bar{U}}{\partial\theta} \quad (1)$$

and

$$\mathrm{PROD}_{\overline{vw}} = -\overline{uv}\frac{\partial\bar{W}}{\partial z} - \overline{v^2}\frac{\partial\bar{W}}{\partial r} - \overline{vw}\left(\frac{1}{r}\frac{\partial\bar{W}}{\partial\theta} + \frac{\bar{V}}{r}\right) - \overline{uw}\frac{\partial\bar{V}}{\partial z} - \overline{vw}\frac{\partial\bar{V}}{\partial r} - \overline{w^2}\left(\frac{1}{r}\frac{\partial\bar{V}}{\partial\theta} - \frac{\bar{W}}{r}\right) \quad (2)$$

These shear stresses affect the circumferential motion by way of their appearance in the angular momentum equation, viz:

$$\bar{U}\frac{\partial r\bar{w}}{\partial z} + \bar{V}\frac{\partial}{\partial r}(r\bar{W}) + \frac{\bar{W}}{r}\frac{\partial}{\partial\theta}(r\bar{W}) = -\frac{1}{\rho}\frac{\partial\bar{P}}{\partial\theta} - \left[r\frac{\partial\overline{uw}}{\partial z} + \frac{1}{r}\frac{\partial}{\partial r}(r^2\overline{vw}) + \frac{\partial\overline{w^2}}{\partial\theta}\right] \quad (3)$$

© IMechE 1980

where $\partial P/\partial\theta$ denotes the circumferential pressure gradient. Equations (1) and (2) show that, in the initial absence of swirl, $\overline{uw}$ and $\overline{vw}$ are created by the action of the normal stress $\overline{w^2}$ against θ-derivatives of $\bar{U}$ and $\bar{V}$ respectively. Once created, the stresses become interactive, $\overline{uw}$ acting against other strain rates to produce $\overline{vw}$ and vice versa. At the same time, these stresses induce a circumferential motion, so that all six production terms in the transport equations become non-zero. Thus the cross-stream motion in the primary and corner vortices evolves independently of the jet motion, and provides a rational ground for the magnitude and direction of the swirl velocities observed. The complexity of the stress and strain fields does however preclude an immediate understanding of the reason for the change in the rotational sense of the vortices at $\theta = 144°$ (see Fig. 10). Note that the induced motion in the cross-stream plane is not associated with the piston movement, since time-derivatives are not crucial to the argument presented above. Similar flow patterns would therefore be expected to prevail in a steady flow through the same port.

5 CONCLUSIONS

Although carried out in a very much simplified engine configuration, the present measurements provide a direct quantification of the effects of an asymmetric entry on the flow patterns inside the cylinder. The extent of the in-cylinder mixing process, as evidenced by the length of the primary vortex behind the port, has been found to be intermediate between the results of references (1) and (2), obtained with a symmetric port without swirl and with a strong, ordered swirl respectively. A further increase in mixing would therefore presumably occur if swirl vanes were incorporated upstream of the off-centre port arrangement.

The measurements reveal a vortex structure which is consistent with the results obtained by Ekchian and Hoult (7) using photographic flow visualization techniques. These authors employed a similar off-set port arrangement to that used here, but with a finite 'valve' lift. The primary vortex generated behind the port is clearly in evidence, as is the large vortex which forms near the piston face on the side of the flow remote from the port axis (see Fig. 9). However, as a consequence of the valve lift, the plane of rotation of the primary vortex is more inclined to the centreline of the cylinder than in the present investigation, and the corner vortices near the cylinder head are of different size. There is no description of the flow in the cross-stream plane. Similar flow records were made by Willis *et al* (8), but with a shrouded valve, giving rise to a much stronger spiralling motion than that recorded here, and with two centres of rotation. These should be useful for comparison of future measurements obtained in an off-centre arrangement with ordered swirl.

The present measurements also provide a useful testing ground for the development and refinement of computational procedures in comparatively simple reciprocating flows to increase the confidence behind their use in real engine configurations. Predictions of the flow with the symmetric port arrangement have already been made (9) and the degree of correspondence with experimental data is encouraging. The present three-dimensional measurements suggest that a corresponding calculation will require as many grid nodes in the circumferential, as in the axial and radial directions. As a consequence, numerical inaccuracies may prove, in the short term, to be more significant than those which are likely to arise from turbulence models. It is evident, however, that the accurate prediction of the flow in the cross-stream plane of the vortices, particularly the change in the direction of rotation of the primary vortex past mid-stroke, is likely to require a more elaborate turbulence model than the eddy-viscosity approaches used so far. Models of this type have been found (6) to give poor representation of the shear stresses $\overline{uw}$ and $\overline{vw}$ governing the circumferential motion, and a full solution of the Reynolds stress transport equations may be desirable.

ACKNOWLEDGEMENTS

The authors are glad to acknowledge financial support from the Science Research Council and the Mechanical Engineering Machine Tools Requirements Board through the Internal Combustion Engine Project at Atomic Energy Research Establishment, Harwell.

REFERENCES

(1) MORSE, A. P., WHITELAW, J. H. and YIANNESKIS, M. Turbulent flow measurements by laser-Doppler anemometry in motored piston-cylinder assemblies. *J. Fluids Engng.*, 1979, **101**, 208

(2) MORSE, A. P., WHITELAW, J. H. and YIANNESKIS, M. Influence of swirl on the flow characteristics of a reciprocating piston-cylinder assembly. Imperial College, Mech. Eng. Dept. Report FS/78/41, Nov. 1978. (To be published in *J. Fluids Engng.*, Dec. 1980.)

(3) BICEN, A., VLACHOS, N. S. and WHITELAW, J. H. The creation and destruction of vortices in unsteady flows. *Letters in Heat and Mass Transfer*, 1980, **7**, 77.

(4) GOSMAN, A. D., MELLING, A., WATKINS, A. P. and WHITELAW, J. H. Axisymmetric flow in a motored reciprocating engine. *Proc. Instn. Mech. Engrs.*, 1977, **192**, 213.

(5) GOSMAN, A. D., JOHNS, R. J. R. and WATKINS, A. P. Assessment of a prediction method for in-cylinder processes in reciprocating engines. Proc. General Motors Symposium, Detroit, Feb. 1978.

(6) MORSE, A. P. Axisymmetric free shear flows with and without swirl. PhD thesis, University of London, 1980.

(7) EKCHIAN, A. and HOULT, D. P. Flow visualization study of the intake process of an internal combustion engine. SAE Paper 790095, 1979.

(8) WILLIS, D. A., MEYER, W. E. and BIRNIE, C. Mapping of airflow patterns in engines with induction swirl. SAE Paper 660093, 1966.

(9) JOHNS, R. J. R. Prediction of flow in Diesel engine cylinders. PhD Thesis, University of London, 1980.

This paper is published for written discussion. The MS was received on 17 October 1979 and was accepted for publication on 26 June 1980. 22.

©IMechE 1980

APPENDIX 2.2

MEAN AND R.M.S. VELOCITY PROFILES FOR PIPE AND VALVE INLET CONFIGURATIONS IN THE NON-COMPRESSING ENGINE WITHOUT SWIRL

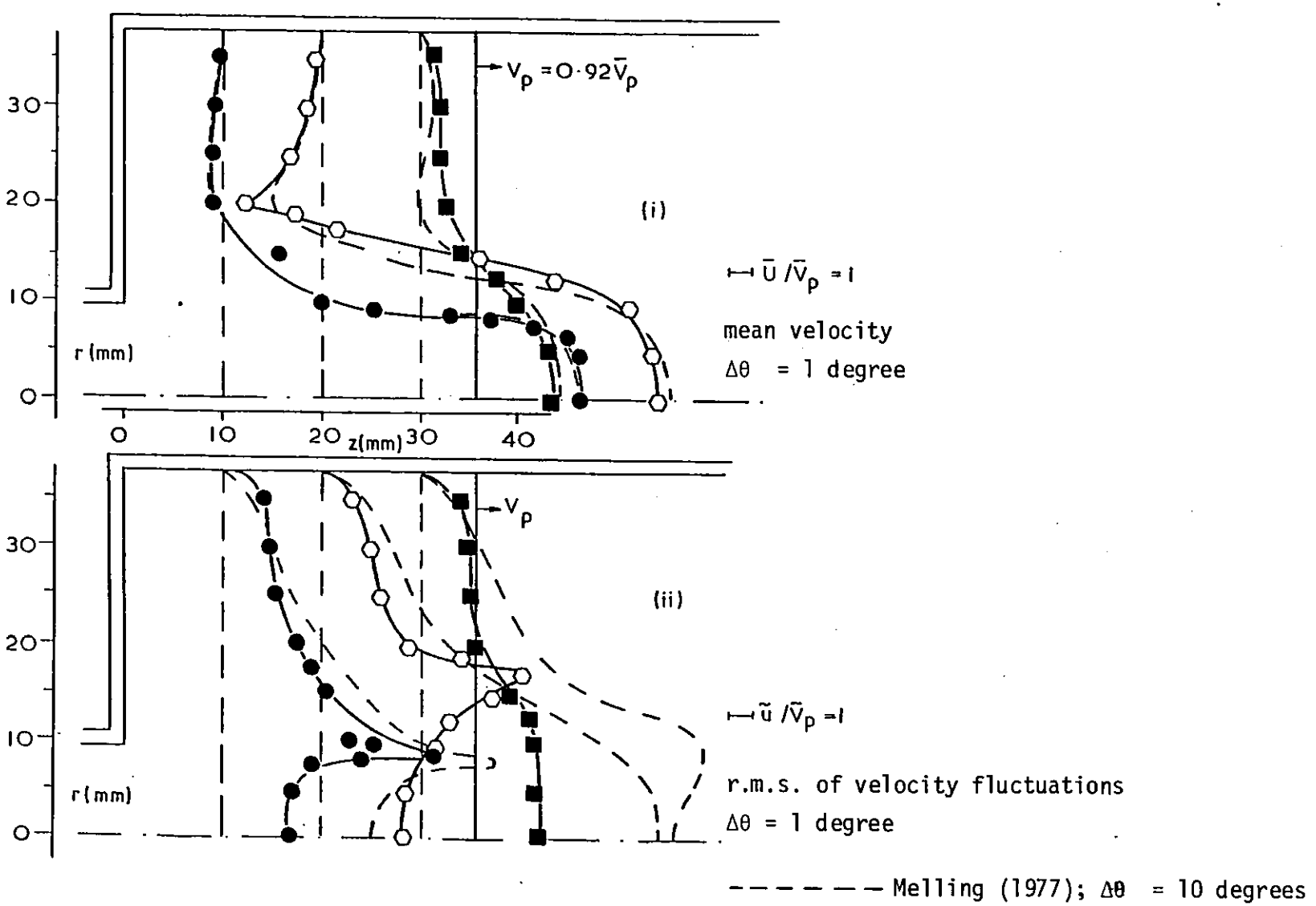


Figure 1 Profiles of axial velocity: pipe inlet, plane piston, 36 degrees

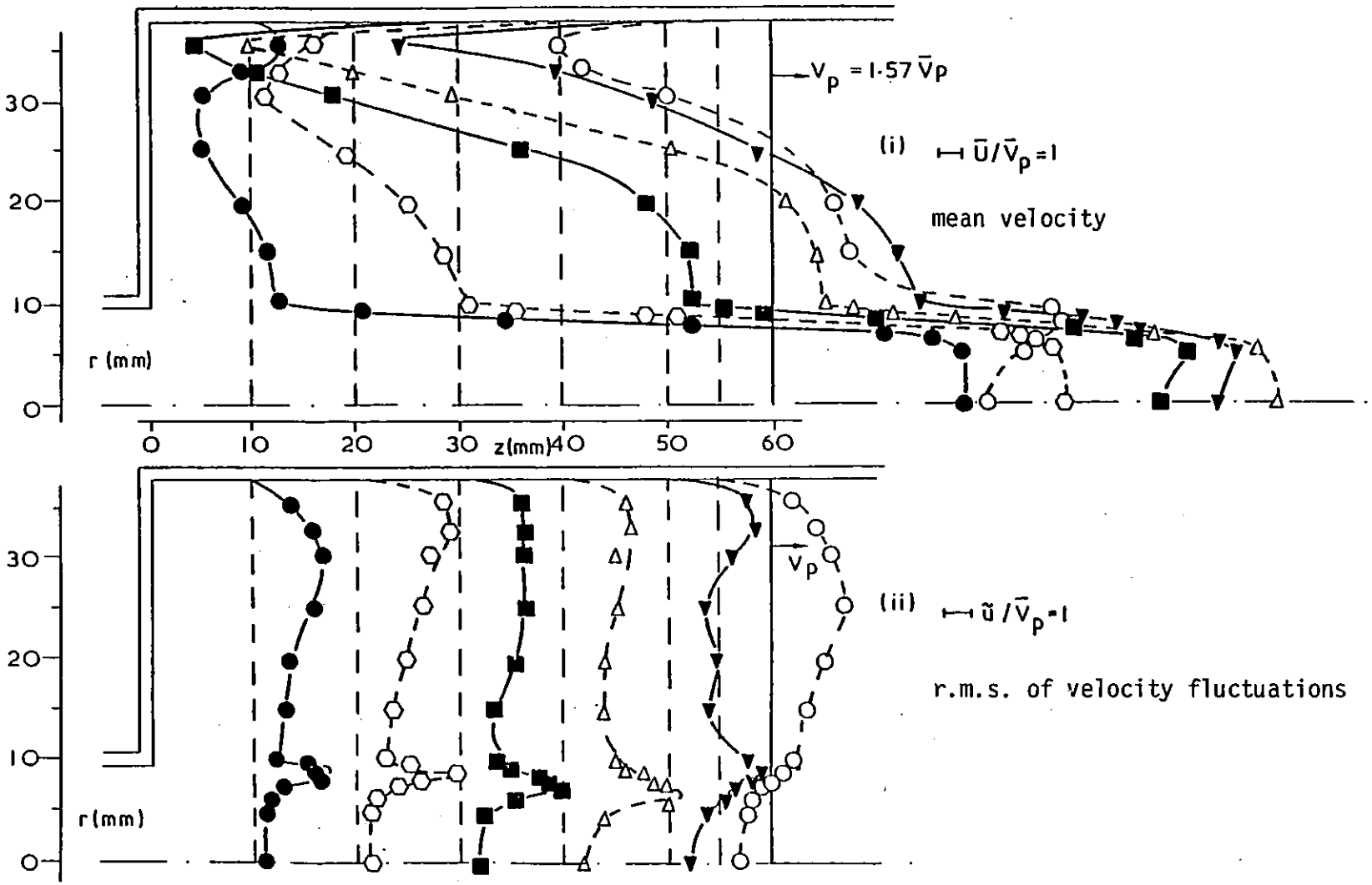


Figure 2 Profiles of axial velocity: pipe inlet, plane piston, 90 degrees

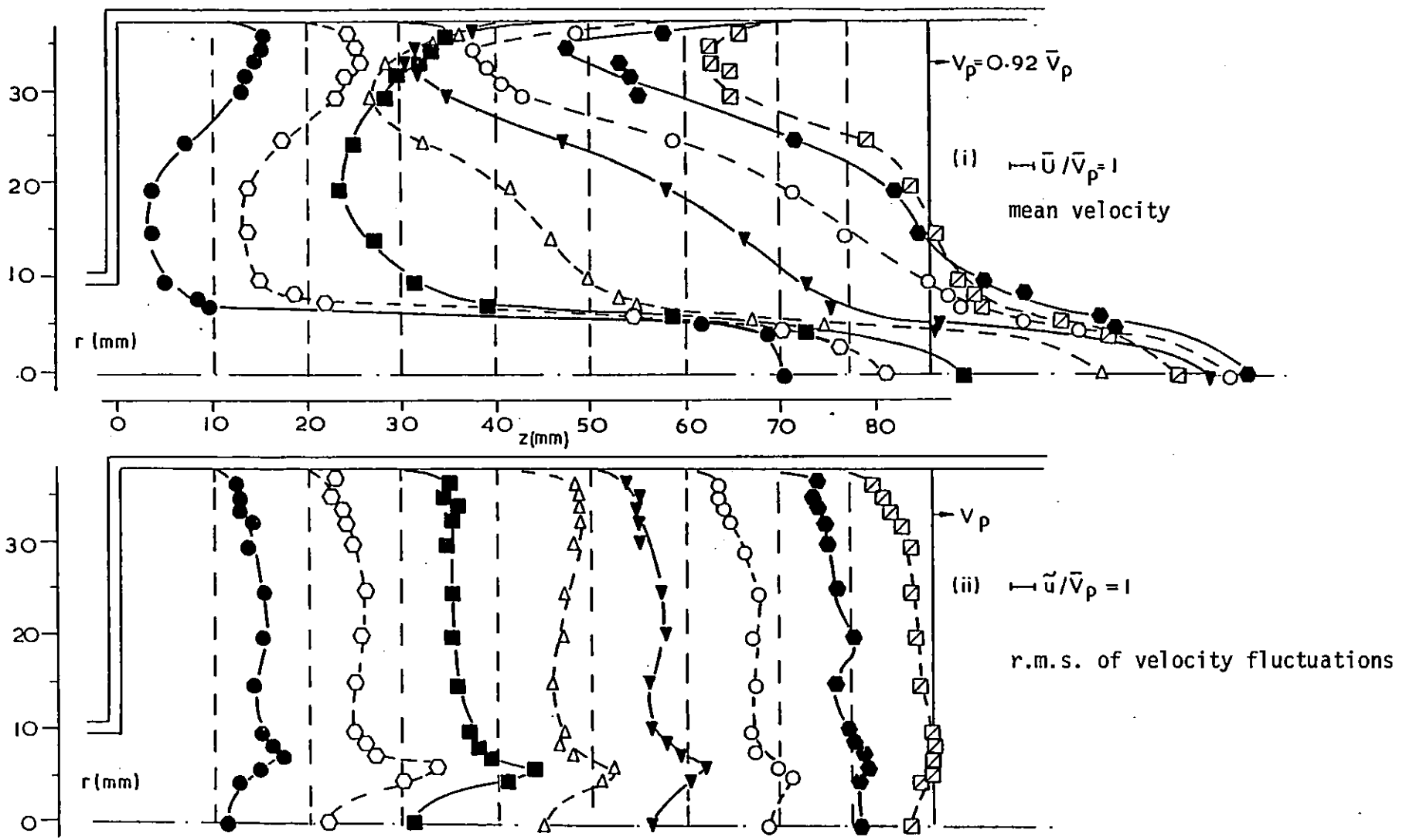


Figure 3 Profiles of axial velocity: pipe inlet, plane piston, 144 degrees

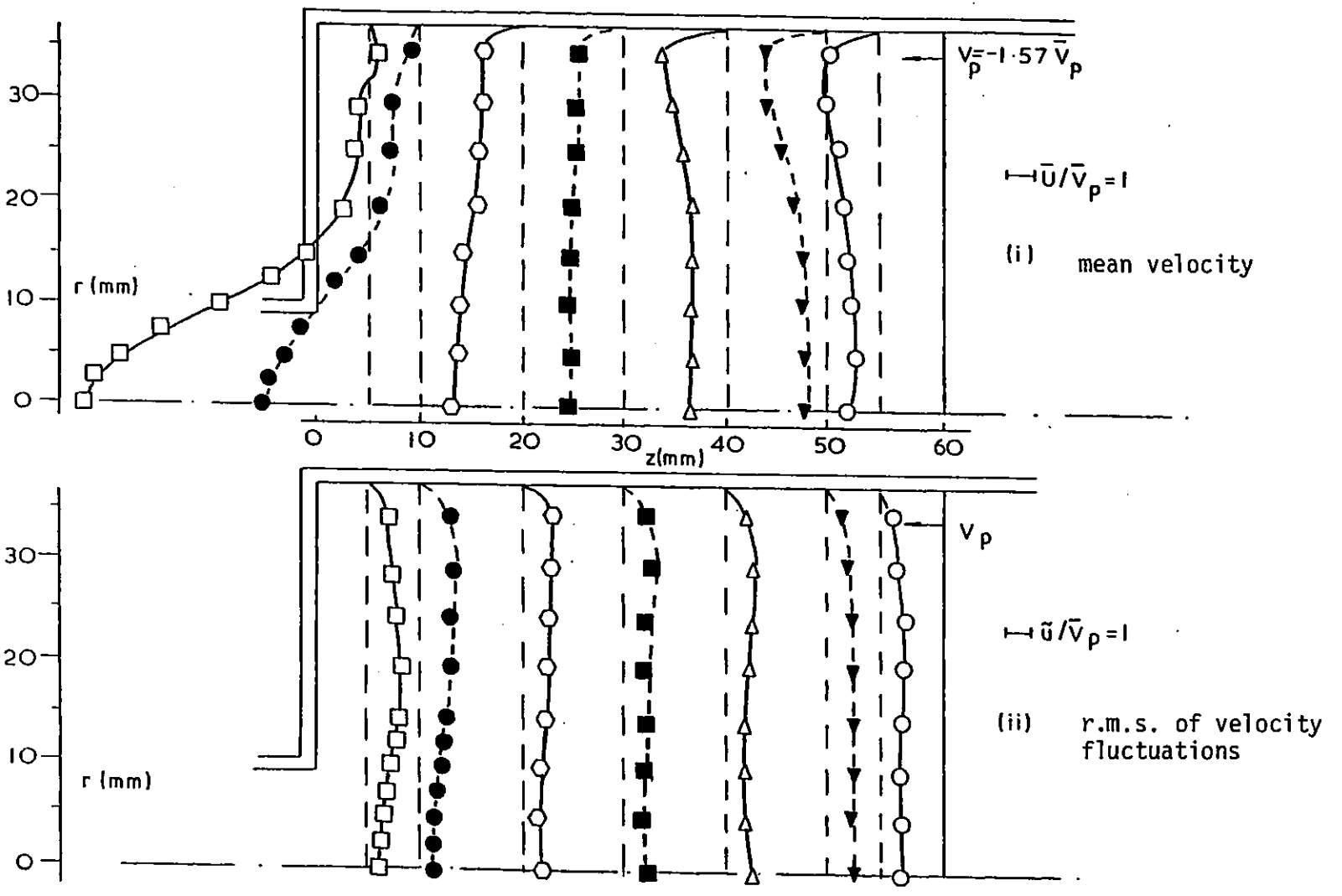


Figure 4 Profiles of axial velocity: pipe inlet, plane piston, 270 degrees

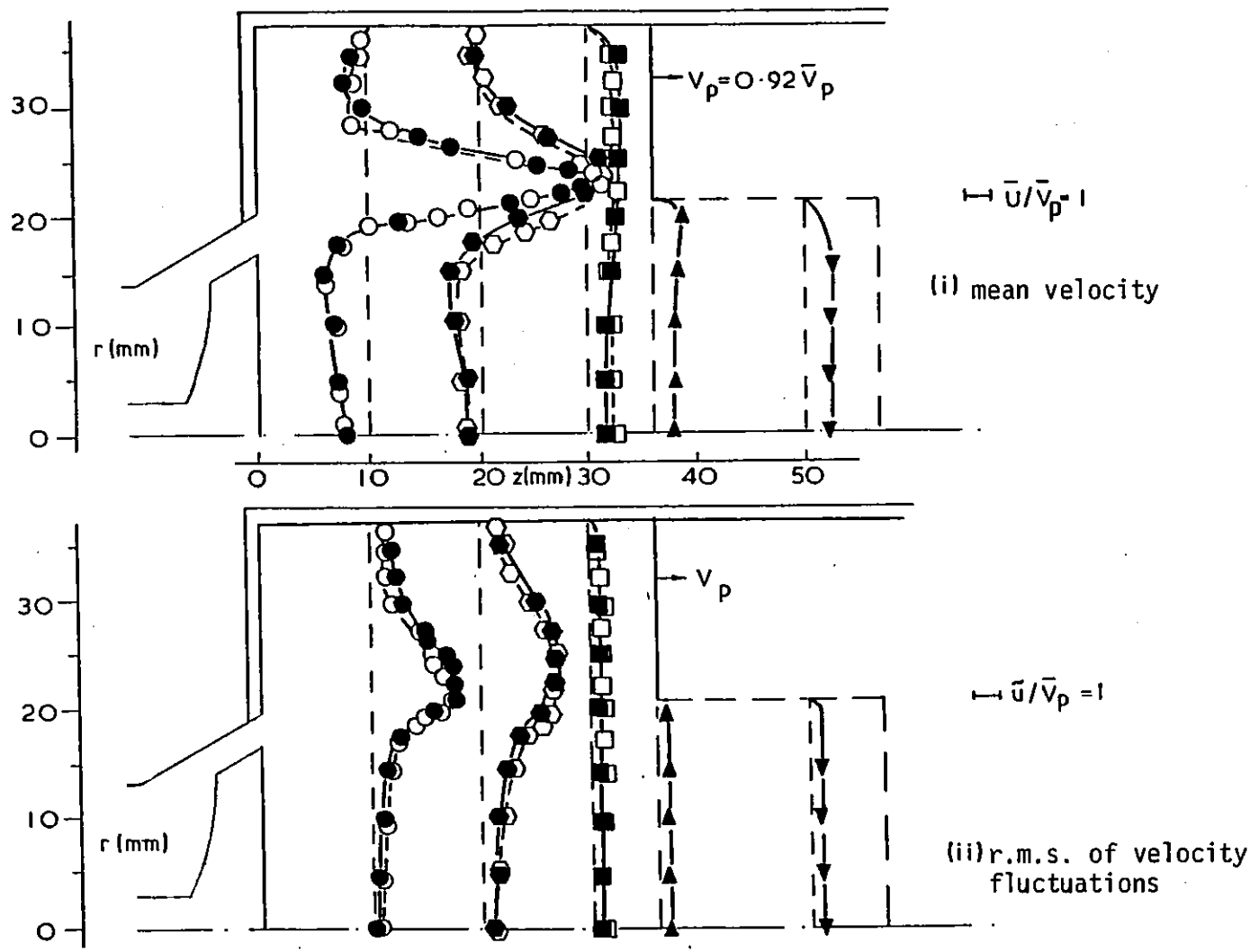


Figure 5 Profiles of axial velocity: valve inlet, 36 degrees

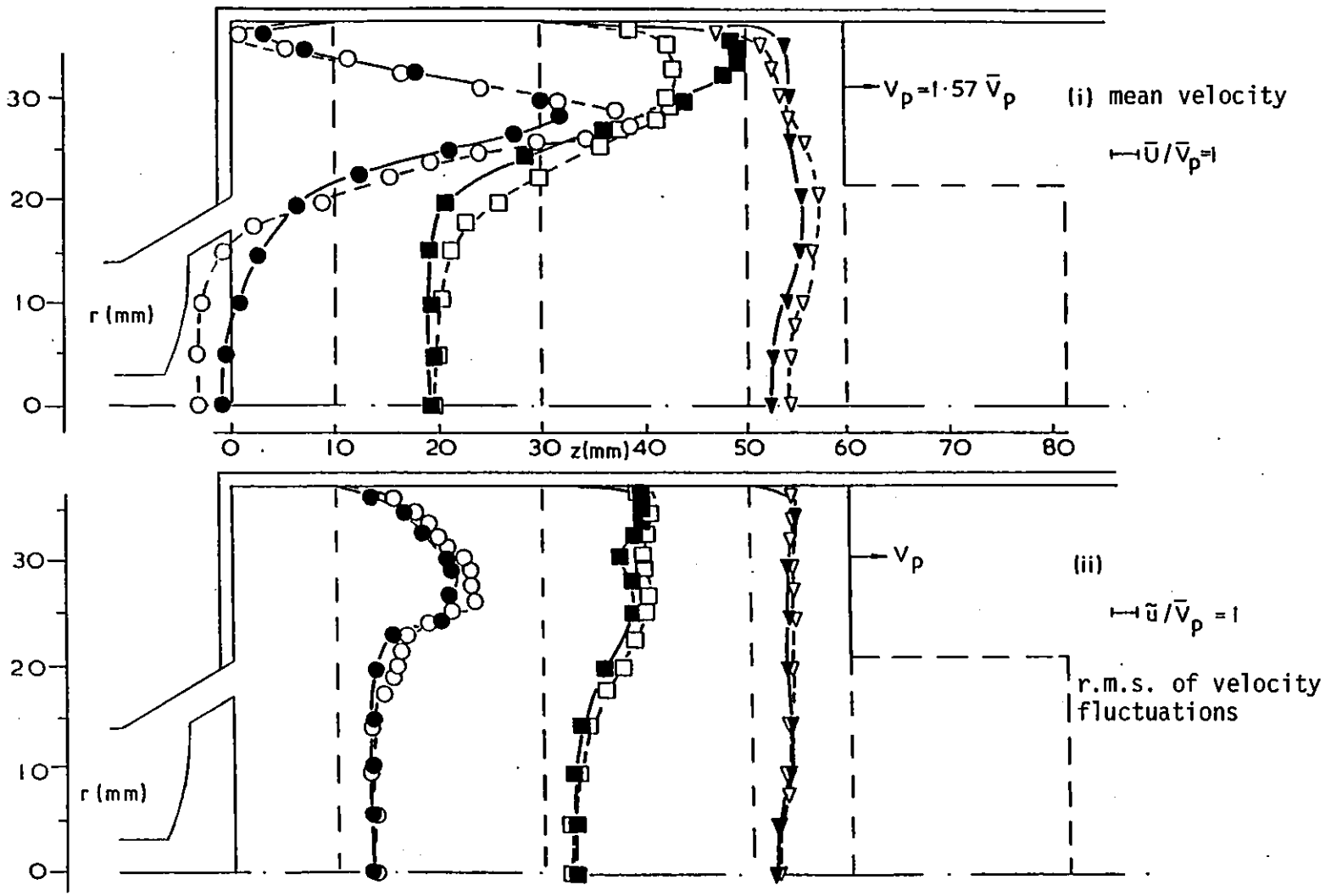


Figure 6(a) Profiles of axial velocity: valve inlet, 90 degrees

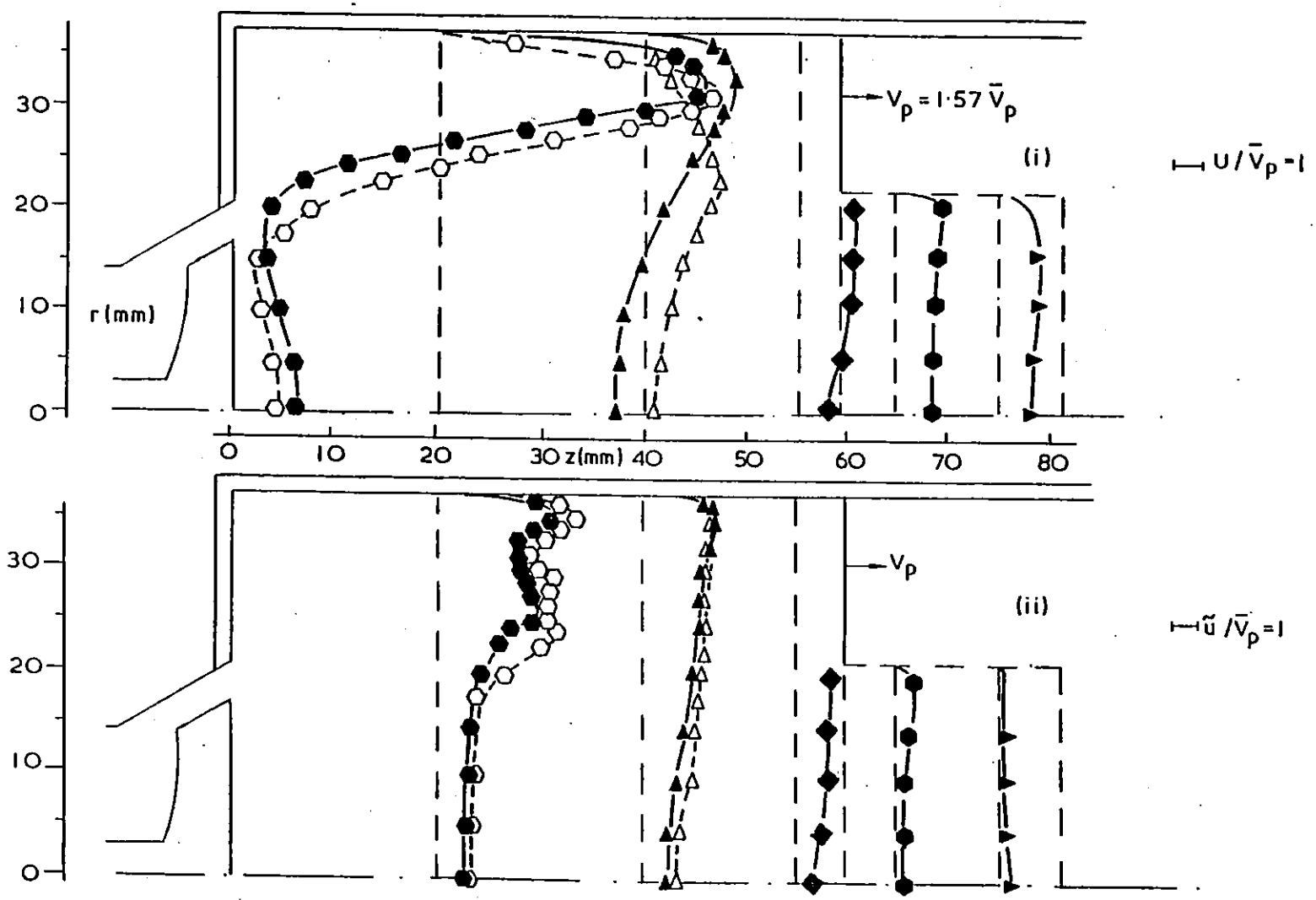


Figure 6(b) Profiles of axial velocity: valve inlet, 90 degrees

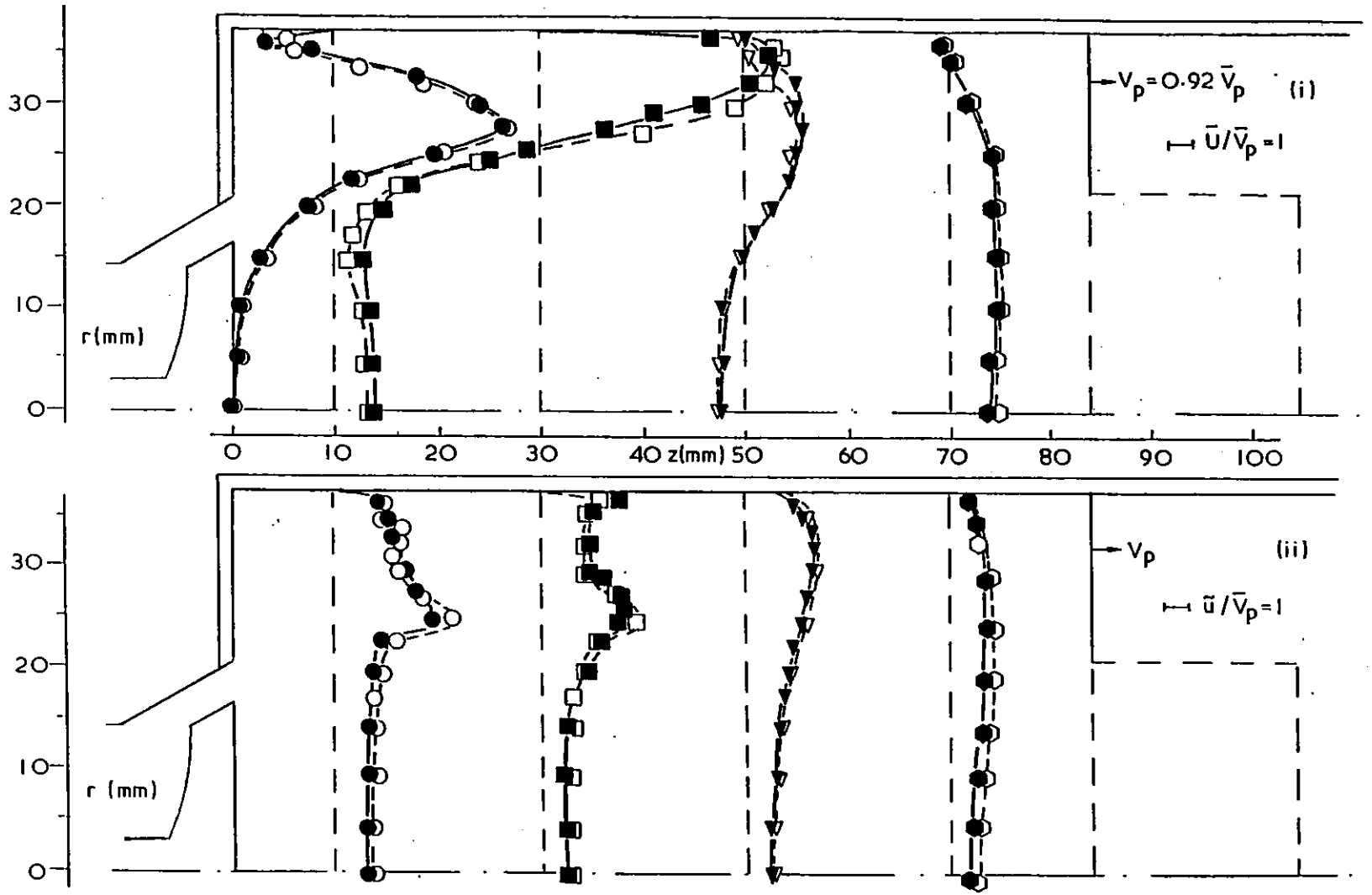


Figure 7(a) Profiles of axial velocity: valve inlet, 144 degrees
(i) mean velocity
(ii) r.m.s. of velocity fluctuations

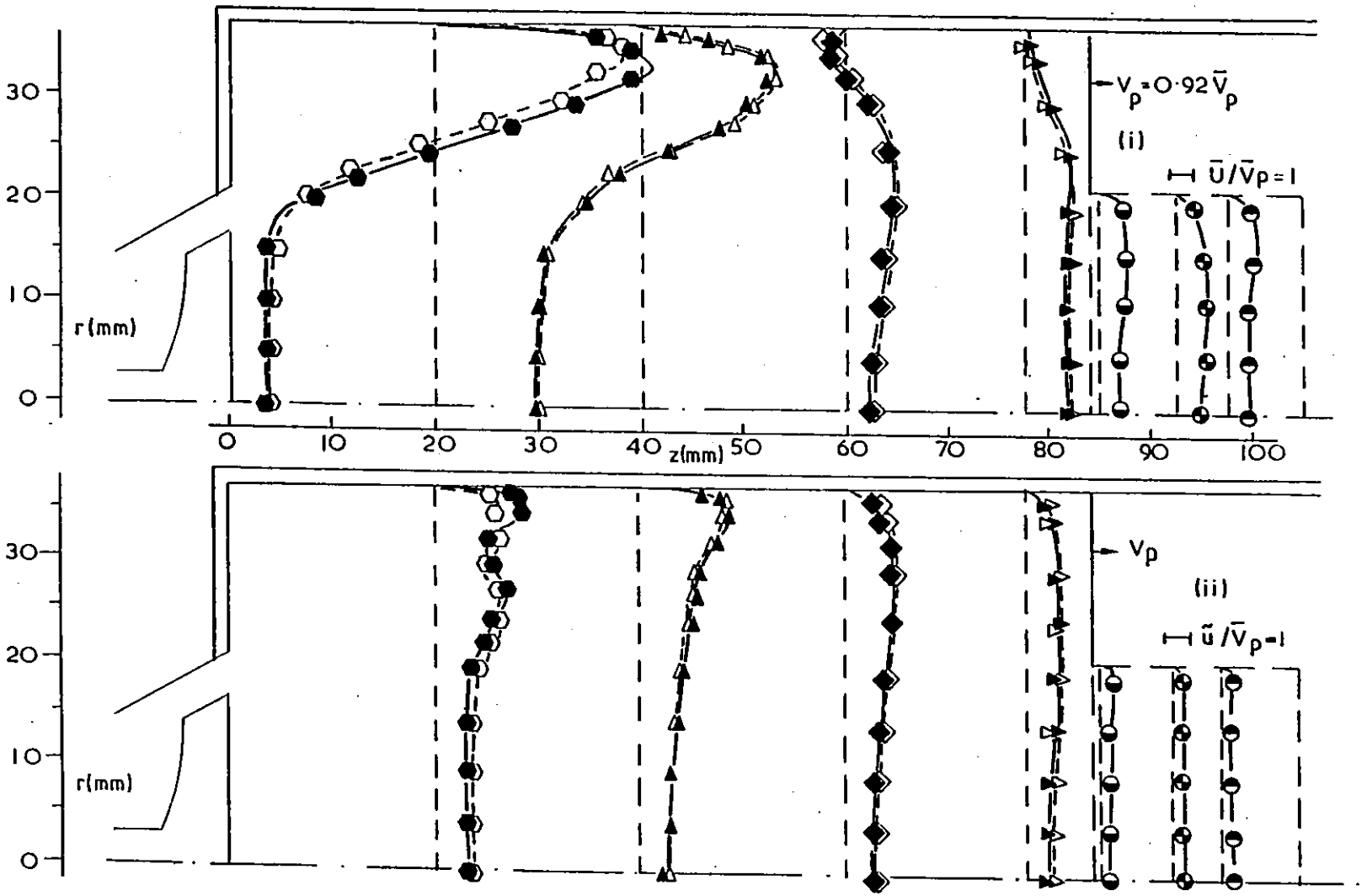


Figure 7(b) Profiles of axial velocity: valve inlet, 144 degrees

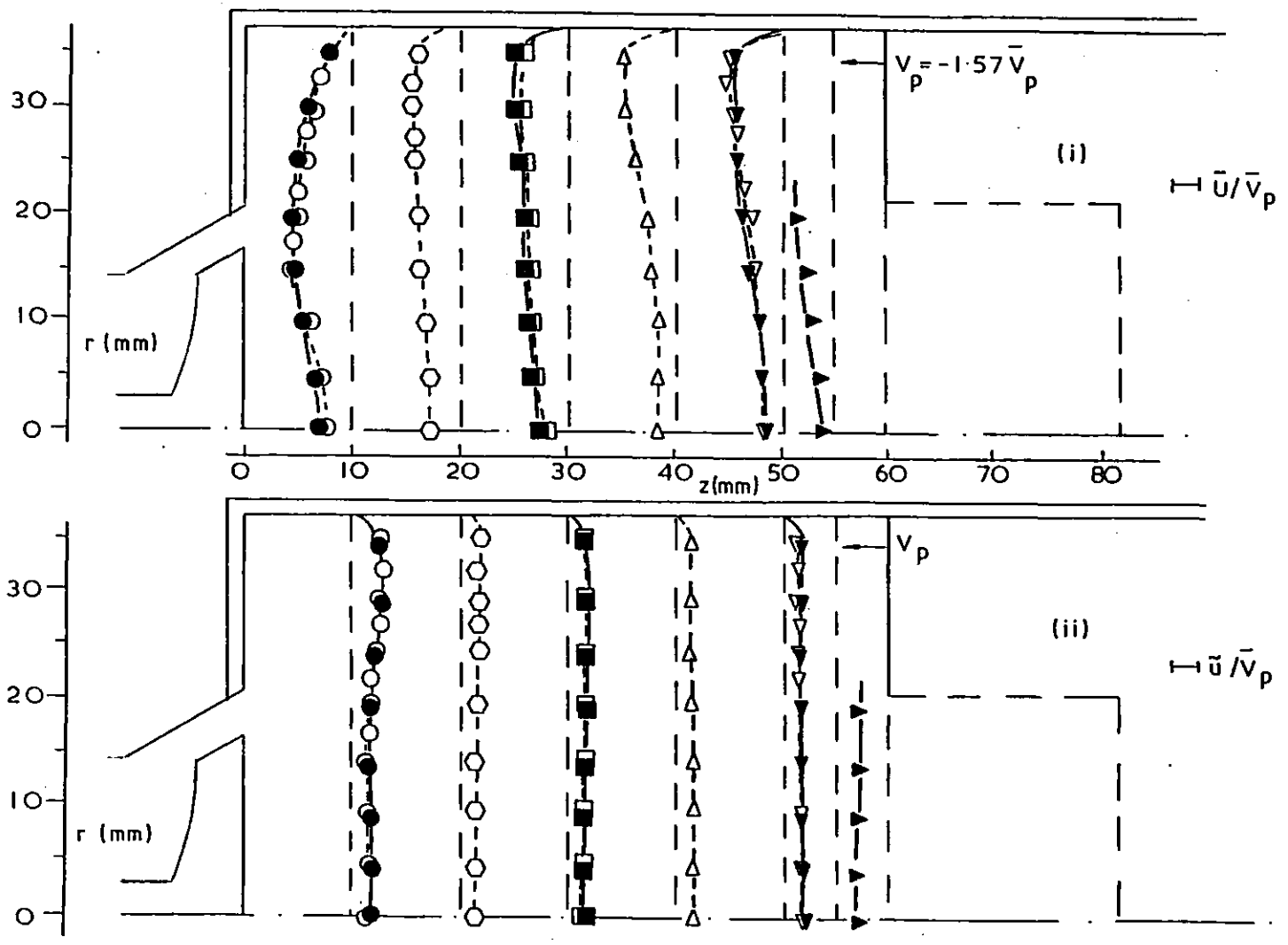


Figure 8 Profiles of axial velocity: valve inlet, 270 degrees
(i) mean velocity
(ii) r.m.s. of velocity fluctuations

APPENDIX 2.3

LISTING OF PDP 8/e MINI-COMPUTER PROGRAM SAMPLING DATA FROM THE FREQUENCY COUNTER AND SPECTRUM ANALYSER AND STORING DATA ON MAGNETIC TAPE

```
                    /       FREQUENCY ANALYSER MAGENG
                    /       MODIFICATION 1
                    /       LOAD IN FIELD 0
                    /       STARTING ADDRESS 0003


                    /   ROUTINE TO ACCEPT COMMANDS
                    /
                    *1200
1200    7300        BACKG,CLA CLL
1201    6046        TLS
1202    4420        WRITE
1203    1253        DOLAR
1204    7300        CLA CLL
1205    3256        DCA COMM
1206    7344        LOOP70,CLA CLL CMA RAL
1207    3252        DCA MN2
1210    1256        LOOP71,TAD COMM
1211    7002        BSW
1212    3256        DCA COMM
1213    4421        GET
1214    4452        TEOC
1215    5200        JMP BACKG
1216    5205        JMP LOOP70-1
1217    0255        AND MB7
1220    1256        TAD COMM
1221    3256        DCA COMM
1222    2252        ISZ MN2
1223    5210        JMP LOOP71
1224    4421        LOOP72,GET
1225    4452        TEOC
1226    5232        JMP OUTH
1227    5205        JMP LOOP70-1
1230    7300        CLA CLL
1231    5224        JMP LOOP72
1232    1256        OUTH,TAD COMM
1233    1257        TAD IN
1234    7450        SNA
1235    5263        JMP AIN   /INIT FILE
1236    1260        TAD GO
1237    7450        SNA
1240    5455        JMP I SAMPLE
1241    1261        TAD RE
1242    7450        SNA
1243    5456        JMP I REP
1244    1262        TAD EF
1245    7450        SNA
1246    5423         MARK
1247    4420        WRITE
1250    0370        COMILE
1251    5200        JMP BACKG
1252    0000        MN2,0
1253    3743        DOLAR,3743
1254    0000        0000
1255    0077        MB7,0077
1256    0000        COMM,0000
1257    6662        IN,6662
1260    0177        GO,0177
1261    6512        RE,6512
1262    1477        EF,1477
1263    4450        AIN,BOT
1264    4451        WEOI
1265    5407        JMP I MANG
                    //
```

```
                //
1266  0000  LETTY,0000
1267  6031  KSF
1270  5267  JMP.-1
1271  6036  KRB
1272  6041  TSF
1273  5273  JMP.-1
1274  6046  TLS
1275  5566  JMP I LETTY
1276  0000  EOC,0000  /TEST KEYBOARD CHARACTER
1277  1314  TAD CRN
1300  7450  SNA
1301  5311  JMP WASCR
1302  1315  TAD BARROW
1303  7450  SNA
1304  5307  JMP WASBA
1305  1316  TAD MBARCR
1306  2276  ISZ EOC
1307  2276  WASBA,ISZ EOC
1310  5676  JMP I EOC
1311  4422  WASCR,WRITE
1312  0235  CRLF
1313  5675  JMP I EOC
1314  7563  CRN,7563
1315  7656  BARROW,7656
1316  0337  MBARCR,0337
```

Insert sampling routine here

```
                /
                /
                /       MANAGEMENT
                /
                *200
0200  7300  START,CLA CLL
0201  4450  BOT
0202  4453  EOI
0203  7300  BEAT,CLA CLL
0204  1110  TAD NBLOCK
0205  7041  CMA IAC
0206  3111  DCA MNBLOC
0207  7240  LOOP01,CLA CMA
0210  3011  DCA STADC
0211  1112  TAD ADD5
0212  3113  DCA ADCNTS
0213  4631  LOOP05,JMS I SAD
0214  4422  WBLOCK
0215  0000  0000
0216  0001  0001
0217  2111  ISZ MNBLOC
0220  7410  SKP
0221  5227  JMP OUT1
0222  4422  WBLOCK
0223  3720  3720
0224  0001  0001
0225  2111  ISZ MNBLOCK
0226  5207  JMP LOOP01
0227  7300  OUT1,CLA CLL
0230  5407  JMP I MANG
0231  0400  SAD,BEGIN
```

```
                / / WRIITE DATA BLOCK
                /
                *600
0600  0000      WBLOC,0000
0601  7300      CLA CLL
0602  1270      TAD DF
0603  6214      RDF
0604  3271      DCA OLDFLD
0605  1600      TAD I WBLOC
0606  3272      DCA INAD
0607  2200      ISZ WBLOC
0610  1600            TAD I WBLOC
0611  7004      RAL
0612  7006      RTL
0613  0273      AND M0070
0614  1270      TAD DF
0615  3216      DCA.+1
0616  0000      0000
0617  2200      ISZ WBLOC
0620  1025      TAD NCWAR
0621  3274      DCA COUNTR
0622  6711      FOBSY
0623  5222      JMP.-1
0624  1041      TAD WDB
0625  6714      WCR
0626  7200      CLA
0627  1272      TAD INAD
0630  3275      DCA CADM
0631  1675      TAD I CADM
0632  7002      BSW
0633  0276      AND M0077
0634  6724      WDR
0635  7344      CLA CMA CLL RAL
0636  3277      DCA COUNTT
0637  6712      GOT
0640  2277      LOOP91,ISZ COUNTT
0641  5250      JMP FW
0642  2275      ISZ CADM
0643  7344      CLA CMA CLL RAL
0644  3277      DCA COUNTT
0645  1675      TAD I CADM
0646  7002      BSW
0647  5251      JMP FW+1
0650  1675      FW,TAD I CADM
0651  0276      AND M0077
0652  2274      ISZ COUNTR
0653  5255      JMP.+2
0654  1300      TAD M4100
0655  6721      WESY
0656  5255      JMP.-1
0657  6724      WDR
0660  7700      SMA CLA
0661  5240      JMP LOOP91
0662  1271      TAD OLDFLD
0663  3264      DCA.+1
0664  0000      0000
0665  5600      JMP I WBLOC
                /
```

```
                / MARKER ROUTINE
0666  4451      MAR0,NEOI
0667  5407      JMP I MANG
                /
                /
0670  6201      DF,6201
0671  0000      OLDFLD,0000
0672  0000      INAD,0000
0673  0070      M0070,0070
0674  0000      COUNTR,0000
0675  0000      CADM,0000
0676  0077      M0077,0077
0677  0000      COUNTT,0000
0700  4100      M4100,4100
```

```
                /
                /
                /       PAGE ZERO
                /     COMMANDS AND ADDRESSES
                /
                /MESSAGEA
                COMILE=0370
                CRLF=0235
                / READ WRITE BUFFER
                FIEL2=4200
                FIEL1=4000
                /
                / IOP TAPE
                /
                FOBSY=6711
                GOT=6712
                WCR=6714
                RBSY=6701
                RDR=6702
                WBSY=6721
                WDR=6724
                FMD=6722
                /
```

Insert interface IOP codes here

```
                /
                / NON EXIST PAL CODE
                /
                      BSW=7002
                /
                /
                /    STARTING ADDRESS
                /
                *0003
0003  6402            6402
0004  6412            6412
0005  7300            CLA CLL
0006  5407            JMP I MANG
```

```
                *0007
0007  1200    MANG,BACKG
                *0011
0011  0000    STADC,0000
                *0022
                WRITE=JMS I .
0020  1020    ESCRVE
                GET=JMS I .
0021  1266    LETTY
                WBLOCK=JMS I .
0022  0600    WBLOC
                MARK=JMP I .
0023  0656    MARQ
0024  7660    PDPCH,7660
0025  0140    NCHAR,0140
0026  0000    FIADD,0000
                *0040
0040  0000    RDB,0000  /CONTROLS FOR DFU
0041  0002    WDB,0002
0042  0004    REW,0004
0043  0042    WFM,0042
0044  0010    RBR,0010
                *50
                BOT=JMS I .
0050  1074    REWBT  /REWIND
                WEOI=JMS I .
0051  1057    REINF   /EOF MARK
                TEOC=JMS I .
0052  1276    EOC
                EOI=JMS I .
0053  1117    DEINF  /POSITION TAPE
                RDBREV=JMS I .
0054  1104    RBREV  /READ REV
0055  0200    SAMPLE,START
0056  0203    REP,REAT
                *0100
0100  0000    COUNT1,0000
0101  0000    COUNT2,0000
0102  0000    COUNT3,0000
0103  0000    COUNT4,0000
0104  0000    LOFREQ,0000
0105  0000    HIFREQ,0000
0106  0011    COMP,0011
0107  0000    CRANK,0000
0110  0024    NBLOCK,0024
0111  0000    MNBLOC,0000
0112  6340    ADD5,6340
0113  0000    ADCNTS,0000


                /
                / WRITE ROUTINE
                /
                *1000
1000  0000    ESCRVE,0000
1001  7300    CLA CLL
1002  1600    TAD I ESCRVE
1003  3214    DCA TYPNT
1004  2200    ISZ ESCRVE
1005  1614    TYPX1,TAD I TYPNT
1006  7002    BSW
1007  4215    JMS TYPY
1010  1614    TAD I TYPNT
1011  2214    ISZ TYPNT
1012  4215    JMS TYPY
1013  5205    JMP TYPX1
1014  0000    TYPNT,0000
```

```
                    /
1015  0000  TYPY,0000
1016  0233  AND TK77
1017  7450  SNA
1020  5620  JMP I ESCRVE
1021  1234  TAD TKM37
1022  7440  SZA
1023  5225  JMP TYPY1
1024  4237  JMS TCRLF
1025  5615  JMP I TYPY
                    /
1026  7510  TYPY1,SPA
1027  1235  TAD TK100
1030  1236  TAD TK237
1031  4251  JMS TLSY
1032  5615  JMP I TYPY
                    /
1033  0077  TK77,0077
1034  7741  TKM37,-37
1035  0100  TK100,0100
1036  0237  TK237,0237
                    /
1037  0000  TCRLF,0
1040  7300  CLA CLL
1041  1247  TAD ASCCR
1042  4251  JMS TLSY
1043  7300  CLA CLL
1044  1250  TAD ASCLF
1045  4251  JMS TLSY
1046  5637  JMP I TCRLF
                    /
1047  0215  ASCCR,0215
1050  0212  ASCLF,0212
                    /
1051  0000  TLSY,0
1052  6041  TSF
1053  5252  JMP.-1
1054  6046  TLS
1055  7200  CLA
1056  5651  JMP I TLSY
                    /
                    / ROUTINE TO WRITE EOF
                    /
1057  0000  PEINF,0
1060  7344  CLA CLL CMA RAL
1061  3273  DCA MSL1
1062  1043  LOOP30,TAD WFM
1063  6711  FOBSY
1064  5263  JMP.-1
1065  6714  WCR
1066  6712  GOT
1067  7300  CLA CLL
1070  2273  ISZ MSL1
1071  5262  JMP LOOP30
1072  5657  JMP I PEINF
1073  0000  MSL1,0
                    /
                    /  REWIND TO BOT
                    /
1074  0000  REWBT,0
1075  7300  CLA CLL
1076  1042  TAD REW
1077  6711  FOBSY
1100  5277  JMP.-1
1101  6714  WCR
1102  6712  GOT
1103  5674  JMP I REWBT
```

```
                /READ REV
1124  0000      RBREV,0000
1125  7300      CLA CLL
1126  1244      TAD RBR
1127  6711      FOBSY
1130  5307      JMP.-1
1131  6714      WCR
1132  6712      GOT
1133  6711      FOBSY
1134  5313      JMP.-1

1135  7300      CLA CLL

1136  5704      JMP I RBREV
                / DETECT TWO EOF
1137  0000      DEINF,0
1140  7344      CLA CLL CMA RAL
1141  3340      DCA MSI
1142  1040      TAD RDB
1143  6711      FOBSY
1144  5323      JMP.-1
1145  6714      WCR
1146  6712      GOT
1147  6711      FOBSY
1150  5327      JMP.-1
1151  6722      FMD
1152  5320      JMP DEINF+1
1153  7300      CLA CLL
1154  2340      ISZ MSI
1155  5322      JMP DEINF+3
1156  4454      RDBREV
1157  5717      JMP I DEINF
1160  0000      MSI,0000
                *235
0235  0037      0037
                *370
0370  1114      1114
0371  1405      1405
0372  0701      0701
0373  1440      1440
0374  0317      0317
0375  1515      1515
0376  0116      0116
```

Sampling routine for spectrum analyser interface

```
                /  SAMPLING ROUTINE
                /
                /
                /
                /
                *0
0000  0000    0000/INTERRUPT LOCATIONS
0001  5402        JMP I 2
0002  0424        SERV
                *400
0400  0000    BEGIN,0000
0401  0577        CAF
0402  6001       ION
0403  7300        CLL CLA
0404  1273       TAD NSTEP
0405  3274       DCA STP
0406  1270       TAD V0
0407  3275        DCA VOLTAG
0410  1272        TAD SWTIME
0411  3276        DCA STIME
0412  1275        TAD VOLTAG
0413  1271        TAD DELV
0414  6404       6404
0415  3275        DCA VOLTAG
0416  7000       NOP
0417  2276       ISZ STIME
0420  5216       JMP.-2
0421  2274       ISZ STP
0422  5210       JMP .-12
0423  5203       JMP .-20
                /
                /
                /
                /
0424  3265    SERV,DCA AC
0425  7004        RAL
0426  3266        DCA L
0427  6401         6401/CHECK IF FREQ.ANALYSER FLAG ON
0430  5263         JMP RELEAS
0431  6402         6402/CLEAR INTERRUPT REQUEST
0432  7300    FA,CLL CLA
0433  1275         TAD VOLTAG
0434  3267         DCA FREQUE
0435  6412        6412
0436  3107        DCA CRANK
                /
0437  6211    STORE,CDF 10
0440  1105         TAD HIFREQ
0441  3411         DCA I STADC
0442  1267         TAD FREQUE
0443  3411         DCA I STADC
0444  1107         TAD CRANK
0445  3411         DCA I STADC
0446  1103         TAD COUNT4
0447  3411         DCA I STADC
0450  1102         TAD COUNT3
0451  3411         DCA I STADC
0452  6201         CDF 00
0453  2113         ISZ ADCNTS
0454  5256         JMP EXIT/CONTINUE,BLOCK NOT FULL
0455  5600         JMP I BEGIN
0456  1266    EXIT,TAD L
0457  7110         CLL RAR
0460  1265         TAD AC
0461  6001         ION
0462  5400         JMP I 0
```

```
0463  6402  RELEAS,6402/CLEAR INT REQ
0464  5256        JMP EXIT
0465  0000  AC,0000
0466  0000  L,0000
0467  0000  FREQUE,0000

0470  0000  VA,0000
0471  0001  DELV,0001
0472  7777  SWTIME,7777
0473  7400  NSTEP,7400
0474  0000  STO,0000
0475  0000  VOLTAG,0000
0476  0000  STIME,0000
            /
```

IOP Codes for analyser interface

```
/
/   NOTIFICATION OF INTERFACE CODES
/
/       6401: FREQ.ANALYSER IOT/TEST FOR INTERRUPT
/       6402 :CLEAR INTERRUPT REQUEST
/       6404: TRANSFER AC VALUE INTO SWEEP VOL.
/       6411: TDC FLAG
/       6412: READ CRANK AND TRANSFER TO AC
/
```

Sampling routine for frequency counter interface

```
                /  SAMPLING ROUTINE
                /
                /
                *400
0400  0000  BEGIN,0000
0401  6151  SIN,MPSF
0402  6151  MPSF
0403  5202  JMP.-1
0404  6174  CARD
0405  7300  SAMCON,CLA CLL
0406  3100  DCA COUNT1
0407  3101  DCA COUNT2
0410  2100  PIN1,ISZ COUNT1
0411  5213  JMP PIN2
0412  5221  JMP PIN3
0413  6151  PIN2,MPSF
0414  7410  SKP
0415  5205  JMP SAMCON
0416  6171  DSSF
0417  5210  JMP PIN1
0420  5224  JMP SIGRED
0421  2101  PIN3,ISZ COUNT2
0422  5210  JMP PIN1
0423  5302  JMP FAULT
0424  6174  SIGRED,CARD
0425  3107  DCA CRANK
0426  1100  TAD COUNT1
0427  3102  DCA COUNT3
0430  1101  TAD COUNT2
0431  3103  DCA COUNT4
0432  1703  PIN4,TAD I DUM
0433  2100  ISZ COUNT1
0434  5236  JMP PIN5
0435  5241  JMP PIN6
0436  6141  PIN5,FRSF   /FREQ READY SF
0437  5232  JMP PIN4
0440  5244  JMP SIGSAM
0441  2101  PIN6,ISZ COUNT2
0442  5232  JMP PIN4
0443  5302  JMP FAULT
0444  6144  SIGSAM,FRRL  /FREQ READ DATA LSB
0445  3104  DCA LOFREQ
0446  6154  FRRH    /FREQ READ DATA MSB
0447  3105  DCA HIFREQ
0450  6211  CDF 10
0451  1105  TAD HIFREQ
0452  3411  DCA I STADC
0453  1104  TAD LOFREQ
0454  3411  DCA I STADC
0455  1107  TAD CRANK
0456  3411  DCA I STADC
0457  1103  TAD COUNT4
0460  3411  DCA I STADC
0461  1102  TAD COUNT3
0462  3411  DCA I STADC
0463  6201  CDF 00
0464  2113  ISZ ADCNTS
0465  7410  SKP
0466  5600  JMP I BEGIN
0467  7300  CLA CLL
0470  1106  TAD COMP
0471  1100  TAD COUNT1
0472  7430  SZL   /OVERFLOW
```

```
0473  2101  ISZ COUNT2
0474  7410  SKP
0475  5302  JMP FAULT
0476  3100  DCA COUNT1
0477  6151  MPSF
0500  5210  JMP PIN1
0501  5201  JMP SIN
            /
0502  7402  FAULT,HLT
0503  0504  DUM,DIM
0504  0000  DIM,0000
```

IOP Codes for counter interface

```
            /
            / IOP COUNTER INTERFACE
            /
            RESET=6142
            FRSF=6141
            FRRL=6144
            FRRH=6154
            /
            /IOP REVOLUTION DIGITISER
            /
            MPSF=6151
            CARD=6174
            DSSF=6171
            /
```

In operation with counter interface replace contents of locations 0000 to 0007 by:

```
            *0000
0000  6142  RESET
0001  6174  CARD
0002  7300  CLA CLL
0003  5406  JMP I MANG
            *0006
0006  1200  MANG,BACKG
```

APPENDIX 2.4

LISTING OF MAIN-FRAME COMPUTER PROGRAM DECODING AND PROCESSING DATA STORED ON MAGNETIC TAPE

```
      PROGRAM PROCES(OUTPUT,TAPE6=OUTPUT,TAPE1,TAPE31)
C     ******************************************************************
C     ******            INTERNAL COMBUSTION ENGINE PROJECT            ******
C     ******    PROGRAM DECODING AND PROCESSING DATA STORED VIA       ******
C     ******    THE PDP ON THE MAGNETIC TAPE IN THE CDC SYSTEM        ******
C     ******                                                          ******
C     ******************************************************************
      COMMON/PROBO/PROB(256,10),PEAN(10),PIM(10),FRE(400),NOINT,COFPR,IN
     1DEX,IFRE,L,NS,N,FRDIV
      DIMENSION CRITH(30),CRITL(30),X(25),Y(30),JNT(30),JOX(30)
      DIMENSION IC(400),IP(400),IANG(400)
      DIMENSION FREM(30),FREMR(30),ICL(30),ICR(30)
      DIMENSION UMEAN(30),URMS(30),VELMEAN(30),TURBINT(30)
      DIMENSION VELOCIT(16,30),TURBULC(16,30),KOUNTS(16,30),NCOUNT(16,30
     1)
      DIMENSION FREMS(30),FREMK(30),EN(30),SKEWNES(16,30),CURTOSI(16,30)
      DIMENSION PSIWALL(16),PSI(16,30),PSITOT(16,30),COEFPSI(16)
      DATA MASK1,MASK2,MASK3/77777777B,7777B,17B/
C*****************************************************************
C     ACTIVATING INDICES AND TITLE DATA
C    --ENSURE EVERYTHING IS CORRECT WITHIN THIS BLOCK---------------
C
C     ***   TAPE PROCESSED
C     ******    30 DEGREE SWIRL VANES - AXIAL VELOCITY COMPONENT   ******
C
      DATA ICL/86,236,386,736/
      DATA ICR/114,264,414,764/
      DATA JNT/30,55,80,55/
      DATA JOX/36,90,144,270/
      DATA PSIWALL/649.,1106.,649.,-1106./
      DATA X/3.,10.,20.,30.,40.,50.,60./
C
C     --      JTYPE=1 (U), =2 (V), =3 (W) ----------
C
      JTYPE=1
C
      NRAD=16
      NAX=10
      NW=4
      UNPMEAN=0.0985
      FRSHIFT=1.5
      DR=2.5
C     ******    NOTEST=1 FOR NO 3.5 RMS LIMITS TEST   ********************
      NOTEST=0
      FREMIN=0.25
      FREMAX=4.
      COF=3.5
C     ******
C        NAP=NUMBER OF PRECEDING PROFILES TO BE IGNORED
      NAP=0
C     ******    INDEX NO34=1 FOR 3RD AND 4TH MOMENT CALCULATION   ********
      NO34=0
C
C     ******    INDEX=1 FOR COUNTER, INDEX=2 FOR FREQ.ANALYSER    *********
      INDEX=1
C     ******    FREQUENCY ANALYSER FREQ.DECODING   ***********************
      NSTEP=236
      FNDELV=1.
      DELV=0.02
      FRINIT=0.2
C     ******    NOPROB=1 FOR NO PROB.DISTRIBUTION    ******
C     ******    N.B. NOTEST=0 NECESSARY FOR NOPROB=0    ******
      NOPROB=1
      NOINT=30
      IF(INDEX.EQ.2) NOINT=NSTEP
      COFPR=4.
C
      NMES=400
      NBLOC=20
C     *********    PRODUCT=PIE*R**2
      PRODUCT=4417.861
C*****************************************************************
```

```
C
      DO 1008 I=1,NAX
C
C     ******   ZERO STREAM FUNCTION VALUES OF PREVIOUS PROFILE   *******
C
      DO 2121 J=1,NRAD
      DO 2220 L=1,NW
      PSI(L,J)=1.E-30
      PSITOT(L,J)=1.E-30
      COEFPSI(L)=1.E-30
      SKEWNES(L,J)=1.E-30
      CURTOSI(L,J)=1.E-30
 2220 CONTINUE
 2121 CONTINUE
      DO 1001 J=1,NRAD
C
C     ******   DEFINE RADIAL DISTANCE   ******
C
      Y(J)=(FLOAT(J)-1.)*DR
C
C     ******   ZERO WALL VALUES   ******
C
      DO 11 L=1,NW
      FREM(L)=1.E-10
      FREMR(L)=1.E-10
      FREMK(L)=1.E-10
      FREMS(L)=1.E-10
      KOUNTS(L,J)=0
   11 CONTINUE
C     *-*-*-*-*-*-*-*-*-*-*-*-*-*-*-*-*-*-*-*-*-*-*-*-*-*-*-*-*-*-*-*-*-*-*-*-*-
      IF(J.EQ.NRAD.AND.I.LE.NAP) GO TO 3465
C     *-*-*-*-*-*-*-*-*-*-*-*-*-*-*-*-*-*-*-*-*-*-*-*-*-*-*-*-*-*-*-*-*-*-*-*-*-
      IF(J.EQ.NRAD) GO TO 3333
      IF(NOTEST.EQ.1) GO TO 5005
      DO 1007 NB=1,NBLOC
      READ(1) IC
      IF(EOF(1)) 52,53
   53 CONTINUE
      DO 100 N=1,NMES
C
C     ****** *******   DECODING THE MAGNETIC TAPE DATA   ************
C
      IP(N)=IC(N).AND.MASK1
      IC(N)=SHIFT(IC(N),-24)
      IANG(N)=IC(N).AND.MASK2


      IC(N)=SHIFT(IC(N),-12)
      IFRE=IC(N).AND.MASK1
      FRE(N)=0.0
      IF(INDEX.EQ.1) GO TO 4567
      FRDIV=FLOAT(IFRE)/FNOELV
      FRE(N)=FRE(N)+FRINIT+FRDIV*DELV
      GO TO 1357
 4567 CONTINUE
      DO 400 K=1,6
      FRE(N)=FRE(N)+(FLOAT(IFRE.AND.MASK3))*10.**(K-4)
      IFRE=SHIFT(IFRE,-4)
  400 CONTINUE
 1357 CONTINUE
C     *-*-*-*-*-*-*-*-*-*-*-*-*-*-*-*-*-*-*-*-*-*-*-*-*-*-*-*-*-*-*-*-*-*-*-*-*-
      IF(I.LE.NAP) GO TO 1003
C     *-*-*-*-*-*-*-*-*-*-*-*-*-*-*-*-*-*-*-*-*-*-*-*-*-*-*-*-*-*-*-*-*-*-*-*-*-
      DO 130 L=1,NW
C
C     ******      IGNORE PROFILES OF NO INTEREST IN THE        ******
C     ******                CRANK ANGLE CONCERNED            ************
C
      IF(X(I).GT.FLOAT(JNT(L))*1.001) GO TO 120
C
C     ******   PRECAUTION FOR MEASUREMENTS AT TDC                ******
C
      IF(IANG(N).LE.14) IANG(N)=IANG(N)+1000
      IF(IANG(N).LT.ICL(L).OR.IANG(N).GT.ICR(L)) GO TO 110
C
C     ******   RE-FILTERING DATA TO ALLOW FREQS.                  ******
C     ******   IN THE REGION 0.25-4.0 MHZ ONLY                   ******
C
      IF(FRE(N).LT.FREMIN.OR.FRE(N).GT.FREMAX) GO TO 109
C
C     ******   STORE THE SUM OF THE MEAN AND MEAN SQUARE OF THE   ******
C     ******   DATA BELONGING TO THE CRANK ANGLE WINDOWS OF INTEREST   *
C
      FREM(L)=FREM(L)+FRE(N)
      FREMR(L)=FREMR(L)+FRE(N)*FRE(N)
      KOUNTS(L,J)=KOUNTS(L,J)+1
      GO TO 700
```

```
  120 FREM(L)=FREM(L)+1.0E-30
      FREMR(L)=FREMR(L)+1.0E-30
  700 CONTINUE
  109 CONTINUE
  110 CONTINUE
  130 CONTINUE
 1003 CONTINUE
  100 CONTINUE
 1007 CONTINUE
C
C     ******   REPEAT OPERATION TO REJECT  ERRONEOUS MEASUREMENTS   ******
C     ******    ACCORDING TO THE CRITERION                          ******
C     ******    (IF OUTSIDE THE UMEAN+/-3.5((URMS)2) RANGE)         ******
C
C     *-*-*-*-*-*-*-*-*-*-*-*-*-*-*-*-*-*-*-*-*-*-*-*-*-*-*-*-*-*-*-*-*-*-*-*-
      IF(I.LT.NAP) GO TO 3465
C     *-*-*-*-*-*-*-*-*-*-*-*-*-*-*-*-*-*-*-*-*-*-*-*-*-*-*-*-*-*-*-*-*-*-*-*-
      DO 1999 L=1,NW
      EN(L)=FLOAT(KOUNTS(L,J))
      EN(L)=AMAX1(EN(L),1.)
      UDEL=FREMR(L)/EN(L)-(FREM(L)/EN(L))**2
      UDEL=AMAX1(UDEL,1.E-10)
      CRITL(L)=FREM(L)/EN(L)-COF*SQRT(UDEL)
      CRITH(L)=FREM(L)/EN(L)+COF*SQRT(UDEL)
      PEAN(L)=FREM(L)/EN(L)
      PIM(L)=SQRT(UDEL)
 1999 CONTINUE
 5005 CONTINUE
      DO 22 L=1,NW
      FREM(L)=1.E-10
      FREMR(L)=1.E-10
      FREMS(L)=1.E-10
      FREMK(L)=1.E-10
      NCOUNT(L,J)=0
      DO 22 NS=1,NOINT
      PROB(NS,L)=0.0
   22 CONTINUE
      IF(NOTEST.EQ.1) GO TO 5006
      DO 9999 NT=1,NBLOC
      BACKSPACE 1
 9999 CONTINUE
 5006 CONTINUE
      DO 1234 NB=1,NBLOC
      READ(1) IC
      DO 200 N=1,NMES
      IP(N)=IC(N).AND.MASK1

      IC(N)=SHIFT(IC(N),-24)
      IANG(N)=IC(N).AND.MASK2
      IC(N)=SHIFT(IC(N),-12)
      IFRE=IC(N).AND.MASK1
      FRE(N)=0.0
      IF(INDEX.EQ.1) GO TO 9876
      FRDIV=FLOAT(IFRE)/FNDELV
      FRE(N)=FRE(N)+FRINIT+FRDIV*DELV
      GO TO 6789
 9876 CONTINUE
      DO 444 K=1,6
      FRE(N)=FRE(N)+(FLOAT(IFRE.AND.MASK3))*10.**(K-4)
      IFRE=SHIFT(IFRE,-4)
  444 CONTINUE
 6789 CONTINUE
      DO 301 L=1,NW
      IF(X(I).GT.FLOAT(JNT(L))*1.001) GO TO 201
      IF(IANG(N).LE.14) IANG(N)=IANG(N)+1000
      IF(IANG(N).LT.ICL(L).OR.IANG(N).GT.ICR(L)) GO TO 101
C     ******       PROBABILITY DISTRIBUTION     ******
      IF(NOPROB.EQ.0) CALL PROBAB
      IF(FRE(N).LT.FREMIN.OR.FRE(N).GT.FREMAX) GO TO 901
      IF(FRE(N).LT.CRITL(L).OR.FRE(N).GT.CRITH(L)) GO TO 104
      FREM(L)=FREM(L)+FRE(N)
      TEMP=FRE(N)*FRE(N)
      FREMR(L)=FREMR(L)+TEMP
      TEMP=TEMP*FRE(N)
      FREMS(L)=FREMS(L)+TEMP
      TEMP=TEMP*FRE(N)
      FREMK(L)=FREMK(L)+TEMP
  525 CONTINUE
      NCOUNT(L,J)=NCOUNT(L,J)+1
      GO TO 800
  201 FREM(L)=FREM(L)+1.0E-30
      FREMR(L)=FREMR(L)+1.0E-30
      FREMS(L)=FREMS(L)+1.0E-30
      FREMK(L)=FREMK(L)+1.0E-30
  800 CONTINUE
  104 CONTINUE
  901 CONTINUE
  101 CONTINUE
  301 CONTINUE
  200 CONTINUE
 1234 CONTINUE
```

```
C     ********************      EVALUATE THE MEAN AND RMS VELOCITIES    *****
C
 3333 CONTINUE
      DO 140 L=1,NW
      IF(J.NE.NRAD) GO TO 3111
      NCOUNT(L,J)=0
      VELMEAN(L)=0.0
      TURBINT(L)=0.0
      SKEWNES(L,J)=0.
      CURTOSI(L,J)=0.
      GO TO 3333
 3111 EN(L)=FLOAT(NCOUNT(L,J))
      EN(L)=AMAX1(EN(L),1.)
      UMEAN(L)=FRSM(L)/EN(L)
      UDEL=FRSMR(L)/EN(L)-UMEAN(L)*UMEAN(L)
      UDEL=AMAX1(UDEL,1.E-10)
      URMS(L)=SQRT(UDEL)
      URMS(L)=AMAX1(URMS(L),1.E-10)
C     **********    NORMALISE BY THE MEAN PISTON VELOCITY    **************
C***** ENSURE DIRECTION OF FREQUENCY SHIFT
      VELMEAN(L)=(UMEAN(L)-FRSHIFT)/UNPMEAN
      TURBINT(L)=URMS(L)/UNPMEAN
C     ******    CALCULATION OF 3RD AND 4TH MOMENT                       ******
      IF(NU34.EQ.0) GO TO 3000
 4321 CONTINUE
      TEMP1=FRSM(L)/EN(L)
      TEMP2=FRSMR(L)/EN(L)
      TEMP3=FRSMS(L)/EN(L)
      TEMP4=FRSMK(L)/EN(L)
      TEMP5=TEMP1*TEMP1
      TEMP6=TEMP1*TEMP5
      TEMP7=TEMP1*TEMP6
      TEMP8=URMS(L)**3
      TEMP9=TEMP8*URMS(L)
      SKEWNES(L,J)=(TEMP3-3.*TEMP1*TEMP2+2.*TEMP6)/TEMP8
      CURTOSI(L,J)=(TEMP4-4.*TEMP1*TEMP3+6.*TEMP2*TEMP5-3.*TEMP7)/TEMP9
 3000 CONTINUE
      VELOCIT(L,J)=VELMEAN(L)
      TURBULC(L,J)=TURBINT(L)

      IF(JTYPE.NE.1) GO TO 2265
C     ******    CALCULATION AND CORRECTION OF STREAM FUNCTION           ******
      M=J-1
      IF(J.EQ.1)GO TO 2266
      PSI(L,J)=((VELOCIT(L,J)+VELOCIT(L,M))/2.)*((Y(J)+Y(M))/2.)*DR
      PSITOT(L,J)=PSI(L,J)+PSITOT(L,M)
      IF(J.NE.NRAD) GO TO 2265
      COEFPSI(L)=PSITOT(L,J)/PSIWALL(L)+1.E-30
 2265 CONTINUE
 2266 CONTINUE
      IF(NPROB.EQ.0) WRITE(31) (I,J,PROB(NS,L),NS=1,NOINT)
  140 CONTINUE
C     ******************************************************************
 3465 CONTINUE
C     ******************************************************************
 1001 CONTINUE
C     ******************************************************************
      IF(I.LE.NAP) GO TO 1008
C     ******************************************************************
      DO 6611 J=1,NRAD
      NC=(I-1)*NRAD+J
      WRITE(6,202) NC,X(I),Y(J)
  202 FORMAT(1HJ,10X,*   LOCATION NO.  *,I3,5X,*AXIAL DIST.FROM CYL.HEAD
     1=*,F6.3,5X,*RADIAL DIST.FROM AXIS=*,F6.3)
      DO 1166 L=1,NW
      IF(JTYPE.NE.1) GO TO 3096
C     *****  ASSUME DEL(U) CONSTANT ACROSS FLOW -----
      DELTA=PSIWALL(L)*(1.-COEFPSI(L))
      PSITOT(L,J)=PSITOT(L,J)+DELTA*(Y(J)/Y(NRAD))**2
      PSITOT(L,J)=PSITOT(L,J)/PRODUCT
 3096 CONTINUE
      WRITE(6,6161) JDX(L),KOUNTS(L,J),NCOUNT(L,J),VELOCIT(L,J),TURBULC(
     1L,J),SKEWNES(L,J),CURTOSI(L,J),COEFPSI(L),PSITOT(L,J)
 6161 FORMAT(1H0,1X,*CRANK=*,I3,1X,*NC1=*,I4,1X,*NC2=*,I4,1X,*UMEAN=*,1P
     1E10.3,1X,*URMS=*,1PE10.3,1X,*SK.=*,1PE10.3,1X,*KU.=*,1PE10.3,1X,*C
     2OEFF=*,1PE10.3,1X,*PSI=*,1PE10.3)
 1166 CONTINUE
 6611 CONTINUE
 1008 CONTINUE
      GO TO 50
   52 CONTINUE
      WRITE(6,600)
  600 FORMAT(1X,*ATTENTION THE MAGNETIC TAPE IS EMPTY*)
   50 CONTINUE
      STOP
      END
```

```
      SUBROUTINE PROBAB
      COMMON/PROBC/PROB(256,10),PEAN(10),PIM(10),FRE(400),NOINT,COFPR,IN
     1DEX,IFRE,L,NS,N,FRDIV
      IF(INDEX.EQ.1) GO TO 3109
      NS=FIX(FRDIV)
      PROB(NS,L)=PROB(NS,L)+1.0
      GO TO 3111
 3109 PLOWER=PEAN(L)-COFPR*PIM(L)
      STEP=(2.*COFPR*PIM(L))/FLOAT(NOINT)
      DO 3110 NS=1,NOINT
      PLOWER=PLOWER+STEP
      IF(FRE(N).GT.PLOWER) GO TO 3110
      PROB(NS,L)=PROB(NS,L)+1.0
      GO TO 3111
 3110 CONTINUE
 3111 RETURN
      END
```

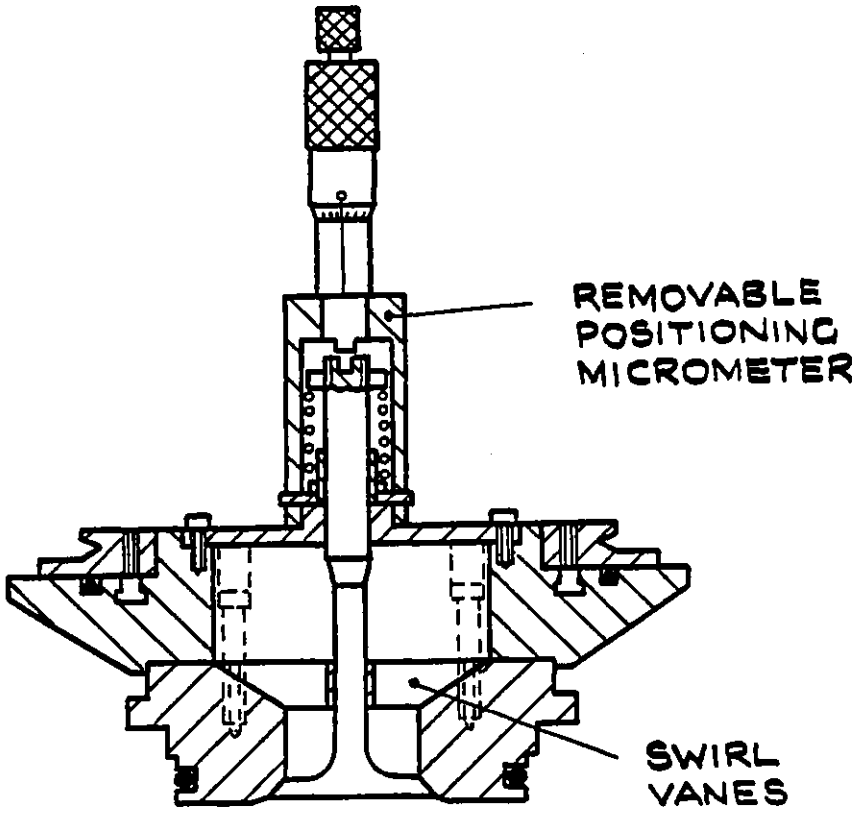


Figure 2.1 Valve inlet: cross-section of cylinder head arrangement with valve positioning attachment

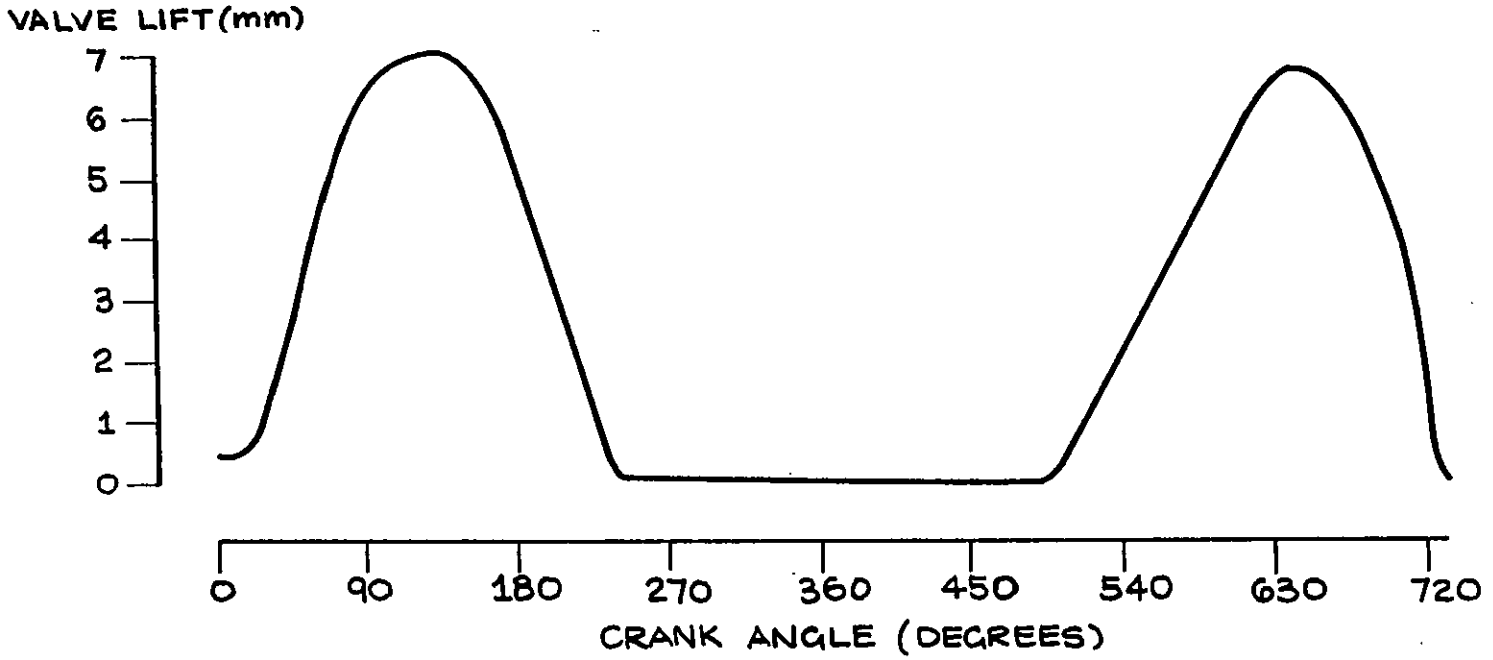


Figure 2.2 Compressing engine valve lift diagram

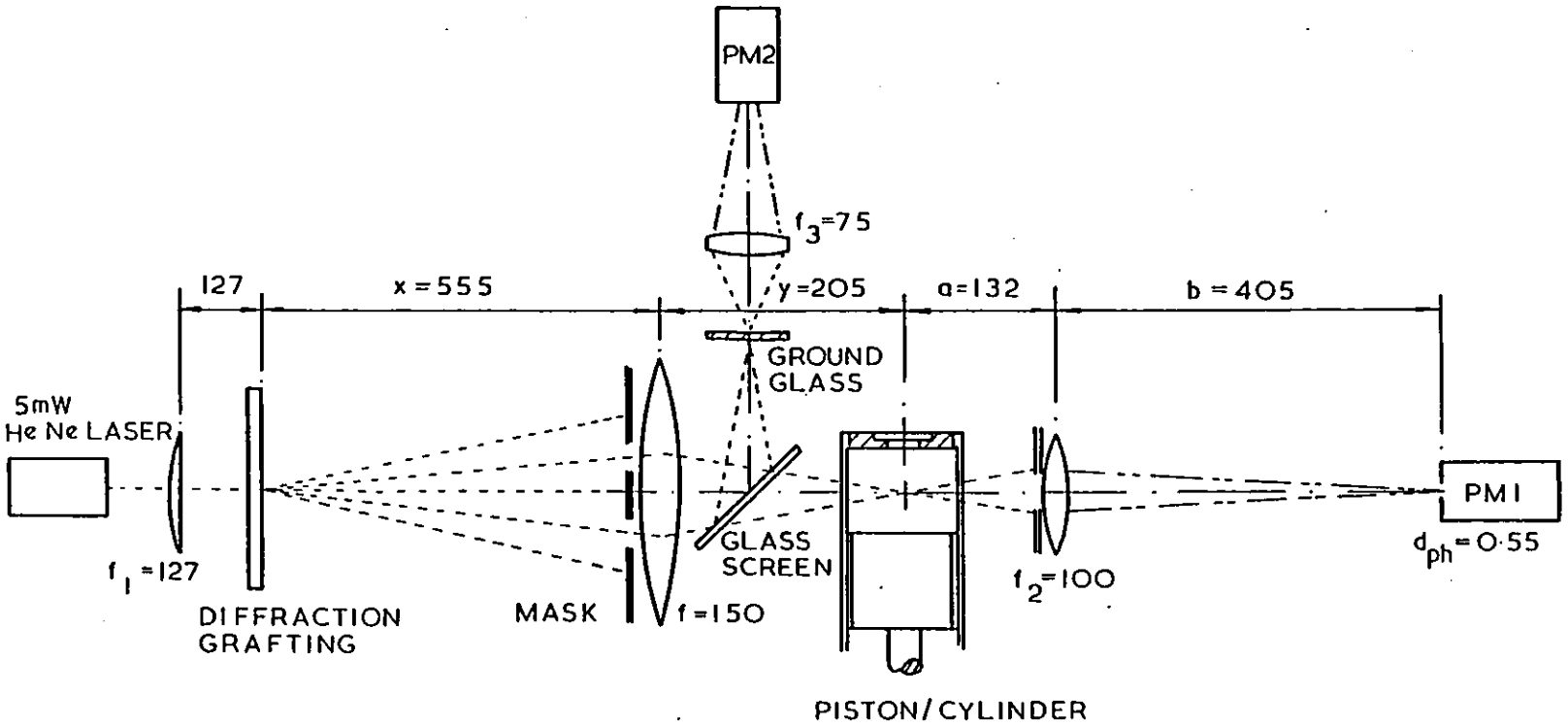


Figure 2.3(a) Laser Doppler anemometer optical system - Schematic diagram

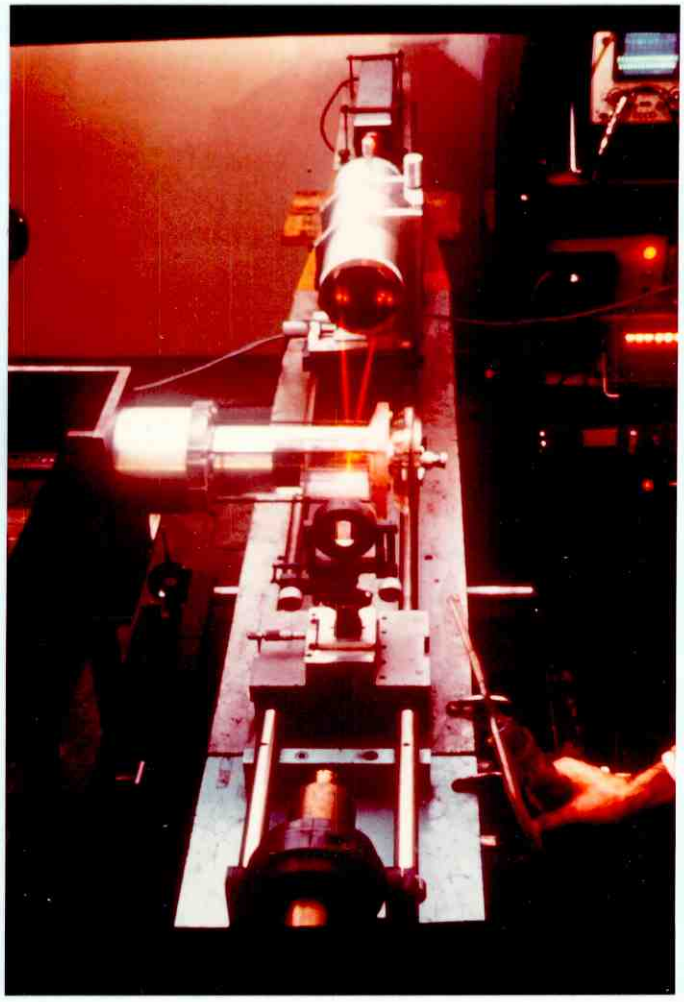


Figure 2.3(b) Laser Doppler anemometer system - Photograph

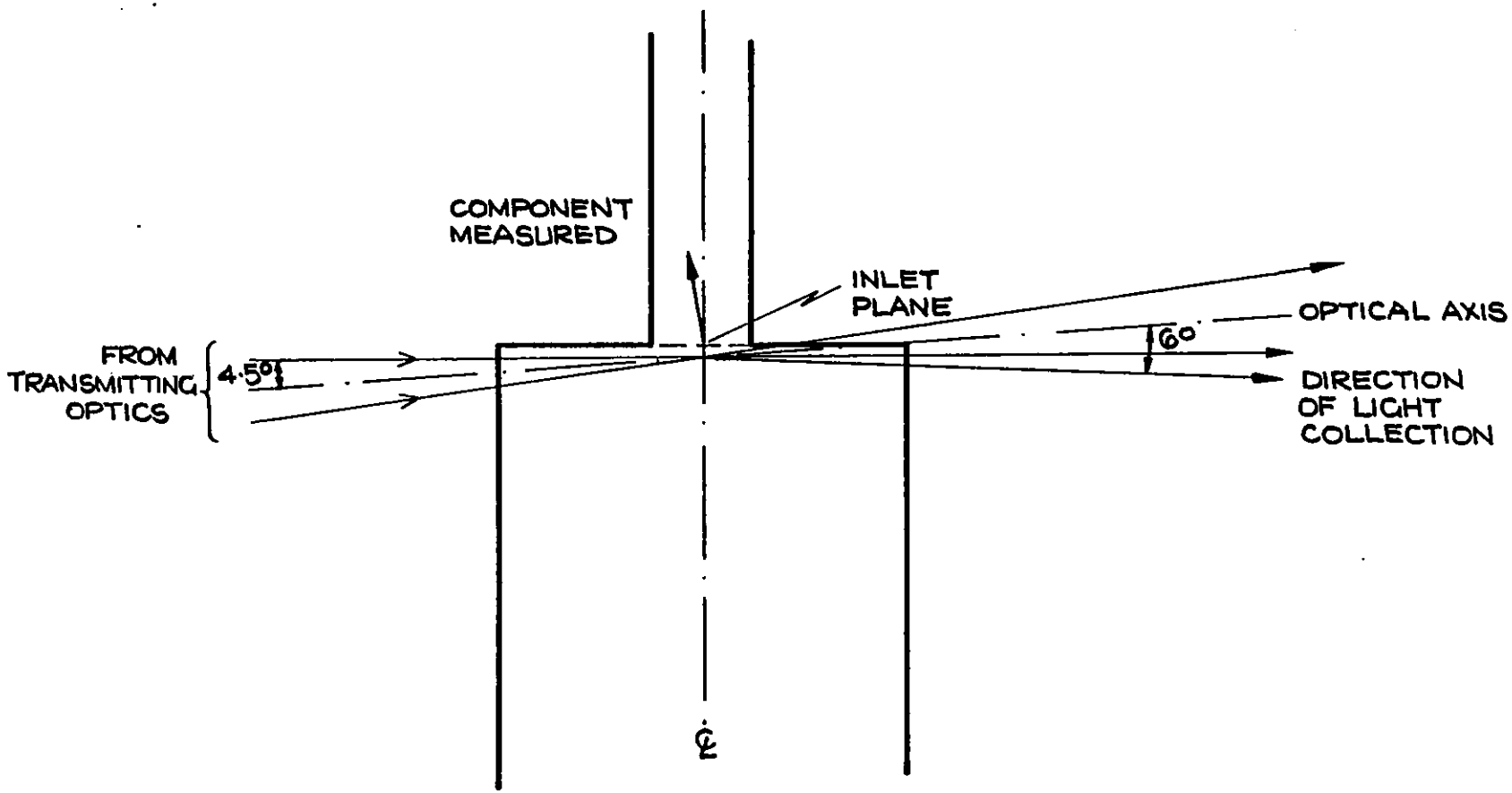


Figure 2.4 Schematic diagram of optical arrangement for inlet profiles (z = 0.5 mm) measurements

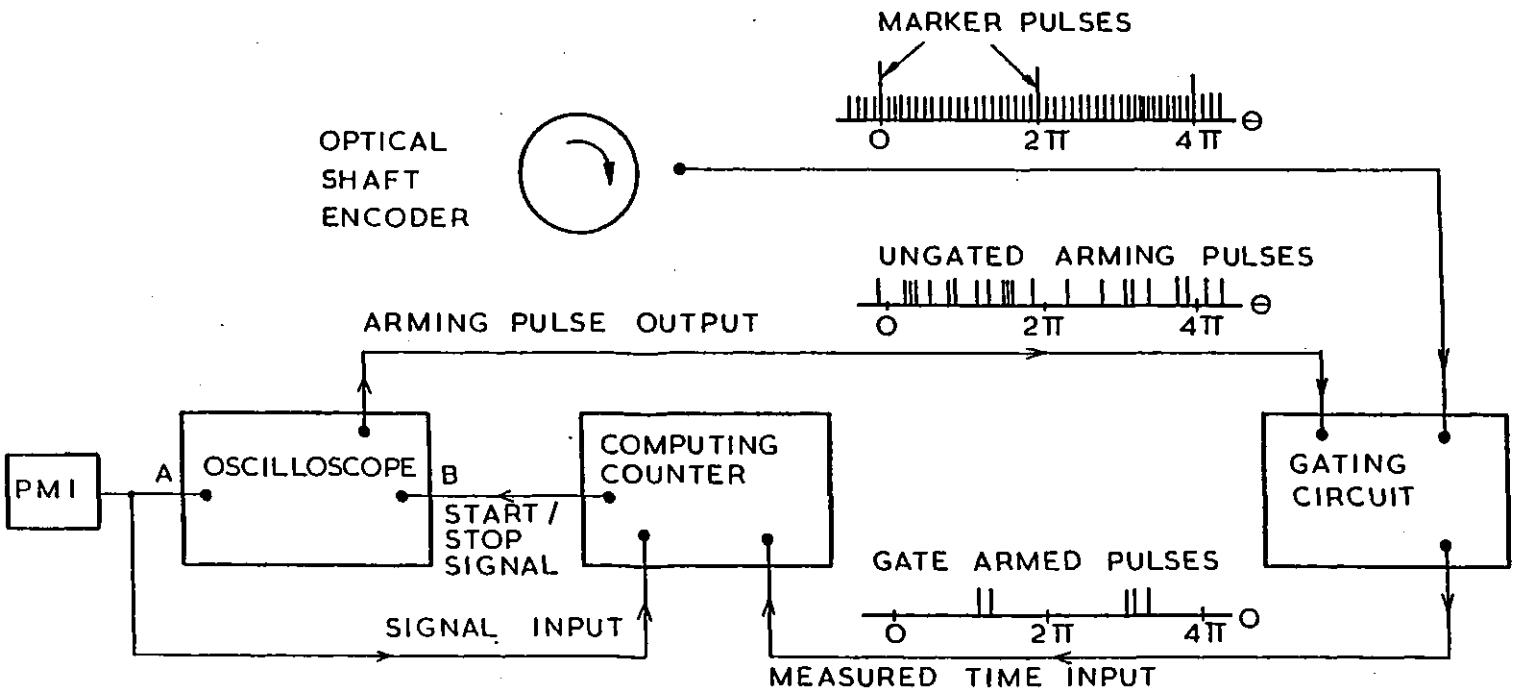


Figure 2.5(a) Laser Doppler anemometer signal processing
Frequency counter/keyboard programmed system

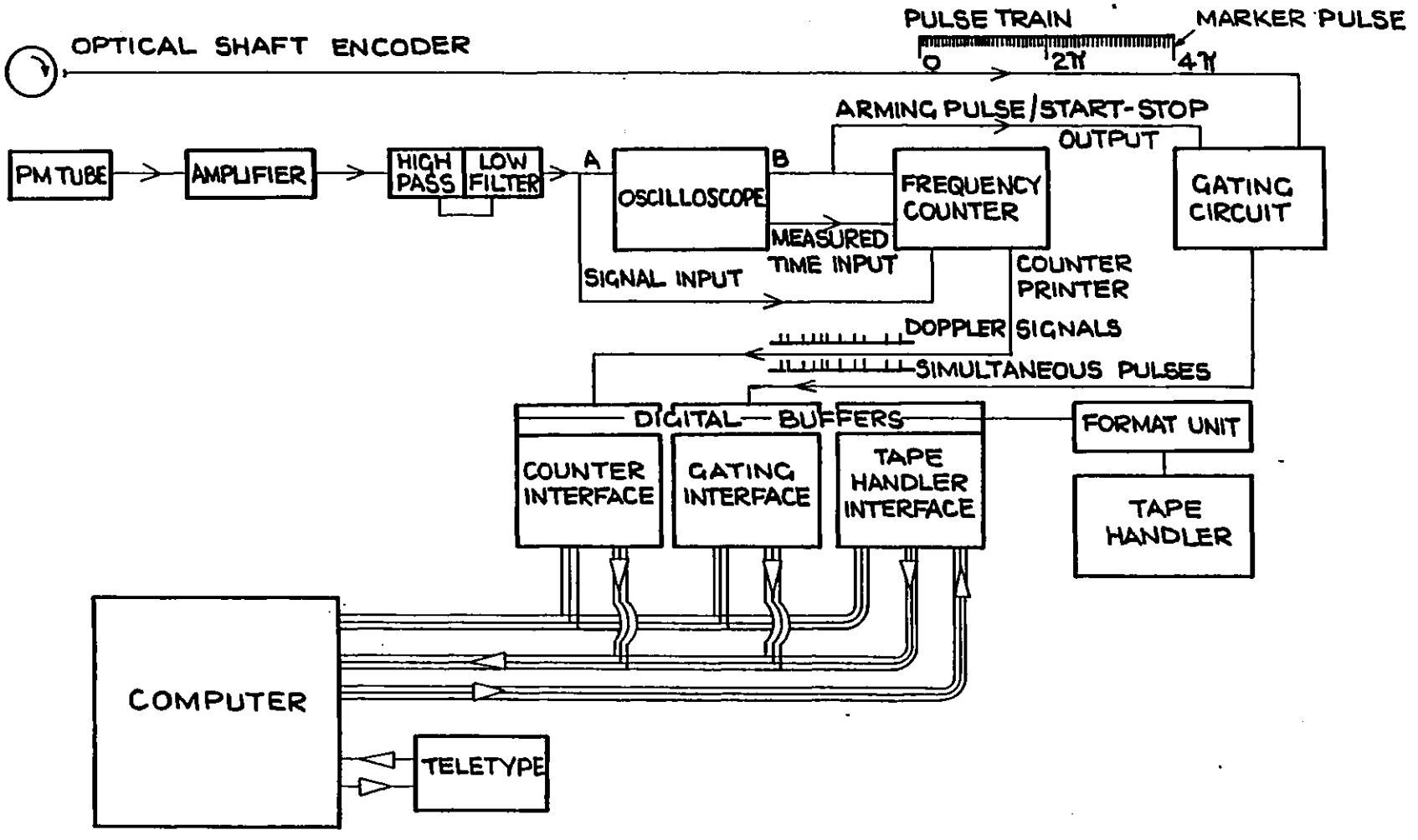


Figure 2.5(b) Laser Doppler anemometer signal processing - Frequency counter/PDP 8/e mini-computer system

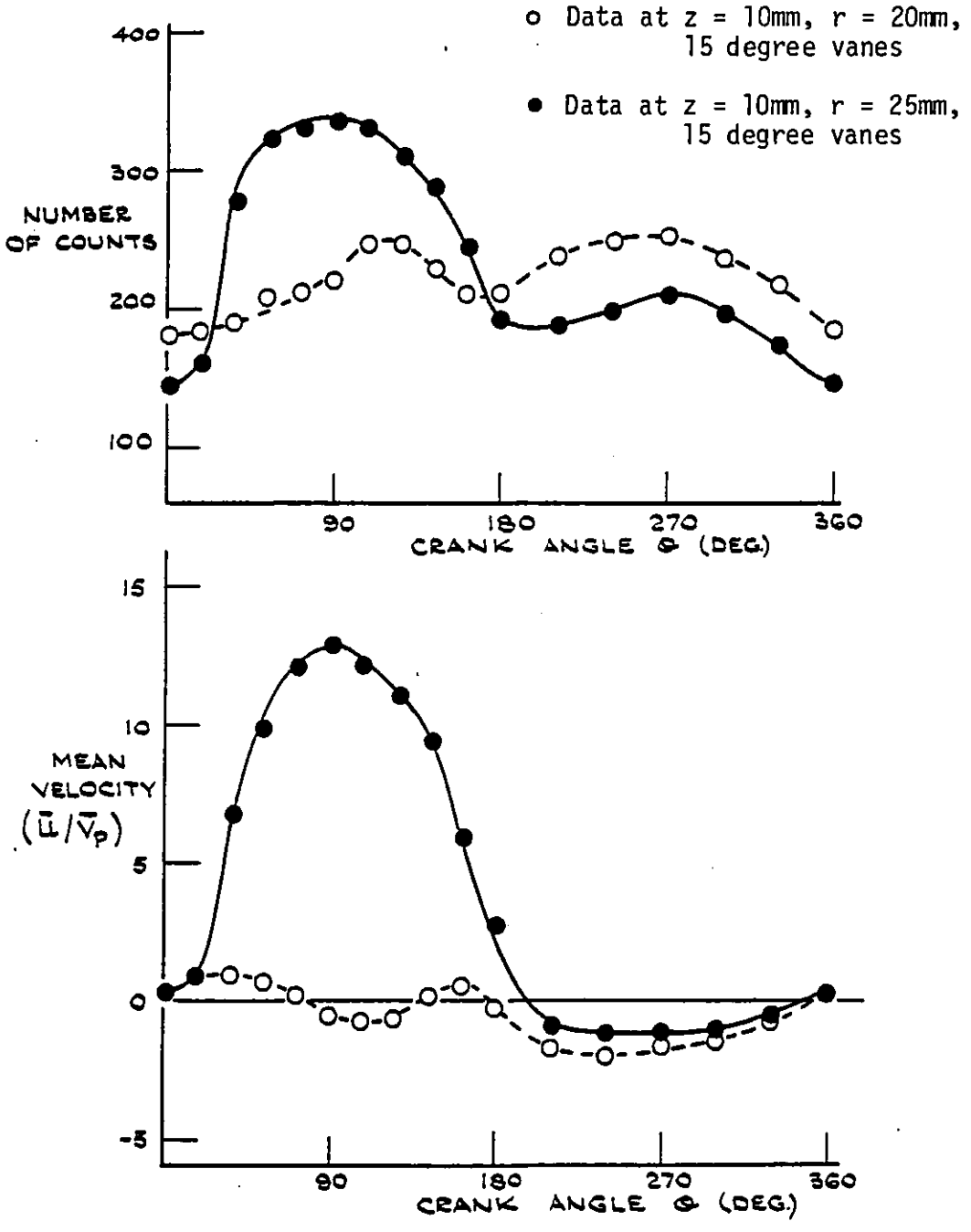


FIG. 3

Figure 2.6 Variation of count rate and mean velocity with crank angle

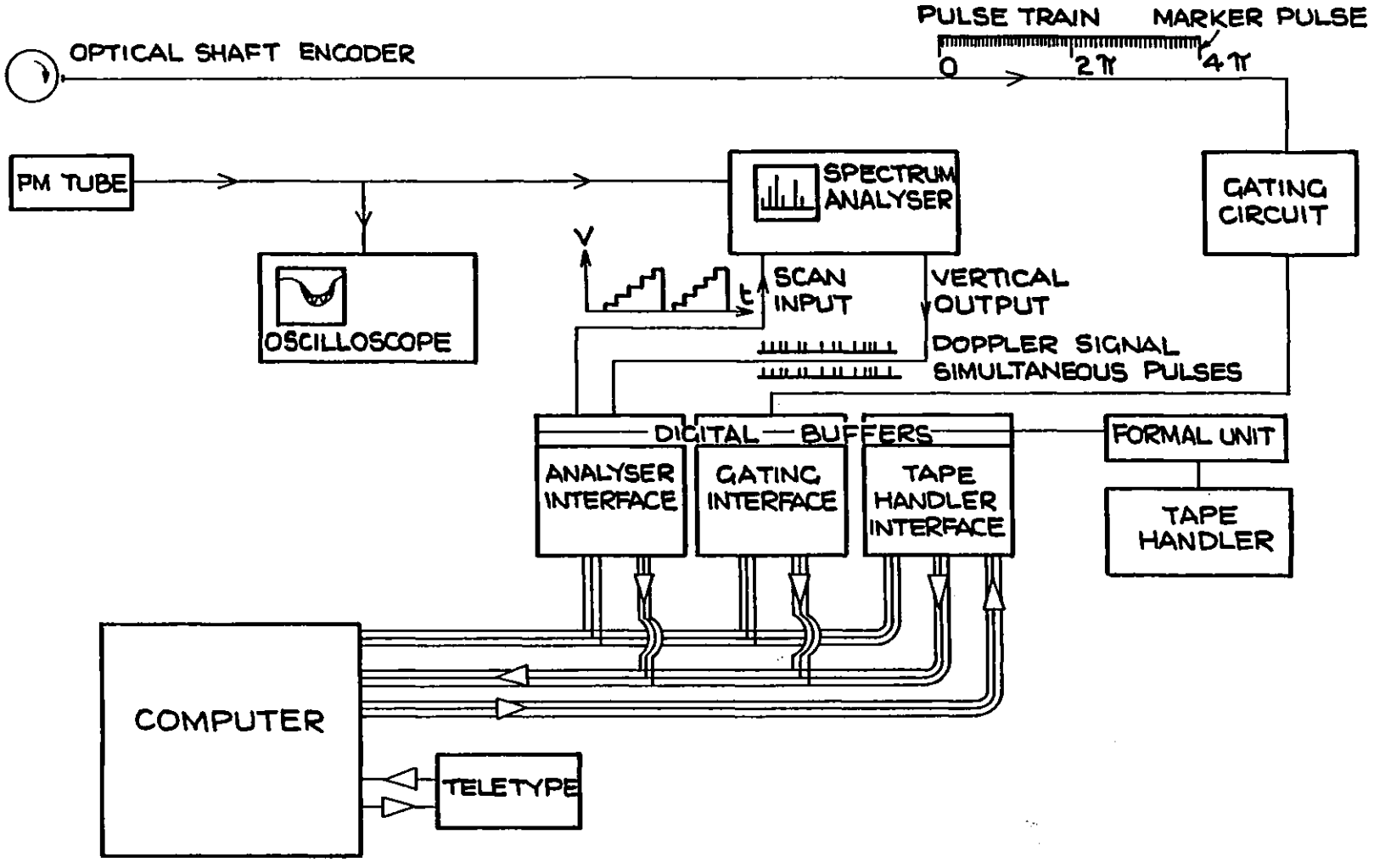


Figure 2.7(a) Spectrum analyser/PDP 8/e mini-computer signal processing system

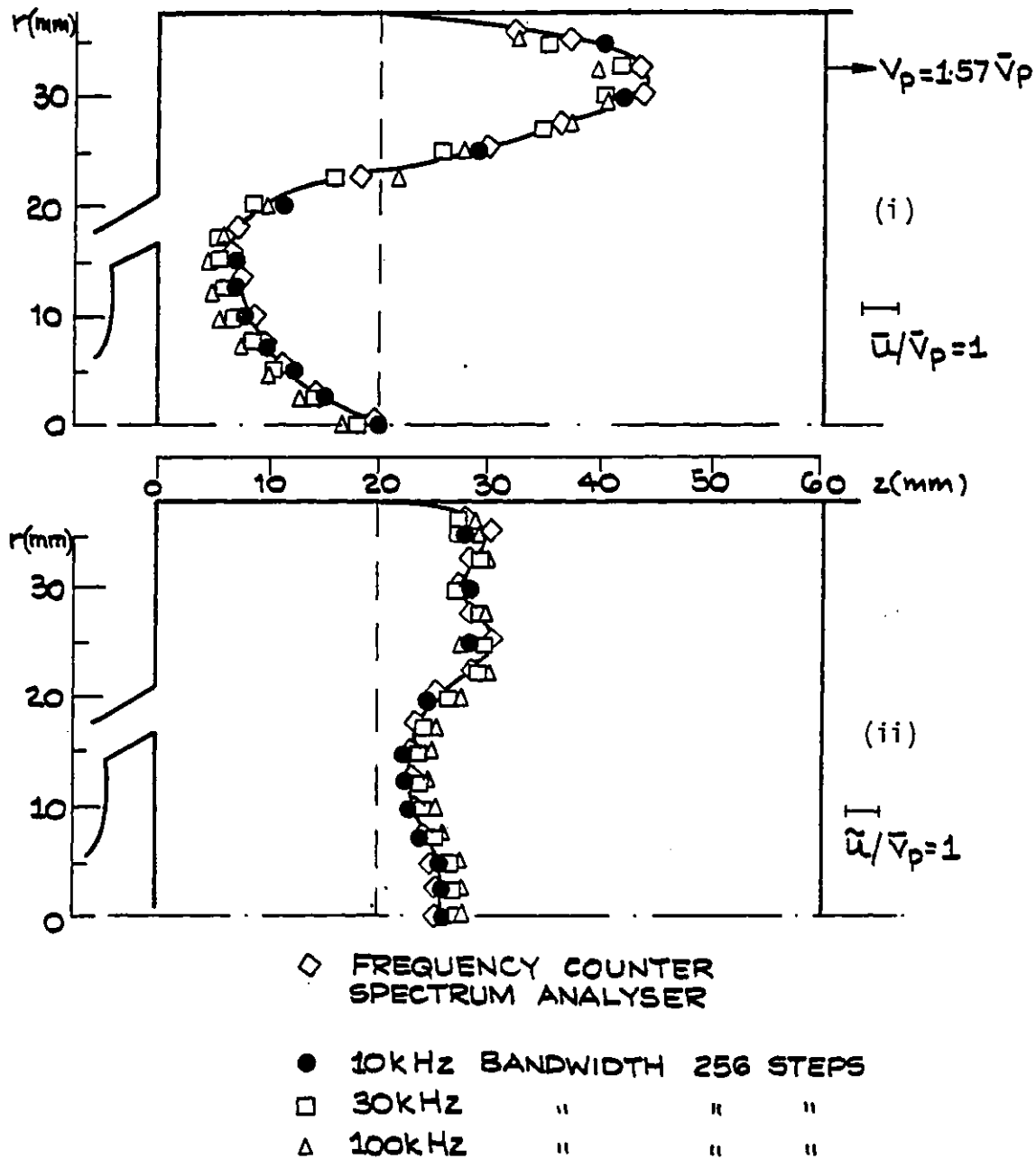


Figure 2.7(b) Profiles measured at $\theta = 90^{o}$, z = 20mm with spectrum analyser

(i) Axial mean velocity component with 256 step scan
(ii) Axial r.m.s. velocity component with 256 step scan

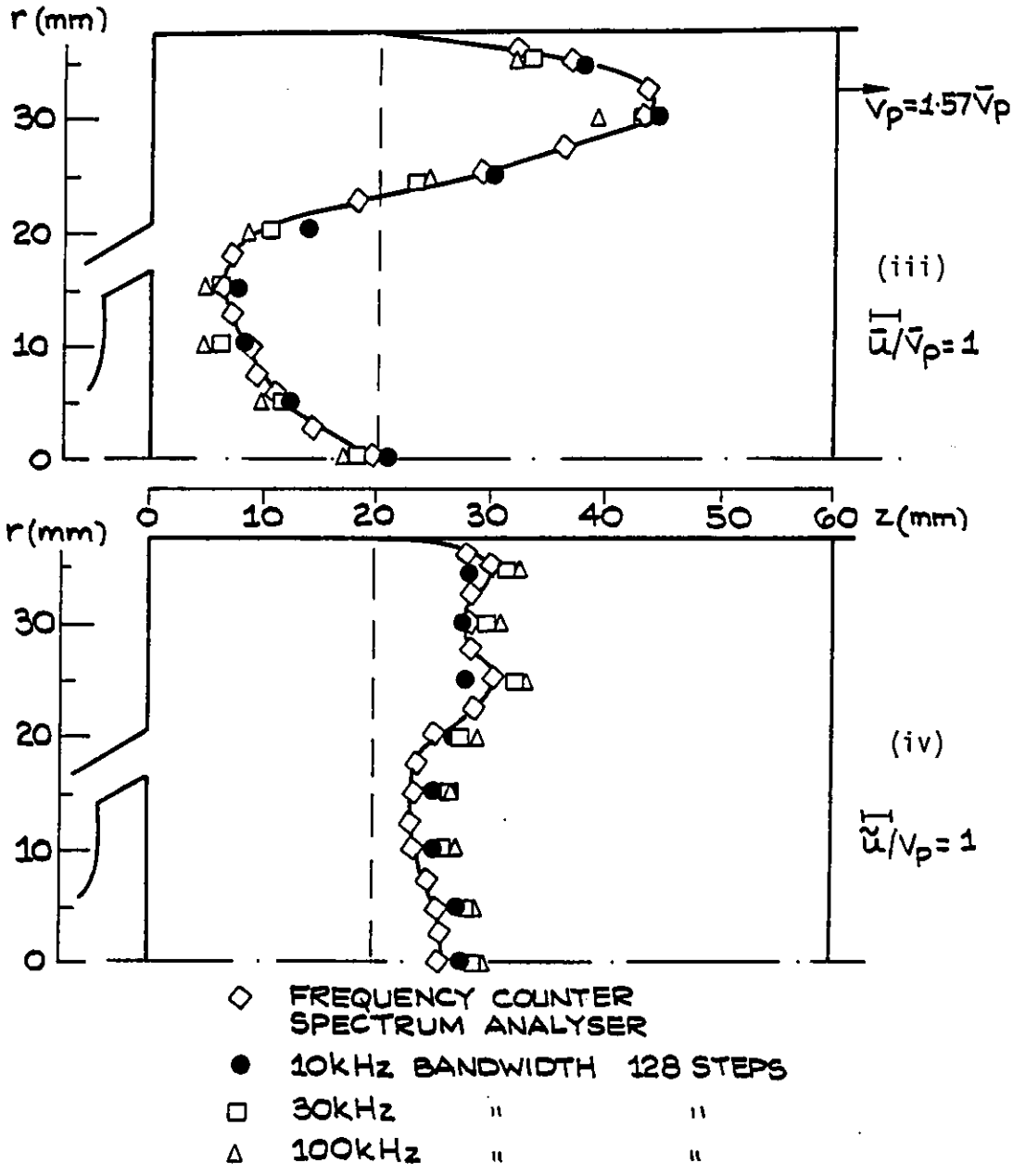
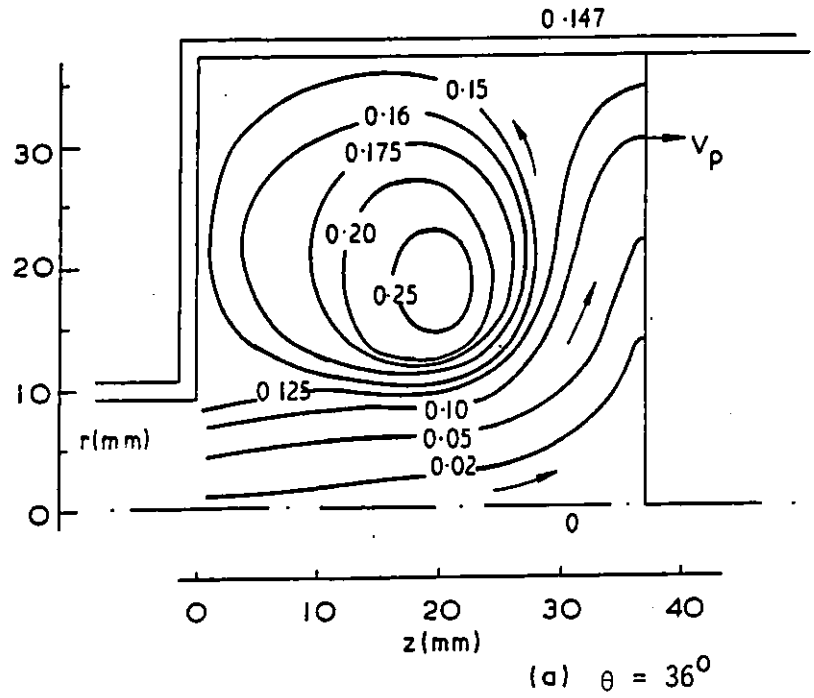


Figure 2.7(b) (cont.)

(iii) Axial mean velocity component with 128 step scan
(iv) Axial r.m.s. velocity component with 128 step scan



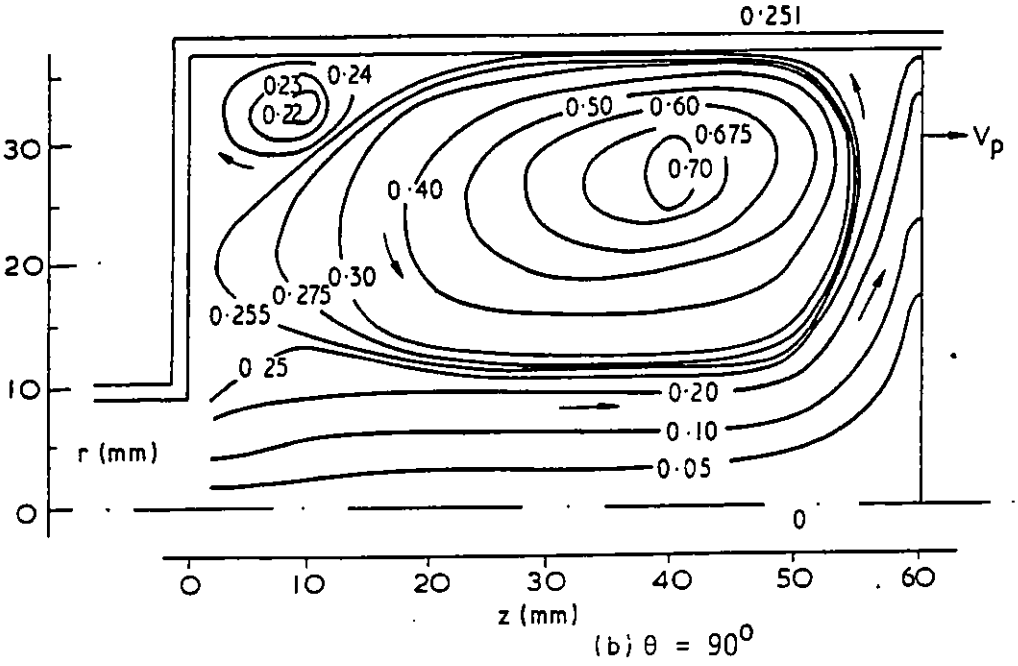
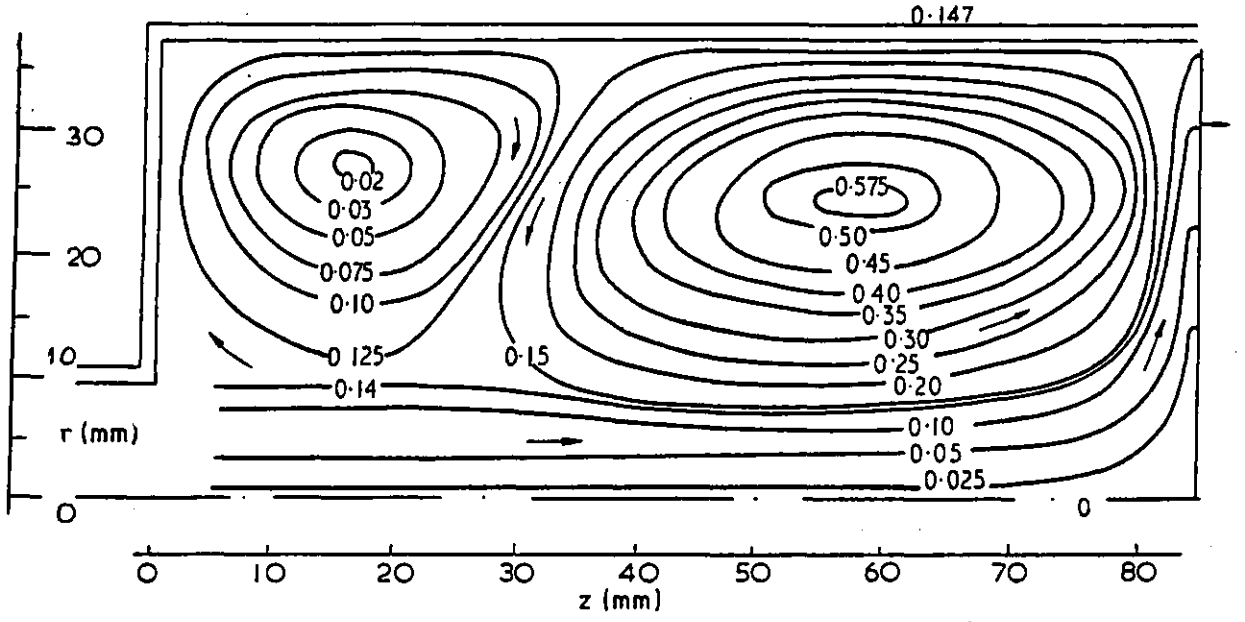
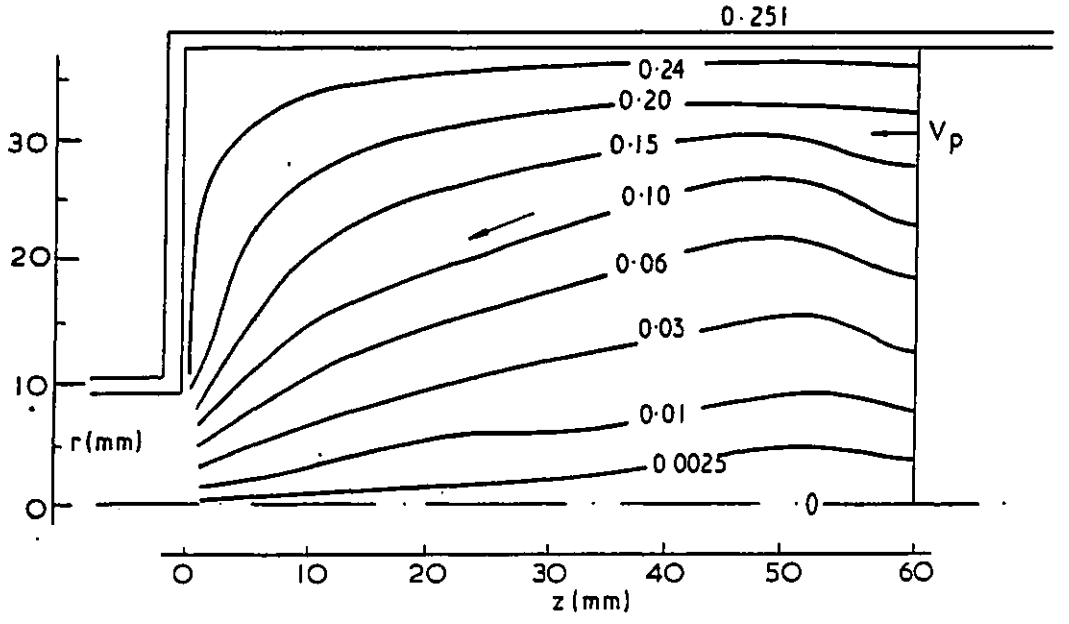


Figure 2.8 Pipe inlet: stream function contours



(c) $\theta = 144^{0}$



(d) $\theta = 270^{0}$

Figure 2.8 (cont.)

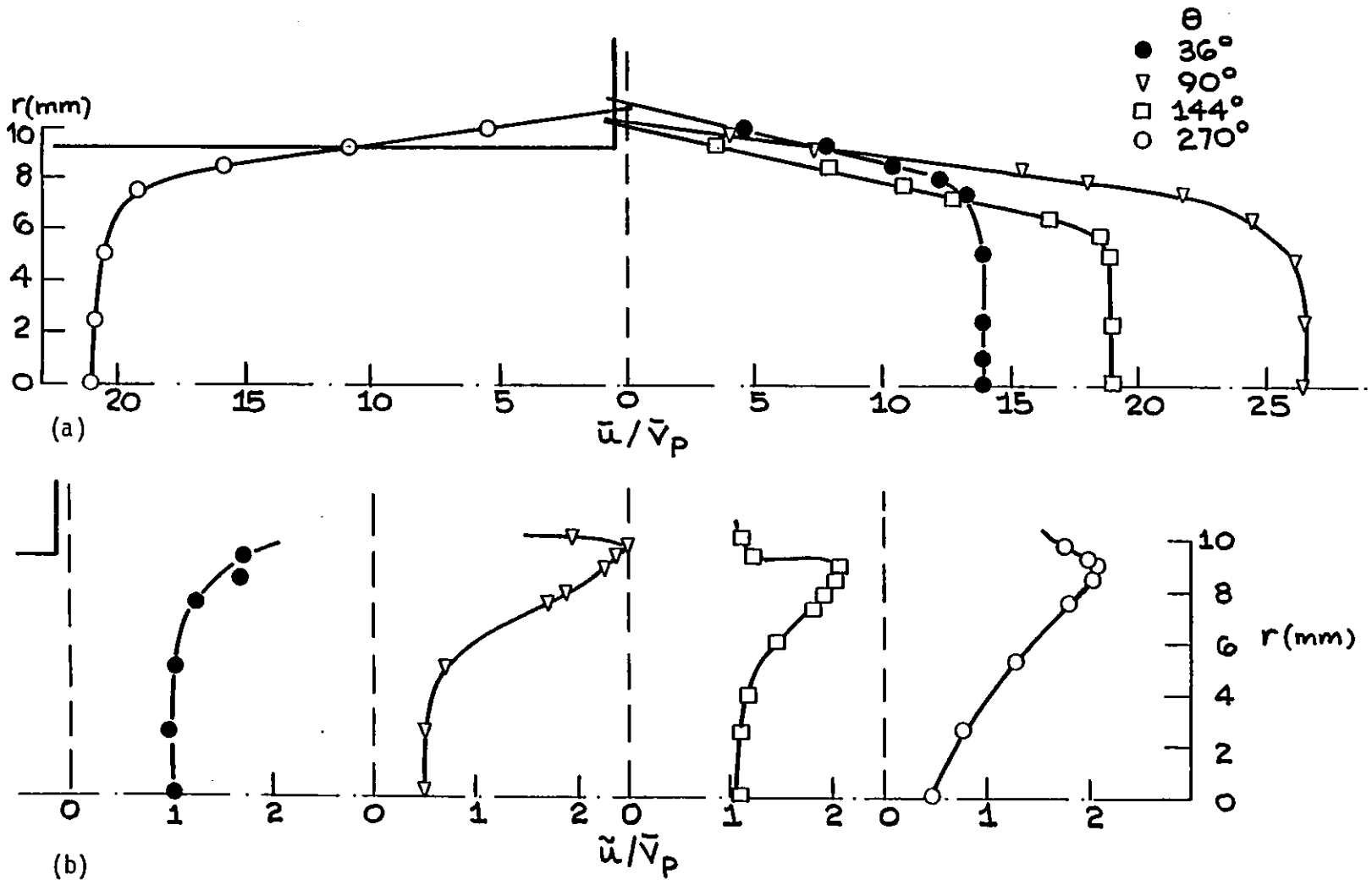


Figure 2.9 Pipe inlet: axial component profiles at z = 0.5 mm
(a) mean velocity (b) r.m.s. velocity

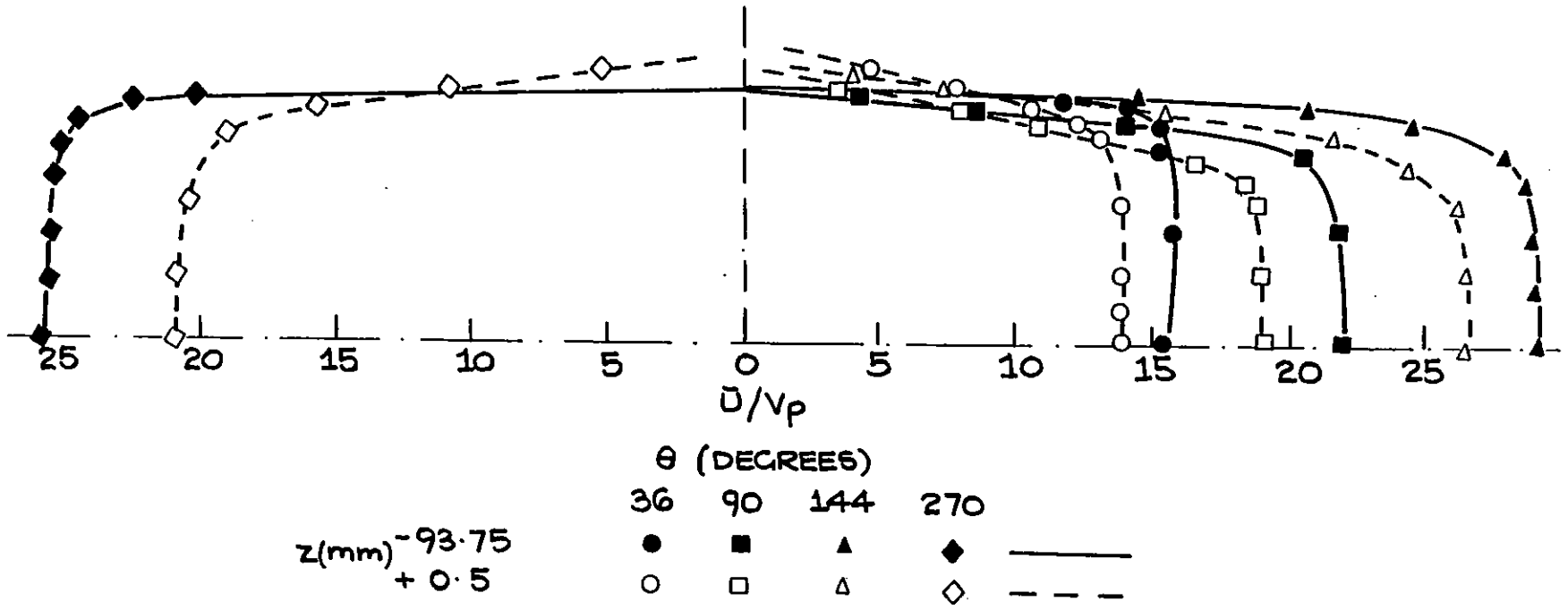
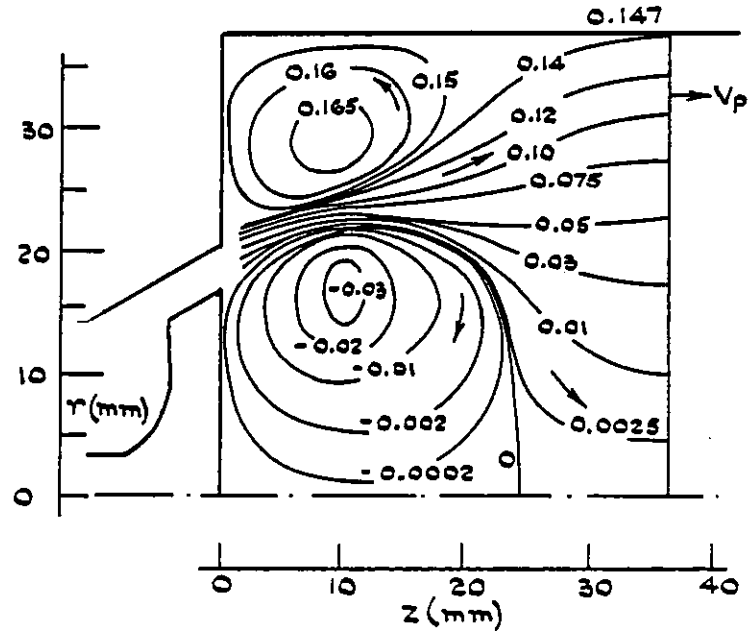
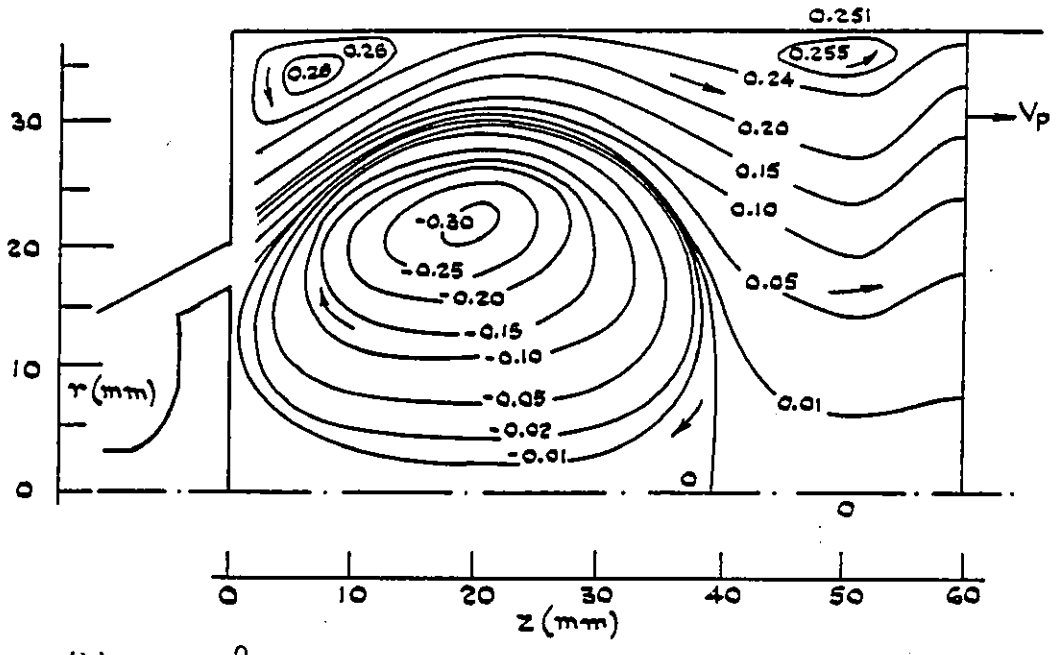


Figure 2.10 Pipe inlet: comparison of mean velocity profiles in the pipe and near the inlet

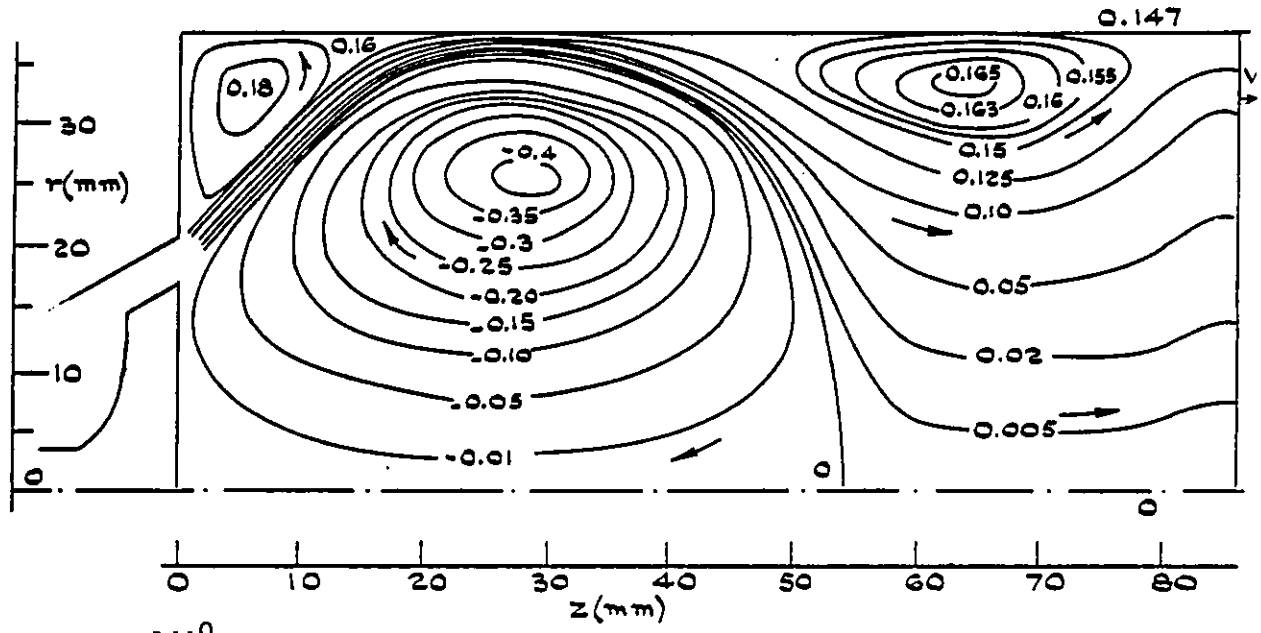


(a) $\theta = 36^{o}$

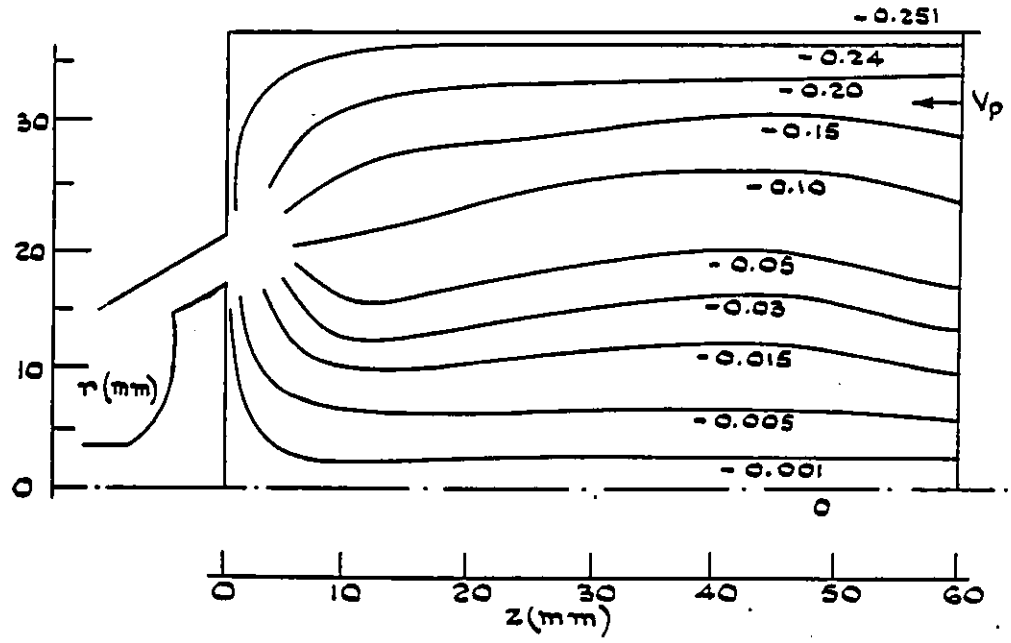


(b) $\theta = 90^{o}$

Figure 2.11 Valve inlet, no swirl: stream function contours



(c) $\theta = 144^{o}$



(d) $\theta = 270^{o}$

Figure 2.11 Valve inlet, no swirl: stream function contours

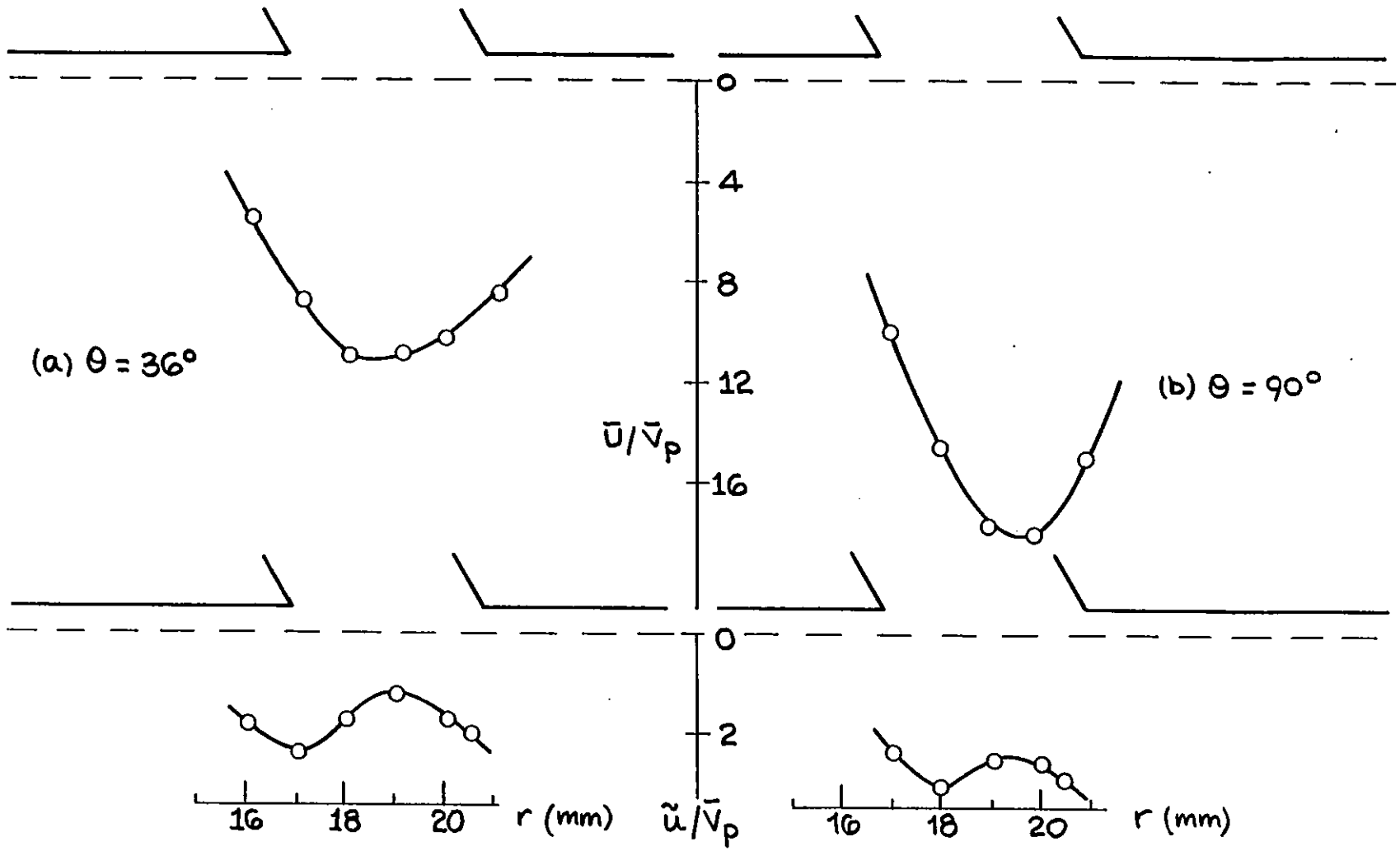


Figure 2.12 Valve inlet, no swirl: axial component profiles at z = 0.5mm

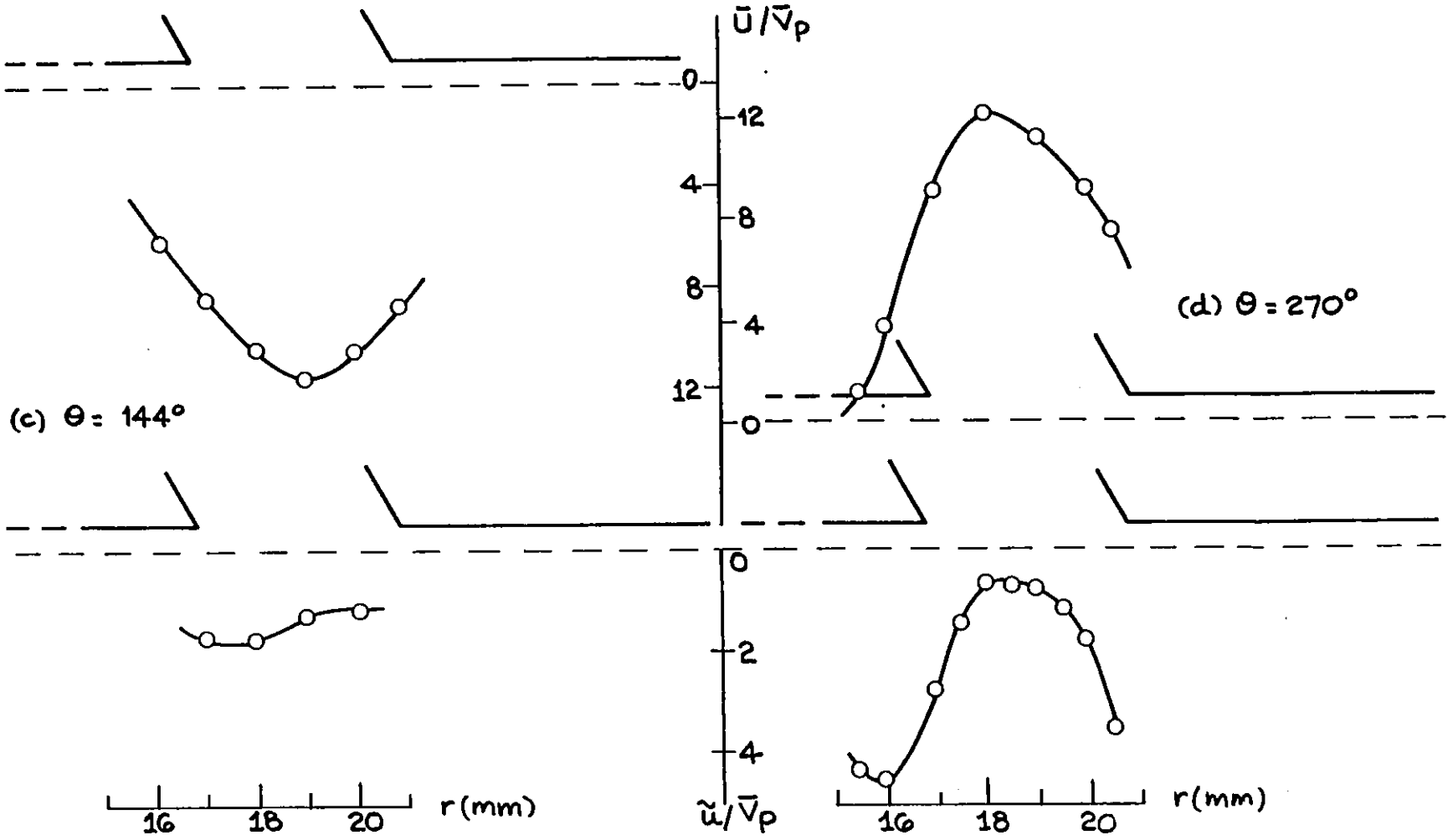


Figure 2.12 (cont.)

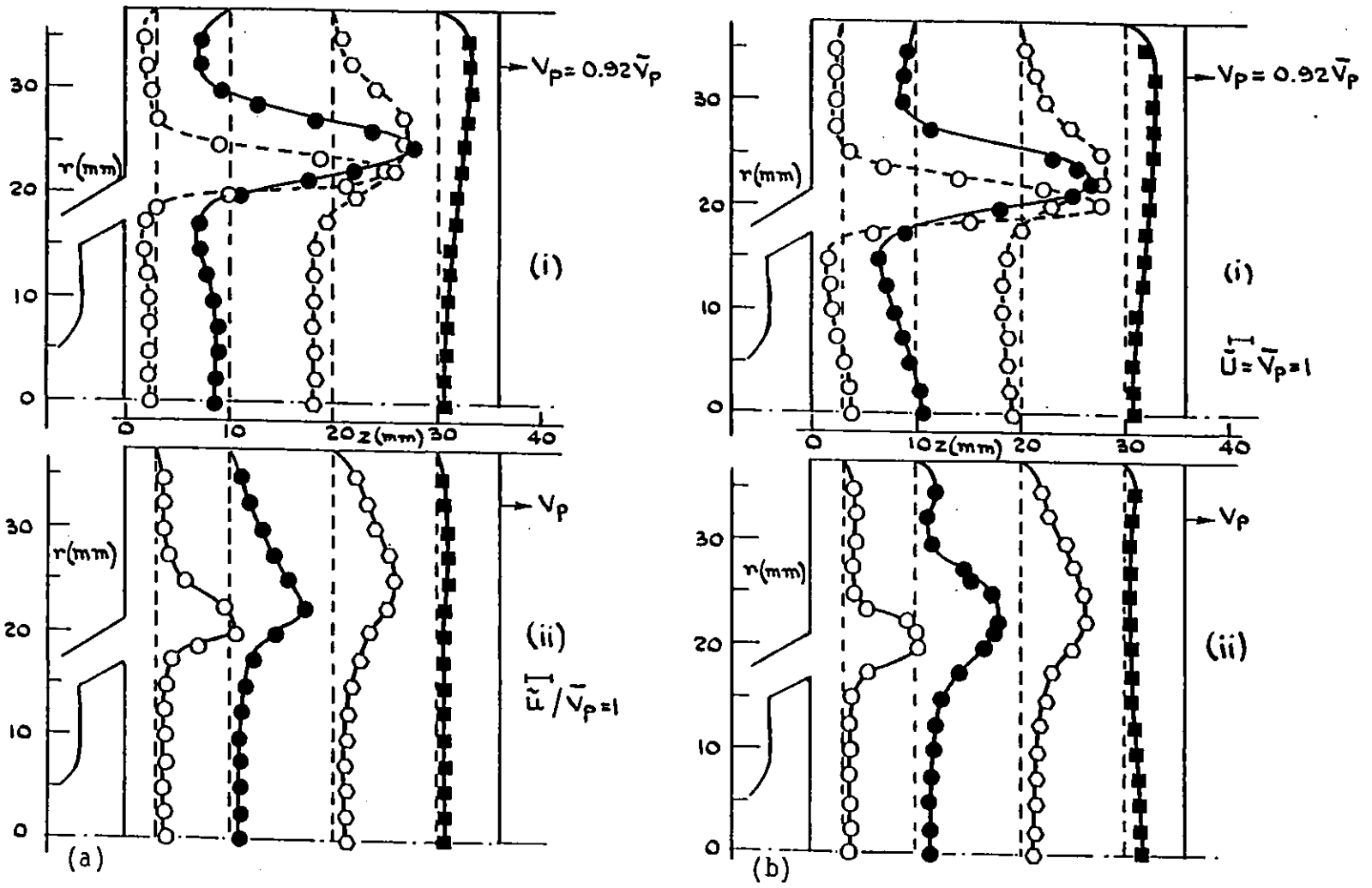


Figure 2.13 Valve inlet: profiles of axial velocity at $\theta = 36^0$
(a) 15 degree vanes)
(b) 30 degree vanes) (i) mean velocity and (ii) r.m.s. component

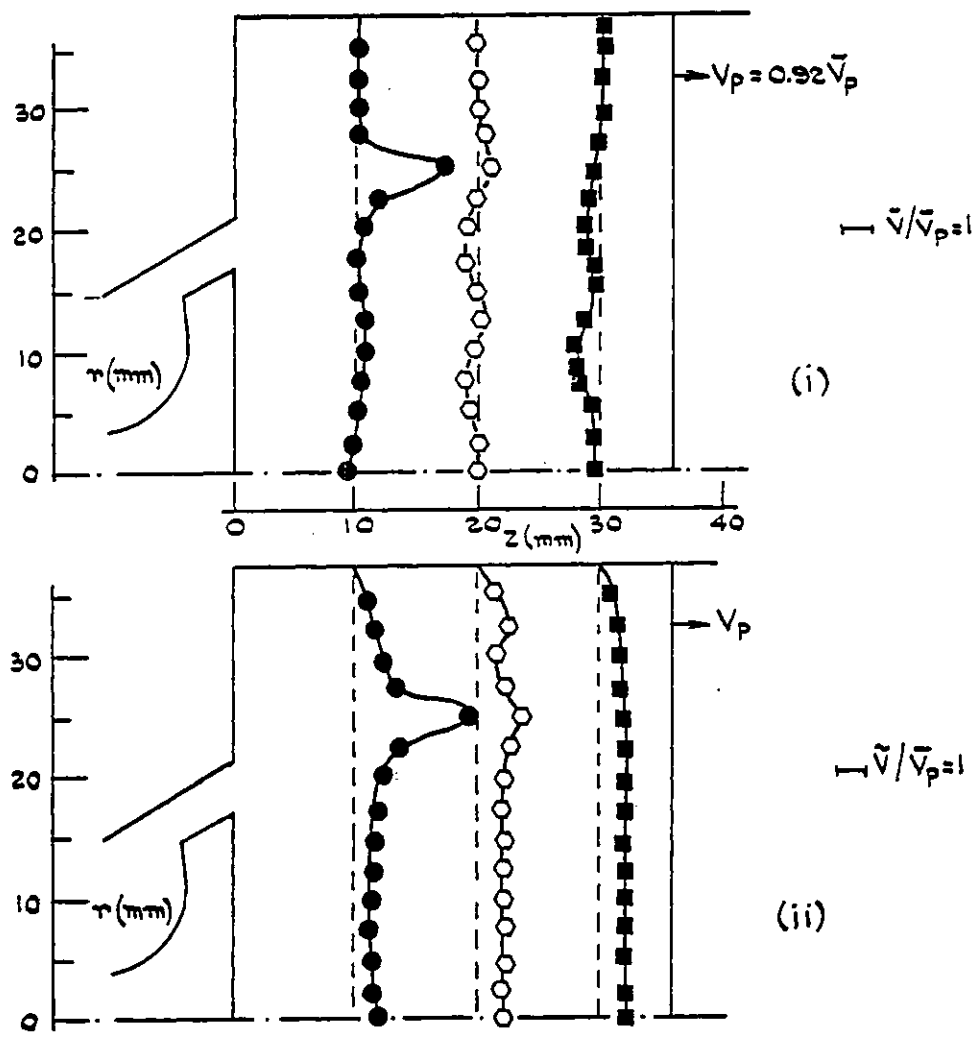


FIG. 6

Figure 2.14 Valve inlet: profiles of radial velocity at $\theta = 36^{o}$
30 degree vanes
(i) mean velocity and (ii) r.m.s. component

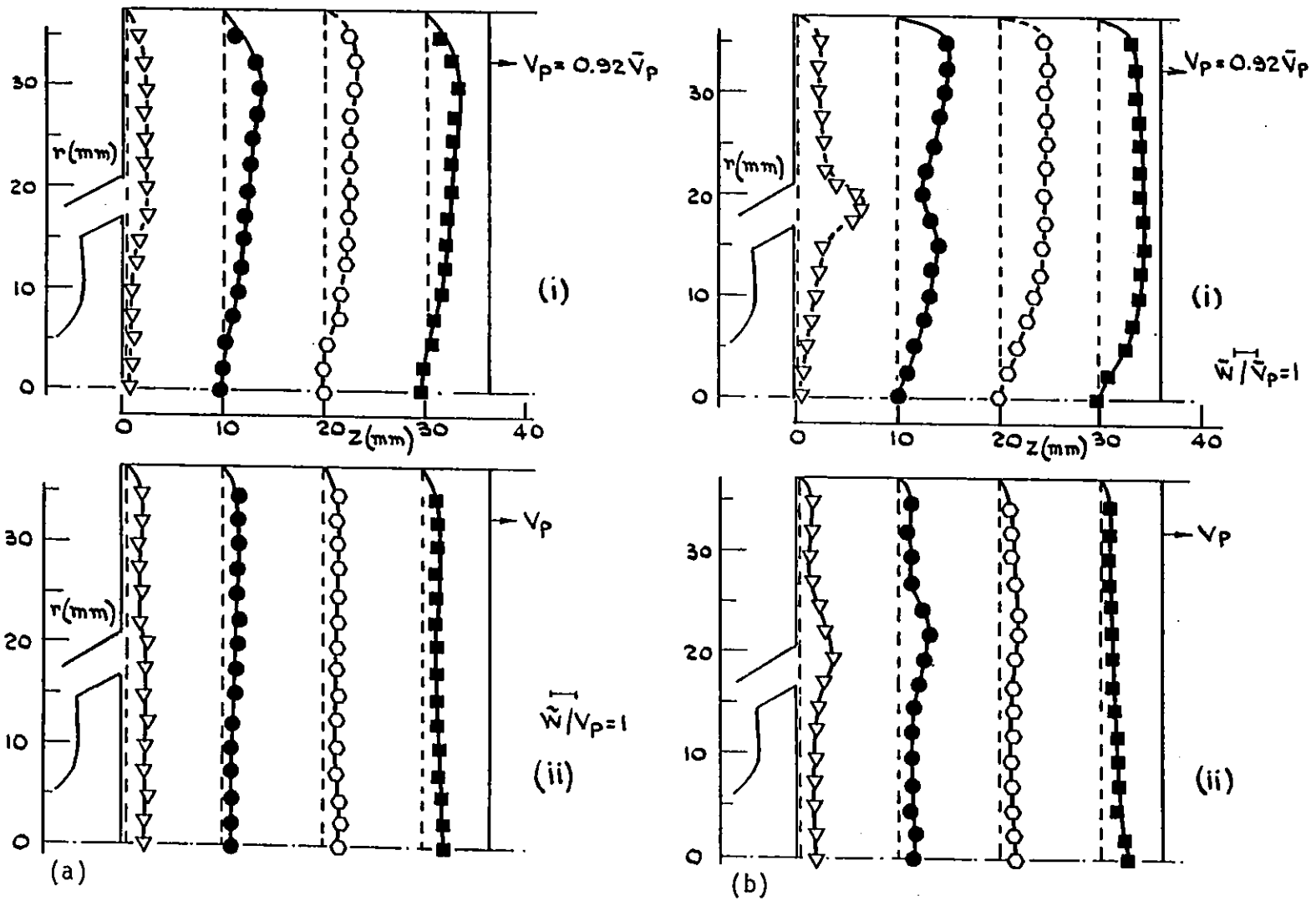


Figure 2.15 Valve inlet: profiles of swirl velocity at $\theta = 36^0$
(a) 15 degree vanes)
(b) 30 degree vanes) (i) mean velocity and (ii) r.m.s. component

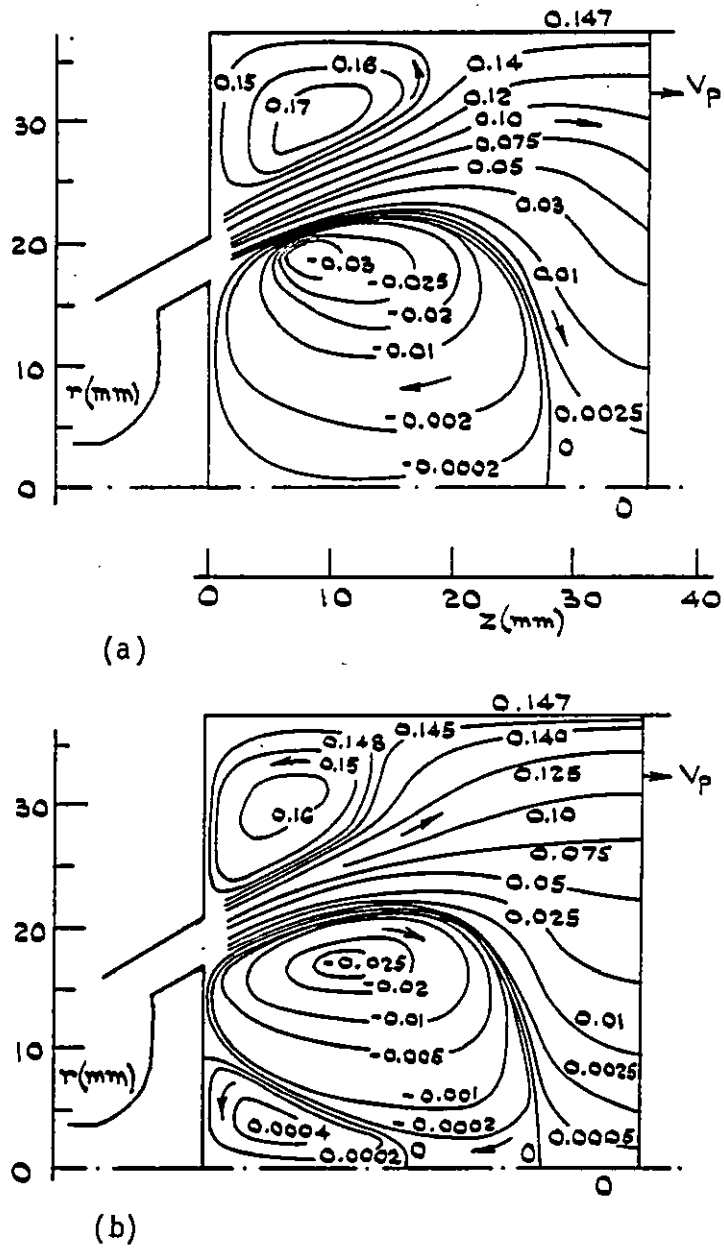


Figure 2.16 Valve inlet: streamline patterns at $\theta = 36^{0}$
(a) 15 degree vanes
(b) 30 degree vanes

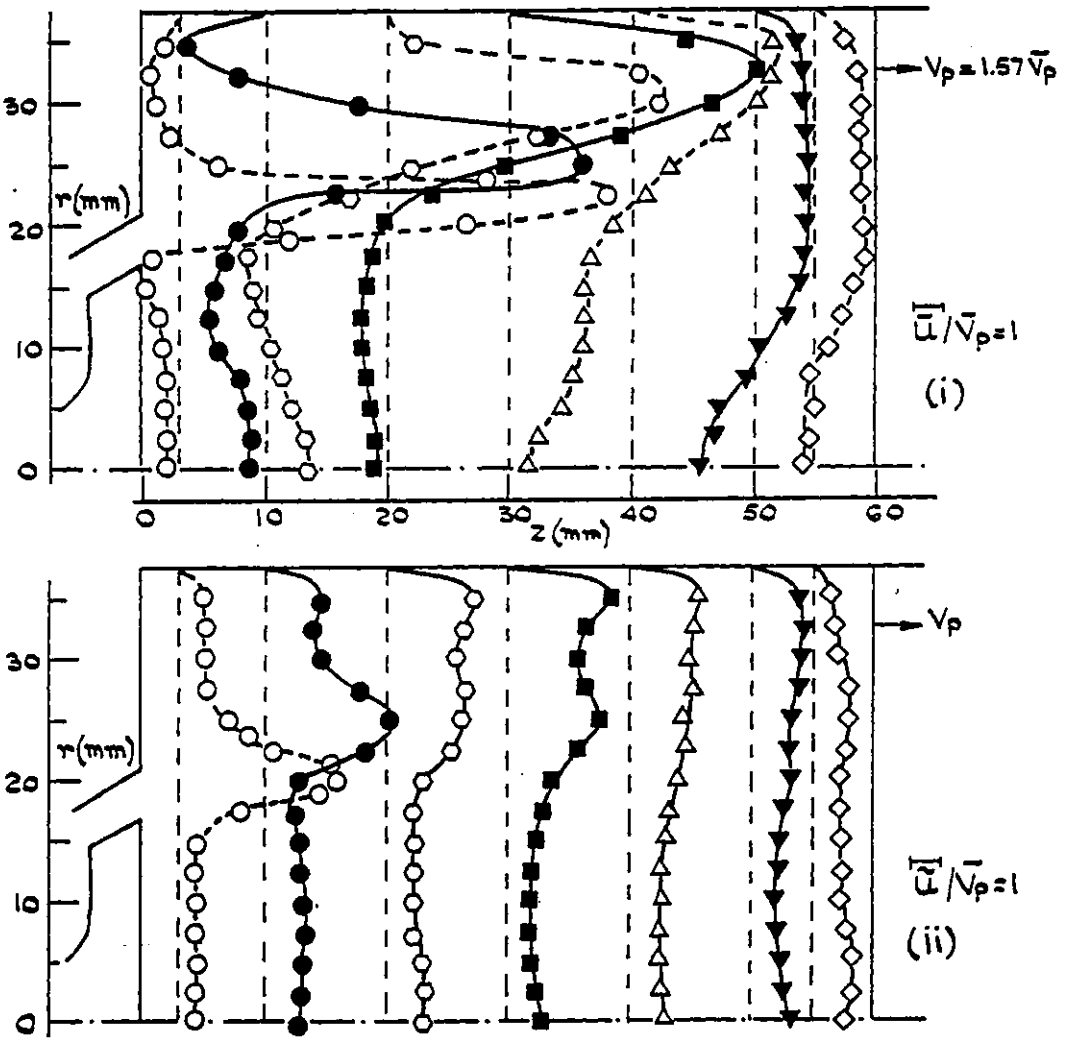


Figure 2.17 Valve inlet: profiles of axial velocity at $\theta = 90^{o}$
(a) 15 degree vanes

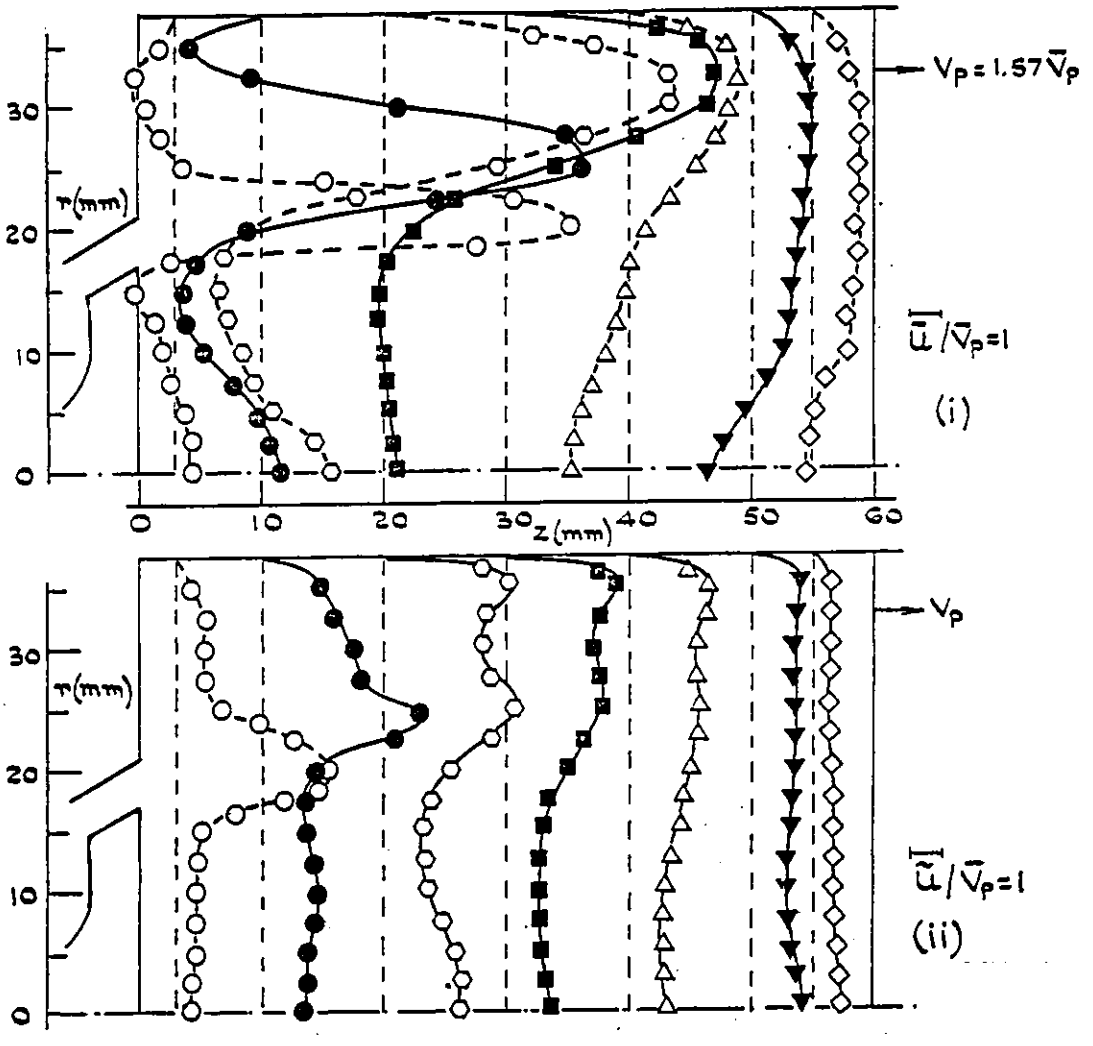


Figure 2.17 (cont.)

(b) 30 degree vanes

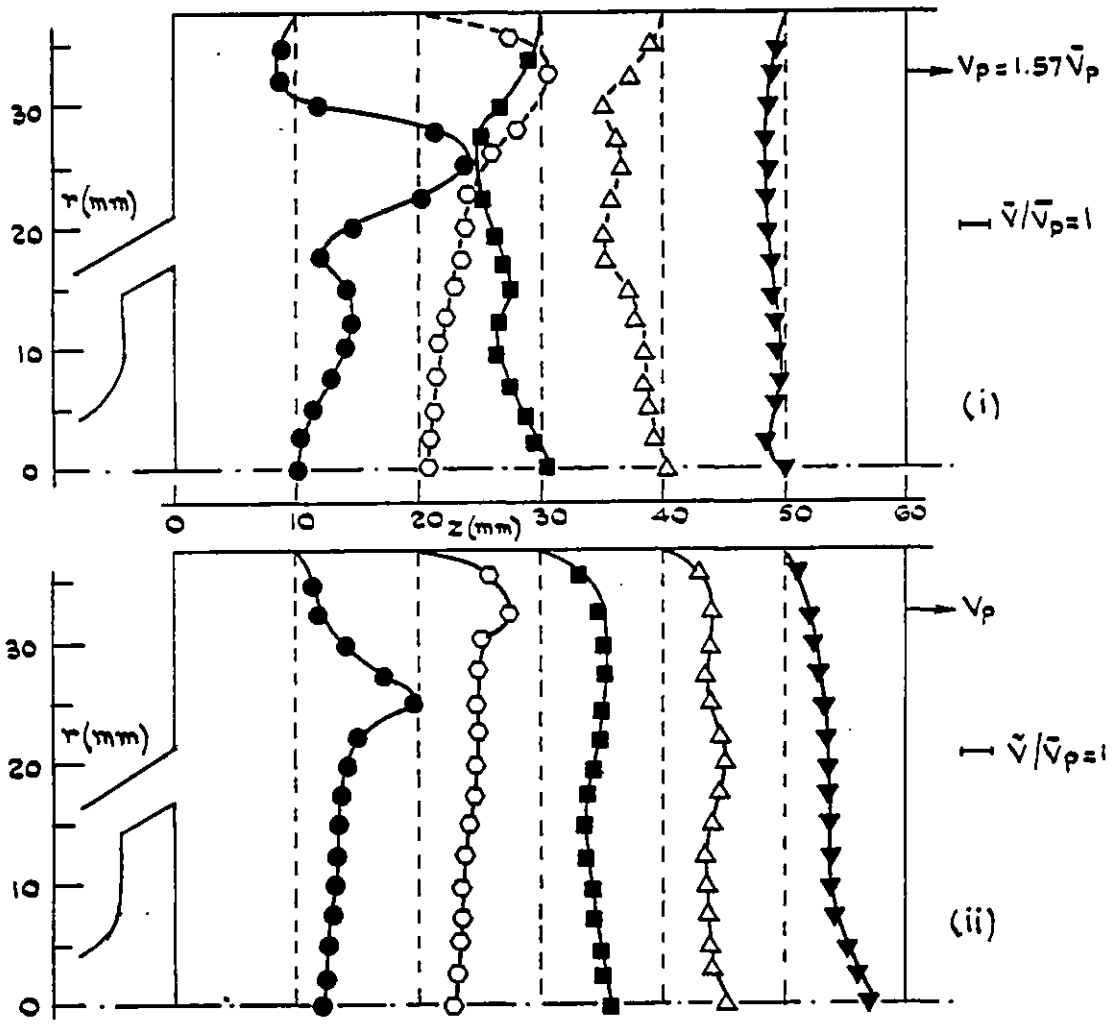


Figure 2.18 Valve inlet: profiles of radial velocity at $\theta = 90^{o}$
30 degree vanes
(i) mean velocity and (ii) r.m.s. component

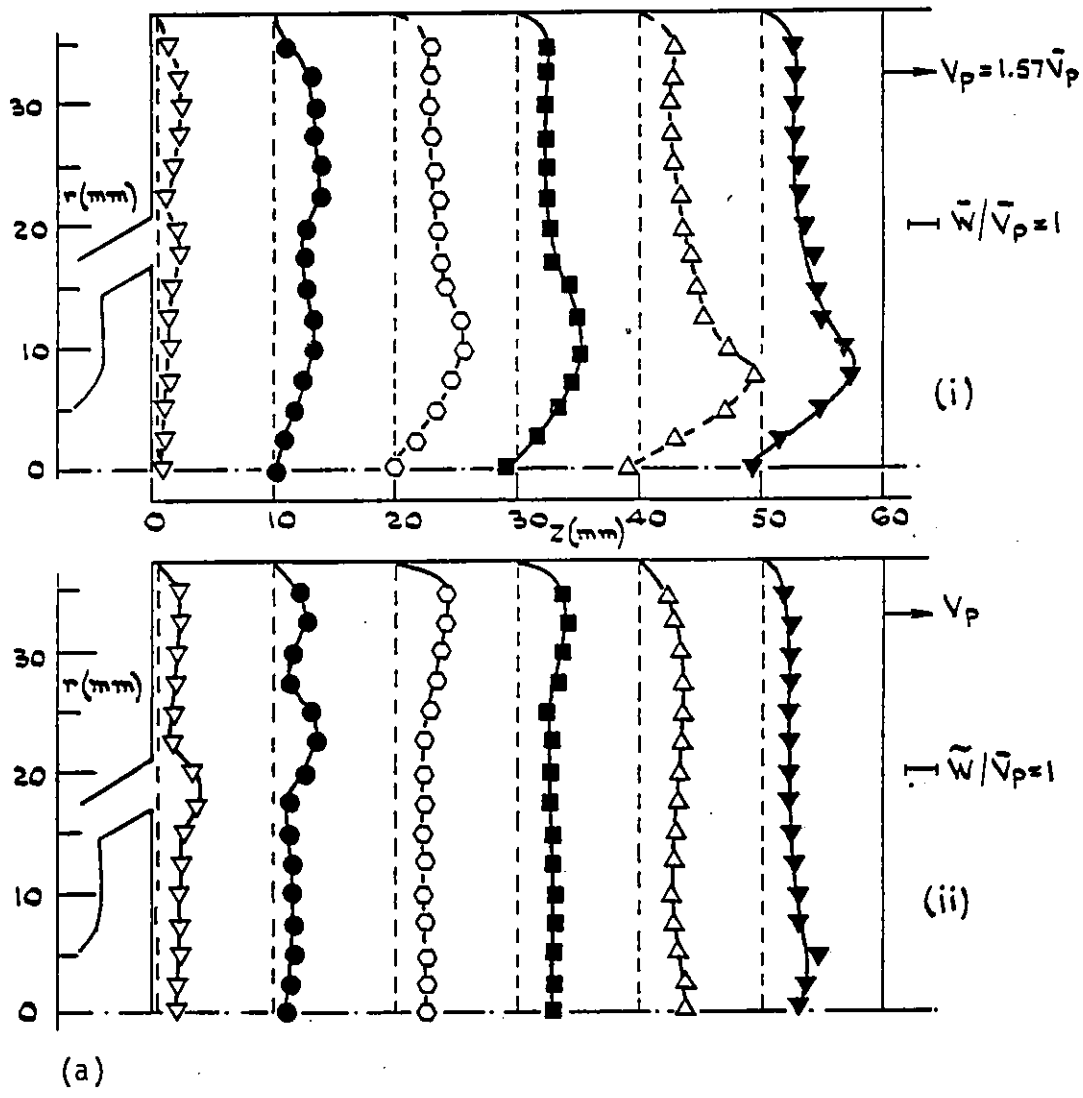


Figure 2.19 Valve inlet: profiles of swirl velocity at $\theta = 90^{o}$
(a) 15 degree vanes

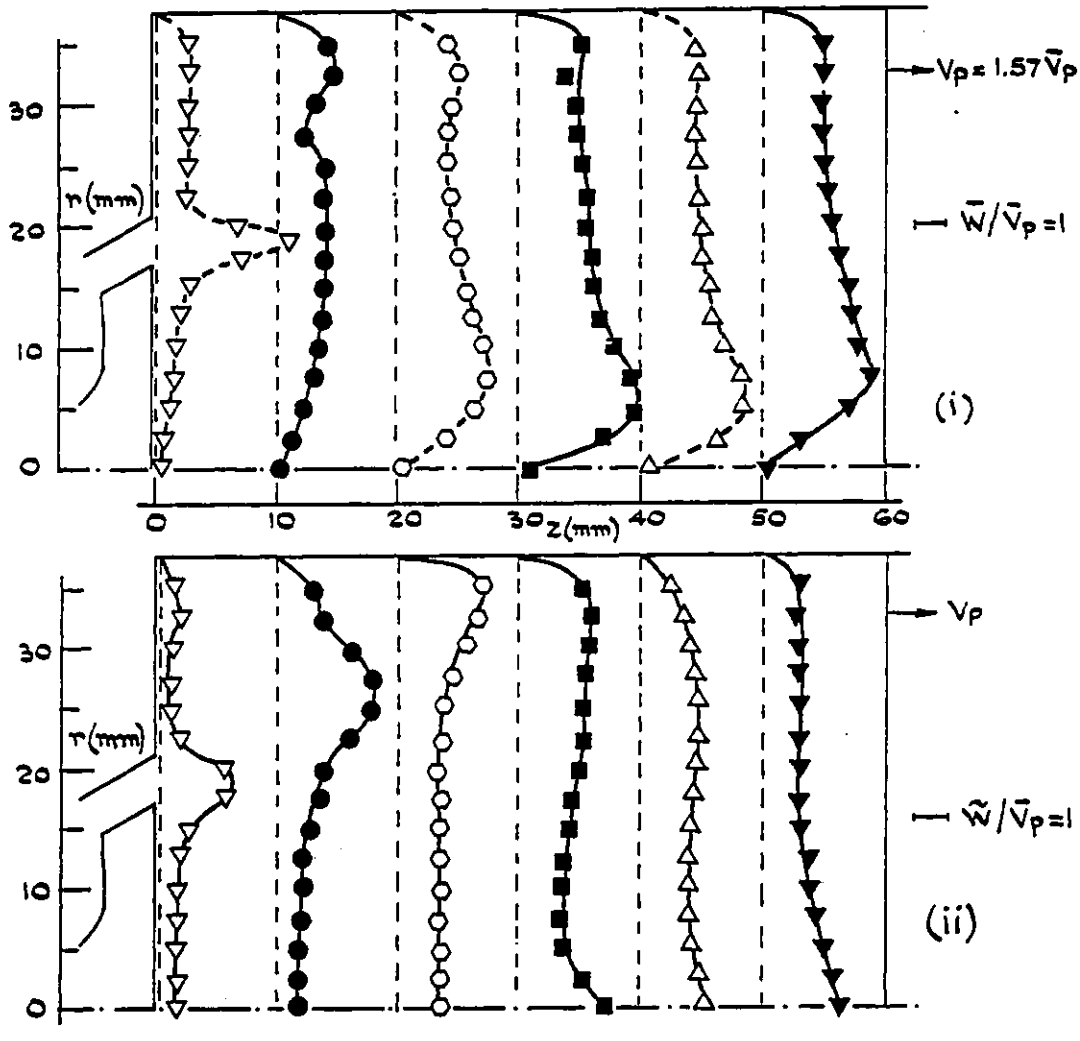


Figure 2.19 Valve inlet: profiles of swirl velocity at $\theta = 90^{o}$
(b) 30 degree vanes

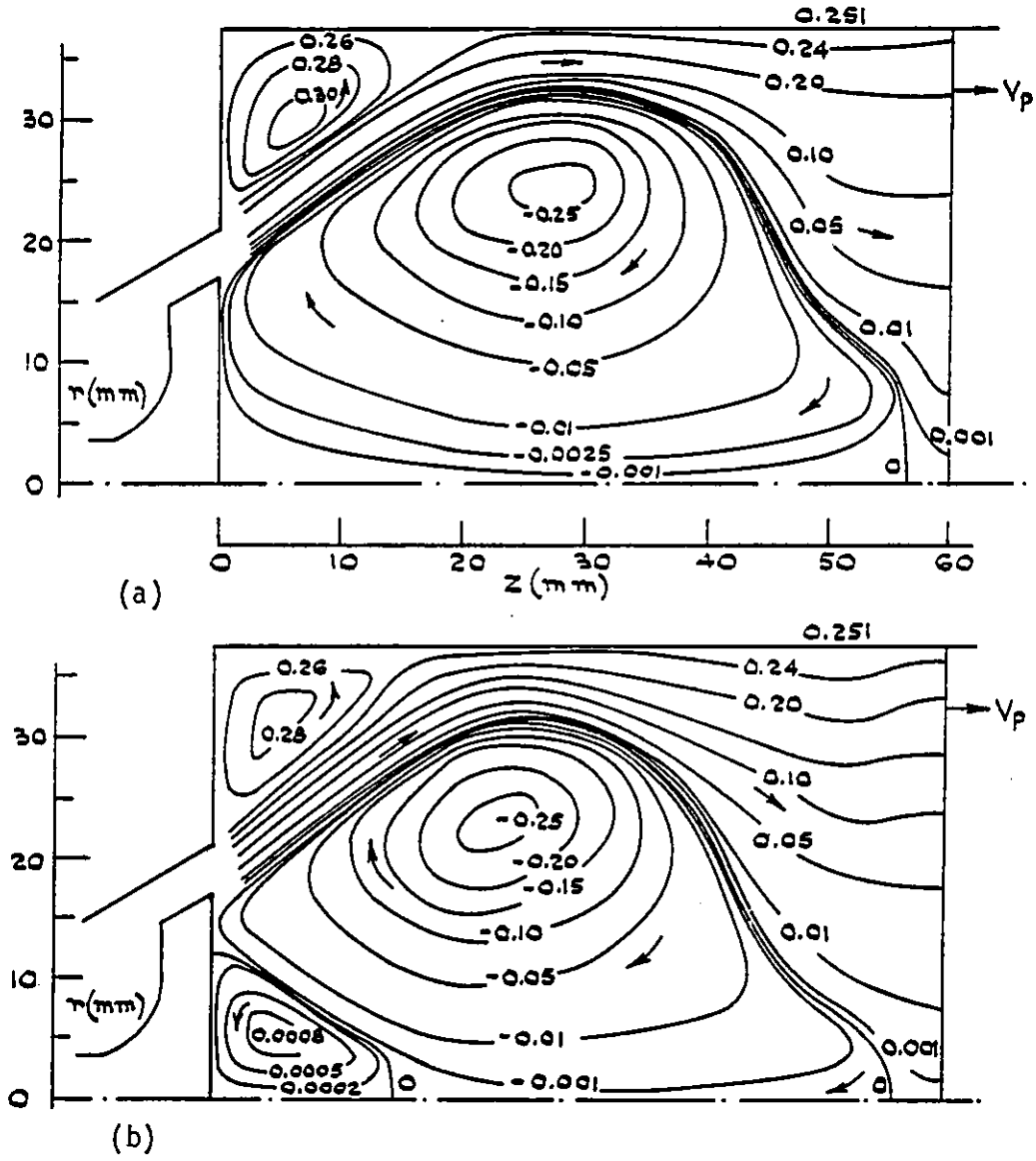


Figure 2.20 Valve inlet: stream function contours at $\theta = 90^0$
(a) 15 degree vanes
(b) 30 degree vanes

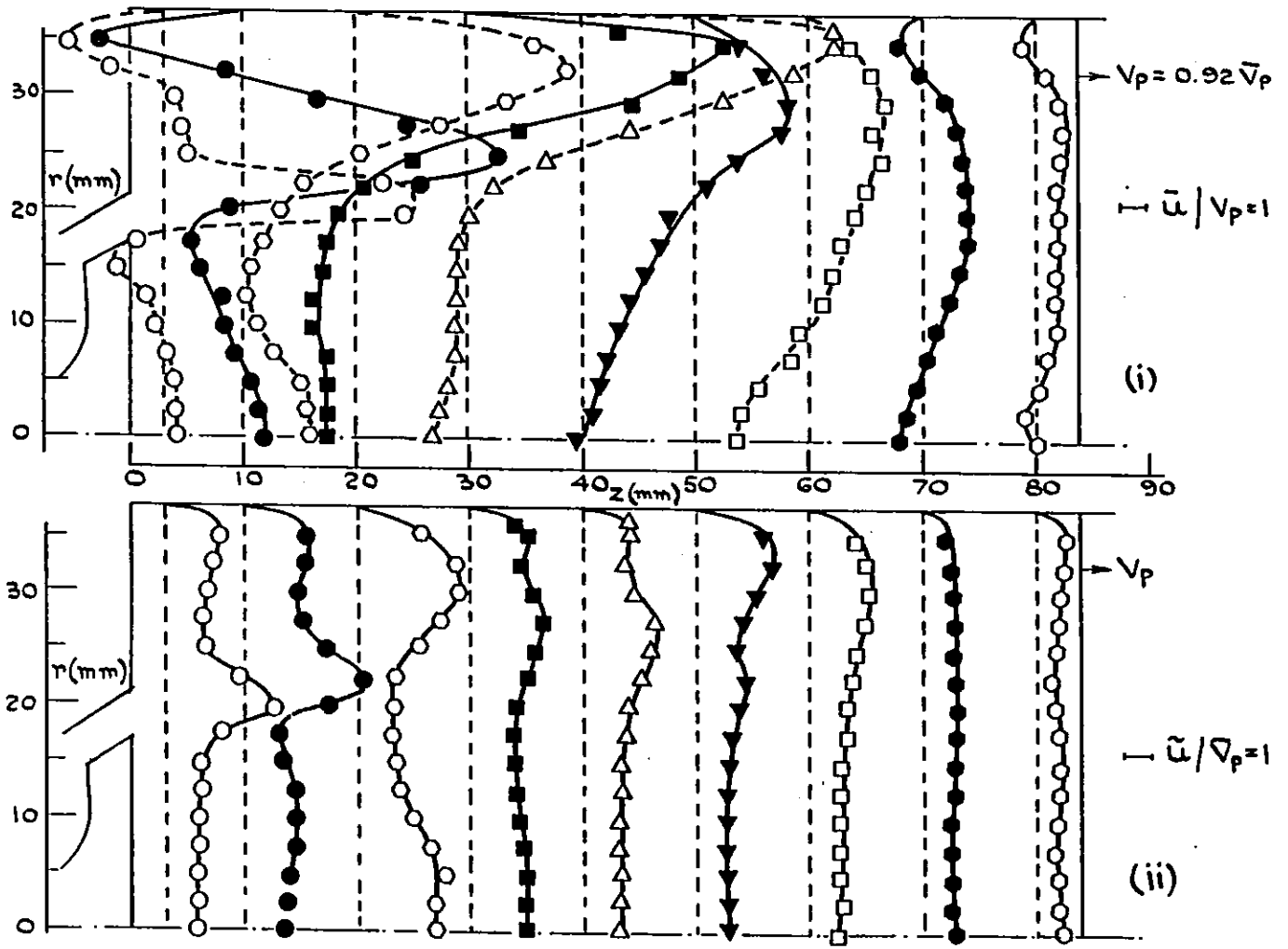


Figure 2.21(a) Valve inlet: profiles of axial velocity at $\theta = 144^0$ - 15 degree vanes

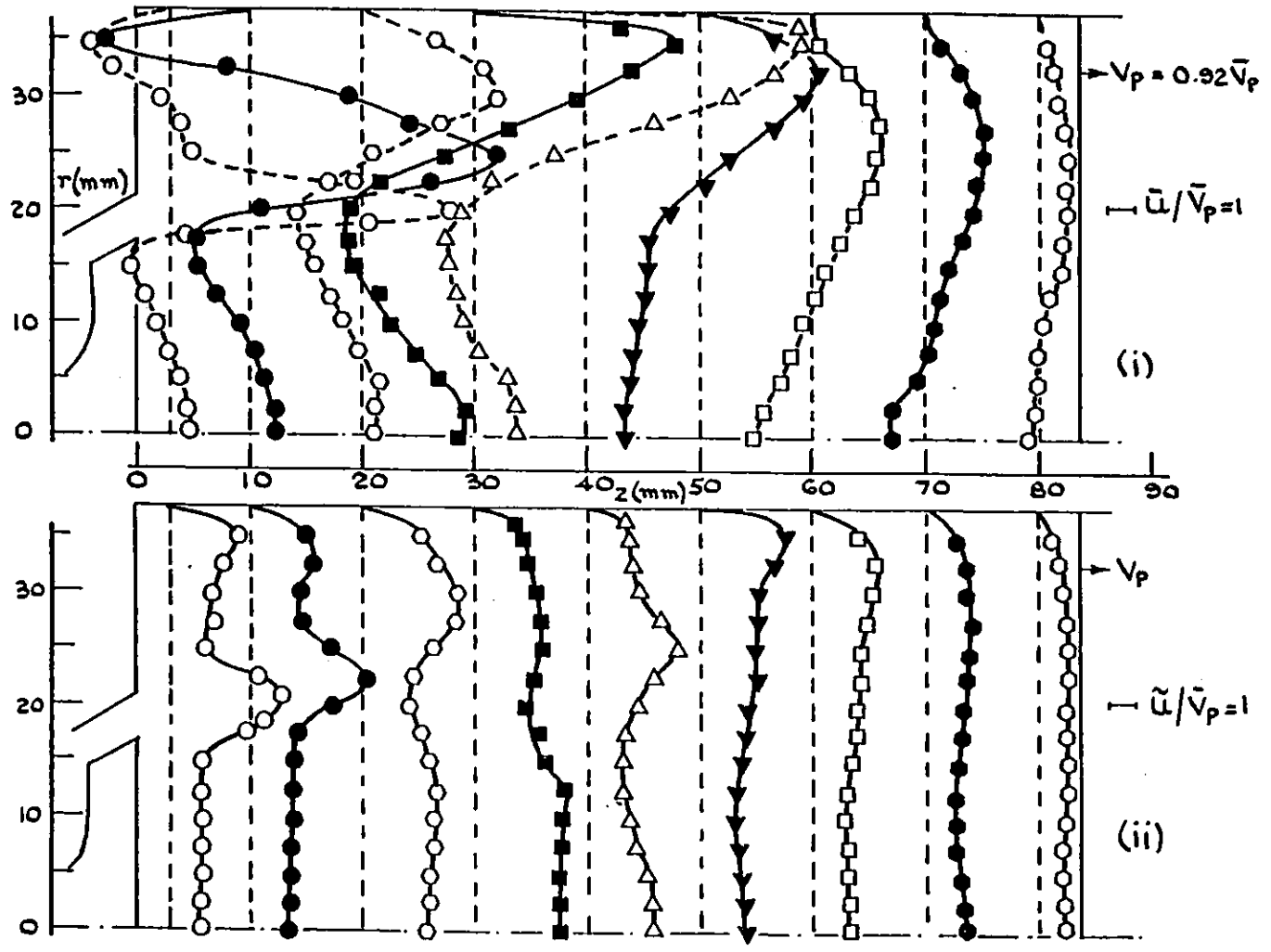


Figure 2.21(b) Valve inlet: profiles of axial velocity at $\theta = 144^0$ - 30 degree vanes

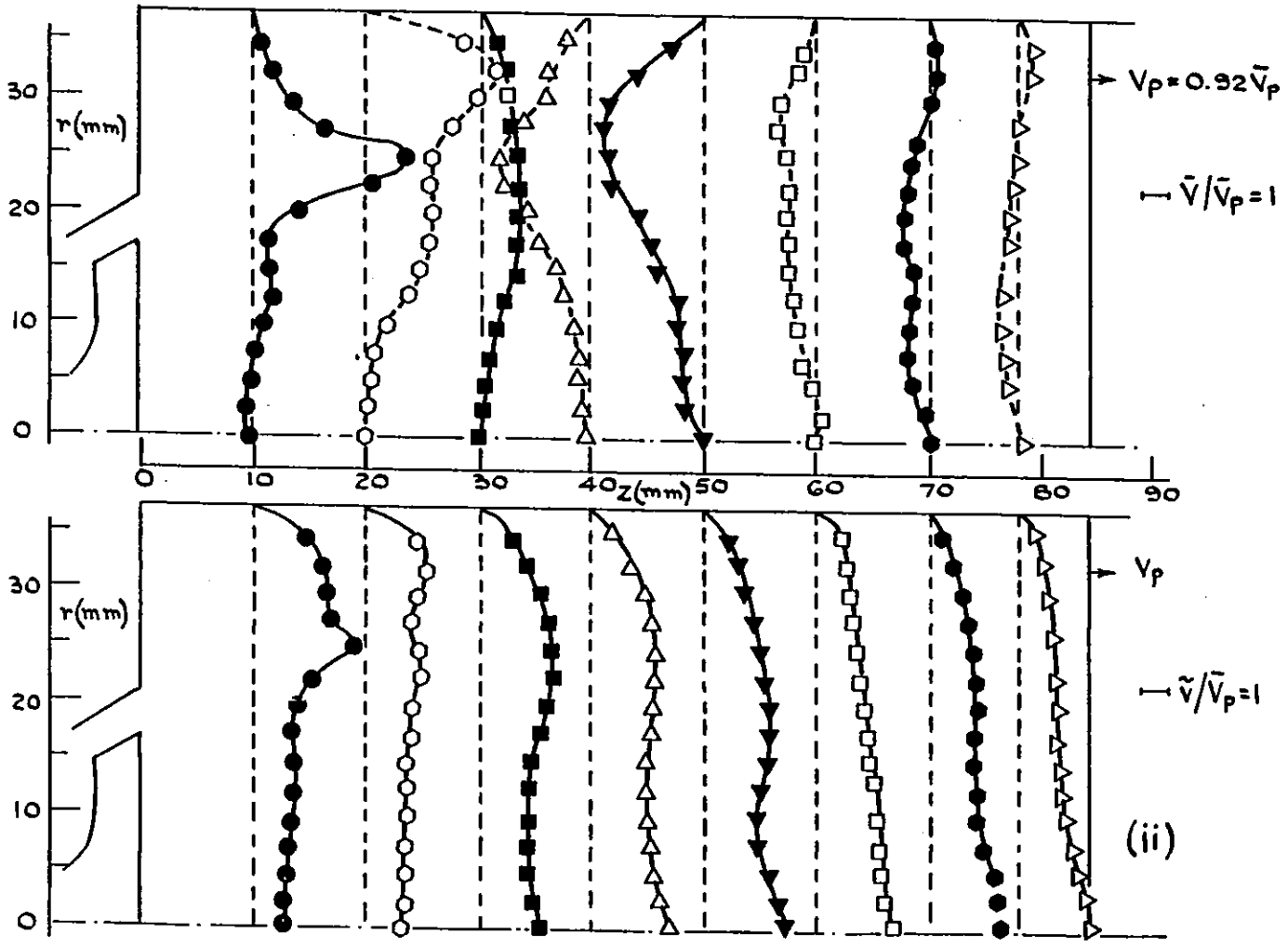


Figure 2.22 Valve inlet: profiles of radial velocity at $\theta = 144^{o}$ - 30 degree vanes

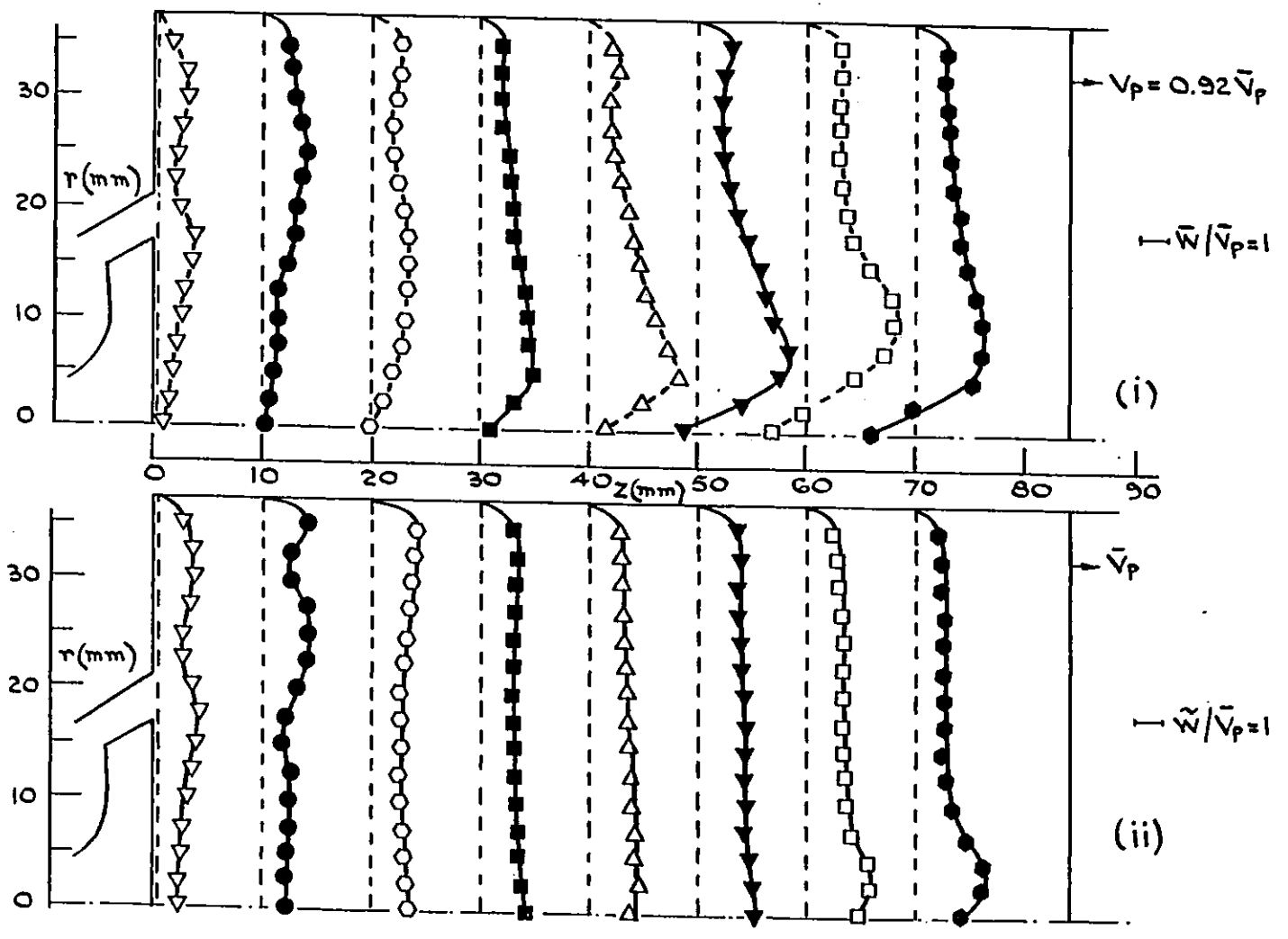


Figure 2.23(a) Valve inlet: profiles of swirl velocity at $\theta = 144^{o}$ - 15 degree vanes

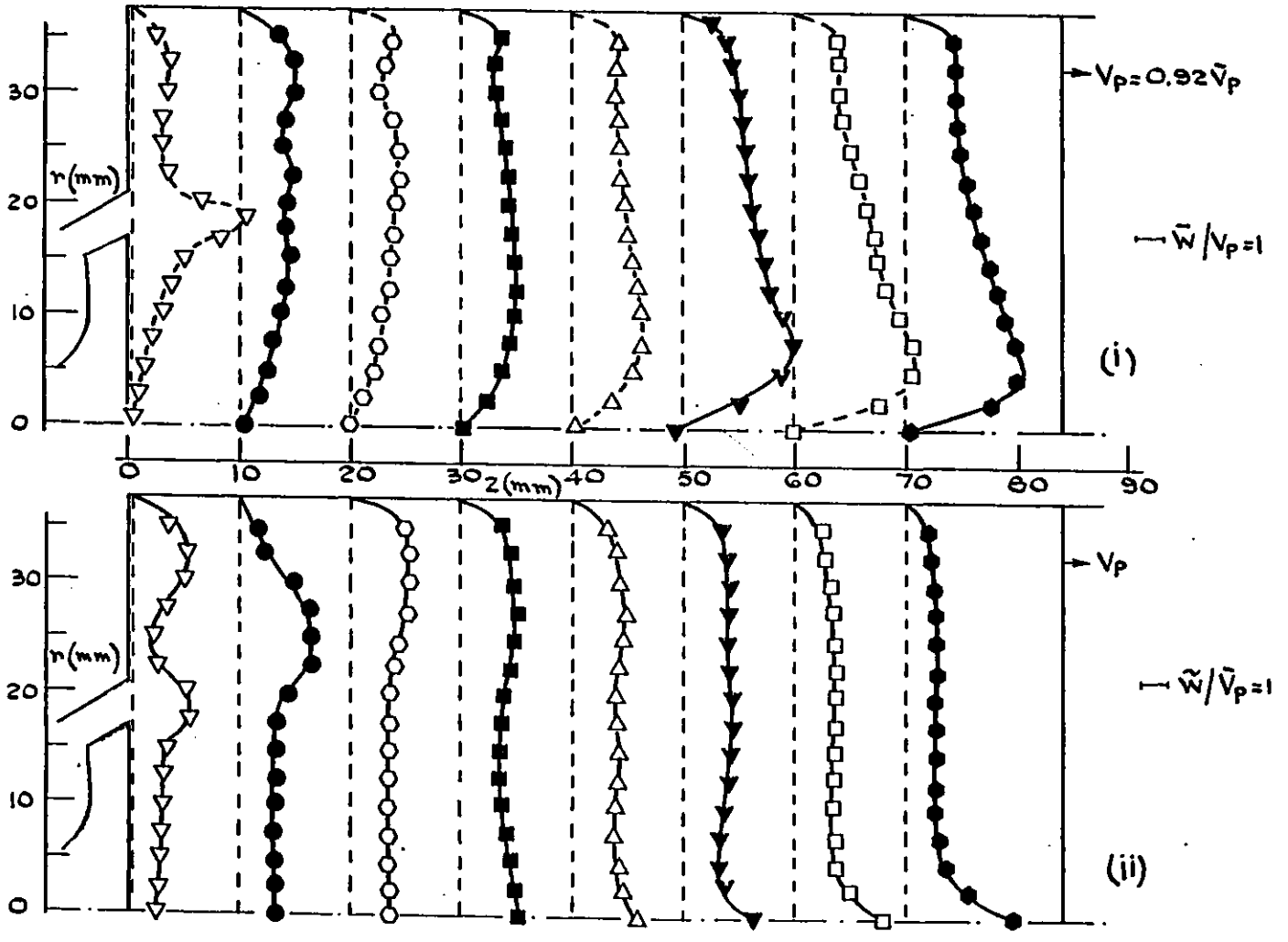


Figure 2.23(b) Valve inlet: profiles of swirl velocity at $\theta = 144^0$ - 30 degree vanes

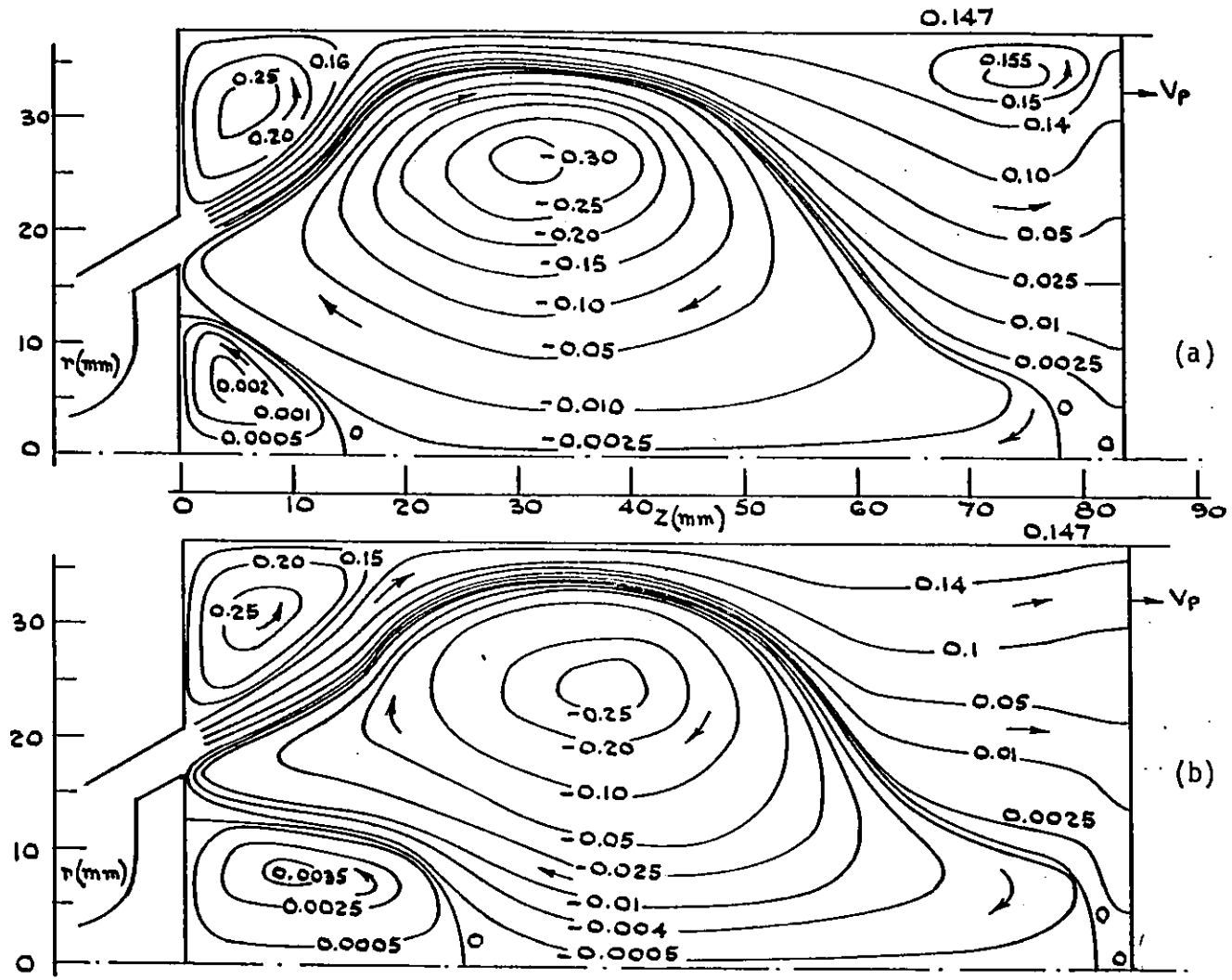


Figure 2.24 Valve inlet: stream function contours at $\theta = 144^{o}$
(a) 15 degree vanes (b) 30 degree vanes

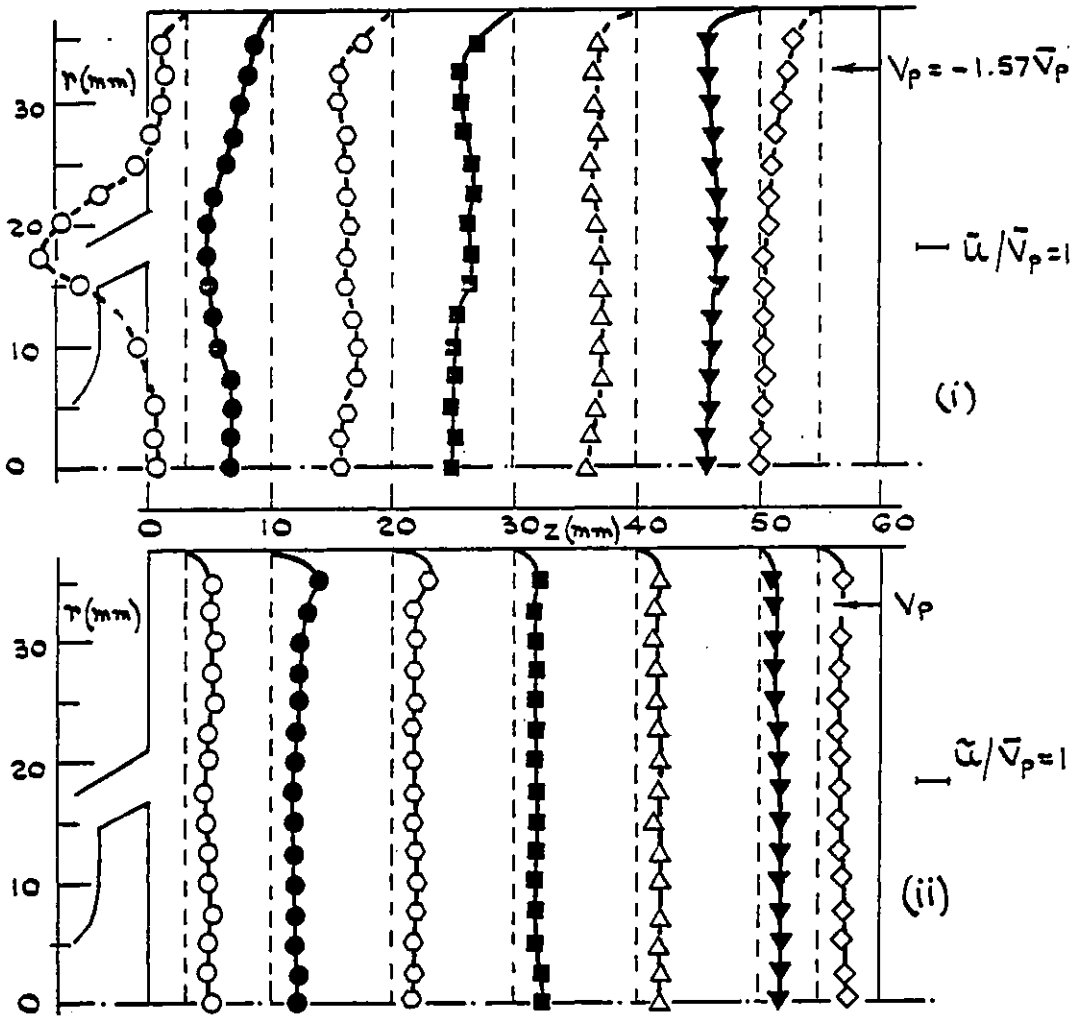


Figure 2.25(a) Valve inlet: profiles of axial velocity at $\theta = 270^{o}$
15 degree vanes

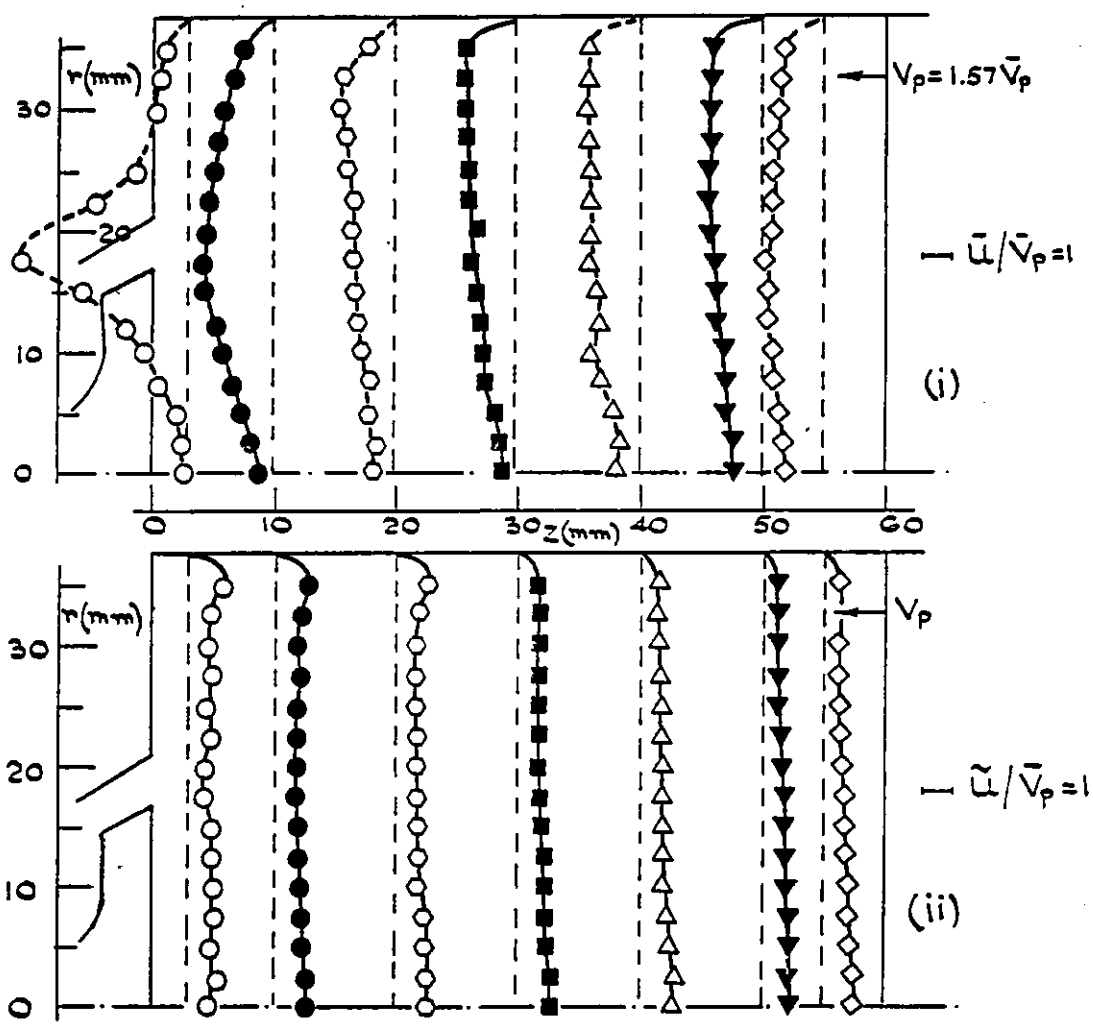


Figure 2.25(b) Valve inlet: profiles of axial velocity at $\theta = 270^0$
30 degree vanes

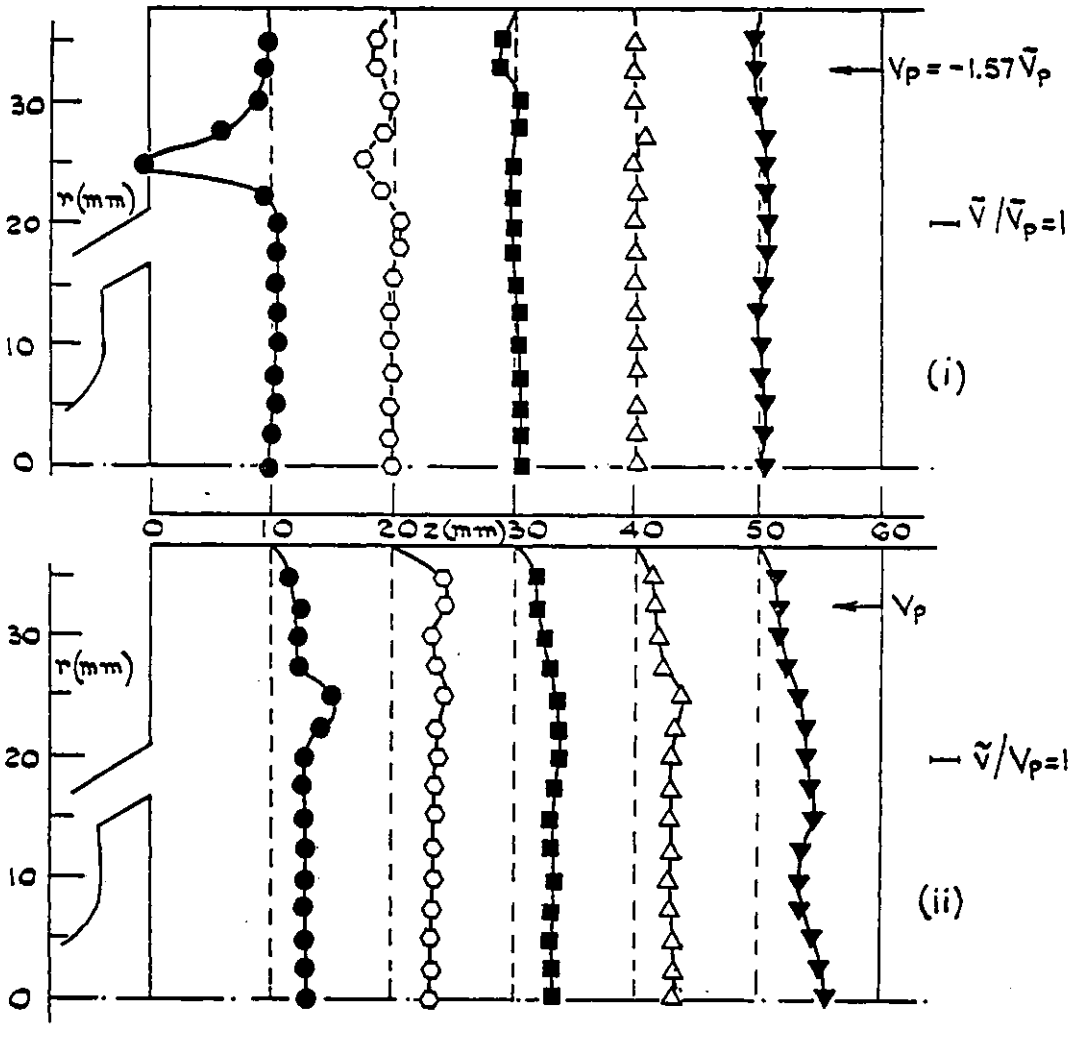


Figure 2.26 Valve inlet: profiles of radial velocity at $\theta = 270^0$
30 degree vanes

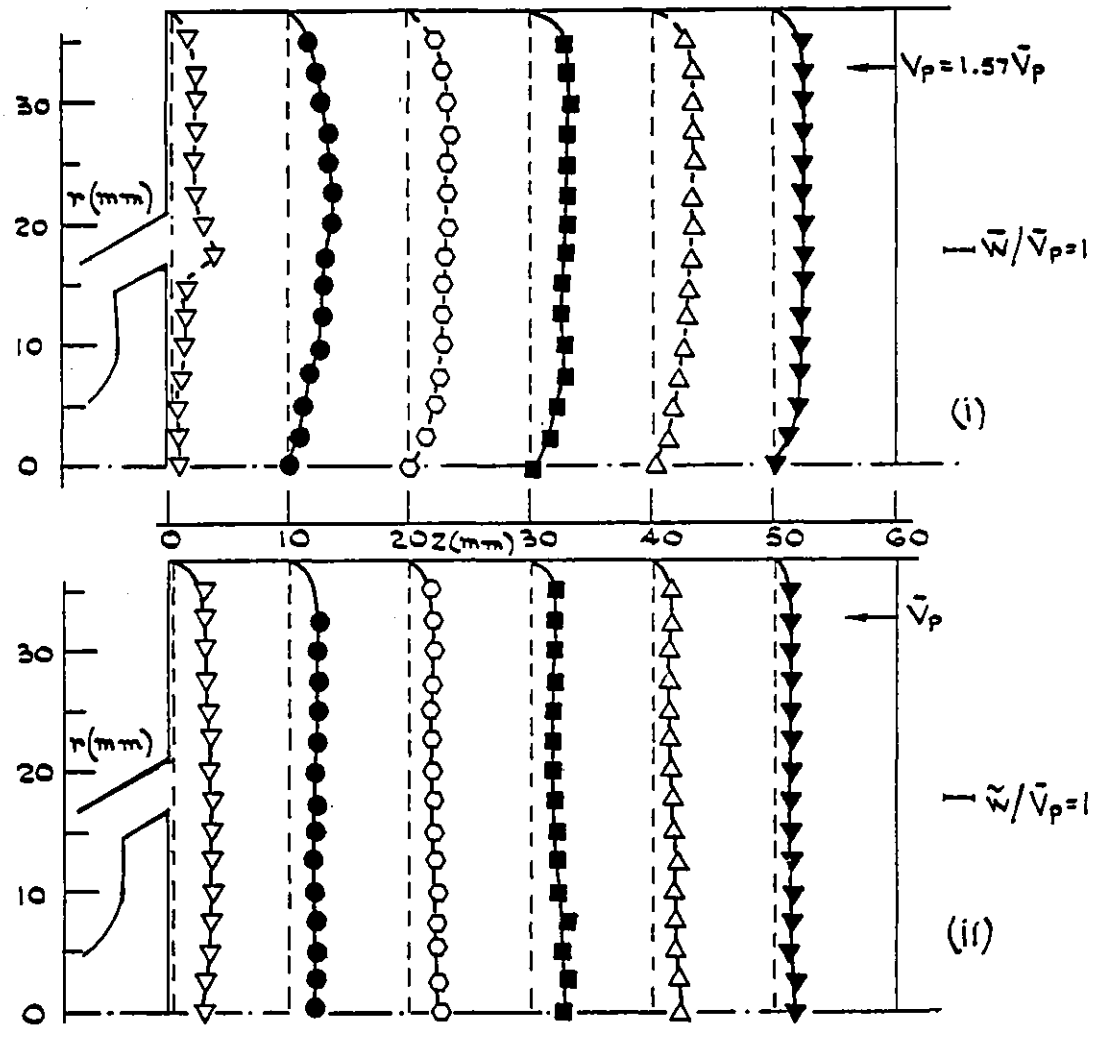


Figure 2.27(a) Valve inlet: profiles of swirl velocity at $\theta = 270^{0}$
15 degree vanes

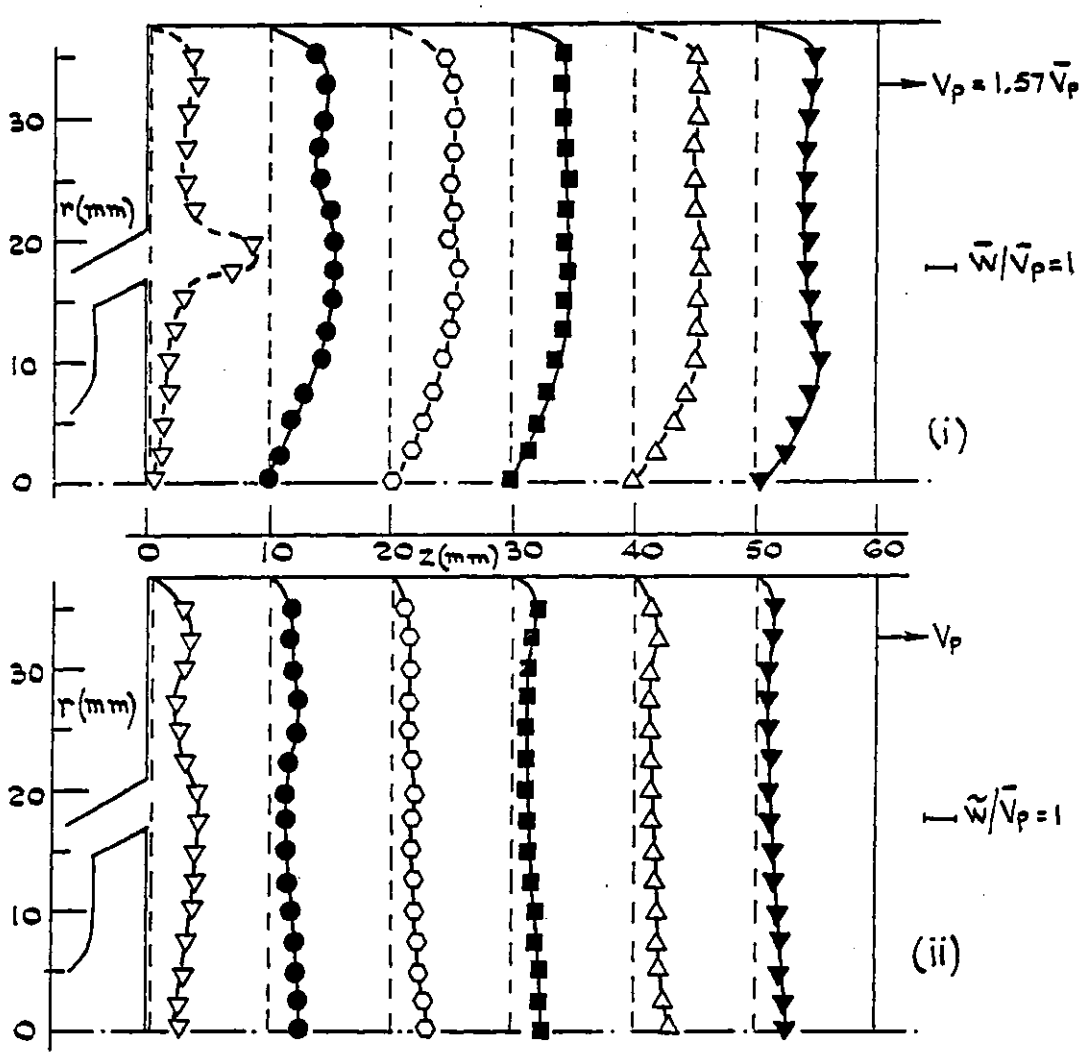


Figure 2.27(b) Valve inlet: profiles of swirl velocity at $\theta = 270^0$
30 degree vanes

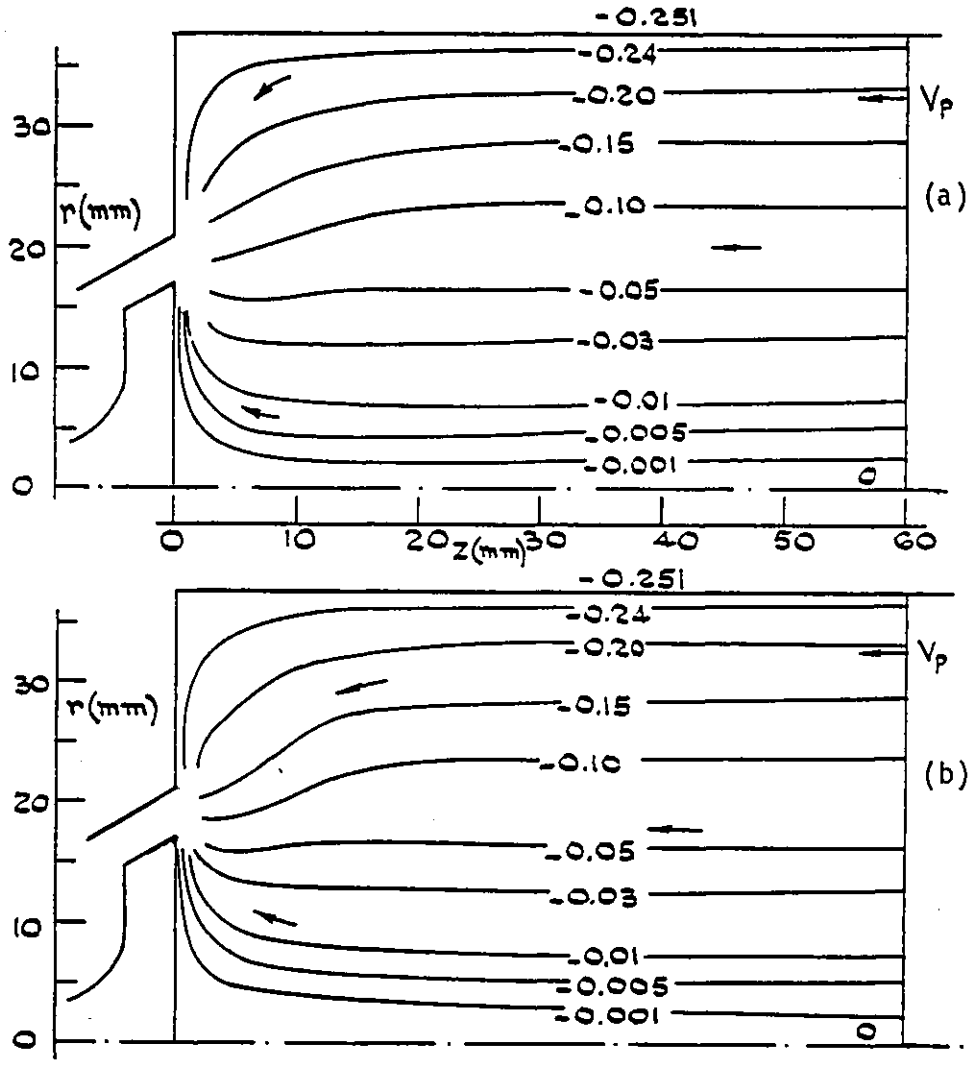


Figure 2.28 Valve inlet: stream function contours at $\theta = 270^{o}$
(a) 15 degree vanes (b) 30 degree vanes

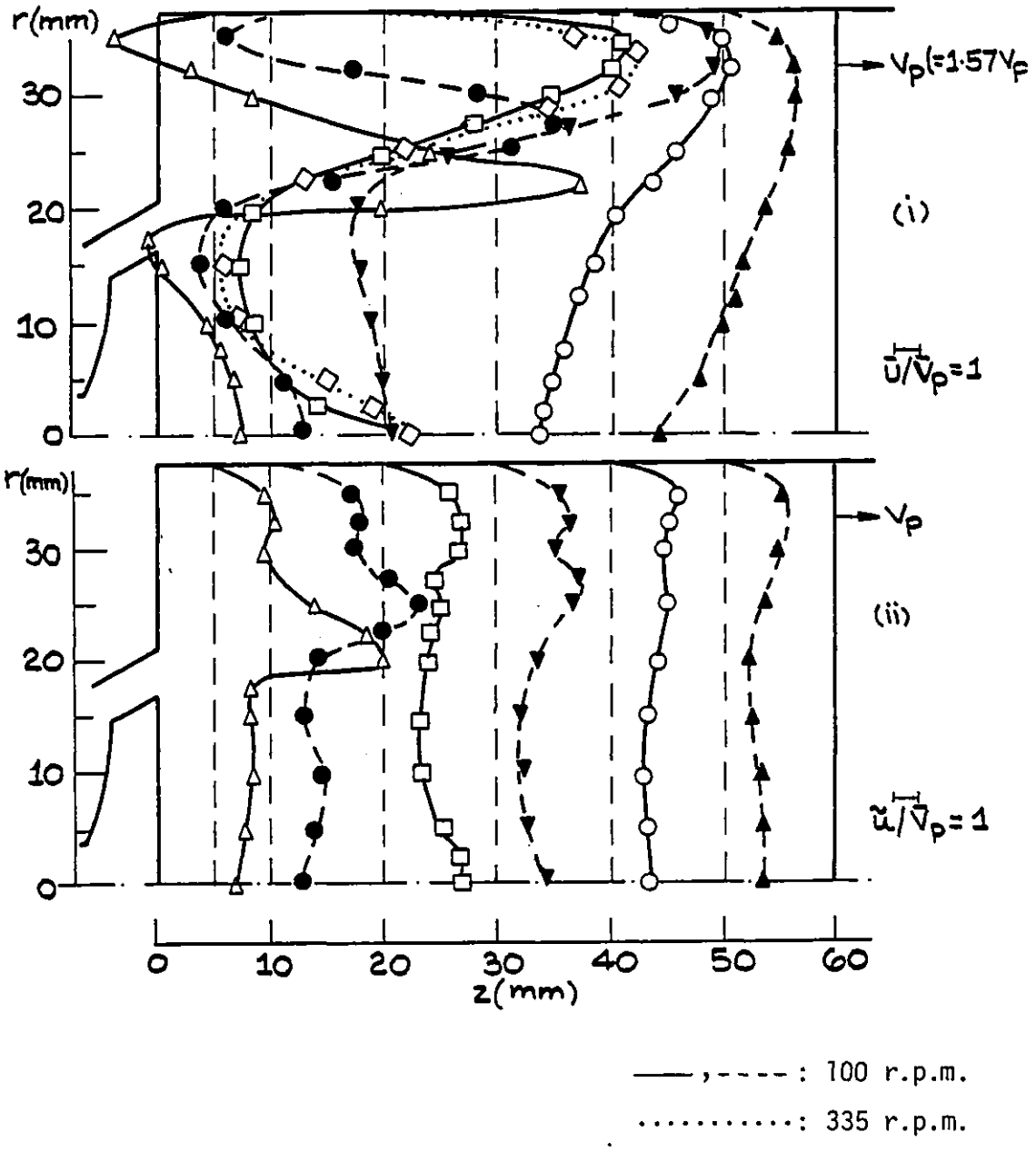


Figure 2.29(a) Profiles of mean and r.m.s. axial velocity at 90 degrees - 100 r.p.m, 335 r.p.m.

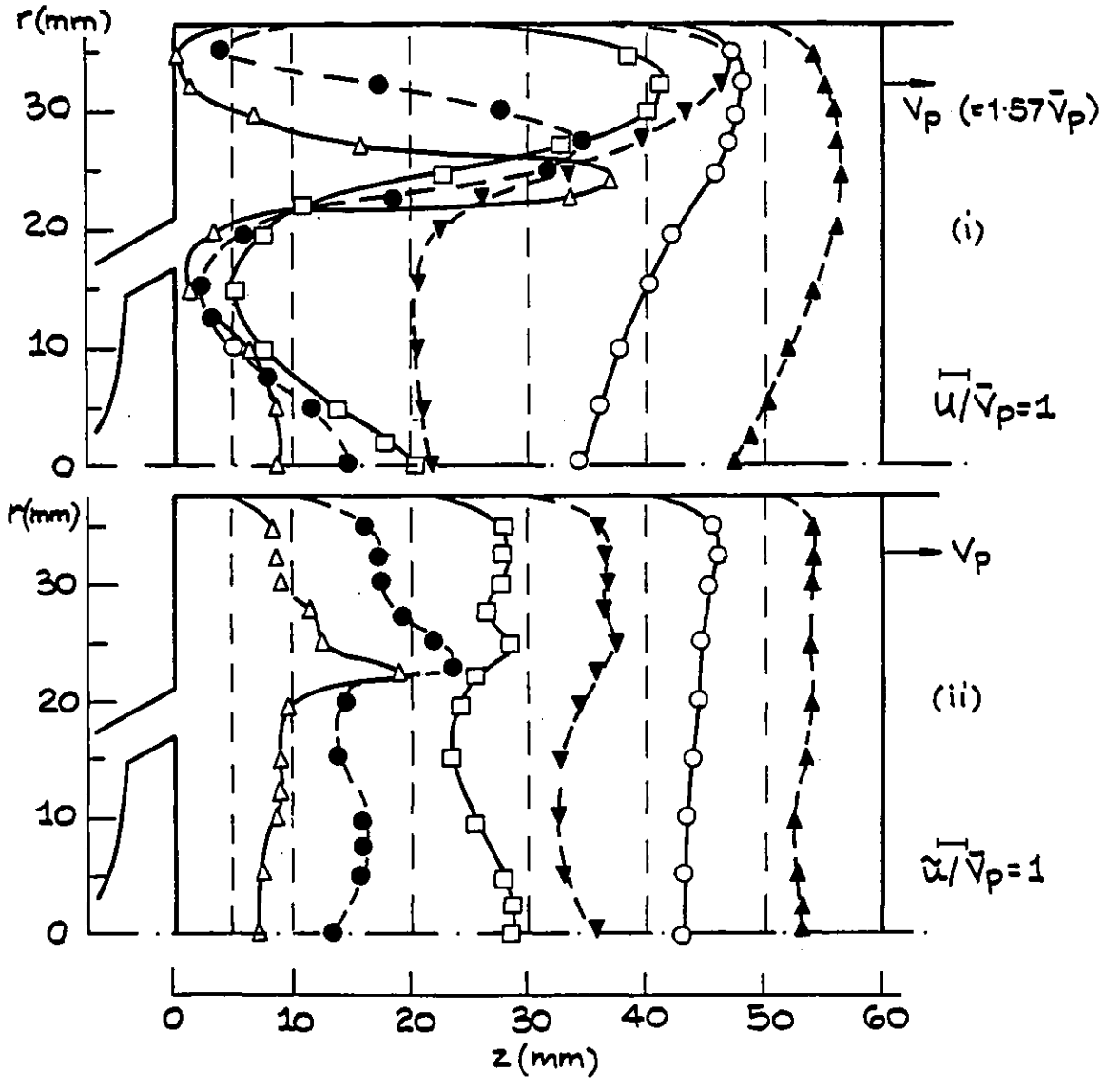


Figure 2.29(b) Profiles of mean and r.m.s. axial velocity at 90 degrees 300 r.p.m.

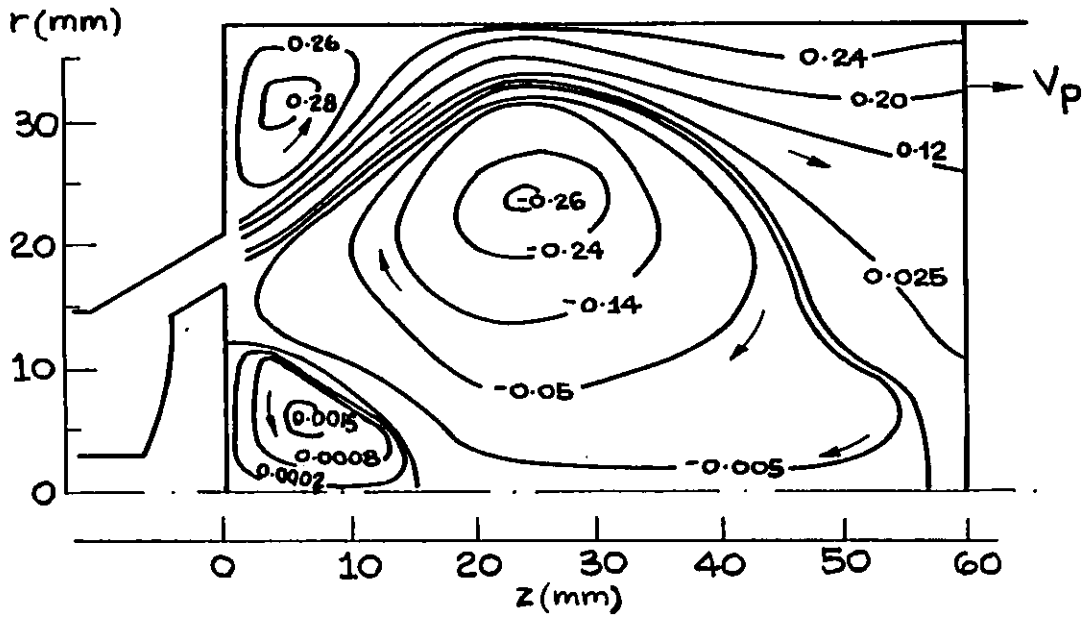


Figure 2.30 Stream function contours at 90 degrees, 100 r.p.m.

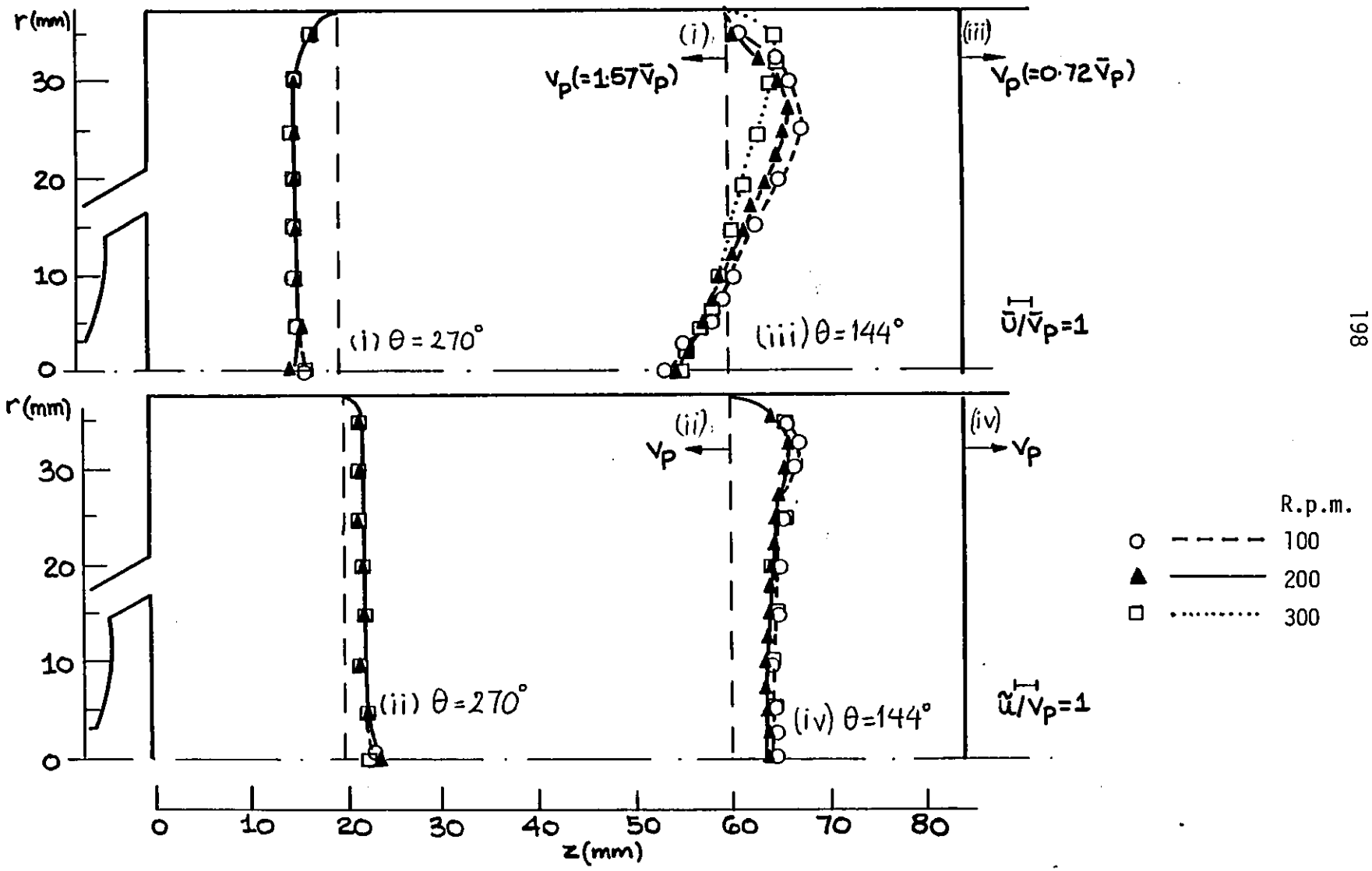


Figure 2.31 Axial component profiles at 100, 200 and 300 r.p.m.

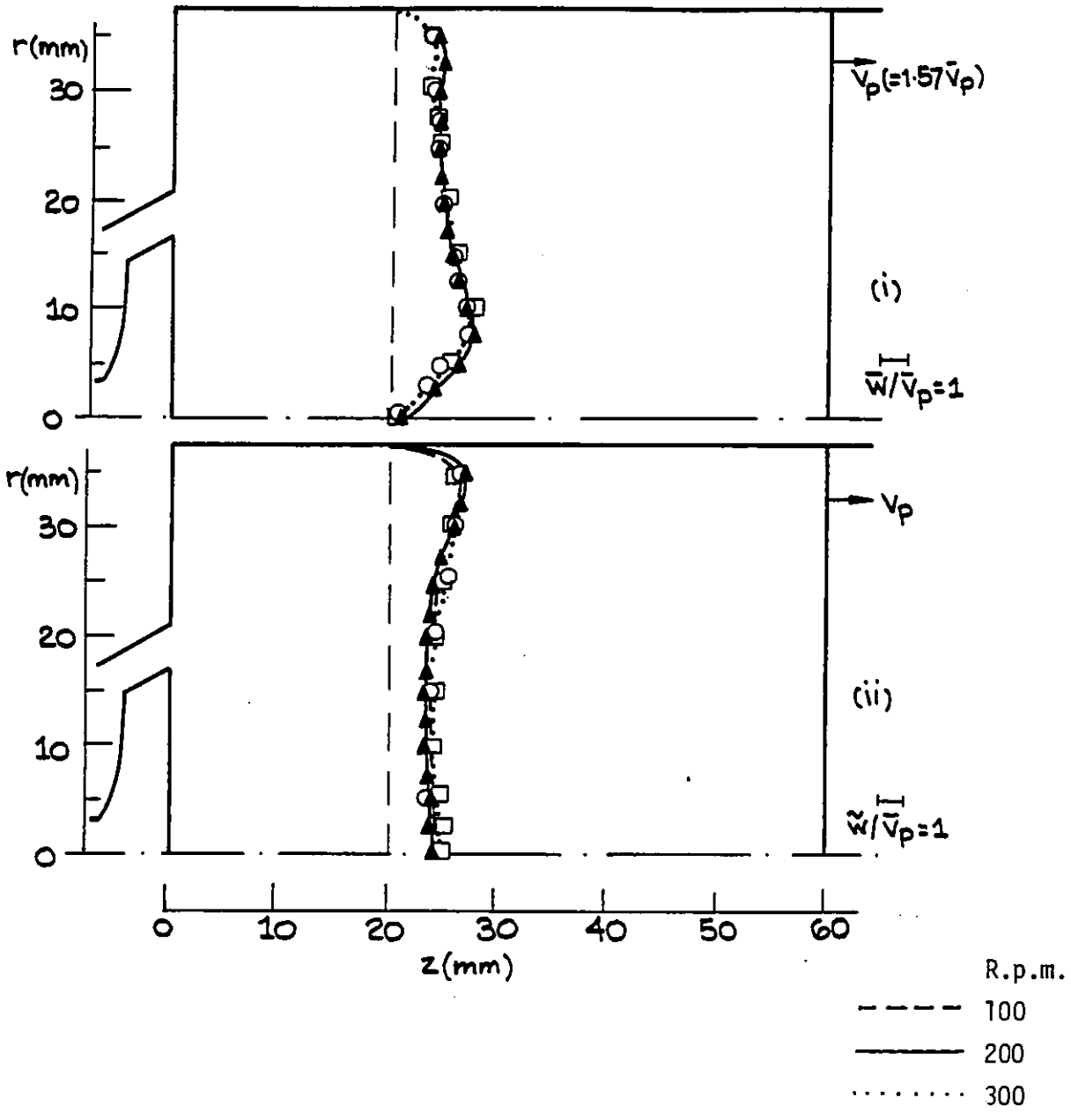


Figure 2.32(a) Swirl component profiles at 100, 200 and 300 r.p.m.
$\theta = 90^{o}$, z = 20mm

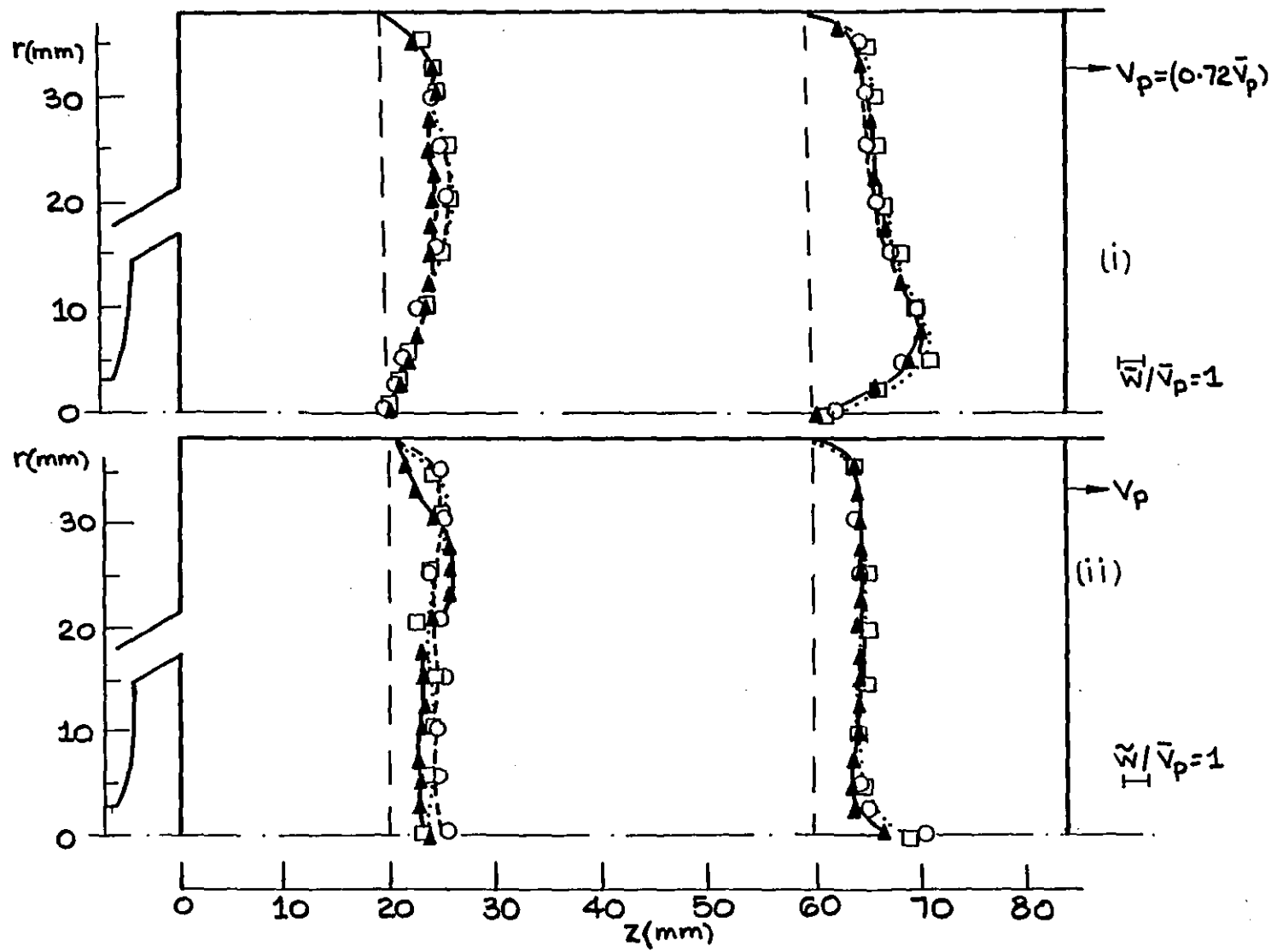


Figure 2.32(b) Swirl component profiles at 100, 200 and 300 r.p.m. - θ = 144°, z = 20 and 60mm

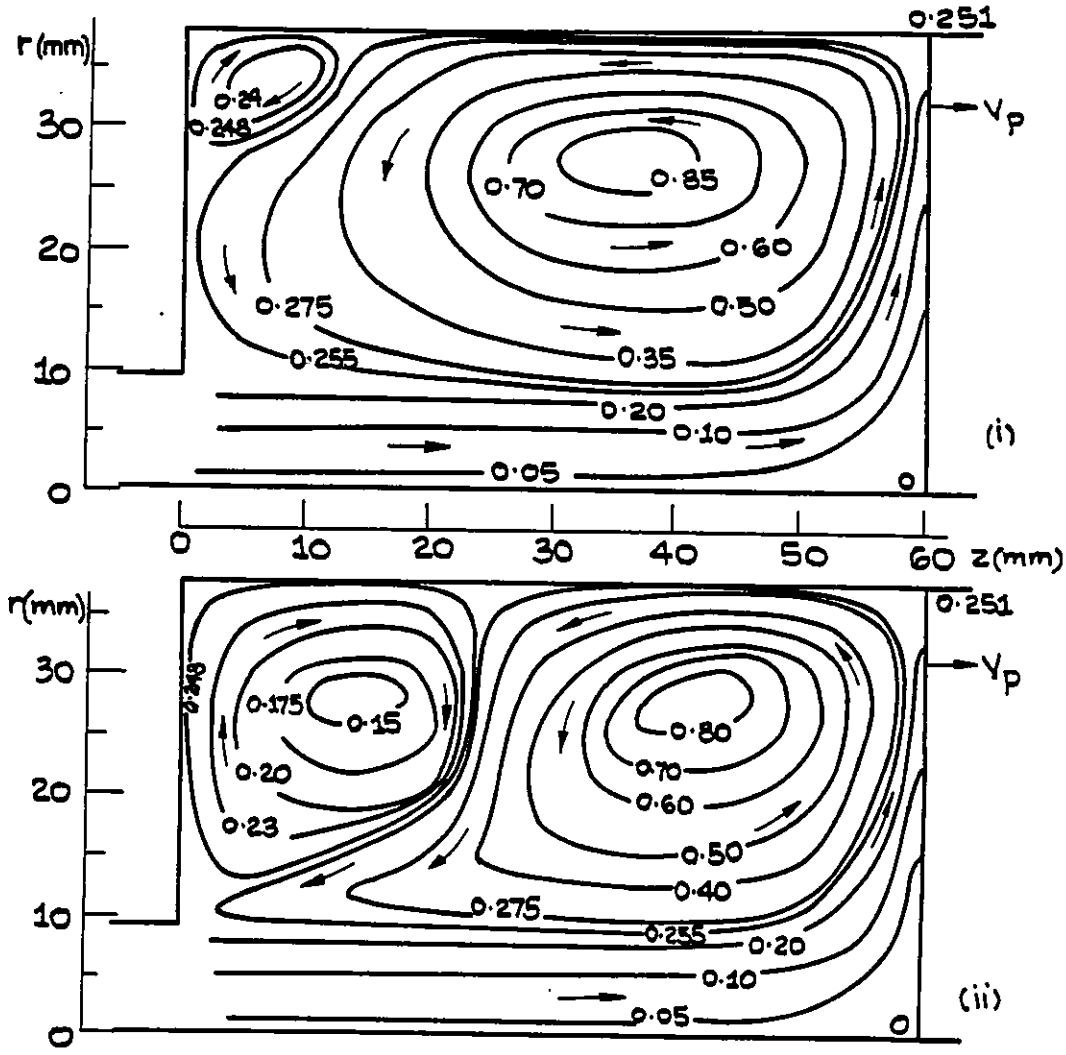


Figure 2.33 Comparison of stream function contours with orifice inlet at 90 degrees

(i) 10 r.p.m.
(ii) 200 r.p.m.

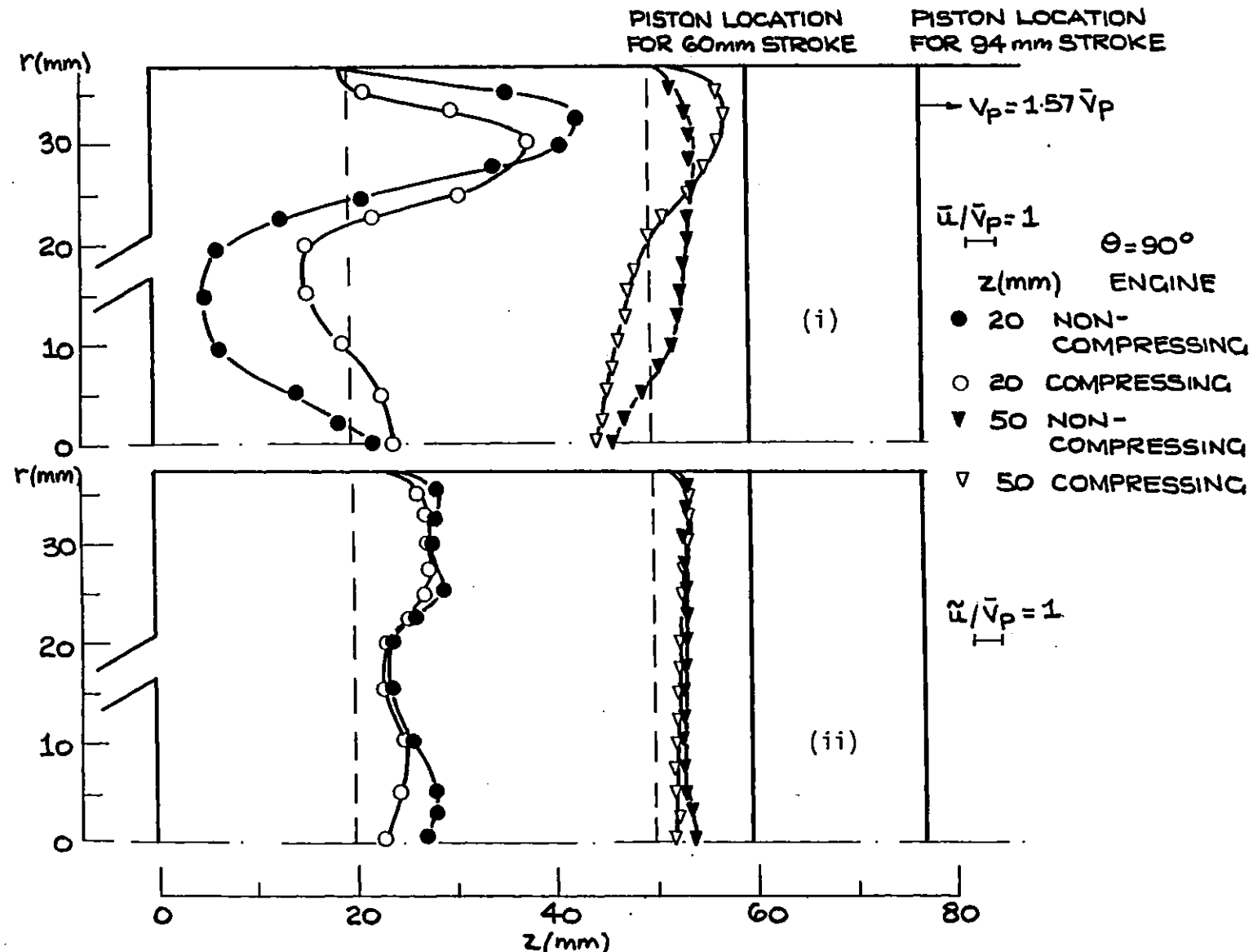


Figure 2.34 Comparison of axial component profiles in the two model engine cylinders without compression

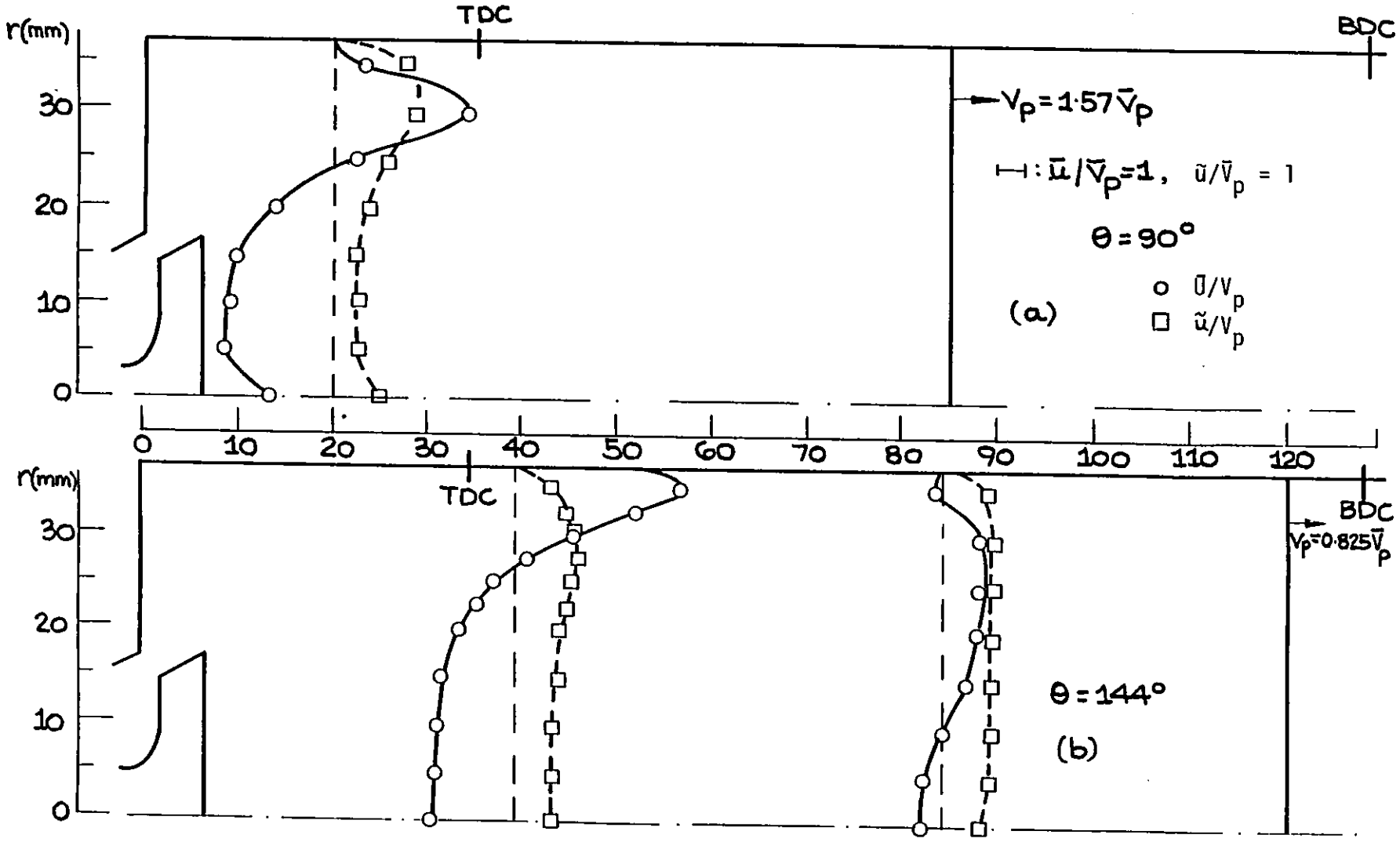


Figure 2.35 Compressing engine: axial mean velocity and r.m.s. component profiles

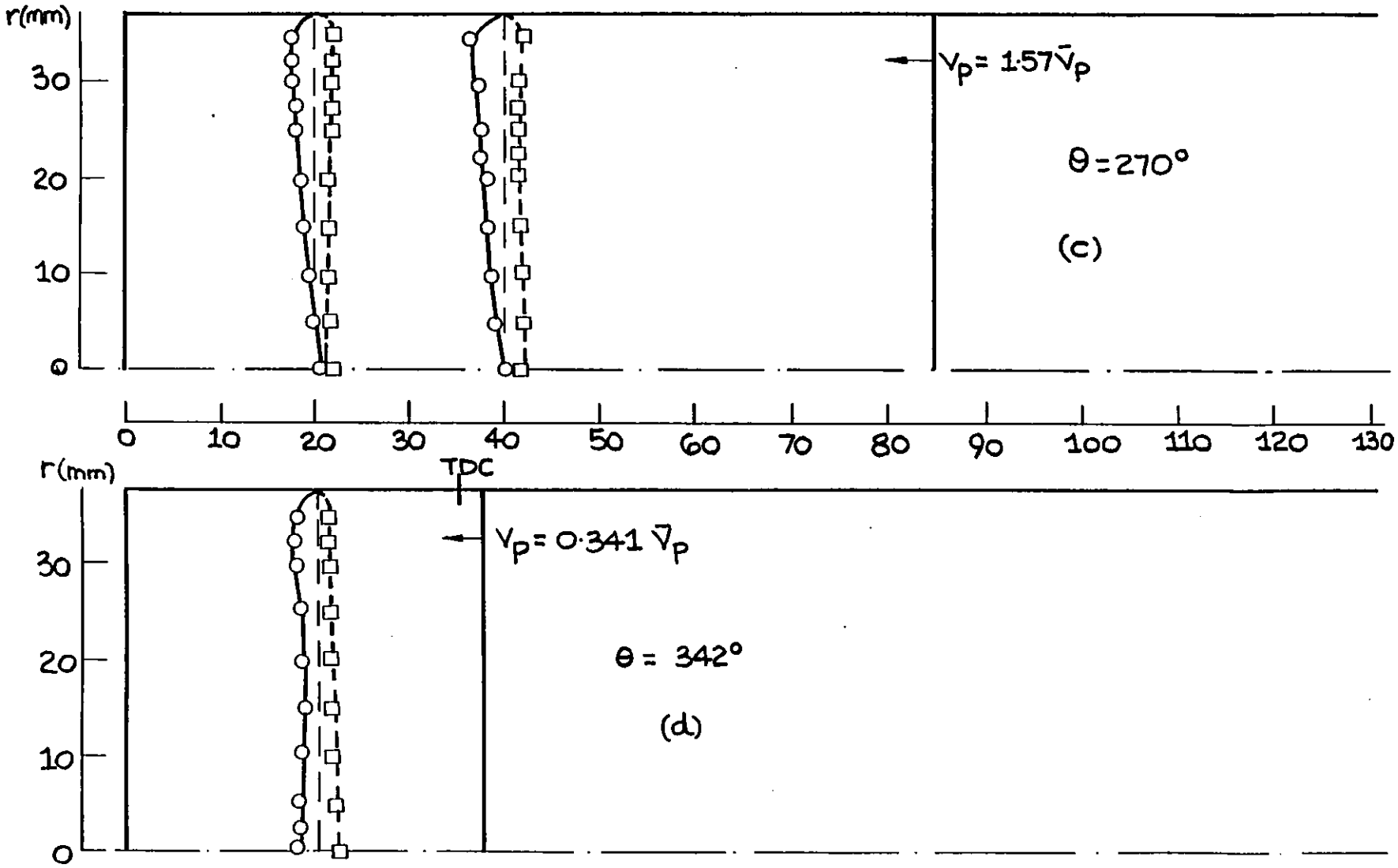


Figure 2.35 (cont.)

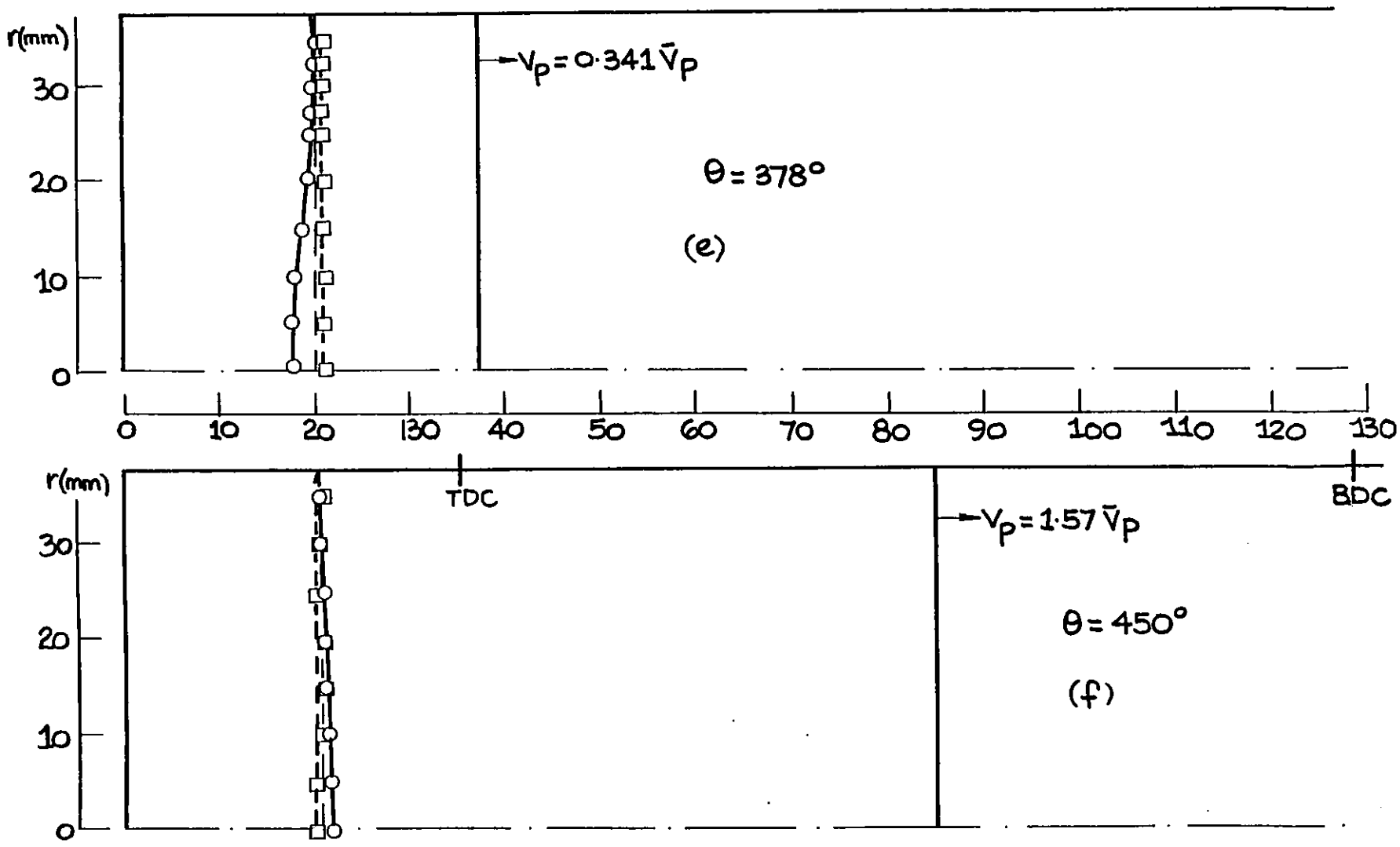


Figure 2.35 (cont.)

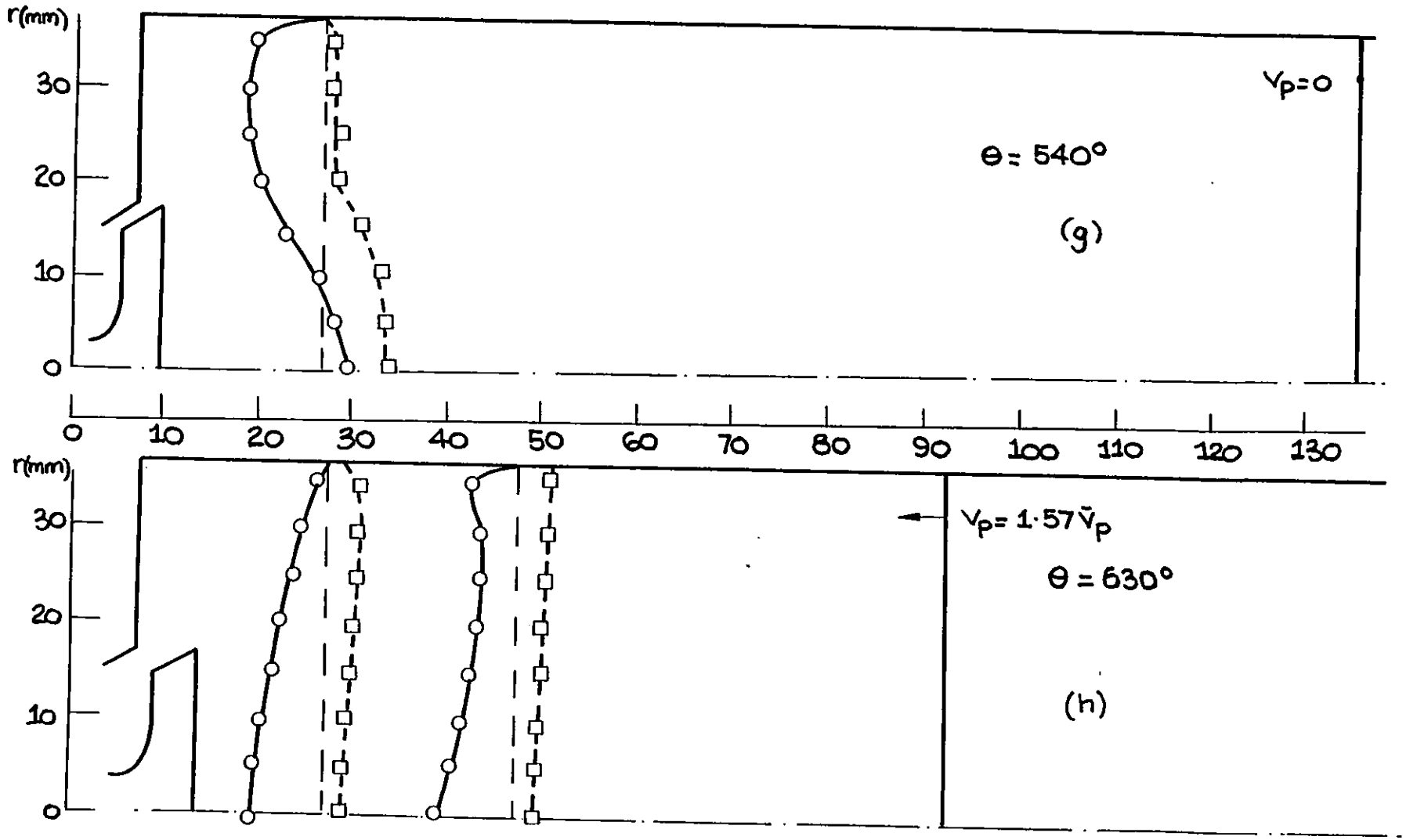


Figure 2.35 (cont.)

CHAPTER THREE

FLOW IN CURVED DUCTS

3.1 Preamble

This chapter describes investigations of the flow in curved ducts relevant to those encountered in internal combustion engine intake passages, in the context of laminar and turbulent developing flows in a square cross-sectioned duct of 90 degree deflection angle and strong curvature. In this way, an investigation of passage flows is made in a simple geometry, which is intended to complement the in-cylinder work of the previous chapter. The geometries normally employed in engine intake design are such that developing rather than fully-developed flows are present at the passage inlet.

A comparative study is made, in conjunction with previous related investigations, of the effect of inlet boundary layer thickness, Reynolds number, curvature and related flow parameters on the mean flow and the turbulence structure. The nature of the flows in curved ducts has been discussed in section 1.1 and sub-section 1.2.2. The flow configuration is described in the following section and the laser Doppler anemometer system, measurement technique and related uncertainties are described in section 3.3. Qualitative information on the flow obtained by flow visualisation is presented in section 3.4 and wall pressure measurements for the turbulent flow case are reported in section 3.5. Measurements of velocity components for the laminar and turbulent flow regimes, and of the associated Reynolds stresses in the turbulent flow case, are presented in section 3.6. The results are discussed and related to previous findings in section 3.7 and their significance for calculations of the flow is assessed. The chapter closes with a summary of the most

important findings.

3.2 Bend flow configuration

The duct was manufactured from Perspex and consisted of a bend of 90 degree deflection angle, of 92mm mean radius of curvature, R_c, and of 2.3 radius ratio, R_r (defined as the ratio of the mean radius of curvature to the hydraulic diameter of the duct given by (3.1)). The upstream and downstream tangents were of 0.3 and 2.0m length respectively. The bend cross-section dimensions, 40 ± 0.1mm x 40 ± 0.1mm, conformed closely to those of the tangents. Within the bend, the method of manufacture restricted optical access so that measurements of only the streamwise and radial components could be made. The geometry is shown in Fig. 3.1 together with the coordinate system adopted.

The bend was installed in a water tunnel with the plane of symmetry located horizontally. Water was employed as the fluid medium so that the same Reynolds number could be obtained with a scale smaller than that obtained with air. A plan view of the water tunnel is shown in Fig. 3.2. The water from a sump tank was pumped to a constant head tank and was subsequently gravity fed into a closed plenum chamber. Perforated screens in the chamber ensured the break-up of large eddies in the flow and a paper honeycomb fitted on the mouth of a 12:1 area ratio contraction provided a uniform entry flow to the upstream tangent. A 0.5mm boundary layer trip was incorporated immediately downstream of the contraction.

The flow rate through the test section was controlled by precision-bore flowmeters located after the downstream tangent. The bulk velocities, V_c, were 1.98cm/s and 1.00 m/s for the laminar and turbulent flows respectively, corresponding to Reynolds numbers of 790 and 40,000, based on the viscosity of water at 20^oC and on the hydraulic diameter of

the duct, defined by:

$$D_H = \frac{4 \times (\text{cross-sectional area})}{(\text{duct perimeter})} \qquad (3.1)$$

so that $D_H = 0.04m$.

A characteristic parameter for curved duct flow is the Dean number, defined by:

$$De \equiv Re \left(\frac{\frac{1}{2} D_H}{R_c}\right)^{\frac{1}{2}} \qquad (3.2)$$

For the laminar and turbulent flows, the Dean numbers were 368 and 18,700 respectively; in turbulent flow, however, Dean number is not a characteristic variable (Schlichting, 1955, White, 1929). Ito (1959) has found the parameter

$$De \left(\frac{\frac{1}{2} D_H}{R_c}\right)^{1.5} \qquad (3.3)$$

to correlate better with resistance coefficient data in turbulent curved duct flows than the Dean number. The above parameter has a value of 1890 for the present turbulent flow.

The temperature of the water was maintained at $20^{o} \pm 2^{o}C$ for all the experiments; heat gains from the pump were compensated by adding fresh water and draining part of the overflow. Within the maximum temperature variation of $4^{o}C$, the ratio of the viscosity over the density (in centipoises /g c^{-3}) is 1.0 ± 0.2 (Spiers, 1962), and well below the viscosity immunity ceilings specified for the laminar and turbulent flow rotameters (Fischer and Porter, FP-½"-27-G-10 tube with ½"-GSVT-45 float and FP-2"-27-G-10/80 tube with 2"-GNSVT-96(T62) float respec-

tively) as 5.1 and 3.3.

3.3 Measurement system and technique

The laser Doppler anemometer used for the measurements of this chapter is described in the two following sub-sections and the measurement uncertainties involved are stated in sub-section 3.3.3. Similar systems employing frequency tracking signal processing in flows with water as the medium have been used and described extensively by Melling (1975) and Humphrey (1977). As details of systems and techniques have already been given in section 2.3, only new information related specifically to the anemometer employed for the measurements of this chapter is given in this section.

3.3.1 Optical system

The laser Doppler anemometer operated in the forward scatter fringe mode and the optical system is similar to that described in the previous chapter (sub-section 2.3.1) employing the two-th diffraction grating. For compactness of the system, the optical axis was turned through 90 degrees with a mirror, flat to one-tenth of the wavelength of light. The system is shown in Fig. 3.3(i) with the sensitivity vector of the anemometer in the radial direction. Figs. 3.3(ii) and (iii) show photographs of the optical system and of the scattering volume in the bend respectively. The principal characteristics of the system are shown in Table 3.1. Frequency shifting of the laser light was not employed.

The local streamwise and radial components of velocity, and for turbulent flow the fluctuating components $\tilde{u}$, $\tilde{v}$ and the cross-correlation $\overline{\tilde{u}\tilde{v}}$, were obtained by making measurements of the Doppler frequency in

X-r planes in three directions (0^o, $\pm 45^o$) relative to the local streamwise direction at each measurement point. These frequencies were resolved into streamwise and radial components in the manner described by Melling (1975). The third component of velocity, W, and the associated quantities $\tilde{w}$ and $\overline{uw}$, were measured in a similar manner in the downstream tangent at $X_H = 2.50$, with the three measurements being made in the X - z plane. The beams entered the test section through the side wall for the X - r plane measurements and through the outer ($r^* = 0$) wall of the downstream tangent for the X - z plane ones.

TABLE 3.1

Characteristics of the optical arrangements	Laminar Flow	Turbulent Flow
Focal length of imaging lens (mm)	300	200
Half-angle of intersection	5.9^o	9.3^o
Fringe separation (line-pair spacing) (μm)	3	2
No. of fringes in measuring volume observed by photomultiplier	52	84
Intersection volume diameter calculated at $1/e^2$ intensity (mm)	0.158	0.167
Intersection volume length calculated at $1/e^2$ intensity (mm)	1.500	1.357
Photomultiplier pinhole diameter (mm)	0.33	0.50
Transform constant (MHz/ms^{-1})	0.324	0.510

Naturally occurring water contaminants provided scattering centres in the flow, but the flow was seeded with minute quantities of milk to increase the scattering particle concentration and thereby increase the particle arrival rate.

3.3.2 Signal processing system

The Doppler signals were detected by a photomultiplier tube (E.M.I. 9658B) and demodulated by a frequency tracker (Cambridge Consultants CC01). Frequency tracking demodulators operate in the frequency domain, providing real time demodulation of the Doppler signals and yielding an analogue signal continually proportional to the velocity of the fluid. The operation of the frequency tracker employed for the present work has been described in detail by Taylor (1981). The voltage analogue of the Doppler frequency was averaged to give a mean (DISA model 52B30 True Integrator) and r.m.s. voltage (DISA model 55D35 R.m.s. Voltmeter), which were read on a digital voltmeter (Solartron LM1450). The signal processing system is shown schematically in Fig. 3.4.

The averages were carried out over 50s, so that approximately 10^5 Doppler signals contributed to a measurement in the turbulent regime and 2,000 in the laminar regime. Each measurement was repeated five times to establish the reproducibility of the results.

3.3.3 Measurement uncertainties

The main contributions to measurement errors were from velocity gradient broadening (see sub-section 2.3.4) in the steep gradient regions near the walls, and for the $\bar{V}$, $\bar{W}$, $\overline{uv}$ and $\overline{uw}$ measurements, from the systematic error in the angle of the orientation of the measurement. Away from the wall regions with the gradients associated with the boundary layers, velocity broadening errors were negligible.

A possible source of error which is not important in the frequency counting system of the previous chapter but can be significant in tracking systems is finite transit time broadening. This broadening of the Doppler spectrum arises because signals from individual scattering particles last only for the time required to traverse the scattering

volume and the random arrivals and departures of individual particles into and out of the scattering volume cause phase and frequency fluctuations which give a finite width to the measured Doppler spectrum. An estimation of the magnitude of finite transit time broadening for the present turbulent flow case (see Durst et al, 1976, p.205), shows that the broadening effect for a particle crossing all 84 fringes observed by the photomultiplier is only 0.75 percent of the measured mean frequency; the quoted figure increases as the number of crossings is reduced, but even for only 40 crossings, it is 1.5 percent of the measured frequency.

Broadening of the Doppler spectrum can also occur due to instrument noise as the analogue output of the tracker has a noise component associated with it. This broadening was measured directly with a signal generator. It is negligible near the centre frequencies in any frequency range of the instrument and care was taken in the measurements to operate the tracker in the mid-range region. The accuracy (systematic error) of the voltage output of the tracker is one percent of full scale deflection (according to manufacturer's specification and certified by tests), and corresponds to a systematic error of 0.02 V_c which is removed by calibration. The departure from linearity of the tracker transfer function is entirely negligible. Random errors in the true integrator output are ±1 percent of the mean voltage measured. Random errors in the output of the r.m.s. unit are 1 percent of full scale deflection corresponding to a maximum of 3 percent for the smallest value measured in any one range of the unit.

Detailed analyses of the errors involved in frequency tracking of water flows are given by Melling (1975) and Melling and Whitelaw (1976b). Table 3.2 summarises the estimates of accuracy (systematic error) and precision (random error) associated with the measurements presented.

All positional and finite transit time, mean velocity gradient and instrument noise errors have been included in the estimates, together with those resulting from the one percent precision of the true integrator and r.m.s. unit instruments.

TABLE 3.2

ESTIMATES OF MEASUREMENT UNCERTAINTIES

Quantity	Systematic error	Random error
X_H	±0.5 mm	±0.02 mm
r^*, z^*	±0.2 mm	±0.02 mm
θ	$\pm 0.3^o$	$\pm 0.17^o$
ϕ	$\pm 0.05^o$	nil
V_c (laminar)	±0.8%	±0.8%
V_c (turbulent)	±1/2%	±½%
h (manometer fluid height)	±0.5 mm	±0.5 mm ($0.009\frac{1}{2}\rho V_c^2$)
U/V_c	up to 2½%	±1½%
V/V_c	up to 3%	±1½%
W/V_c	up to 3%	±1½%
$\tilde{u}/V_c$	up to 3%	±1 to ±3%
$\tilde{v}/V_c$	up to 3%	±1½% to ±5%
$\tilde{w}/V_c$	up to 3%	±1½% to ±5%
$\overline{uv}/V_c^2$	±1½%	±2½% to ±8½%
$\overline{uw}/V_c^2$	±1½%	±2½% to ±8½%
k/V_c^2	±7%	±8%

As the beams entered the test section through plane surfaces, corrections to the location of the scattering volume were made to account only for the apparent depth and wall thickness refractions. The error in the frequency-to-voltage transfer constant can be deduced from the error in the measurement of the angle ϕ to be less than 0.5%.

Turbulent broadening from velocity fluctuations within the control volume can be calculated by (George and Lumley, 1973)

$$\sigma_T^2 \approx \frac{2}{15} k^2 \sigma_3^2 \frac{\varepsilon}{\nu} \tag{3.4}$$

where σ_3 is an appropriate control volume dimension and ε the rate of dissipation of the kinetic energy of turbulence. Exact calculations of σ_T^2 are difficult, but an estimate of ε correct to approximately one order of magnitude can be obtained using the Kolmogorov length micro-scale, η, given by (Tenekes and Lumley, 1972)

$$\frac{\eta}{\ell} \approx (Re)^{-3/4} \tag{3.5}$$

where ℓ is a typical flow dimension for the largest eddy size, and

$$\eta \equiv \left(\frac{\nu^3}{\varepsilon}\right)^{1/4} \tag{3.6}$$

For $Re = 4.0 \times 10^4$ and $\ell = D_H = 0.04m$, $\eta = 1.4 \times 10^{-5}m$. Therefore $\varepsilon = 26.18 m^2 s^{-3}$ from (3.6), and for σ_3 = 150μm (control volume size) and $k = 3.2 \times 10^6$ rad/m, $\sigma_T = 28.33 \times 10^3$ rad/s or 4.5kHz. The broadening from turbulent fluctuations is thus of the order of 0.9 percent of the bulk velocity which corresponds to 0.494MHz. This result, although approximate to an order of magnitude, is indicative of the broadening

contribution and is in agreement with the calculation of Melling (1975), who estimated it to be of the same order as finite transit time broadening (i.e. about 1 percent of the measured frequency in this flow).

Velocity and photomultiplier characteristic bias effects are not important in the measurements of this chapter, in view of the small range of frequencies measured and the therefore negligible variation in signal amplitude and of the small turbulence intensities encountered in the flow.

3.4 Flow visualisation

The hydrogen bubble technique (see e.g. Schraub et al, 1965, and Clayton et al, 1973) was used to visualise the flow in the bend. The bubbles were produced on 0.375mm Nichrome wires inserted through the pressure tappings. Still and cine photography recordings were made for laminar flow, as turbulent flow visualisation was difficult to achieve and record. Laminar flow recordings were made for the same Reynolds number as the measurements (790) but better visualisation was achieved at Reynolds numbers of 1275 and 3000. There were no recirculation regions revealed by the visualisation in any part of the flow.

Figs. 3.5(a) and 3.5(b)(i)-(iv) show the flow visualised at Reynolds numbers of 790 and 1275 respectively. The three wires were inserted at $r^* = 0.1$, 0.5 and 0.9 at four stations along the bend (0^o, 45^o, 71^o and 90^o corresponding to Figs. (i)-(iv)). The displacement of the flow at the entry towards the bend outer wall can be seen from Figs. 3.5(a)(i) and (b)(i). The secondary flow region is visible in Figs. 3.5 (a)(ii) and (b)(ii), as the bubbles spread near the inner wall in a vortical motion after the 45^o station. Further downstream, the flow near the outer wall is observed to accelerate following the bend curvature

and the secondary flow can be observed in this region by the bubbles accumulating near the top side wall as the fluid in that vicinity follows the cross-stream motion (Fig. 3.5(a) (iii)). The sheet of bubbles produced by the wire located at $r^* = 0.5$ in the same picture is fairly uniform, while the secondary flow activity is again noticed at the region of the wire located at $r^* = 0.9$. On exit from the bend (Fig. 3.5 (a)(iv)), the decay of the strength of the secondary motion present at $\theta = 71^o$ is evident, and the flow near the outer wall is almost parallel to that wall. In all the photographs of Fig. 3.5(a), the effects of the wake of the wires on the sheets of bubbles produced are evident.

However, better results were obtained at Re = 1275, as shown in Fig. 3.5(b). The trends in the flow patterns are similar as for Re = 790, but the trajectories of the bubble paths can be observed more clearly. The flow in Fig. 3.5(b)(i) migrates from $r^* = 0.5$ at $\theta = 0^o$ to $r^* = 0.3$ at $\theta = 45^o$ and $r^* = 0.1$ at $\theta = 90^o$. The vortical flow region along the inner wall is seen to extend more towards the duct centreline as the bend exit is approached. Figs. 3.5(b)(ii) - (iv) show clearly that the increase in Reynolds number has not altered the flow structure qualitatively.

Fig. 3.5(c) shows the hydrogen bubbles produced at the bend inlet at Re = 1,275 being convected by the secondary flow near the side wall towards the inner wall. The cross-stream motion takes place at approximately 45 degrees to the local streamwise direction. The bubbles produced near the top of the wire follow the secondary flow motion and the larger ones accumulate on the top side wall because of buoyancy, while those produced near the middle of the wire follow the core flow and can be observed as two streaks of bubbles migrating towards the outer wall.

The helical nature of the secondary flow near the inner wall was clearly visualised at Re $\simeq$ 3000 and can be observed in Fig. 3.5(d). The flow past the wire can be seen to generate two streaks of bubbles rotating counter-clockwise as they move downstream.

3.5 Wall pressure measurements

Wall pressure measurements were obtained by means of pressure tappings let into the walls of the duct. The measurements were made with a water micromanometer. In laminar flow, the pressure differences amounted to about 20μm of water column and were too small for reliable measurement; the measured values were of the order estimated by a centrifugal force - pressure gradient balance calculation (order-of-magnitude estimate, not presented here), and as also calculated by Humphrey et al (1977). The wall pressure distribution is expected to be very similar to Humphrey et al's result, which showed that the gradient is strongly adverse over the inner (suction) surface for about 45^{o} and strongly favourable over the outer (pressure) surface for the same region, with the trends reversed thereafter until the bend exit.

Turbulent flow wall static pressure measurements are presented in Fig. 3.6, as plots of the streamwise and radial distribution of the static pressure coefficient, Cp. Pressure differences of the order of 4cm of water column were measured, and the same magnitude was calculated by considering the centrifugal force - pressure gradient balance; the results of Humphrey (1977) do not agree with this, as it is stated that pressure differences of no more than 3mm of water column were measured in the fully-developed bend flow: it is anticipated that blockage of the pressure tappings or tubes used by Humphrey prevented their accurate measurement.

The large radial pressure gradient at the inlet plane, observed from Fig. 3.6, confirms the influence of the bend on the upstream duct. Initially, an adverse pressure gradient develops on the pressure surface, and a favourable gradient on the suction surface, causing deceleration and acceleration of the fluid near the respective surfaces. The trends are reversed after $\theta \simeq 50^{o}$. The largest values of radial pressure

gradient, at $\theta = 45^o$ and 71^o (see Fig. 3.6(ii)), are associated with the large radial velocities, which were measured at $\theta = 60^o$ and 77.5^o in the bend. The pressure loss in the duct due to the presence of the bend is of the order of $0.1\rho V_c^2$, which is comparable to the value reported by Ward-Smith (1981) for a similar configuration.

3.6 Velocity results

Measurements of the streamwise and radial velocity components, and for the turbulent flow of the associated r.m.s. components and $\overline{uv}$ cross-correlations are presented in Figs. 3.7 - 3.23 for the stations $X_H = -0.25$, $\theta = 30^o$, 60^o and 77.5^o, and $X_H = 0.25$ and 2.50. Within the bend the manufacture of the test section restricted the measurements that could be made as the inner and outer walls of the bend were opaque and the inlet and outlet planes could not be measured. Measurements of the laminar streamwise velocities were also made at $X_H = -0.50$ and $X_H = 0.40$ to establish that, as measurements could not be made in the 0^o and 90^o planes, the changes in the profiles in the inlet and outlet regions were small enough so that the measurements at $X_H = -0.25$ and 0.25 approximated inlet/outlet conditions reasonably. Table 3.3 lists the measurement stations in the bend and the variables measured. For the last station spanwise component measurements and contours of turbulence kinetic energy (calculated from the $\tilde{u}$, $\tilde{v}$ and $\tilde{w}$ measurements) are also presented. Thus in the last station, all components of the stress tensor were measured except $\overline{vw}$ the measurement of which would require an effort not justified by its magnitude or significance.

The results are shown in contour form for ease of presentation; profiles of the three mean velocity components are also shown. The contours have been drawn using linear interpolation between the measurement points (located in a 5 x 10 or 5 x 13 grid); no extrapolation outside

the measured grid has been carried out. The results are available in tabulated, magnetic tape and punched card forms.

Symmetry checks were carried out for both flow regimes. Measurements at equivalent locations on either side of the symmetry plane agreed within the precision of the measurement. No discernable trends were observed.

In the subsequent presentation and discussion, it is useful to refer to the behaviour of the "core" fluid, defined as fluid of velocity greater than about 0.9 of the maximum at each streamwise station.

TABLE 3.3

MEASUREMENT STATIONS AND VARIABLES IN BEND FLOW

Measurement station (relative to bend entry plane)			Flow regime											
			Laminar			Turbulent								
X_H,	θ	variable	U	V	W	$\bar{U}$	$\bar{V}$	$\bar{W}$	$\tilde{u}$	$\tilde{v}$	$\tilde{w}$	$\overline{uv}$	$\overline{uw}$	k
Bend	-0.50		X											
Upstream	-0.25		X	X		X	X		X	X		X		
Tangent														
	30^o		X	X		X	X		X	X		X		
Bend	60^o		X	X		X	X		X	X		X		
	77.5^o		X	X		X	X		X	X		X		
Bend	+0.25		X	X		X	X		X	X		X		
Downstream	+0.40		X											
Tangent	+2.50		X	X	X	X	X	X	X	X	X	X	X	X

3.6.1 Laminar flow results

The development of the streamwise velocity is depicted in Fig. 3.7 as isotachs and the results are shown in profile form in Fig. 3.8. Fig. 3.7(i) shows that the boundary layer thickness at $X_H = -0.25$ (defined at 0.95 of the maximum velocity) is about 0.25 of the hydraulic diameter of the duct. The isotachs in this station show small asymmetries in the inlet flow, and suggest that the bend has little effect on the upstream tangent flow. In Figs. 3.7(ii) - (v), the core is shown to be located progressively nearer to the outer wall and to the sidewalls with a low velocity region adjacent to the suction surface. The development of the streamwise velocities is influenced by the presence of the streamwise and cross-stream pressure gradients mentioned in section 3.5.

The generation of streamwise vorticity (that is, secondary flow) is responsible for the convection of core fluid from the pressure surface along the sidewalls, and the accumulation, at the inner wall, of low momentum boundary layer fluid from the sidewalls. Fig. 3.9 shows profiles of the radial component of secondary velocity. At $X_H = -0.25$ (Fig. 3.9(i)), the velocity is small ($0.05\ V_c$) but directed towards the suction surface of the straight duct. This flow is evidence of a radial pressure gradient upstream of the bend. The profiles in the bend confirm that the fluid near the symmetry plane moves away from the suction surface and that the fluid near the sidewalls moves towards the suction surface. This results in a secondary flow of the "first kind", with a strong helical motion near the suction surface. The largest velocities measured occur at $\theta = 60^o$ with values of the order of $0.6\ V_c$, although the velocity near the symmetry plane and suction surface has decayed and is close to zero. This feature is seen to continue at $\theta = 77.5^o$ and $X_H = 0.25$. It is important to remark that it is the extent of the core

flow, rather than the degree of distortion of the streamwise isotachs at the inner wall which is the better indicator of the importance of the secondary flow.

Downstream of the bend, Fig. 3.7(vi) shows that the streamwise velocity has decelerated on the pressure side of the duct. Fig. 3.9(vi) presents the corresponding profiles of radial velocity which has decreased greatly from the exit plane of the bend and has also reversed direction at $r^* = 0.3$. For this station, the spanwise (W) component of velocity was measured (Fig. 3.11) and confirms that the secondary flow consists of two counter-rotating vortices which is in agreement with the predictions of Humphrey et al (1977) although the calculated values are generally larger over the cross-section. It is associated with the rapid deceleration of streamwise velocity around $r^* = 0.1$ causing a positive radial velocity near the symmetry plane.

3.6.2 Turbulent flow results

The development of the streamwise velocities in the symmetry plane on approach to the bend inlet is shown in Fig. 3.12. The profile at $X_H = -0.75$ is very uniform with asymmetries around the mean radius of less than 1 percent. By $X_H = -0.25$ the influence of the pressure gradients set up in the bend is noticeable, as the flow accelerates on the inside of the bend.

The development of the streamwise component of velocity is shown as profiles in Figs. 3.13 and as the corresponding isotachs in Fig. 3.14. The growth of the turbulent boundary layers in the upstream tangent is slower than for the laminar flow so the boundary layers at $X_H = -0.25$ are thinner (about 0.15 of the hydraulic diameter). In contrast to the results of Fig. 3.7 core fluid is displaced towards the inner wall surface at $X_H = -0.25$, Fig. 3.14(i), although the measurements at $X_H = -0.75$

showed that this effect was negligible. The fluid near the suction surface continues to accelerate at $\theta = 30^{o}$, and the presence of core fluid remains at the inner wall, with no evidence of low momentum fluid being accumulated at this surface, until $\theta = 60^{o}$, Fig. 3.14(iii). Thereafter the rapid creation of a region of low streamwise momentum, at the inner wall, is evident and continues to the exit of the bend with the corresponding migration of core fluid towards the outer wall; the influence of the secondary flow on the contour shapes is evident and continues to the exit of the bend, with the position of maximum velocity migrating from $r^* = 0.7$ to $r^* = 0.4$.

The profiles of radial velocity are presented in Fig. 3.15 and the corresponding isotachs in Fig. 3.16. As expected at $X_H = -0.25$, the velocity is directed towards the suction surface, for the same reasons as in the laminar flow. The streamwise vorticity generated within the bend develops more slowly than for the laminar flow, while the positive velocities occur in the region very close to the sidewalls, corresponding to the thinner boundary layers. The maximum velocities are again found at $\theta = 60^{o}$ and are about 0.4 V_c, thus smaller than for the laminar flow. In common with the laminar flow, the profiles of radial velocity show that the flow is directed away from the inner wall within the core and towards it in the sidewall boundary layers. Local distortions occur, however, in the region of low streamwise momentum near the inner wall. A similar result has also been reported by Agrawal et al (1978) in a laminar flow.

The development downstream of the bend is shown in Figs. 3.14(vi) and 3.15(vi). The position of maximum streamwise velocity lies closer to the pressure wall while fluid near the suction wall has accelerated. The radial velocity has decayed less than was the case for the laminar flow and only one sense of circulation is evident at $X_H = 2.50$. The

third component of velocity, W, is presented in Fig. 3.17 with the positive velocity direction defined as for laminar flow. The results indicate a counter-clockwise rotation in the cross-stream plane as viewed, which is consistent with the radial component measurements.

Fig. 3.18 presents contours of the Reynolds stress $\overline{uv}$. Upstream of the bend the values are low, corresponding to the small boundary layer thicknesses. At successive streamwise planes, large values of $\overline{uv}$ are found near the pressure surface and near the sidewalls indicating that momentum transport is large in the region coinciding with large streamwise velocity gradients. The change in the sign of $\overline{uv}$ is closely associated with changes in the sign of $\partial U/\partial r^*$, at least for the region $z^* \lesssim 0.8$. On the suction side of the bend, the shear stress is generally small except for $\theta = 60^o$.

Figs. 3.19 and 3.20 show the corresponding development of $\tilde{u}$ and $\tilde{v}$. Initially, high values are to be found only within the boundary layers. The influence of the secondary motion can be detected at $\theta = 60^o$ and at the exit, the turbulence is anisotropic with high $\tilde{v}$ near the pressure surface and high $\tilde{u}$ near the suction surface. At $X_H = 2.50$ the behaviour of $\overline{uv}$ is complex with a large area on the suction surface being occupied by positive values of $-\overline{uv}$ and near zero values on the pressure side. Momentum transfer in the span (z^*) direction is accomplished through $\overline{uw}$, which is plotted in Fig. 3.2 1. Values are large near $z^* = 0.5$, as could be expected, because of the large streamwise velocity gradients present. The maximum values of $\overline{uv}$ and $\overline{uw}$ are similar ($0.003\ V_c^2$) although present in different regions. The contours of $\tilde{u}$ and $\tilde{v}$ also show large changes, with maximum values of the order of $0.11\ V_c$. Fig. 3.22 shows contours of the $\tilde{w}$ component of fluctuating velocity. The contours of turbulent kinetic energy were constructed from $\tilde{u}$, $\tilde{v}$ and $\tilde{w}$ measurements are are presented in Fig. 3.23.

3.7 Discussion

The results presented are discussed below primarily with respect to the influence of the bend geometry and of flow conditions on the development of the secondary flow. A distinction is made between the influences of inlet boundary layer thickness and Reynolds number on the flow structure, and the importance of the turbulence structure is assessed. The section closes by considering the calculation of this flow and in particular of the type of numerical technique to be used. Although a general discussion on the bend flows is provided, the considerations made are equally applicable to the flows in both reciprocating engine manifolds and gas turbine intake ducts: in both cases, the generation of the secondary flow affects the port or turbine performance due to the extra pressure loss involved (see e.g. Annand, 1969).

Influence of inlet boundary layer thickness

Comparison of the laminar and turbulent results shows that the influence of the bend results in a greater asymmetry about the mean radius in the upstream tangent for turbulent flow, which is associated with the favourable pressure gradient on the suction side. In contrast, the laminar flow with thicker boundary layers is found to develop larger radial velocities more rapidly, and results in smaller asymmetry at inlet. This mechanism is also evident in the fully-developed turbulent flow of Humphrey et al (1981), where the inlet asymmetry is smaller than in the present turbulent flow.

Within the bend the locii of the maximum streamwise, velocities (Figs. 3.7 and 3.14) are quite different, as a consequence of the secondary flow development. The larger secondary flow in the laminar case is associated with a greater pressure loss in the bend, e.g. $0.4\rho V_c^2$ calculated by Humphrey et al (1977) as compared with $0.1\rho V_c^2$ for the present

turbulent case.

The influence of the boundary layer thickness at the inlet can be assessed by reference to Humphrey et al (1977, 1981). In the case of laminar flow, the maximum streamwise velocity at $\theta = 60^{o}$ is larger and the deceleration of the fluid near the inner wall surface is more extensive for fully-developed inlet boundary layers. These differences reflect a more extensive streamwise vorticity with the thicker inlet boundary layer, although the locii of maximum streamwise velocity, for example, are similar.

Comparison with the turbulent flow results of Humphrey et al (1981) shows little similarity with the redistribution of the streamwise isotachs over the first 60^{o} of the bend, because of the larger secondary flows present at the inlet with the thick inlet boundary layer. For example, the locus of maximum streamwise velocity in the inlet plane of the bend ($z^* = 0$) remains very close to the mean radius of curvature ($r^* = 0.5$). The presence of an extensive irrotational flow at the inlet in the present data results in the first 30^{o} behaving in a manner consistent with a potential irrotational flow with the streamwise velocity maximum occurring close to the suction surface and there is little evidence of the effect of secondary flow on the streamwise isotachs before the $\theta = 60^{o}$ station. Beyond this station, both sets of results show qualitatively similar behaviour with the locii of maximum streamwise velocity occurring near the mean radius of the bend. This coincides with the change in sign of the pressure gradient at the inner wall. The quantitative differences are evident, for example, in the exit plane of the present bend where there are higher negative radial velocities ($-0.3\ V_c$ as opposed to $-0.15\ V_c$) and smaller velocities on the symmetry plane ($0.2\ V_c$ as opposed to $0.28\ V_c$).

The flow of Humphrey et al (1981) is also affected by secondary

flows of the "second kind", driven by normal stresses, (see e.g. Melling, 1975) which influence the flow development in the bend as they are superimposed on the pressure-driven motions. These flows are less than 1.5% of the centreline velocity in a square duct (Melling and Whitelaw, 1976b) in fully-developed flow and in developing flow they are significantly smaller (Melling, 1975). Their contribution to the present measurements is minor: the characteristic "bulging" of the $\bar{U}$ and $\tilde{u}$ contours is not observed in the data.

Comparison of the two flow regimes presented here shows that, given that the upstream tangent to the bend is of fixed length, the primary result of increasing the Reynolds number is to decrease the boundary layer thickness in the entry plane of the bend.

The presence of shear, whether laminar or turbulent, is mostly restricted to the near-wall regions and not directly relevant to the core flow development (see below, however, under the heading of calculation). To explain the differences between the laminar and turbulent flows, it is necessary to discuss those forces which dominate the transport of streamwise vorticity.

The core flow develops under the separate influences of the streamwise pressure gradients and cross-stream convection by the secondary flow. The pressure field within the duct (Fig. 3.6) qualitatively resembles that which would exist in a potential flow: over the first 45^{o} or so of the suction surface the pressure gradient is favourable and thus tends to accelerate the fluid. The secondary flow, which is an inviscid, rotational fluid phenomenon (given the initial viscous development of the boundary layer) convects low momentum (boundary layer) fluid along the sidewalls towards the inner wall surface; the accumulation of this fluid tends to displace the core. Despite the difference in the

laminar boundary layer thickness between this thesis ($\simeq 0.25\ D_H$) and Humphrey et al (1977, 1981), ($0.50\ D_H$), the resulting isotachs from $\theta = 60^o$ onwards are very similar.

The thickness of these layers at inlet is, however, important in determining the magnitude of the secondary velocity, particularly in the first 30^o or so of the bend (cf. Figs. 3.7(ii) and 3.14(ii)). For the purposes of this discussion, the formal connection is

$$d\left(\frac{\partial W}{\partial r} - \frac{\partial V}{\partial z}\right) = -2\left(\frac{\partial U}{\partial z} - \frac{\partial W}{\partial \theta}\right) d\theta \qquad (3.7)$$

which is the Squire and Winter result derived from inviscid flow theory. The equation suggests, and measurements confirm, that the thinner entry boundary layers in the turbulent flow give rise to smaller cross-stream velocities. The consequence is that the turbulent flow is dominated, over the first 45^o, by the acceleration of the core by the pressure gradient near the inner wall surface.

Effect of Reynolds number

The positive cross-stream velocities are restricted to a small region adjacent to the side walls in the turbulent flow case. The same has been observed in the developing laminar flow of Agrawal et al (1978) with very thin inlet boundary layers and confirms that the phenomenon is related to the inlet streamwise velocity distributions rather than the Reynolds number. The measurements of Enayet et al (1981a) also show the effect of increasing Reynolds number in a circular pipe bend for Re = 500 and 1093; the boundary layer thicknesses are comparable in the two cases (23% and 21% of the hydraulic diameter respectively) and the secondary flow generation is similar. The inviscid core flow moves nearer the

outer wall in the higher Re flow as the centrifugal forces imparted on it are higher due to the higher bulk flow velocity. However, the measurements of Enayet et al in the same pipe bend for Re = 43,000 show a much thinner boundary layer and the core flow nearer the inside of the bend. The effect of Reynolds number change is thus related to the increase of the centrifugal forces imposed on the inviscid core flow.

The only source of secondary flow of the first kind is the combination of radial pressure gradients and centripetal accelerations and is almost proportional to Reynolds number (see De Vriend, 1981). Closer examination of the streamwise isotachs of Enayet et al (1981a) shows that, although secondary velocities were not measured, the secondary flows appear to be greater in the higher Reynolds number (1093) case.

Influence of curvature

Flows with small curvature are in general "shear-dominated", while flows with large curvature are "inertia-dominated" and therefore more stable (Hunt and Joubert, 1979). Secondary flows can be generated even under the influence of extremely small curvature. Curved walls in straight passages can induce pressure-driven flows: an example of such a flow in a square-to-round transition duct as encountered in turbine intakes is presented in Appendix 3.1. Cross-stream flows of magnitudes of up to 0.07 of the bulk velocity are generated in the transition due to the difference in pressure over the duct cross-section (see Fig. 4 in Appendix 3.1) and can impair the turbine's performance.

In 90 degree bends of mild curvature, cross-stream flows smaller than the ones encountered in the present bend are found, and the flow patterns are significantly different. The measurements of Enayet et al (1981b), in an identical bend of 7.0 radius ratio at a Reynolds number of 35,200 and almost identical boundary layer thickness at the entrance

to the bend, showed the maximum radial velocities at stations 45 and 90 degrees along the duct to be only 0.21 and 0.09 V_c respectively. The streamwise isotachs show that with the milder curvature, the core fluid is displaced towards the mean radius of the bend by $\theta = 45^o$, although the influence of the secondary flow is less than in the present laminar flow. The core is dispaced to the outer wall ($r^* = 0.25$) by the exit of the bend as opposed to $r^* = 0.5$ in the present turbulent flow.

An order-of-magnitude estimate of the induced pressure gradients and the associated secondary flow velocities in the 2.3 and 7.0 radius ratio bends shows that the pressure gradient is larger by $(7/2.3)^2 \simeq 10$ in the strongly curved duct, while the corresponding secondary velocities are nearly $(7/2.3)^{\frac{1}{2}} \simeq 2$ those in the mildly curved bend. The streamwise pressure gradient is expected to be nearly zero over most of the mildly curved bend (see Ward-Smith, 1971) and have an effect only in the vicinities of the bend inlet and exit. As a result, the inner wall acceleration is not observed at $\theta = 45^o$ for $R_r = 7.0$, and the influence of the secondary flow redistribution is more apparent than for $R_r = 2.3$ (Figs. 3.14(ii) and (iii)). Comparison of the 45 and 90 degree station isotachs of Enayet et al shows the movement of the core flow towards the outer wall near the bend exit as the secondary flow redistributes the streamwise isotachs.

Ward-Smith (1971) concluded from his exit plane total pressure measurements that the secondary flows are weaker and distributed over a larger part of the bend cross-section in bends of milder curvature. The second observation is made from fully developed bend flow results, and it is not in accordance with the findings of Enayet et al, nor with his own thin inlet boundary layer results. In general, a smaller region of weaker secondary flow is present in bends of milder curvature compared to that of strongly curved bends. The shear stresses, although they

were measured to be of the same order in the bends of mild and strong curvature, are shown by an order-of-magnitude analysis to be ten times more significant in relation to the pressure gradient in the large radius ratio bend. While the pressure losses become less significant, the frictional losses are expected to be more important in bends of milder curvature (Ward-Smith, 1971, Eskinazi and Yeh, 1956), an observation which is in accordance with the aforementioned estimate. It is noted, however, that the rapid decay of the secondary velocities on approaching the exit plane of the bend, which has been observed in all the bends, is also an irrotational, and not a viscid, fluid phenomenon. The decay is associated with the production of streamwise vorticity of the opposite direction to that produced at the bend inlet by the presence of positive $\frac{\partial U}{\partial z}$ at the inner wall of the bend. This can be seen from equation (3.7) and has been noted by Rowe (1970). It is this mechanism that accounts for Agrawal et al's (1978) unexplained measurements of positive radial velocity at the inner wall surface.

The effects of curvature (radius ratio) and boundary layer thickness are related in the criterion described below for two-dimensional flows. Additional terms introduced by streamline curvature are present in, for example, the turbulence kinetic energy equation for a plane boundary layer when applied to the flow over a curved surface. These extra terms can be shown to be negligible by an order-of-magnitude analysis if $\delta/R_c \ll 1$ and if $\delta/R_c \ll \partial\phi/\partial r$, where δ is the boundary layer thickness and ϕ is a property such as $\bar{U}$, $\bar{V}$, $\tilde{u}$, $\tilde{v}$, $\overline{\tilde{u}\tilde{v}}$ etc. (Ramaprian and Shivaprasad, 1978). In the present results δ/R_c is 0.1 and 0.06 for the Reynolds numbers of 790 and 40,000 respectively, but the ϕ criterion is difficult to establish due to the complexity of the flow.

Curvature affects also the transition to turbulence and flow stability. Using the relation provided by Ito (1959) for the critical

Reynolds number for transition in curved pipes (Re_{crit}), it is observed that Re_{crit} is inversely proportional to the radius of curvature. Thus curvature has a stabilising effect on turbulence, a result which has been verified by White (1929) and Taylor (1929). Moreover, Martin and Deverson (1960) specify a relation for the bend angle needed, θ, for a complete oscillation of the secondary flow. Again, θ is inversely proportional to the radius of curvature and the flow is more oscillatory in bends of milder curvature.

Effect of duct cross-sectional shape and bend deflection angle

Similarities of the aforementioned effects of curvature in both round and rectangular cross-sectioned bends have been indicated by Nippert (1929). Strong similarities in the streamwise isotachs are also evident by comparison of the present results with those of Enayet et al (1981a) obtained in a curved pipe of 2.8 radius ratio. However, the smaller "core" region in the pipe results suggests that larger secondary velocities are present in that flow; this observation is consistent with the higher pressure drop measured across the bend ($0.15\rho V_c^2$ as opposed to $0.1\rho V_c^2$ in the present data), which indicates the existence of larger secondary flows.

Although no firm conclusions can be drawn, it can be anticipated that in general the trends observed will apply qualitatively for any duct cross-sectional shape, provided the aspect ratio (in the case of rectangular ducts or the major-to-minor axis length ratio in ducts of elliptical cross-section) is close to unity so that the flow is three-dimensional. In ducts of large aspect ratio the secondary flows are restricted to the sidewalls and have no effect on the flow in the symmetry plane of the duct which is two-dimensional (see, for example, Hoffmann

and Bradshaw, 1978).

The angle by which the flow is turned is important to the flow development in the bend, for angles up to around 180^{o}. Depending on the curvature of the bend, fully developed laminar flow conditions are obtained after, for example, 121 to 211 degrees of bend deflection angle in ducts of radius ratios of 7.0 and 2.3 respectively (see Austin and Seader, 1974). The deflection angle is not very important to the flow development in bends of mild curvature, as the streamwise pressure gradient in the bend is practically zero except near the bend inlet and exit (for example for $15^{o}<\theta<75^{o}$ in 90^{o} bends; Ward Smith, 1971). The generation of secondary flow depends on the bend deflection angle; stronger flows are present in 90 degree than in 45 degree bends (Miller, 1978).

The generation of instabilities in the form of Taylor-Görtler vortices (see, for example, Smith, 1955) can also occur in concave surfaces. No such vortices were revealed by the flow visualisation or the measurements and they would have been if they had existed. The Görtler numbers (see Crane and Winoto, 1979) for the two flow regimes cannot be calculated precisely as a significant number of measurements in the concave wall boundary layer are required. It is expected that the small radius ratio, the small aspect ratio and therefore the three-dimensionality of the flow and the related strong secondary flows over the bend cross-section have either suppressed the generation of such vortices or rendered them too weak to be detected.

Ramaprian and Shivaprasad (1978) did not detect any such vortices in a bend of 2.5 aspect ratio with secondary flows occupying much less of the duct cross-sectional area. However, the presence of Görtler vortices has been reported for both mildly and strongly curved two-dimensional flows (see e.g. Tani, 1962, So and Mellor, 1972 and Meroney and

Bradshaw, 1975).

Cheng et al (1979) also found similar vortices present in their laminar flow visualisation in the exit planes of 180^{o} bends of aspect ratios between 1 and 12. Rowe (1970) found an additional pair of vortices near the outer wall after 90^{o} in an 180 degree curved pipe and after 75^{o} in a 90 degree pipe, both of a radius ratio of 12. Both Rowe's and Cheng et al's vortices are large, however, compared to the Görtler vortices normally encountered and their origins are not well understood (Crane, 1981). They are normally present in bends of large radius ratio; for instance, in the measurements of Enayet et al (1981b) in a 7.0 radius ratio square duct, an extra pair of vortices is noticeable near the outer wall by the 45^{o} station, although it is too weak for its circulation to be precisely defined. In general, small deflection angle, small aspect ratio and strong curvature seem to suppress such flow instabilities, as in the present ("inertia-dominated", Hunt and Joubert, 1979) flow. Choi et al (1979) have also observed the stabilising effect of secondary flow in a curved tube.

Effects on the turbulence structure

For the fluctuating velocities there is qualitative agreement between the developing and fully developed bend flows; for example, $-\overline{uv}$ is large near the suction surface and, at the exit of the bend, $\tilde{v}$ is large near the suction surface while $\tilde{u}$ is large near the pressure surface. Quantitative agreement is not found and is not expected. For example, at the inlet $\overline{uv}$ is up to $0.0013\ V_c^2$ in the present flow as compared to $0.004\ V_c^2$ with the thicker boundary layers; at exit, the respective values are $0.003\ V_c^2$ and $0.007\ V_c^2$. The influence of streamline curvature is expected to increase turbulence levels near the suction (convex) surface and to

decrease them near the pressure (concave) surface and the behaviour of $\overline{\tilde{u}\tilde{v}}$ and $\tilde{v}$ support this expectation although the increase in $\tilde{u}$ might appear anomalous. Wall shear stresses measured by Eskinazi and Yeh (1956) in two-dimensional curved flow exhibited the same trends. The contours of zero $\overline{\tilde{u}\tilde{v}}$ and $\overline{\tilde{u}\tilde{w}}$ follow closely the locations of zero $\partial U/\partial r^*$ and $\partial U/\partial z^*$ as expected.

The effect of streamline curvature on the turbulence structure can best be analysed by examining the structural parameters $R = \frac{\overline{\tilde{u}\tilde{v}}}{\tilde{u}\tilde{v}}$ and $\alpha_1' = -\overline{\tilde{u}\tilde{v}}/1.5\ (\tilde{u}^2 + \tilde{v}^2)$ (see e.g. Hoffmann and Bradshaw, 1978) which were calculated at each measurement station. Although it is important to note that these are strictly appropriate only for two-dimensional flows, where $\overline{\tilde{u}\tilde{v}}$ is the dominant shearing strain, they should be sufficiently accurate for qualitative interpretation of this flow.

The correlation coefficient, R, increases from an initial maximum value of 0.4 near the outer wall to about 0.8 by $\theta = 60^o$ and thereafter decreases. The trends near the inner wall are more complicated, presumably because of the strong three-dimensionality of the boundary layer. The anisotropy coefficient, α_1', follows very similar trends to the correlation coefficient, reaching a maximum value of about 0.25 by $\theta = 60^o$. The correlation and anisotropy coefficients are typically 0.4 and 0.15 respectively for turbulent shear flows: the increase in their values which is observed on the pressure surface, corresponding to destabilising curvature, is consistent with the expected influence of streamline curvature.

The effect of curvature on the turbulence structure was reported by Ramaprian and Shivaprasad (1978) to be more important on the outer region of the boundary layer than close to the wall and $\tilde{v}$ fluctuations to be affected more than $\tilde{u}$ ones; convex curvature was found to suppress the diffusion of turbulent energy away from the wall and concave curvature to

have an opposite effect. The three-dimensionality of the present flow does not allow direct comparisons, although the values of k are generally higher near the inner (corresponding to the convex surface) wall at $X_H = 2.50$.

Calculation of the flow in curved ducts

The calculation of flows in curved ducts can be performed, in principle, by numerical integration of the equations of fluid motion (see, for example, Humphrey et al, 1977 and 1981, Leschziner and Rodi, 1979 and Moore and Moore, 1979). In turbulent flow, the Reynolds averaged equations are used, together with turbulence models of various degrees of complexity. Although it is possible to understand the flow on the basis of inviscid, rotational theory, the inclusion of viscous effects in the equations of motion is important for a number of reasons. The presence of rotational flow at the inlet plane of the bend, in the absence of which there would be no secondary flow, is due to viscous effects; the continued generation of vorticity at the outer and side walls within the bend is also important (particularly, say, in river bend flows: see Scorer, 1978); and Rowe (1970) has suggested that vortex dissipation at the inner wall is also important.

Previously reported calculations of laminar flow by Humphrey et al (1977) have shown that numerical meshes of 20 (streamwise) x 15 (radial) x 10 (spanwise) nodes are insufficient to resolve the flow field in the 90^{o} bend accurately. Calculations of the laminar flow of this chapter (Buggeln et al, 1980) with the numerical scheme of Briley and McDonald (1977) and (1980) and using 26 x 28 x 13 nodes still show some quantitative, though not qualitative, disagreement. This finer grid represents an increase in the spatial resolution of between 1.3 and 1.9 in the various coordinate directions in comparison to that of Humphrey et

al. Since the upwind-differencing representation of convection (e.g. Spalding, 1972) - which is probably used at least for the streamwise convection fluxes - possesses a truncation error proportional to the grid spacing, the reduction in this error is also related to the factors quoted above. The storage requirement of Buggeln et al's is, however, greater than that of Humphrey et al's by a factor of 3.2.

These two examples well illustrate that grid node resolution hinders accurate numerical solution: however, a further increase in the number of nodes may result in prohibiting computational costs or even exceeding the core storage of some machines. The use of "partially parabolic", rather than "fully elliptic" numerical solution schemes (Pratap and Spalding, 1975), may offer an attractive way of increasing the resolution of the area of integration, provided that the flow fulfills the physical requirements of the partially parabolic approximation. These are the existence of a predominant flow direction along which diffusion fluxes are small and convective influences are exerted only in that direction. The measurements suggest that these requirements are fulfilled, although Buggeln et al report a small (calculated) region of flow separation on exit from the bend. Whatever the chosen numerical scheme, the results of this chapter describe, in careful detail, the flow conditions at the inlet to the bend and these may form the boundary conditions at this station. As a result, it is not necessary for the calculation scheme to expend effort on the flow in the upstream tangent (cf. Humphrey et al, 1977). The measurements are available on magnetic tape and in punched card form, to facilitate future comparisons with calculation methods.

In the absence of truly "grid-independent" solutions for laminar flow, it is premature to judge the comparative virtues, or otherwise, of various turbulence models for flows in bends. A priori, the ratio of

boundary layer thickness at inlet to the mean radius of curvature is sufficiently large ($\simeq 10^{-1}$) to expect some influence of streamline curvature (an "extra rate of strain": see Bradshaw, 1973) on the turbulence. Hence the use of advanced turbulence models (such as the Reynolds stress closure: Launder, Reece and Rodi, 1975) would be indicated. It should be added, however, that the calculation of Buggeln et al (1980) using a simple Prandtl-Kolmogorov relationship, gives results which are in closer agreement with the measurements than is the case for the laminar flow. This indicates that numerical errors are significant and would most probably nullify the improvements to turbulence modelling that the extra equations would bring. In addition, the predominance of the pressure-controlled processes in the flow over the turbulence-controlled ones suggests that the accurate prediction of the former is necessary before the turbulence modelling improvements are made.

In contrast to the above studies, the calculation of the flow in reciprocating engine inlet manifolds is currently restricted to two-dimensional geometries (Demirdzic, 1981) to match the concurrent in-cylinder flow predictions. The present results are therefore not strictly appropriate for the assessment of two-dimensional inlet flows in the absence of secondary motion, but should prove useful for the assessment of future three-dimensional calculations of such flows.

3.8 Summary

The more important findings of the work presented in this chapter are listed below.

1. Secondary flows of the first kind are present in the flow in the curved square duct investigated, and are more pronounced with the laminar Reynolds number reaching a maximum of 0.6 of the bulk velocity, as compared with 0.4 in the turbulent case. This is mainly attributed to

the thicker (0.25 versus 0.15 of the hydraulic diameter) boundary layers at the bend inlet.

2. In laminar flow, the core flow migrates from the mean radius of the bend at the inlet towards the outer wall surface at the exit. In the turbulent flow with the thinner inlet boundary layers, the predominance of the streamwise pressure gradient causes the core flow to migrate initially towards the inner wall, but subsequently moves towards the outer wall and is located near the mean radius of the bend at the exit. As a result of the smaller secondary flows, greater asymmetries are evident at the inlet in the turbulent flow case and the flow behaviour is akin to potential irrotational flow.
3. Comparisons with laminar and turbulent flows with fully developed profiles at the inlet to the bend show large differences only in the case of 0.15 D_H inlet boundary layer thickness, for the first 60^o of the bend angle.
4. An increase in Reynolds number without significant change in the inlet boundary layer thickness, is shown to result in greater centrifugal forces imposed on the core flow and larger generation of secondary flow.
5. Secondary flows in the turbulent flow in a duct of mild curvature (7.0 radius ratio) are smaller than in a 2.3 radius ratio bend, reaching a maximum of 0.2 of the bulk velocity, and confined to a smaller region near the sidewalls, but their relative effect on the flow development is greater than for the strongly curved duct.
6. Measured values of the fluctuating velocities are small, reaching maxima of about 0.1 V_c near the walls; shear stress and turbulence kinetic energy distributions show similar trends with values not exceeding 0.004 and 0.014 V_c^2 respectively. The distributions are similar to and the levels approximately half of those measured with fully

developed inlet profiles, as expected. In general, turbulence parameters are only a few percent compared with the pressure gradient.

7. The results indicate that turbulence effects are of minor importance to the flow development over most of the duct cross-section and that the pressure-controlled processes dominate the flow.
8. Consideration of the flow processes involved and of previously reported calculations suggests that partially-parabolic techniques are adequate and appropriate for the calculation of the flow. Current calculations show that turbulence modelling errors appear to be of lesser significance in comparison to numerical ones.

APPENDIX 3.1

NASA Contractor Report 3447

Turbulent Flow in a Square-to-Round Transition

A. M. K. P. Taylor, J. H. Whitelaw,
and M. Yianneskis
Imperial College of Science and Technology
London, England

Prepared for
Lewis Research Center
under Contract NASW-3258

NASA
National Aeronautics
and Space Administration

**Scientific and Technical
Information Branch**

1981

ABSTRACT

Measurements of turbulent flow in a duct with a cross-sectional transition from square to round are presented. Laser Doppler velocimetry was used to measure the mean velocity components, turbulence levels and shear stresses. The boundary layers at the inlet and exit of the transition were approximately 13% and 20% of the hydraulic diameter respectively, becoming thicker near the corner fillets. The results show the development of secondary flow, of magnitudes up to 7% of the bulk velocity. This flow is directed away from the corner fillets and along the periphery of the duct and is associated with the longitudinal curvature of the wall and the related pressure gradients.

Key Words:

Secondary flow
Laser Doppler velocimetry
Ducts - Intake systems.

LIST OF FIGURE TITLES

1. Flow configuration, co-ordinate system and centreline streamwise velocity variation
2. (a)-(e): Streamwise velocity profiles and turbulence levels;
   (f) : Cross-stream turbulence levels
3. Secondary velocity profiles
4. Effect of longitudinal streamline curvature on cross-stream pressure variation.
5. Definition sketch for the estimation of cross-stream pressure variation (Appendix 2)

SUMMARY

Turbulent flow in a duct in which the cross-section undergoes a transition from square to round has been measured at a Reynolds number of 35 350. The hydraulic diameter, 40 mm, was the same in the square inlet and round exit sections, resulting in a cross-sectional area reduction of 21.5%. The transition takes place over two hydraulic diameters. Laser Doppler velocimetry was used to measure the streamwise and secondary mean velocity components and the associated turbulence levels and cross-correlations in stations upstream of, in, and downstream of the transition. The results provide an understanding of the flow and assist the evaluation of numerical techniques.

The boundary layers at inlet and exit of the transition were approximately 13% and 20% respectively of the hydraulic diameter. Thickening of the boundary layers at the duct corners is associated with the secondary flow away from the corner fillets and along the duct walls, towards the duct midplanes. Cross-stream velocities of up to 7% of the bulk velocity were measured; the secondary flow is produced by the longitudinal curvature of the wall and the related pressure gradients.

TABLE OF CONTENTS

	Page
SUMMARY	1
1. INTRODUCTION	2
2. FLOW CONFIGURATION AND INSTRUMENTATION	2
3. RESULTS AND DISCUSSION	3
4. CONCLUDING REMARKS	4
APPENDIX 1 - TABULATED DATA	6
APPENDIX 2 - ESTIMATION OF THE CROSS-STREAM PRESSURE GRADIENT	11
APPENDIX 3 - NOMENCLATURE	12
REFERENCES	13
FIGURES	14

1. INTRODUCTION

Flows in ducts which change cross-sectional area and shape are used in a wide range of engineering configurations and this report is concerned with the flow in a transition from a square to a circular cross-section with a decrease in area of 21.5% over two hydraulic diameters. The lateral convergence of the flow is accompanied by the generation of cross-stream velocities, or secondary motions, which result from the pressure field.

In long ducts of square section, secondary flows of the "second kind" arise and are driven by gradients of Reynolds-stresses with a magnitude of less than 1.5% of the bulk flow velocity: see, for example, reference 1. In the present flow the turbulent boundary layers at the inlet to the transition piece are thin and it can be expected that any secondary flows of the second kind will be much less than, say, 1% of the bulk flow velocity. Any larger cross-stream velocity within the transition piece stems from the change in cross-sectional shape and the related cross-stream pressure gradients.

The measurements of reference 3 provide some information of the flow in a transition from a rectangular to a circular section (and vice versa) with no change in cross-sectional area. The data includes contours of streamwise isotachs and the streamwise pressure variation. Two configurations were investigated in which the transition occurred over 0.69 and 2.76 hydraulic diameters and it is evident that the length of the transition is influential on the flow development. For example, cross-stream velocities presented for the round-to-rectangular transitions reached maxima of about 0.18 and 0.09 of the maximum streamwise velocity for the short and long transition ducts respectively. For the rectangular entry sections, the flows were fully developed at the inlet to the transition ducts and thus stress-driven secondary flows were also present.

The flow investigated in this report is relevant to the case of aircraft intake ducts. The measurements are intended to quantify the mean and fluctuating components of the streamwise and cross-stream velocities of the flow and so provide better understanding and a basis for the testing of design methods. In common with the previous investigations of references 1 and 2, laser-Doppler velocimetry was used to measure the velocity components.

The following section describes the experimental procedure and section 3 presents the measurements. Concluding remarks are provided in section 4.

2. FLOW CONFIGURATION AND INSTRUMENTATION

The transition from a 40 mm square cross-section to a 40 mm diameter circular cross-section took place in a duct length of 80 mm. The duct is

depicted in figure 1 together with the coordinate system adopted in the report. Each cross-section in the transition is formed by the intersection of a square and a circle, which resembles, to within 1.5% of the radius a super ellipse with a shape factor of unity. The radius of the circle decreases linearly along the transition from 28.28 mm to 20.00 mm. The transition piece was installed in the water tunnel previously used in reference 2. The bulk velocity through the square section was 0.885 m/s which corresponds to a Reynolds number of 35 350, based on the hydraulic diameter. The temperature of the water was maintained at 20 $\pm$ 2° C for all the experiments. Measurements of velocity were restricted by limits of optical access, caused by refraction at curved surfaces within the transition piece and in the downstream pipe.

The optical arrangement of the laser-Doppler velocimeter was identical to that of reference 2. Doppler signals were processed by a frequency-tracking demodulator (Cambridge Consultants CC01). A careful appraisal of the measurement errors has already been made in reference 2, where the precision (random error) of the mean and fluctuating components of velocity was assessed as $\pm$ 1½% and from $\pm$ 1½% to $\pm$ 5% respectively. In interpreting the results of the next section, it is important to note that the accuracy (systematic error) of the secondary velocity components is limited by the alignment of the velocimeter to the duct (see reference 1). The resulting systematic error is not more than 0.008 V_c.

3. RESULTS AND DISCUSSION

Symmetry tests on the streamwise flow in the duct upstream of the transition piece were carried out, with the result that measurements at equivalent locations on either side of the symmetry plane of the duct agreed within the precision of the measurement.

Figure 1 shows the development of the streamwise velocity on the centreline of the duct. The velocity increases from 1.12 V_c upstream of the transition to 1.43 downstream, as a consequence of the decrease in cross-section. Figures 2a-2e show profiles of the streamwise mean velocity, U, and the corresponding root mean square velocity, $\tilde{u}$, at a number of stations upstream, within and downstream of the transition piece. The boundary layer thickness on the symmetry plane, defined at 95% of the maximum velocity, is about 13% of the hydraulic diameter at the inlet to the transition piece (figure 2a), but rises to about 20% at the exit (figure 2d). The change in the profiles is comparatively small, as would be expected from the centreline change in figure 1. Careful examination of the profiles near the sidewalls shows that the fluid near the planes x_2/D and x_3/D = 0 accelerates relative to that near to the fillets which form the transition, and that the boundary layers are thinner away from the fillets. The profiles of $\tilde{u}$ (and $\tilde{v}$, figure 2f) are those expected for a turbulent wall boundary layer.

Figure 3 presents profiles of the cross-stream velocity for three stations within the transition piece. The measurements quantify the symmetry about planes at 45^0 to the x_2 or x_3 planes, which is within the limits of the systematic error discussed in section 2, as are the magnitudes of the cross-stream velocities on the symmetry planes (x_2/D or $x_3/D=0$). The measurements show that large values of the cross-stream velocity are found close to the walls and to the fillets which form the transition from the square to the circular cross-section. The largest values shown are of the order of 0.07 V_c, although the shape of the profile suggests that the maximum lies closer to the wall than $x_3/D=0.9$. The magnitude and direction of these velocities indicates that their source is pressure-gradient - rather than Reynolds stress-gradient. The direction of the cross-stream velocities is always away from the channel diagonal (line A-A' on figure 4) and thus cannot satisfy continuity in the cross-stream plane. This implies an acceleration of the streamwise velocity component near the symmetry planes (lines B-B' on figure 4) which is indeed observed, particularly in figure 2(c).

The origin of the lateral pressure-gradient, which drives the cross-stream flow, is due to the increase in pressure near the fillet relative to that in the region of the symmetry planes. This increase is brought about by the streamline curvature occurring in planes containing the channel diagonal and the duct centre-line upon entry to the transition piece, as shown in fig. 4 (a). In contrast, no such curvature occurs with streamlines contained in planes such as that depicted in Fig. 4 (b). It is noted that this mechanism should be reversed on exit from the transition piece and can be expected to cause the rapid decay of the cross-stream components.

These lateral pressure variations were also observed by Mayer (3); the qualitative changes in pressure and the related secondary flow directions are in accordance with the above discussion. However the simultaneous occurrence of longitudinal convergence on one wall and divergence on the other wall of the transition duct results in cross-stream flows not directly comparable to those presented in this report.

An order-of-magnitude estimation of the affect of curvature, given in Appendix 2, suggests secondary flow velocities not more than 0.16 of the bulk velocity. This is, considering the crude nature of the analysis, in good agreement with experiment.

Measurements of the $\overline{uw}$ and $\overline{uv}$ cross correlations were also obtained. As expected they were very low ($< 0.2 \times 10^{-3} V_c^2$) over the central region of the flow, rising to about $0.5 \times 10^{-3} V_c^2$ near the sidewalls. These values are close to the limits of accuracy of the velocimeter and are thus not presented.

The results from which the figures have been plotted are tabulated in Appendix 1.

4. CONCLUDING REMARKS

1. The experiments have quantified the streamwise and cross-stream velocities in a square to circular transition piece with thin inlet boundary layers.

2. The streamwise boundary layers assume smaller thicknesses away from the fillets which form the transition piece. The cross-stream velocity profiles are consistent with this observation; magnitudes of ≈ 0.07 of the bulk velocity have been measured.

3. The secondary velocities are driven by cross-stream pressure gradients induced by the longitudinal curvature of the streamlines on passing through the transition piece.

4. Because of the importance of wall curvature, its accurate representation is crucial to the calculation of the flow.

APPENDIX 1

TABULATED DATA

TABLE I - SQUARE-TO-ROUND TRANSITION MEAN VELOCITY, TURBULENCE LEVEL MEASUREMENTS

REYNOLDS NUMBER 35,350

(All quantities normalised by the bulk velocity, V_c = 0.885 m/s)

D_H	$\frac{x_2}{D}$	$\frac{x_3}{D}$	$\bar{U}/V_c$	$\tilde{u}/V_c$ x10^2	D_H	$\bar{U}/V_c$	$\tilde{u}/V_c$	D_H	$\bar{U}/V_c$	$\tilde{u}/V_c$ x10^2
-2.0	0.0	0.0	1.118	0.721	-1.0	1.136	0.721	0.0	1.145	0.722
		0.1	1.118	0.721		1.136	0.721		1.145	0.768
		0.2	1.118	0.721		1.136	0.721		1.145	0.811
		0.3	1.118	0.721		1.136	0.721		1.145	0.839
		0.4	1.118	0.721		1.136	0.811		1.145	0.901
		0.5	1.118	0.946		1.133	1.117		1.138	1.533
		0.6	1.107	2.389		1.116	2.636		1.109	3.426
		0.7	1.050	4.704		1.068	5.273		1.025	5.409
		0.8	0.964	6.200		0.964	6.698		0.960	6.220
		0.9	0.865	7.341		0.879	7.910		0.865	7.697
3.0	0.0	0.0	1.421	0.914	4.0	1.430	0.959			
		0.1	1.421	0.914		1.430	0.959			
		0.2	1.421	0.959		1 432	1.005			
		0.3	1.421	1.074		1.435	1.188			
		0.4	1.414	1.736		1.427	1.873			
		0.5	1.391	3.290		1.400	3.610			
		0.6	1.343	4.769		1.352	4.769			
		0.7	1.288	5.636		1.297	5.636			
		0.8	1.220	6.214		1.220	6.503			
		0.9	1.119	7.949		1.087	9.683			

D_H	$x_{2/D}$	$x_{3/D}$	$\bar{U}/v_c$	$\tilde{u}/v_c^2$ x10²	$\bar{V}/v_c$ x10²	$\tilde{v}/v_c^2$ x10²	$\bar{W}/v_c$ x10²	$\tilde{w}/v_c^2$ x10²
1.0	0.0	0.0	1.199	0.766	-0.646	0.572	-0.637	0.867
		-0.1	1.199	0.811	-0.646	0.682	-0.637	0.867
		-0.2	1.199	0.766	-0.646	0.706	-0.637	0.867
		-0.3	1.197	0.856	-0.807	0.725	-0.637	0.867
		-0.4	1.194	0.991	-0.646	0.862	-0.797	1.068
		-0.5	1.190	1.690	-0.646	1.646	-0.797	2.134
		-0.6	1.158	3.516	-0.807	2.433	-0.637	3.584
		-0.7	1.098	5.341	-0.646	4.327	-0.797	4.886
		-0.8	1.003	6.693	-0.807	5.327	-0.637	5.288
		-0.9	0.901	6.761	-0.807	-	-0.637	5.685
1.0	0.25	0.0	1.194	0.901	-0.646	0.745	-0.637	0.819
		-0.1	1.194	0.901	-0.606	0.719	-0.637	0.819
		-0.2	1.194	0.946	-0.646	0.765	-0.637	0.959
		-0.3	1.194	1.127	-0.646	0.778	-0.637	0.959
		-0.4	1.193	1.149	-0.646	1.098	-0.637	1.066
		-0.5	1.183	2.118	-0.646	1.698	-0.637	1.753
		-0.6	1.158	3.516	-1.055	3.568	0.000	3.231
		-0.7	1.091	5.612	-0.969	4.301	0.000	5.048
		-0.8	1.010	6.761	-2.642	5.409	1.530	5.171
		-0.9	0.885	7.843	-3.232	5.557	3.188	5.546
1.0	0.50	0.0	1.172	1.680	-0.646	2.042	-0.159	2.050
		-0.1	1.172	1.805	-0.646	1.805	-0.159	2.203
		-0.2	1.174	2.251	-0.646	1.953	0.000	2.209
		-0.3	1.179	2.299	-0.646	2.150	-0.159	2.475
		-0.4	1.172	2.411	-0.969	1.850	-0.159	2.147
		-0.5	1.167	3.074	-1.131	2.444	0.556	2.721
		-0.6	1.127	4.395	-1.707	3.280	0.797	3.186
		-0.7	1.055	5.950	-2.262	4.316	2.231	4.472
		-0.8	0.960	7.234	-3.706	5.334	3.188	5.613
		-0.9	0.842	7.978	-5.171	5.601	5.206	6.168
1.50	0.0	0.0	1.255	0.811	-0.323	0.626	-0.318	0.819
		-0.1	1.260	0.811	-0.646	0.626	-0.318	1.005
		-0.2	1.260	0.811	-0.646	0.626	-0.318	0.968
		-0.3	1.255	0.901	-0.323	0.609	-0.318	1.096
		-0.4	1.249	1.262	-0.646	0.691	-0.318	1.230
		-0.5	1.246	1.848	-0.646	2.307	-0.318	2.303
		-0.6	1.217	3.651	-0.484	3.700	-0.797	3.778
		-0.7	1.145	5.544	-0.807	4.533	-0.797	5.026
		-0.8	1.066	6.558	-0.807	5.648	-0.797	5.719
		-0.9	0.964	7.572	-0.807	6.154	-0.797	2.689
		-0.95	0.824	11.630	-0.807	5.475	-0.797	

*For the $\bar{W}$ and $\tilde{w}$ measurements the absolute values of the coordinate $x_{2/D}$ correspond to $-x_{3/D}$ and of the coordinate $x_{3/D}$ to $x_{2/D}$.

D_H	$x_{2/D}$	$x_{3/D}$	$\bar{U}/V$	$\tilde{u}/V_c$ x10^2	$\bar{V}/V_c$ x10^2	$\tilde{v}/V_c$ x10^2	$\bar{W}/V_c$ x10^2	$\tilde{w}/V_c$ x10^2
1.50	0.25	0.0	1.258	0.856	-0.646	0.672	-0.318	1.051
		-0.1	1.258	0.856	-0.646	0.699	-0.318	1.051
		-0.2	1.258	0.901	-0.646	0.719	-0.159	1.033
		-0.3	1.258	0.946	-0.517	0.765	-0.159	1.051
		-0.4	1.258	1.217	-0.646	1.142	-0.159	1.678
		-0.5	1.246	2.254	-0.807	2.145	-0.159	2.369
		-0.6	1.201	4.327	-0.969	2.943	-0.159	3.698
		-0.7	1.140	5.612	-1.454	4.834	0.478	5.175
		-0.8	1.055	6.693	-2.544	5.373	1.594	5.367
		-0.9	0.947	7.532	-4.124	5.982	3.188	5.803
1.50	0.325	0.0	1.274	1.059	-0.646	1.054	-0.318	1.051
		-0.1	1.274	1.037	-0.646	1.147	-0.318	1.051
		-0.2	1.271	1.082	-0.646	1.122	-0.318	1.051
		-0.3	1.274	1.172	-0.807	1.119	-0.159	1.149
		-0.4	1.269	1.442	-0.969	1.443	0.398	1.548
		-0.5	1.254	2.817	-1.311	2,561	0.669	2.337
		-0.6	1.195	5.000	-2.101	3.583	1.147	3.515
		-0.7	1.123	6.355	-3.236	5.067	2.550	4.903
		-0.8	1.029	7.201	-4.871	5.783	4.622	5.717
		-0.9	0.926	7.883	-7.195	6.048	6.694	6.244
1.75	0.0	0.0	1.316	0.901				
		-0.1	1.316	0.901				
		-0.2	1.316	0.946				
		-0.3	1.316	0.991				
		-0.4	1.311	1.442				
		-0.5	1.293	3.110				
		-0.6	1.253	4.703				
		-0.7	1.189	5.986				
		-0.8	1.113	6.699				
		-0.9	1.036	7.269				
1.75	0.125	0.0	1.307	0.856	-0.646	0.719	-0.478	0.872
		-0.1	1.307	0.901	-0.646	0.745	-0.478	0.961
		-0.2	1.307	0.901	-0.646	0.773	-0.318	0.959
		-0.3	1.307	0.991	-0.646	0.786	-0.318	1.005
		-0.4	1.307	1.127	-0.646	1.210	-0.159	1.883
		-0.5	1.298	2.402	-0.807	1.743	0.000	2.248
		-0.6	1.256	4.192	-1.417	3.542	0.318	4.235
		-0.7	1.197	5.544	-2.101	4.955	1.274	5.482
		-0.8	1.121	7.572	-3.210	5.487	2.039	5.589
		-0.9	1.030	8.056	-3.393	5.784	3.505	6.139

D_H	$x_{2/D}$	$x_{3/D}$	$\overline{U}/V_c$	$\tilde{u}/V_c$ x10^2	$\overline{V}/V_c$ x10^2	$\tilde{v}/V_c$ x10^2	$\overline{W}/V_c$ x10^2	$\tilde{w}/V_c$ x10^2
1.75	0.25	0.0	1.307	0.946	-0.646	-	0.015	-
		-0.1	1.307	0.946	-0.646	-	0.015	-
		-0.2	1.307	1.014	-0.646	-	0.015	
		-0.3	1.307	1.104	-0.807	-	0.337	
		-0.4	1.302	1.532	-0.807	-	0.467	
		-0.5	1.284	3.178	-1.660	-	1.146	
		-0.6	1.239	4.847	-2.224	-	1.377	
		-0.7	1.181	6.130	-3.334	-	2.422	
		-0.8	1.086	7.271	-5.171	-	4.302	
		-0.9	0.987	7.984	-7.093	-	6.697	

APPENDIX 2

Estimation of the cross-stream pressure variation

Referring to figure 5, consider the centripetal force balance due to the streamline curvature for the fluid particle shown :

$$\delta m \frac{V^2}{R} = \delta p \ (\delta x \cdot \delta y) \qquad (1)$$

{where · $\delta m = \rho(\delta x \cdot \delta y \cdot \delta r)$ is the mass of the fluid particle,
· δp is the difference in pressure across the particle in the r direction
· R is the radius of curvature of the streamline}

Hence

$$\rho \frac{V^2}{R} = \frac{\delta p}{\delta r} \qquad (2)$$

Using the following approximations

$$V \simeq U_B$$

$$\frac{\delta p}{\delta r} \simeq \frac{p_2 - p_1}{D/2}$$

{where · U_B is a representative streamwise velocity,
· D is the hydraulic diameter of the duct
· p_2 and p_1 are defined in figure 5}

$$p_2 - p_1 \simeq \rho \frac{U_B^2}{R} \frac{D}{2} \qquad (3)$$

Considering motion in the cross-stream plane (refer to figure 4 (c)) and applying Bernoulli's equation between points near the fillet and points near $x_2 \simeq x_3 \simeq D$

$$\Delta U \simeq \left(\frac{p_2 - p_1}{\frac{1}{2}\rho} \right)^{\frac{1}{2}} \qquad (4)$$

{where ΔU is the induced cross-stream velocity}

Eliminating the term for $(p_2 - p_1)$ in (4) using (3) there results

$$\Delta U \simeq \left(\frac{U_B^2 D}{R} \right)^{\frac{1}{2}}$$

$$\frac{\Delta U}{U_B} \simeq 0.2 \left(\frac{1}{R} \right)^{\frac{1}{2}}, \text{ for } D = 0.04 \text{ m.} \qquad (5)$$

An estimate for R, derived in figure 5, is R > 1·5 m. and hence $\frac{\Delta U}{U_B} < 0.16$: Viscous forces will act so as to lessen the magnitude further still.

APPENDIX 3 - NOMENCLATURE

D	defined as $D_H/2$
D_H	hydraulic diameter (40mm)
U	mean component along X_1 co-ordinate direction
$\tilde{u}$	r.m.s. component along X_1 co-ordinate direction
$\overline{uv}$	cross correlation of fluctuation in $X_1 \sim X_2$ plane
$\overline{uw}$	cross correlation of fluctuation in $X_1 \sim X_3$ plane
V	mean component along X_2 co-ordinate direction
V_c	bulk mean velocity defined in square section
$\tilde{v}$	r.m.s. component along X_2 co-ordinate direction
W	mean component along X_3 co-ordinate direction
$\tilde{w}$	r.m.s. component along X_3 co-ordinate direction
X_1, X_2, X_3	defined in figure 1

REFERENCES

1. Melling, A., and Whitelaw, J.H., (1976), "Turbulent Flow in a Rectangular Duct", J. Fluid Mech., 78, 289.

2. Taylor, A.M.K.P., Whitelaw, J.H., and Yianneskis, M., (1980), "Measurements of Laminar and Turbulent Flow in a Curved Duct with Thin Inlet Boundary Layers", report submitted as NASA Contractor Report.

3. Mayer, E., (1938), "Einfluss der Querschnittsverformung auf die Entwicklung der Geschwindigkeits- und Druckverteilung bei turbulenten Strömungen in Rohren", VDI-Forschungsheft 389.

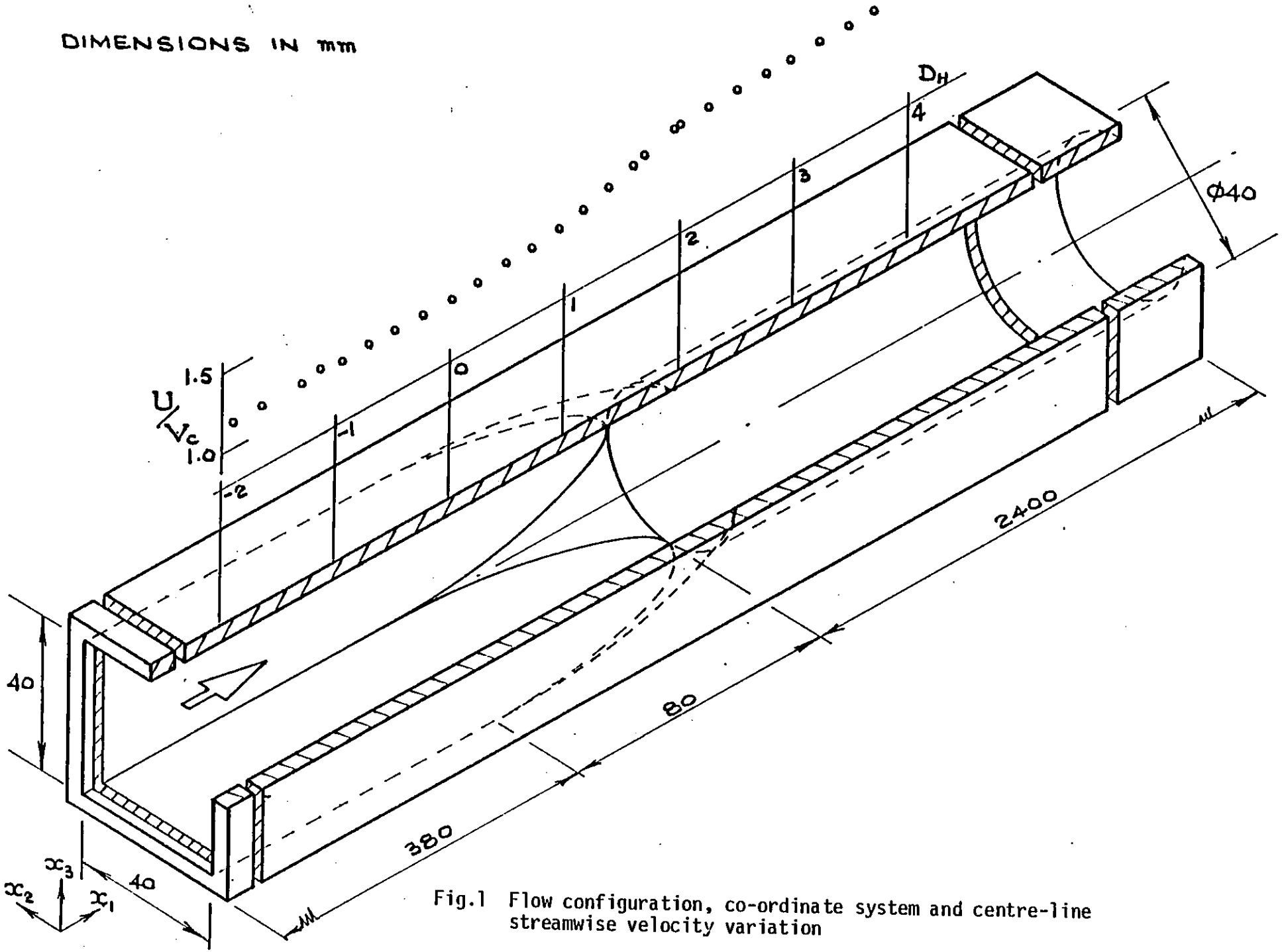


Fig.1 Flow configuration, co-ordinate system and centre-line streamwise velocity variation

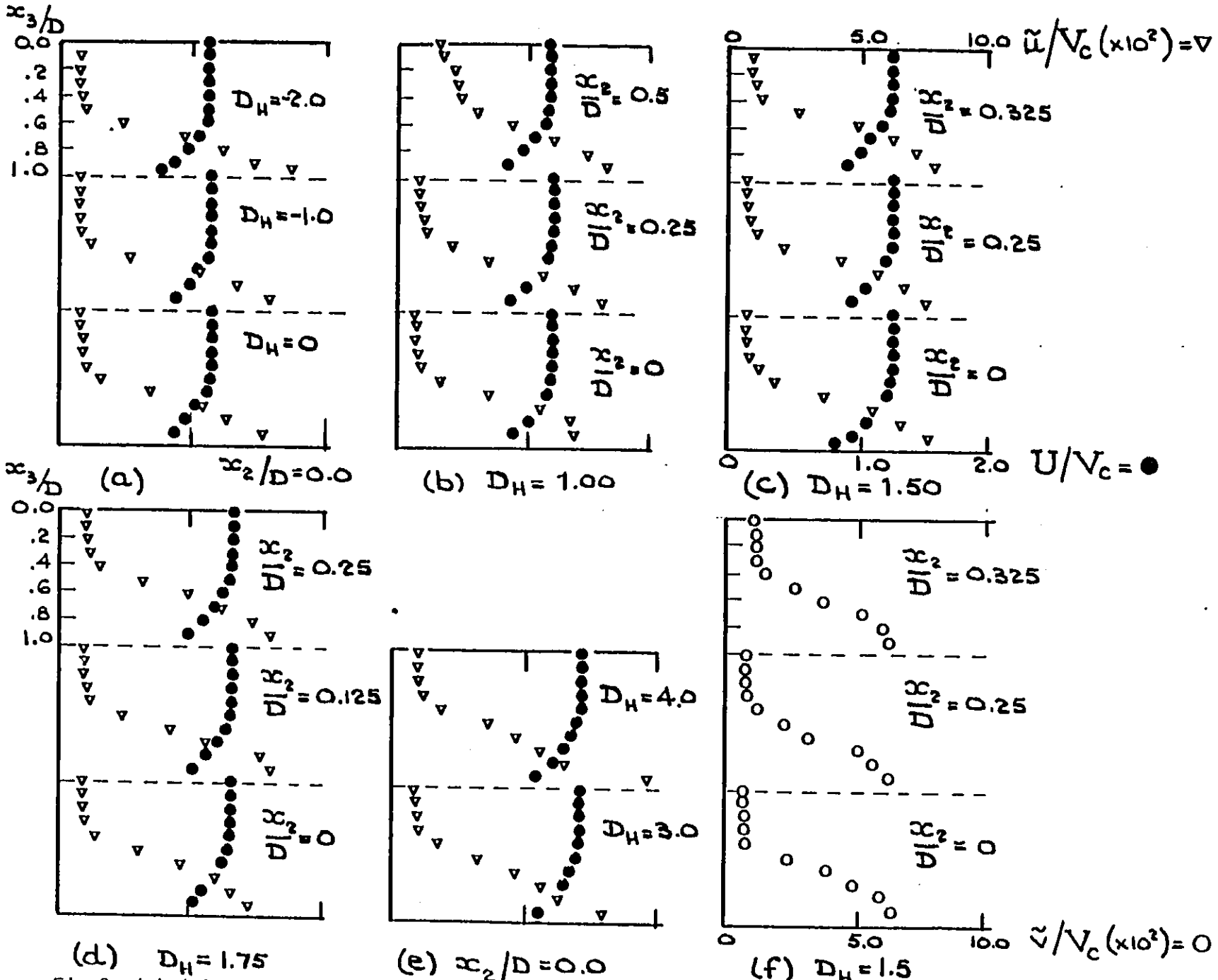


Fig.2 (a)-(e) : Streamwise velocity profiles and turbulence levels;
(f) : Cross-stream turbulence levels

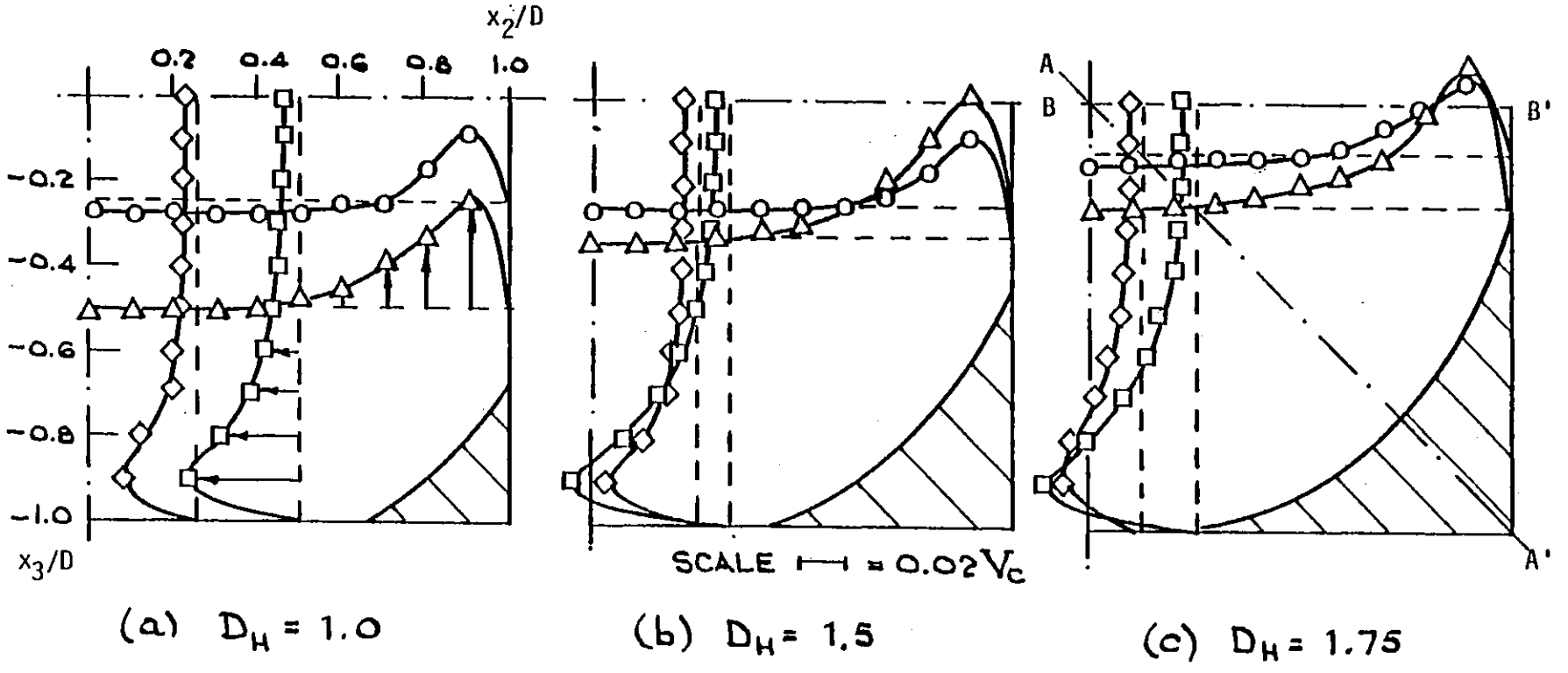


Fig.3 Secondary velocity profiles

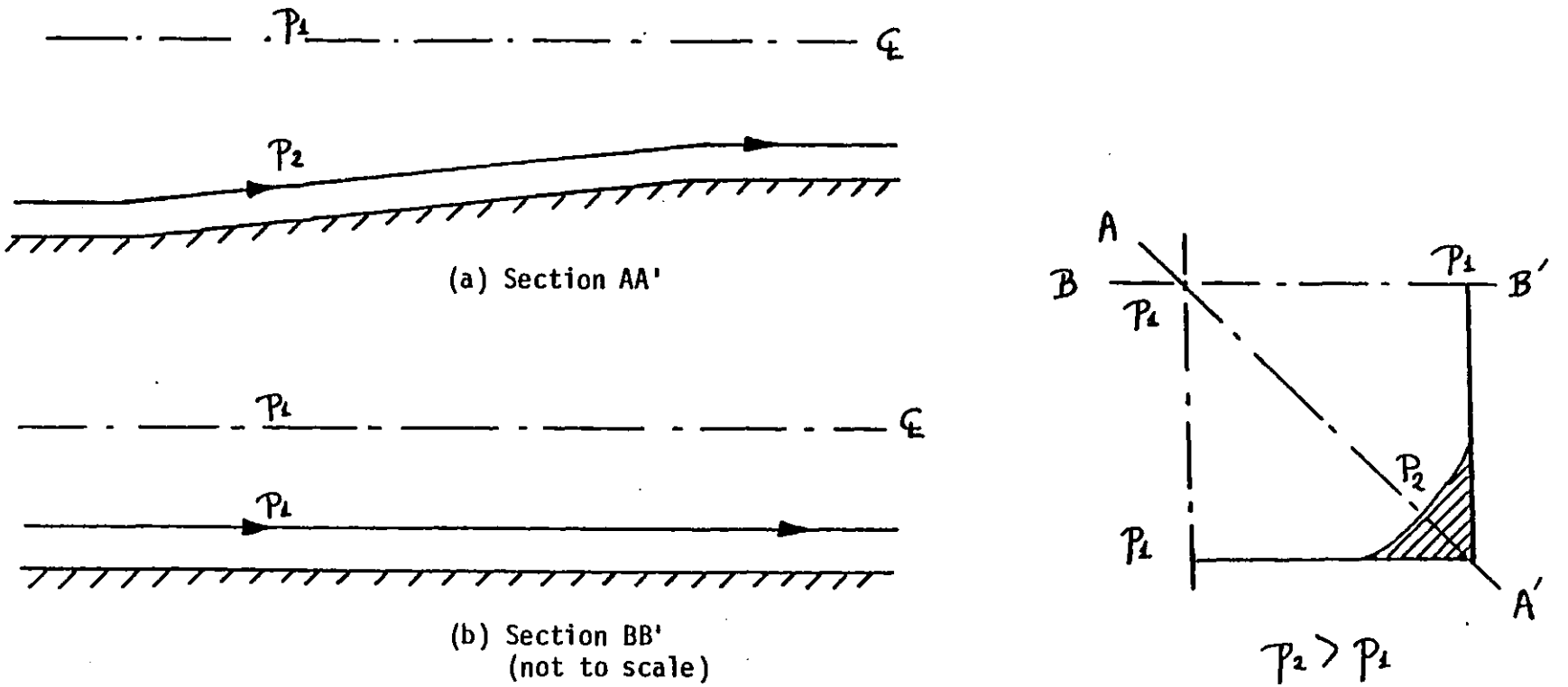
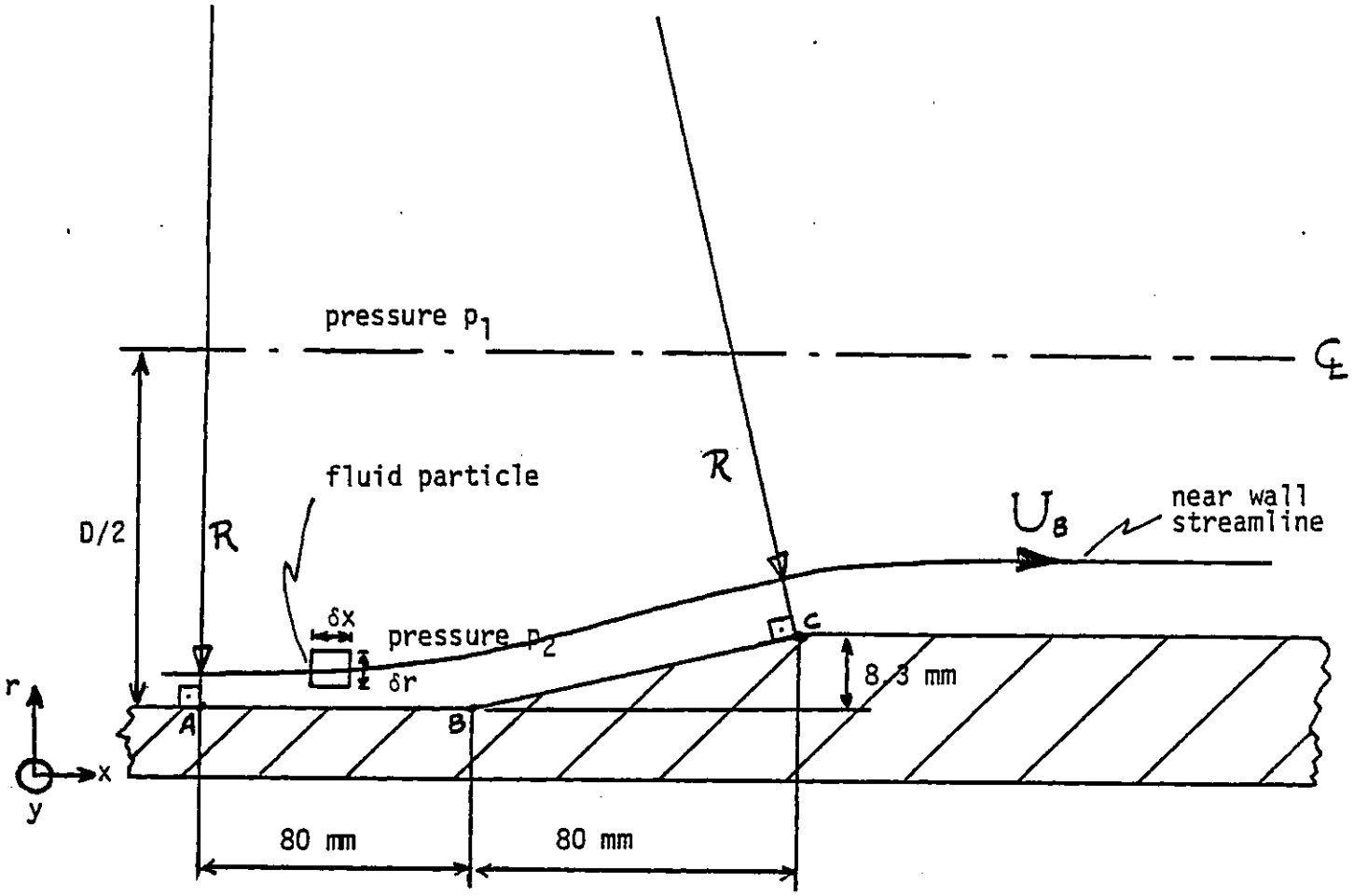


Fig.4 Effect of longitudinal streamline curvature on cross-stream pressure variation



Note: radius of curvature of streamline approximated as radius of circle which inscribes points A, B, C. Hence R ≈ 1.5 m.

Fig.5 Definition sketch for the estimation of the cross-stream pressure variation (Appendix 2).

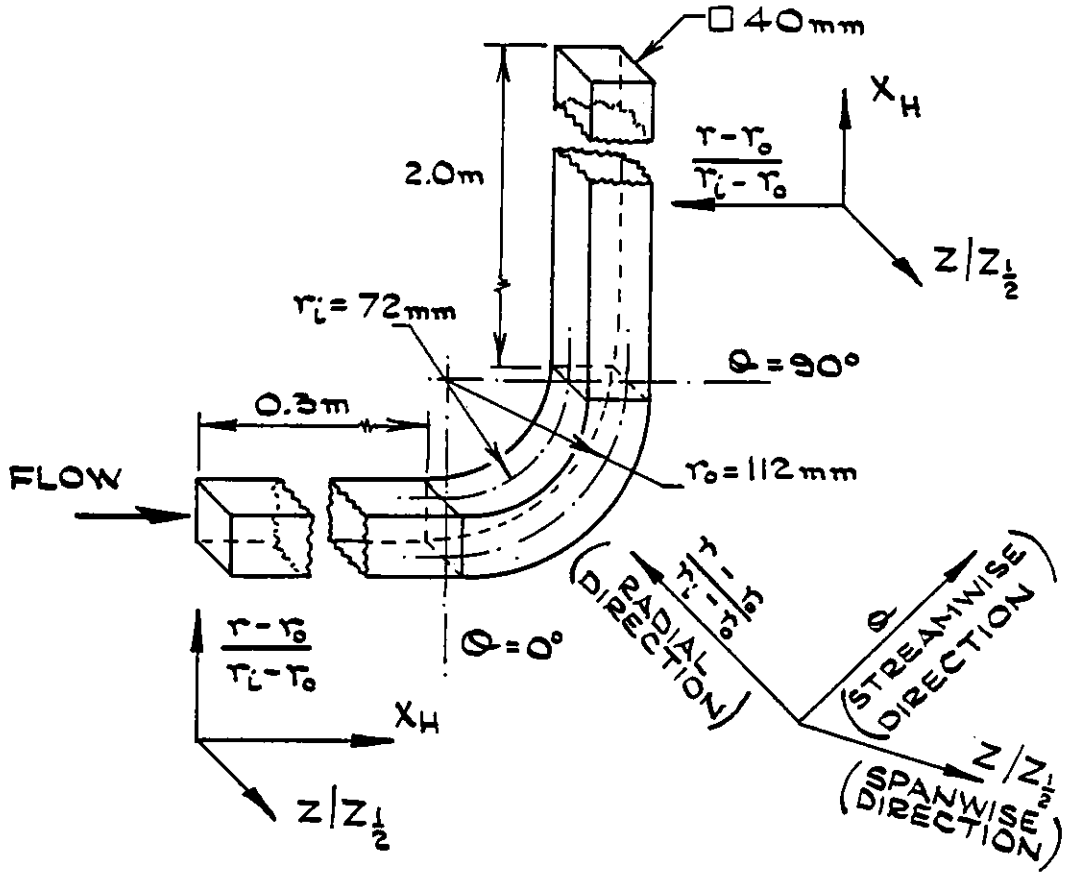


Figure 3.1 Dimensions of bend and coordinate definition sketch

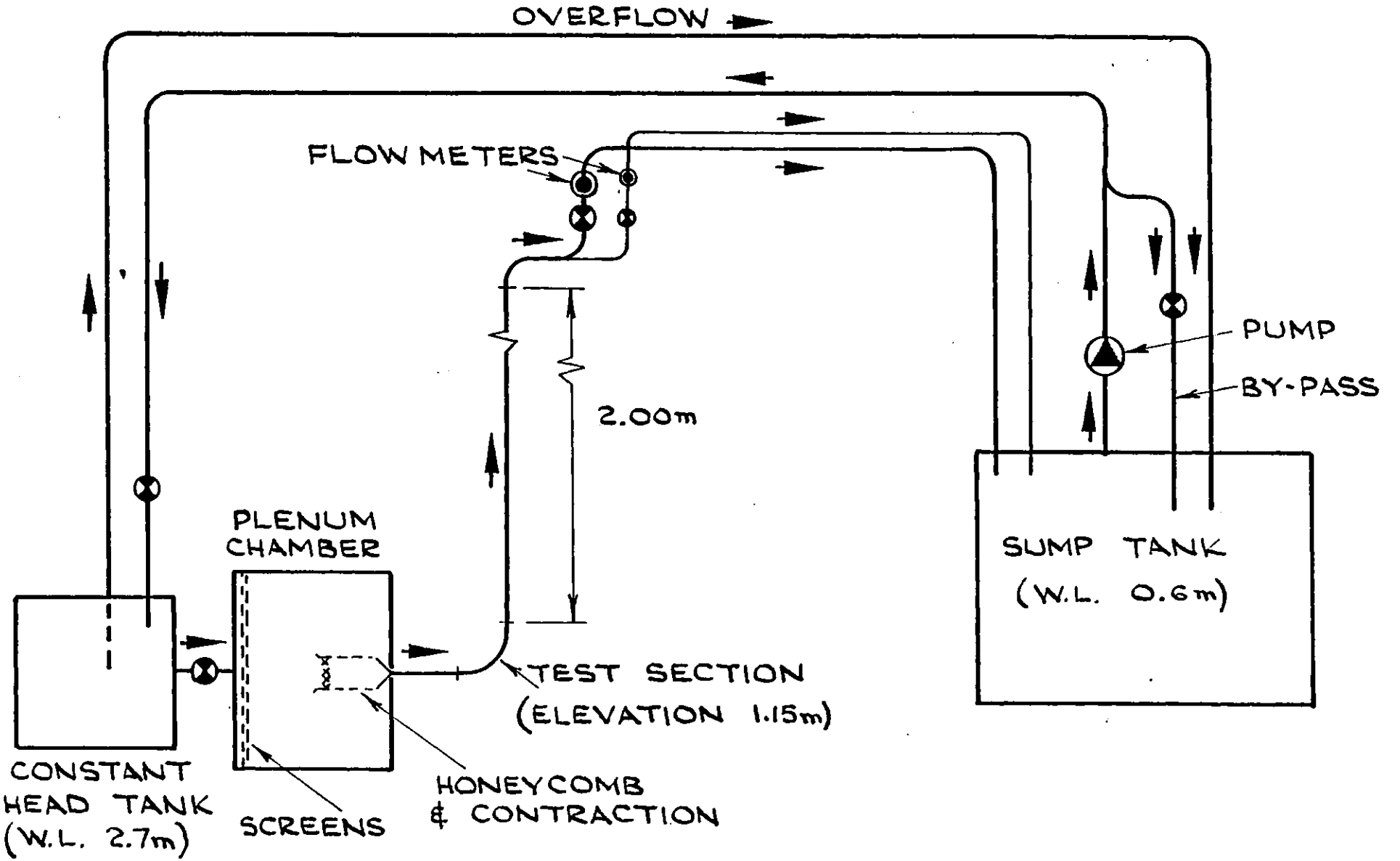


Figure 3.2 Plan view of water tunnel

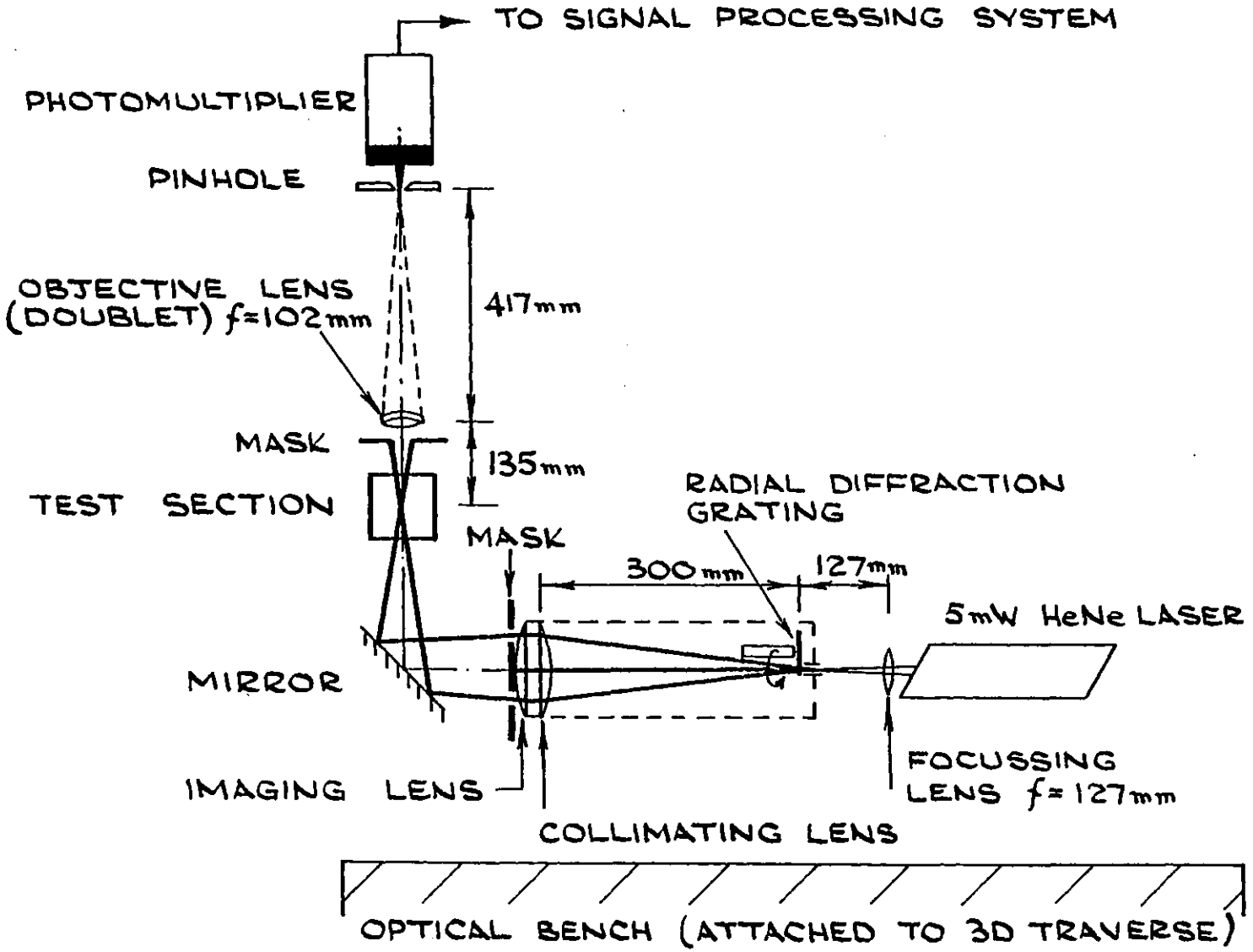


Figure 3.3 (i) Schematic diagram of laser Doppler anemometer optical system

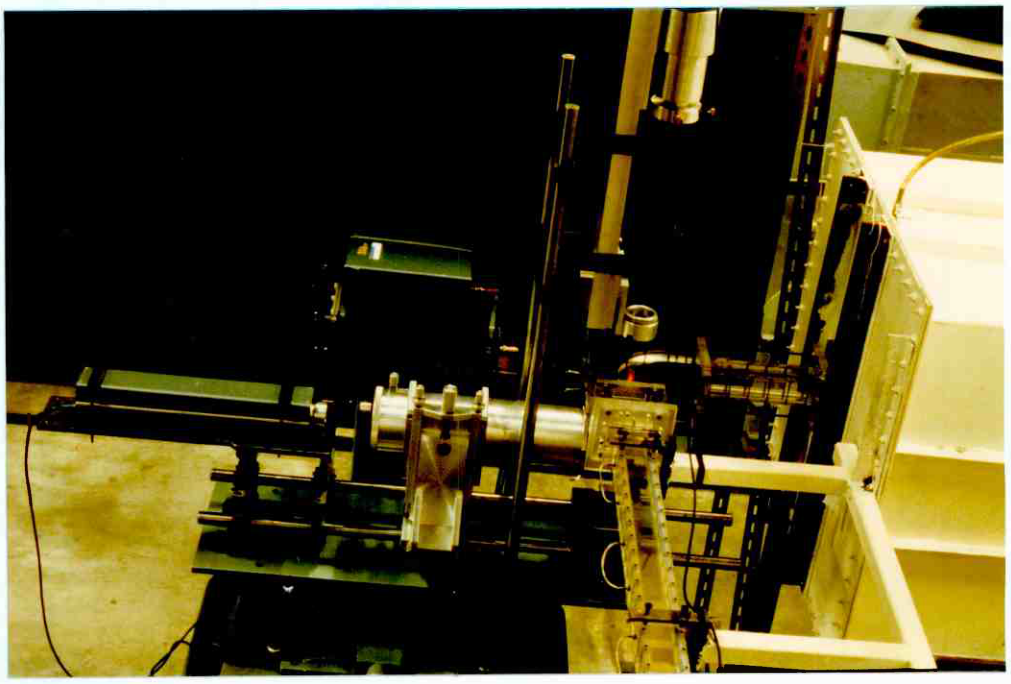


Figure 3.3(ii) Photograph of the optical system

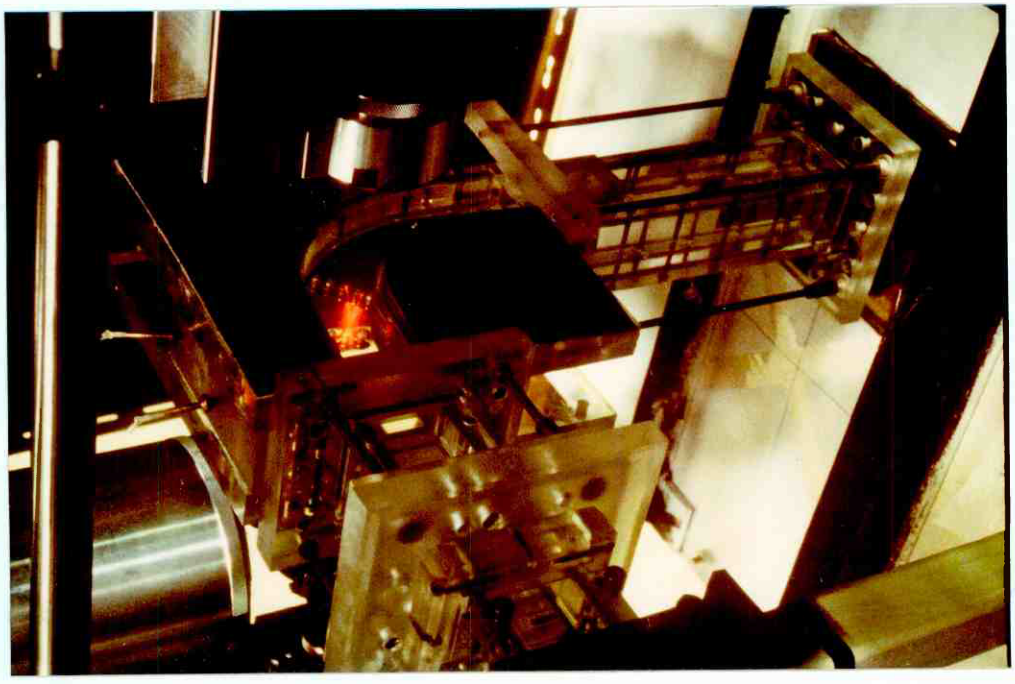


Figure 3.3(iii) Photograph of the bend showing intersection volume

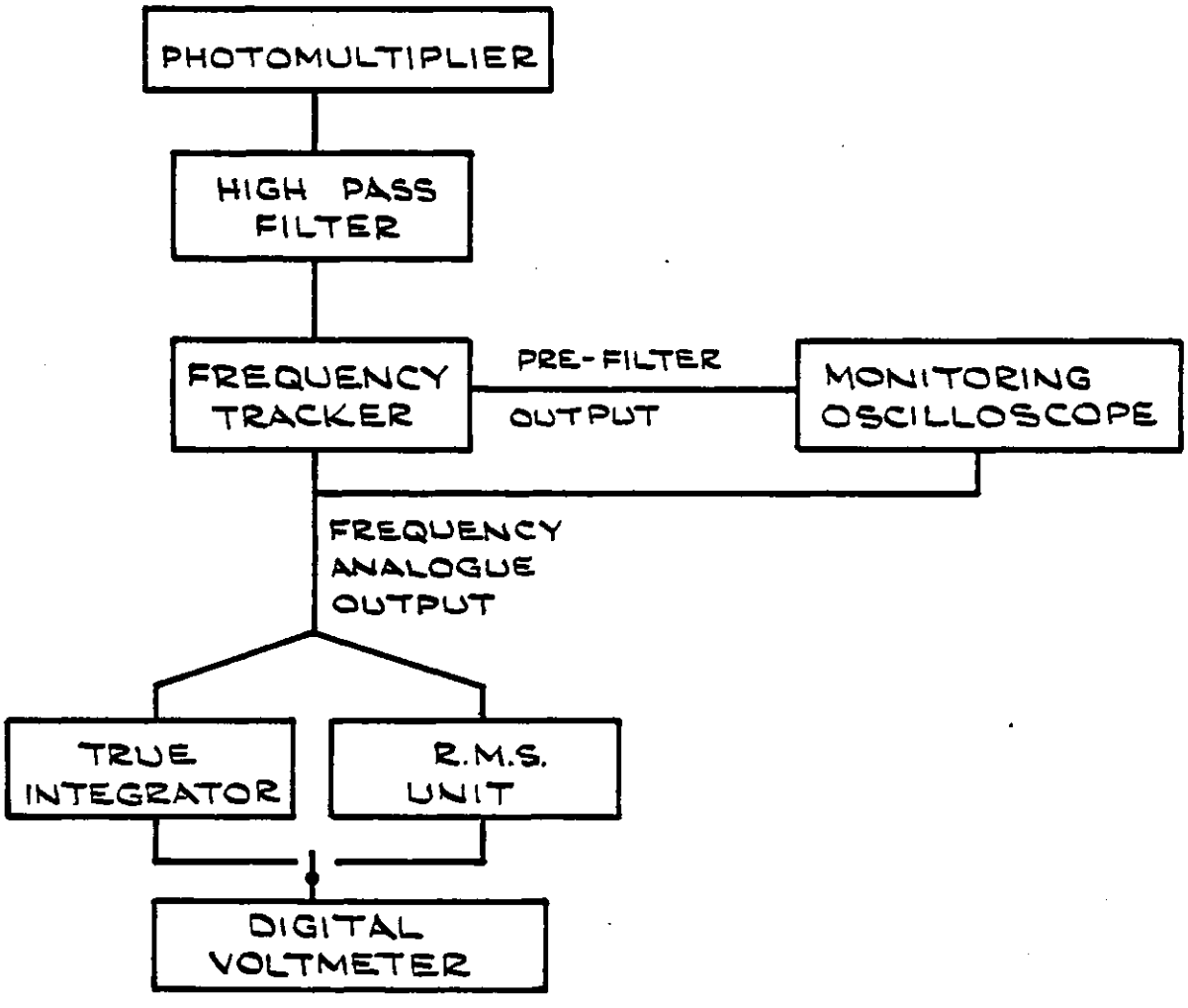


Figure 3.4 Block diagram of laser Doppler anemometer signal processing arrangement

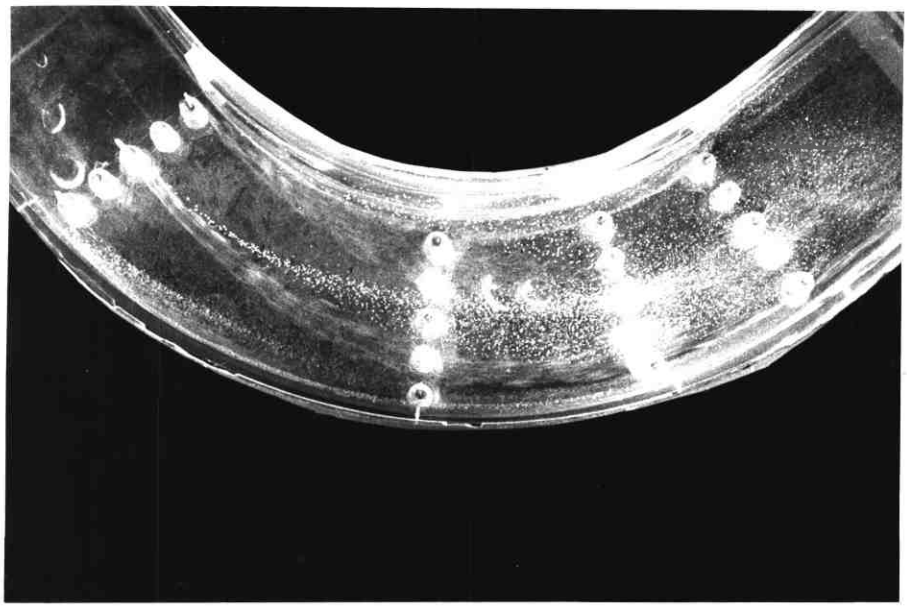


Figure 3.5(a) Flow visualisation at Re = 790; flow direction left to right; wires inserted at $r^* = 0.1$, 0.5 and 0.9
(i) wires located at $\theta = 0^o$

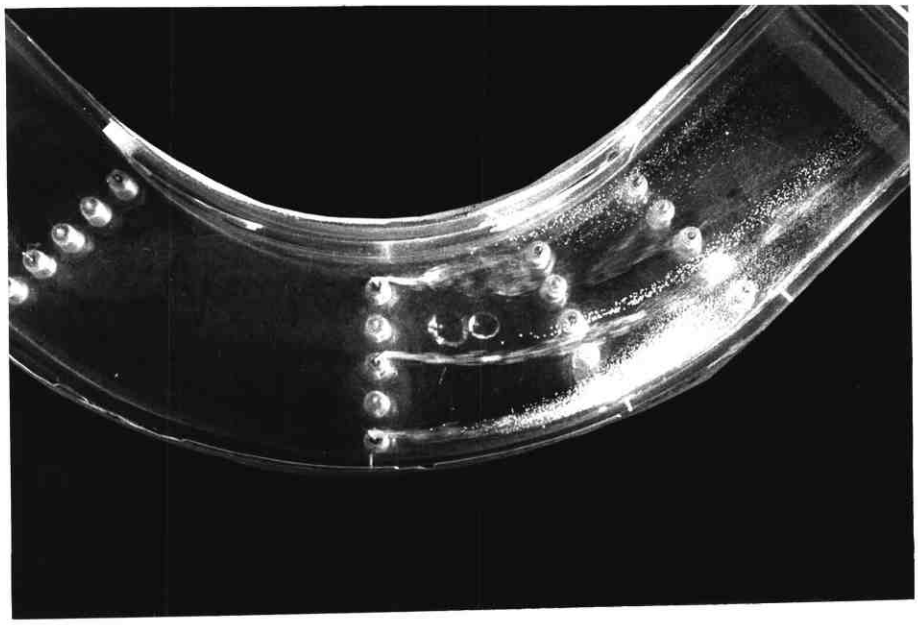


Figure 3.5(a) (cont.)
(ii) wires located at $\theta = 45^o$

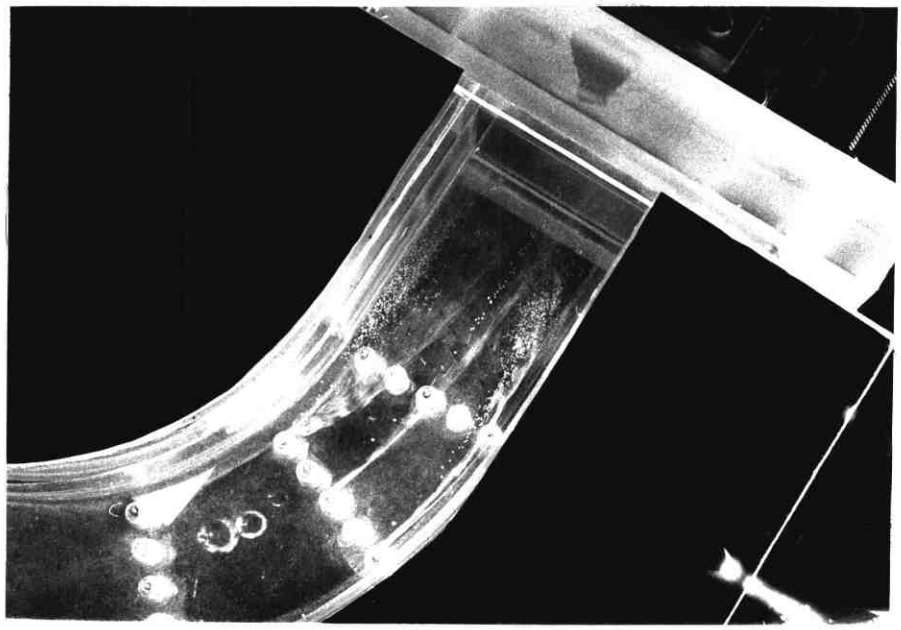


Figure 3.5(a) (cont.)
(iii) wires located at $\theta = 71^{o}$

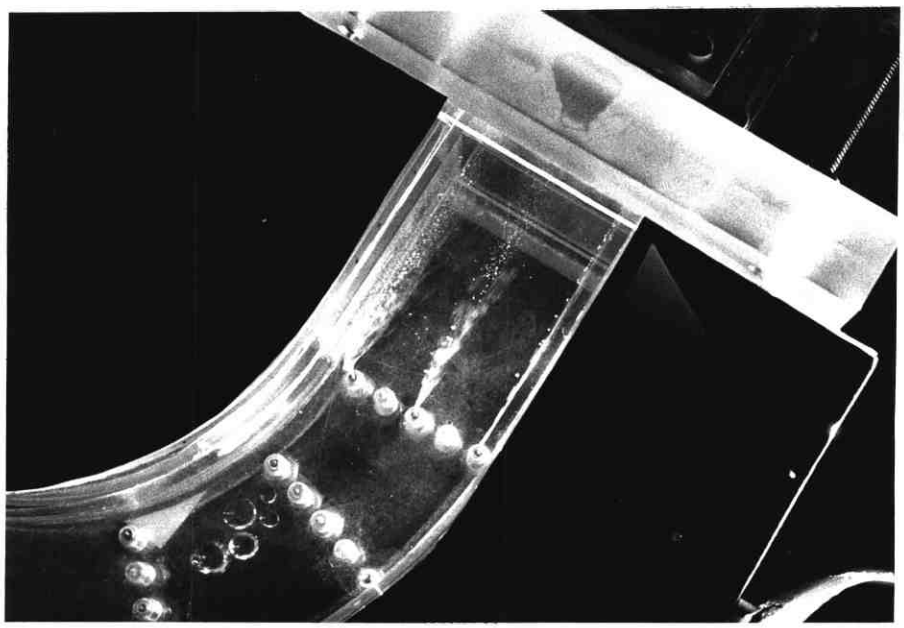


Figure 3.5(a) (cont.)
(iv) wires located at $\theta = 90^{o}$

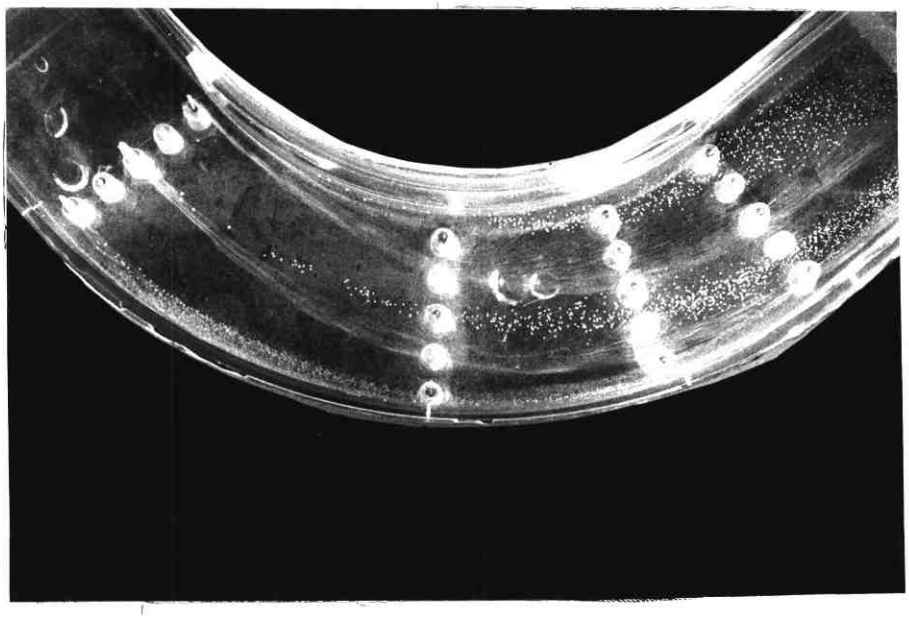


Figure 3.5(b) Flow visualisation at Re = 1275; flow direction left to right; wires inserted at r* = 0.1, 0.5 and 0.9
(i) wires located at $\theta = 0^{o}$

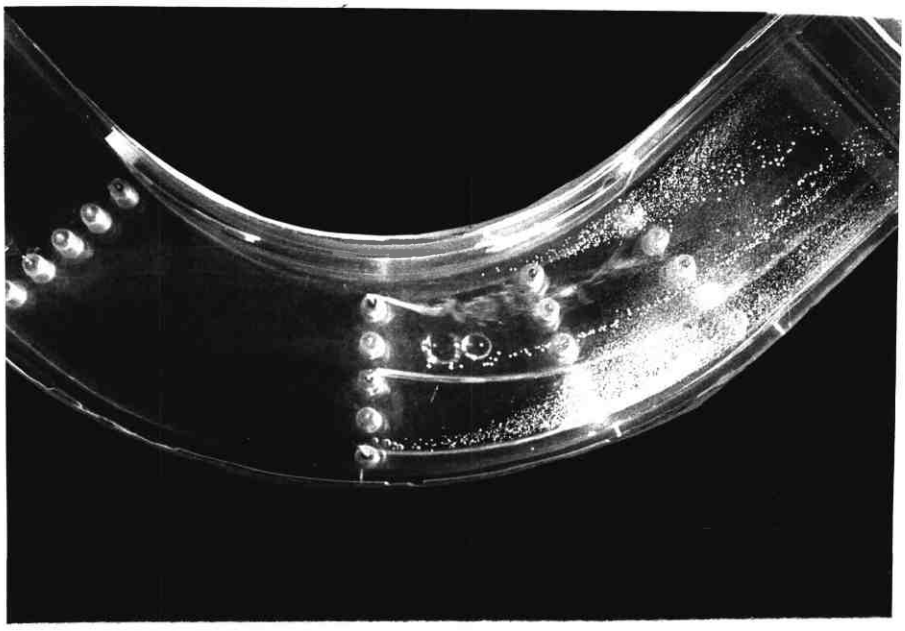


Figure 3.5(b) (cont.)
(ii) wires located at $\theta = 45^{o}$

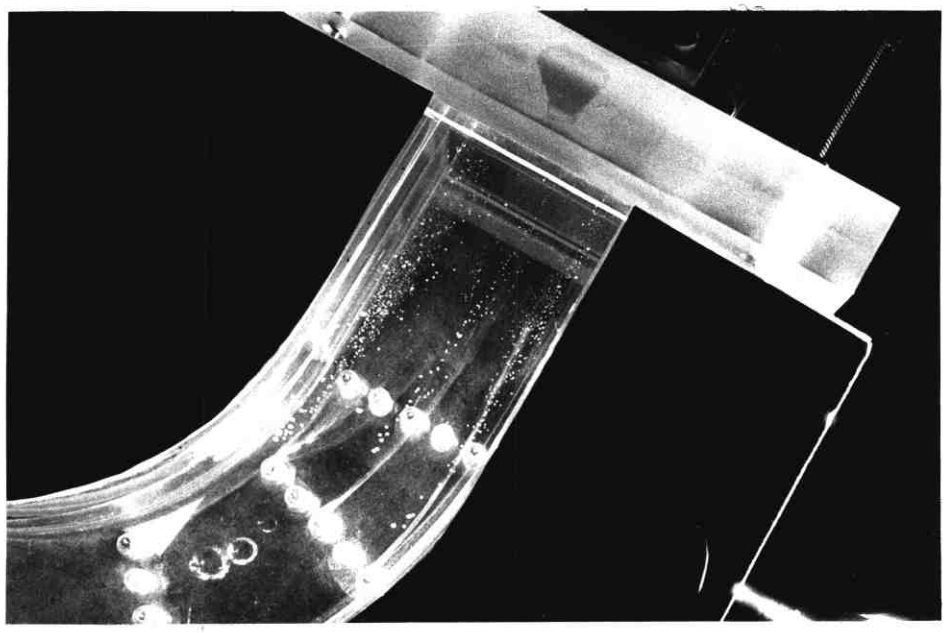


Figure 3.5(b) (cont.)
(iii) wires located at $\theta = 71^{o}$

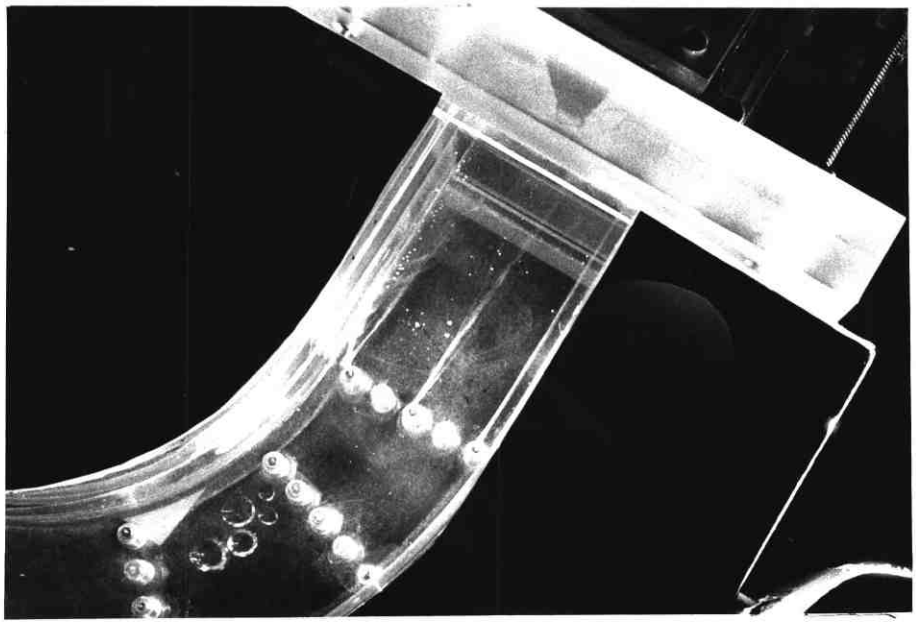


Figure 3.5(b) (cont.)
(iv) wires located at $\theta = 90^{o}$

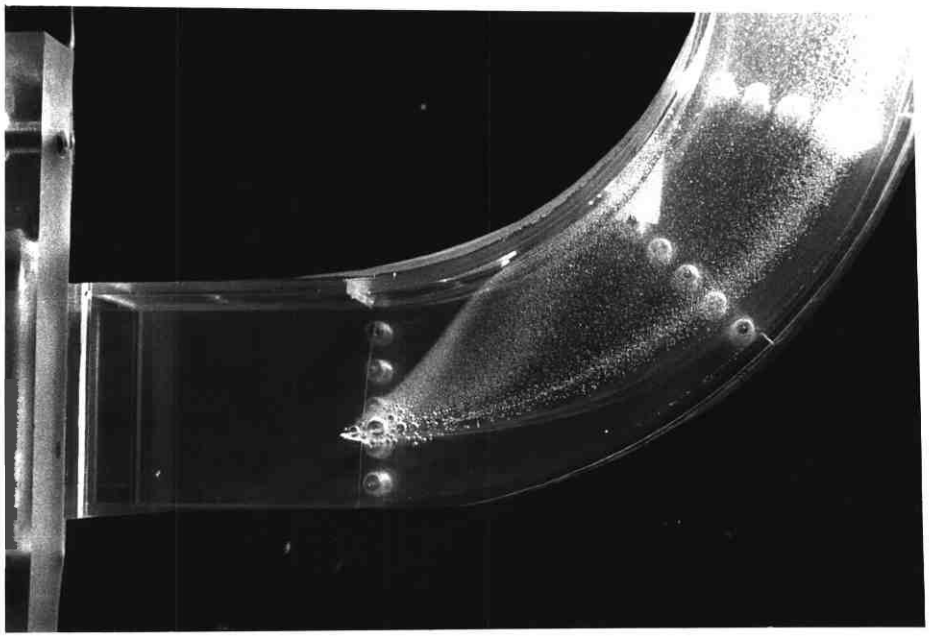


Figure 3.5(c) Visualisation of secondary flow near top side wall at Re = 1275
wire inserted at $\theta = 0^{o}$, $r^{*} = 0.3$; flow direction left to top right

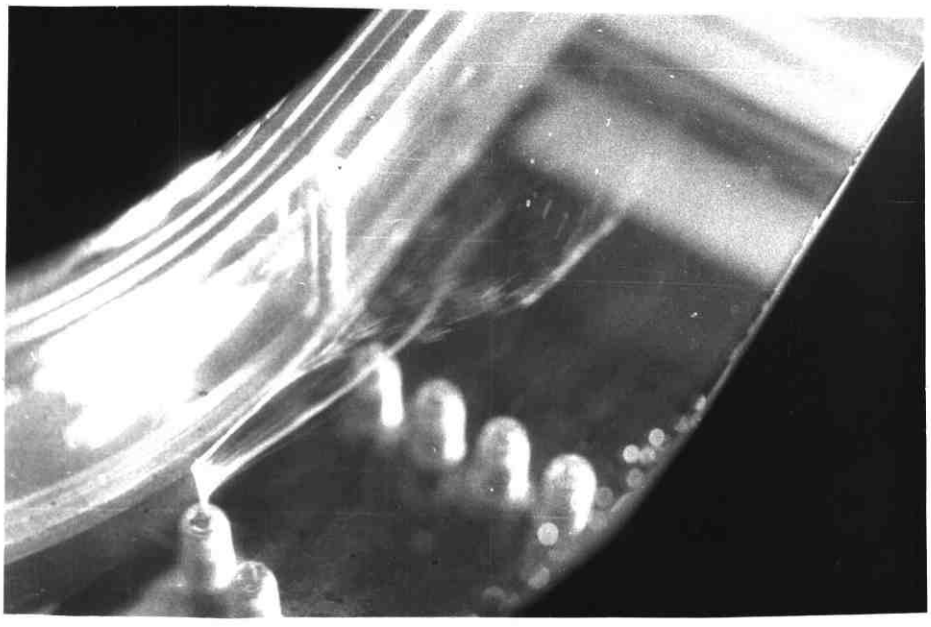


Figure 3.5(d) Visualisation of helical secondary flow near inner wall at Re $\simeq$ 3000
wire inserted at $\theta = 71^{o}$, $r^{*} = 0.9$; flow direction bottom left to top right

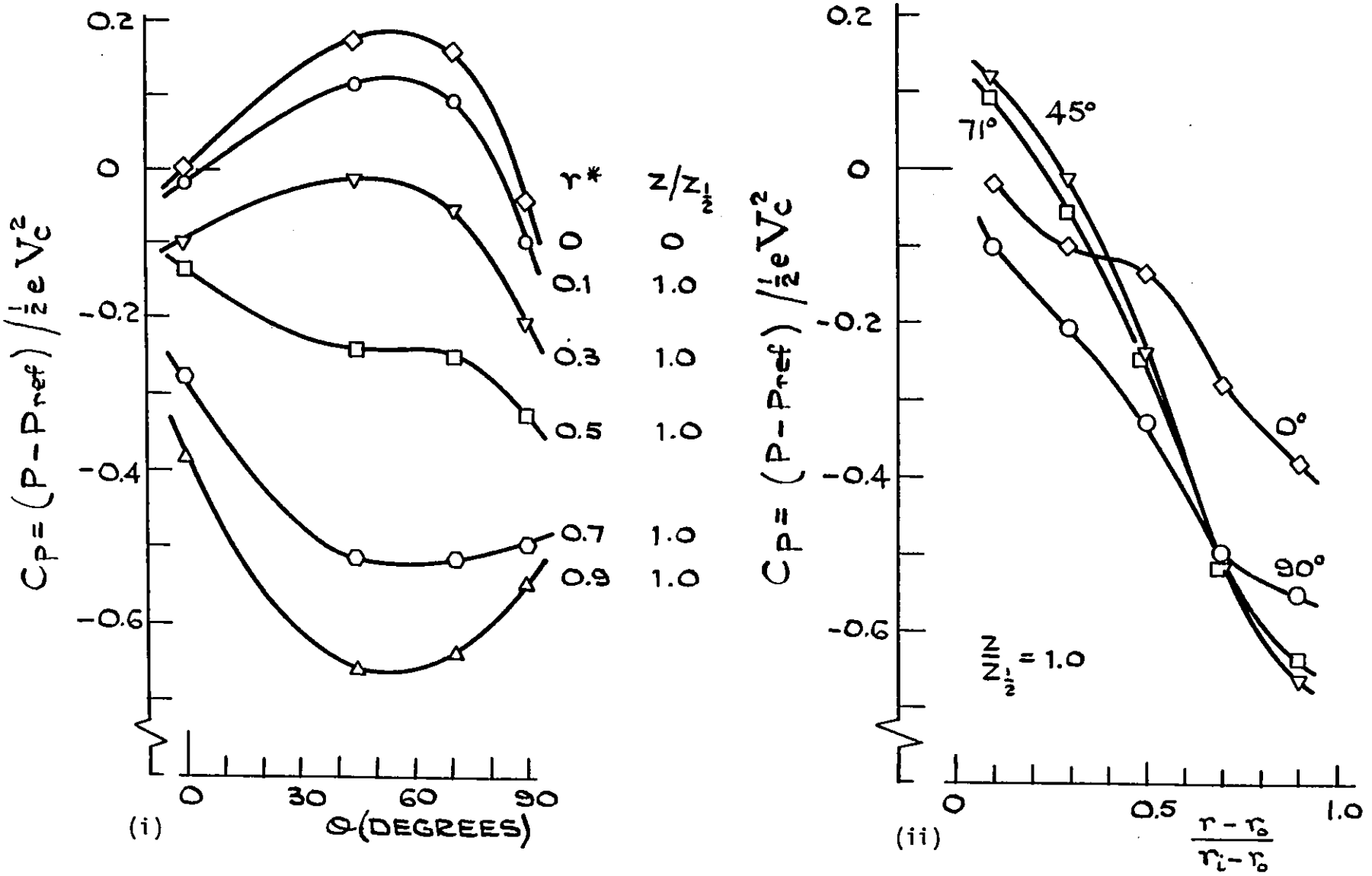


Figure 3.6 Turbulent flow: wall static pressure measurements
(i) streamwise distribution (ii) radial distribution

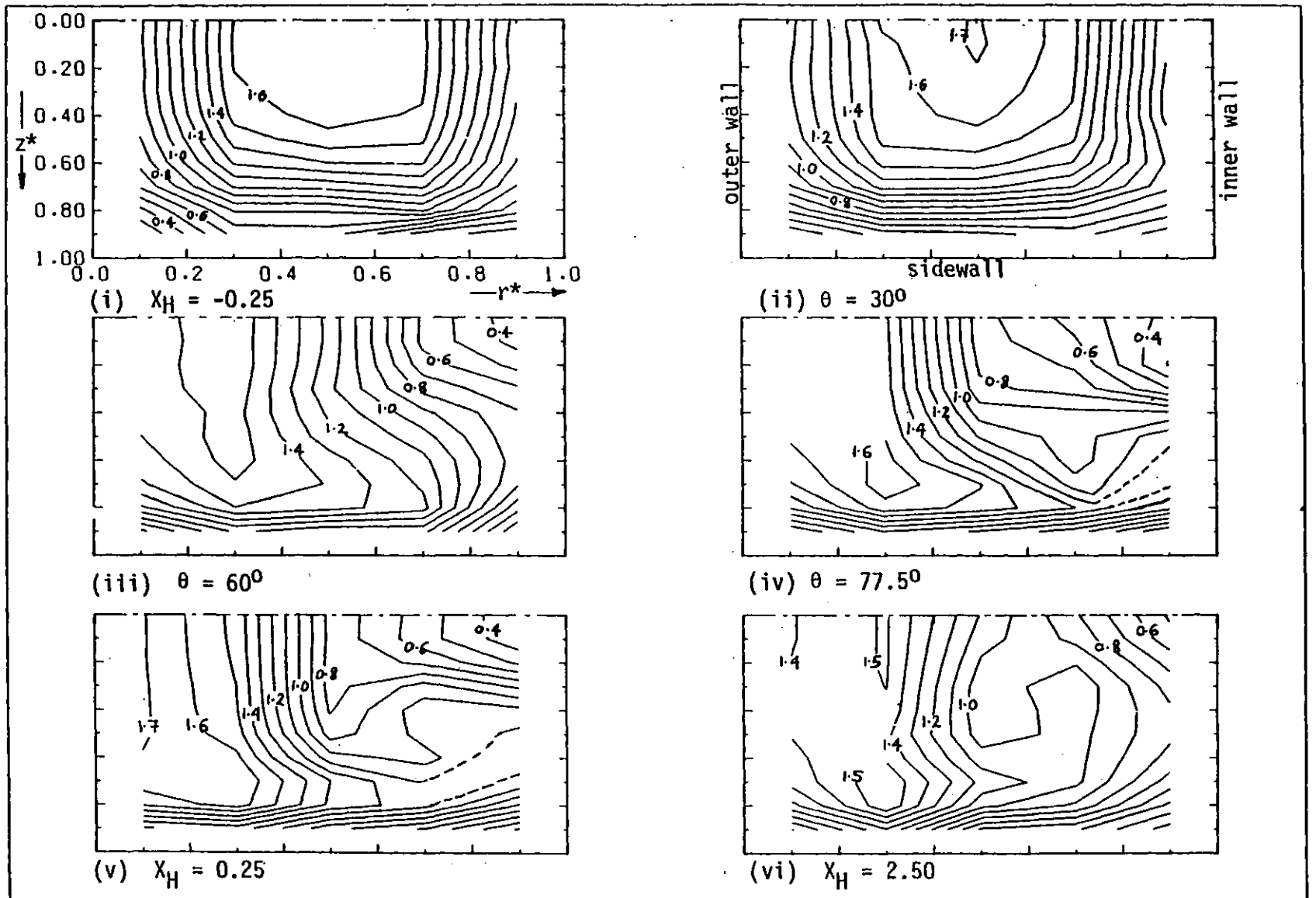


Figure 3.7 Laminar flow: isotachs of U/V_c

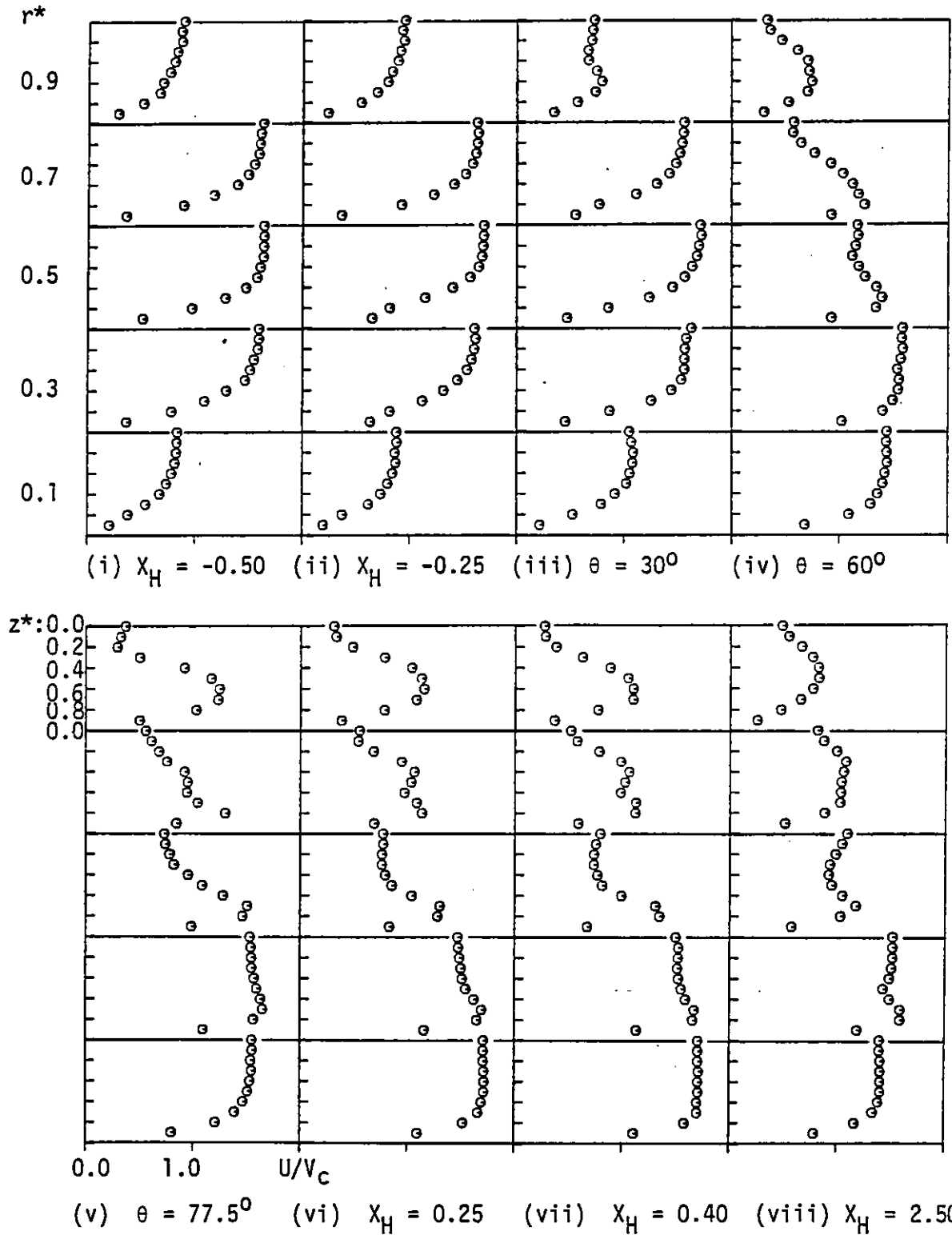


Figure 3.8 Laminar flow: profiles of U/V_C

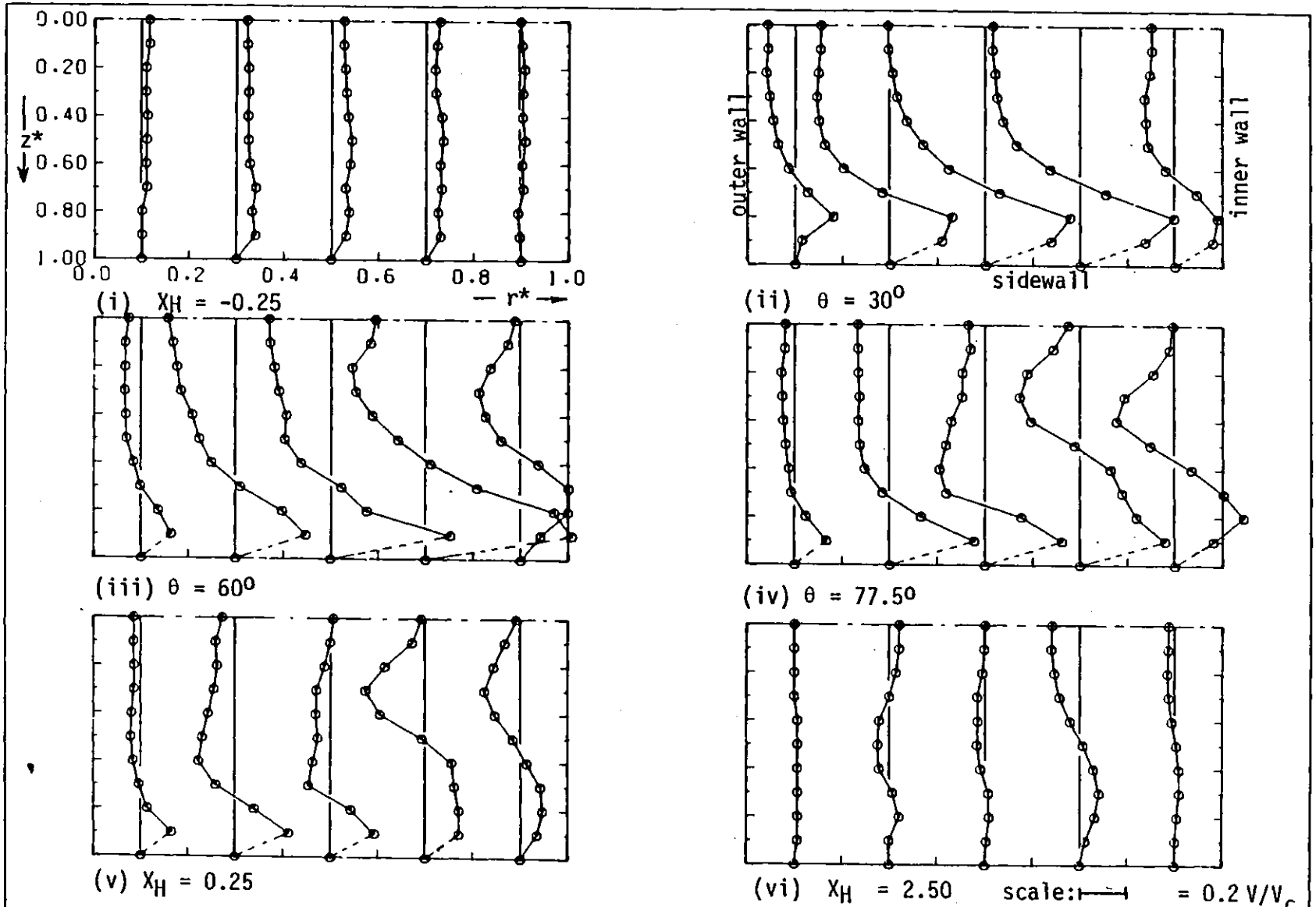


Figure 3.9 Laminar flow: profiles of V/V_c

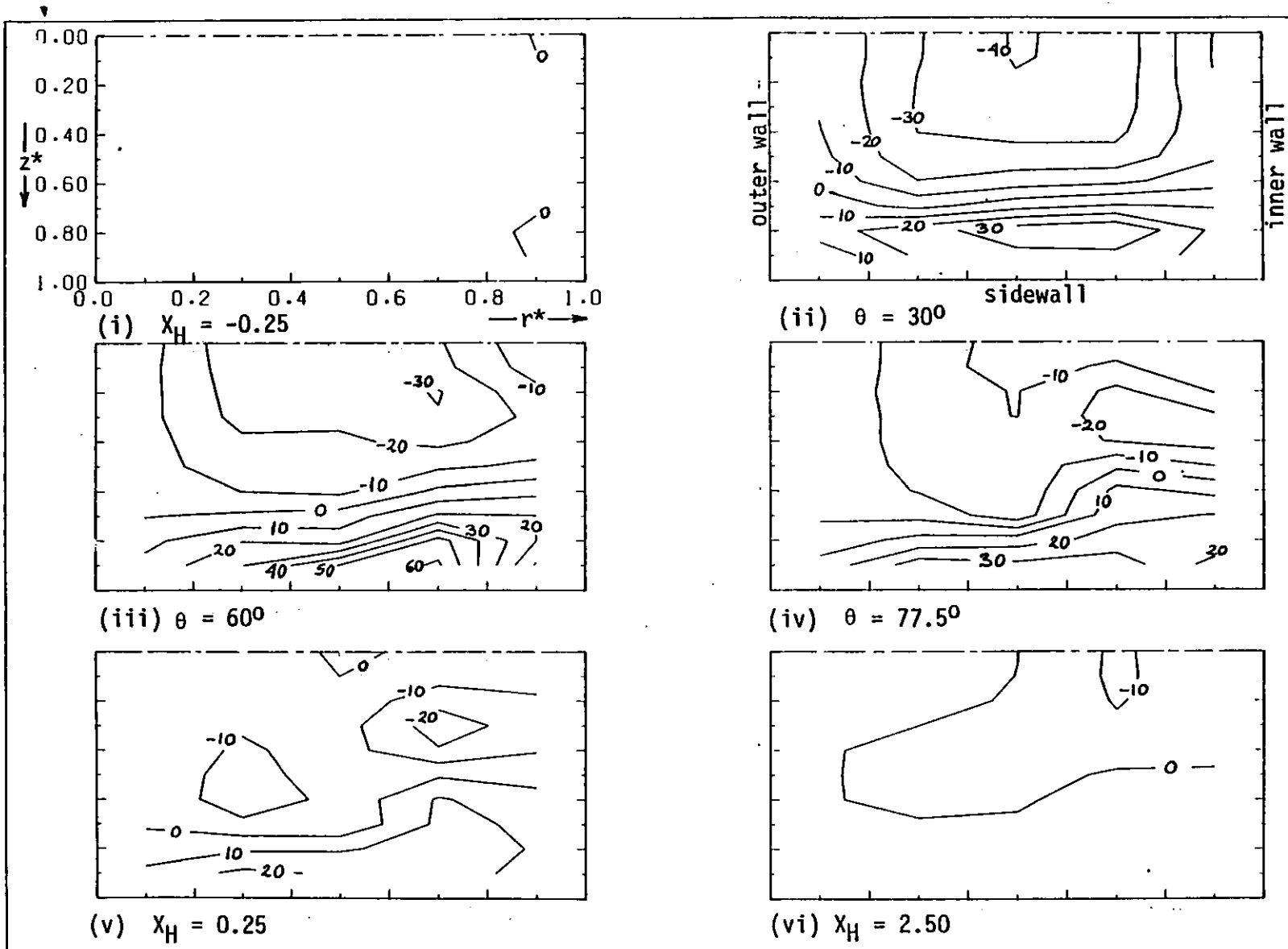


Figure 3.10 Laminar flow: isotachs of V/V_c

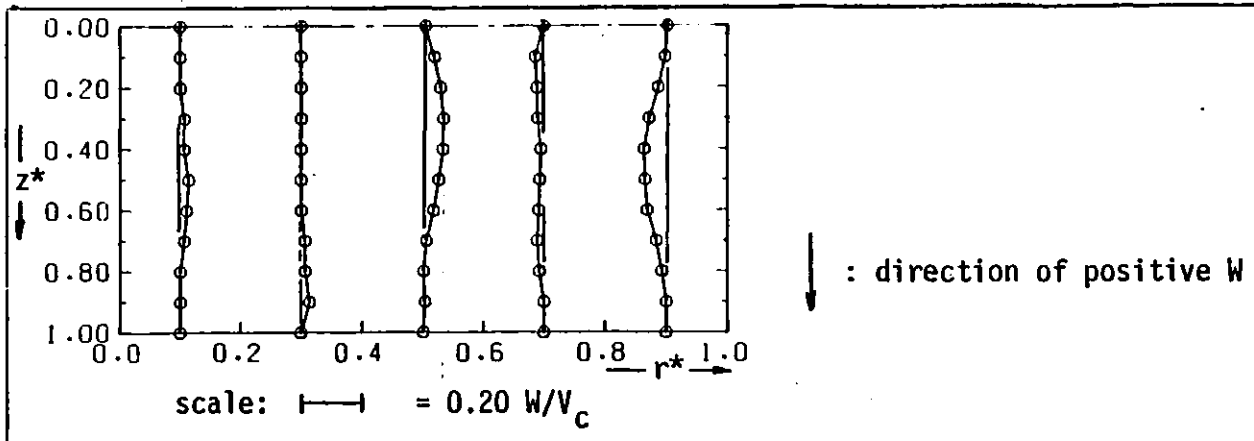


Figure 3.11 Laminar flow: profiles of W/V_c at $X_H = 2.50$.

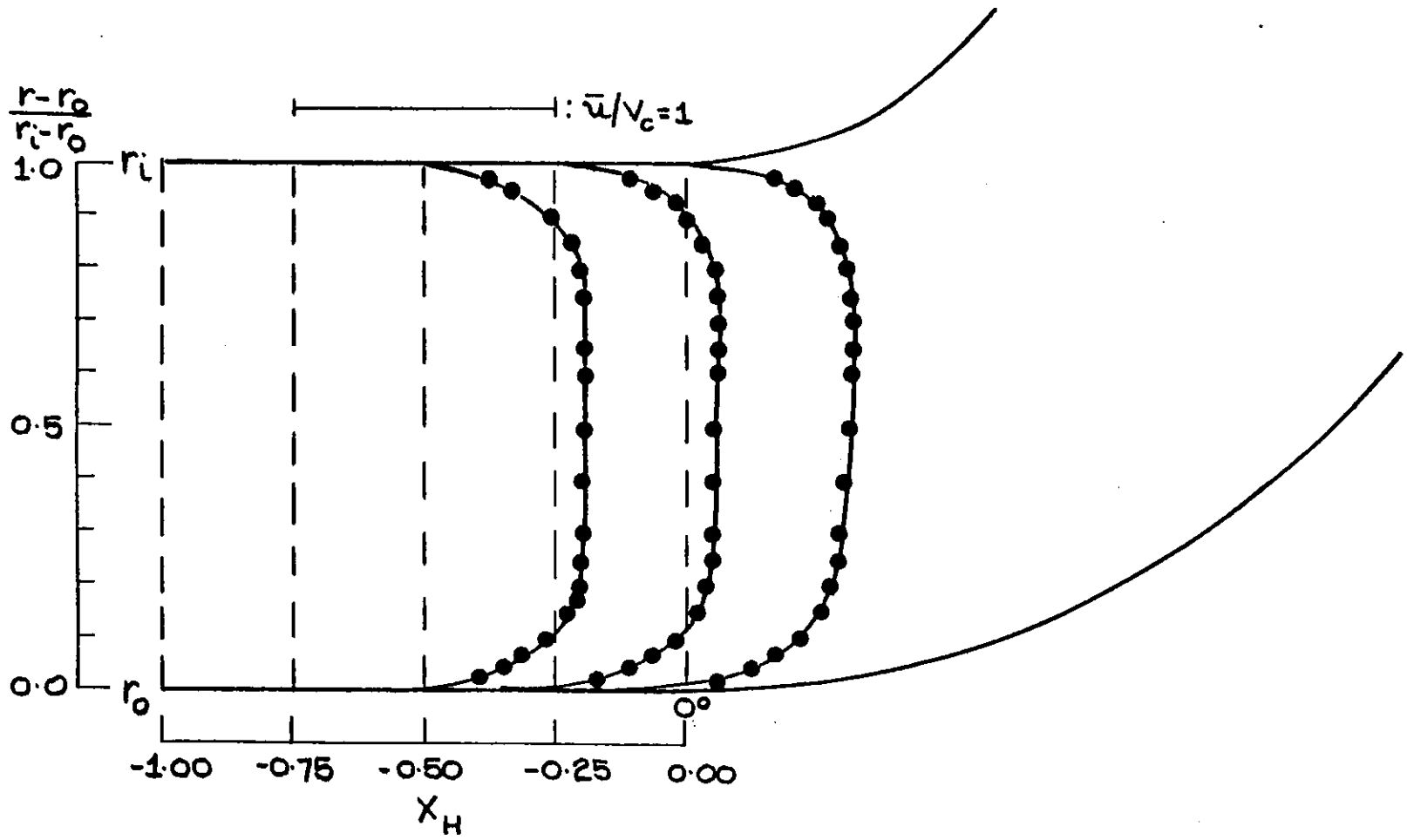


Figure 3.12 Turbulent flow: profiles of $\bar{U}/V_c$ at the symmetry plane near the bend inlet

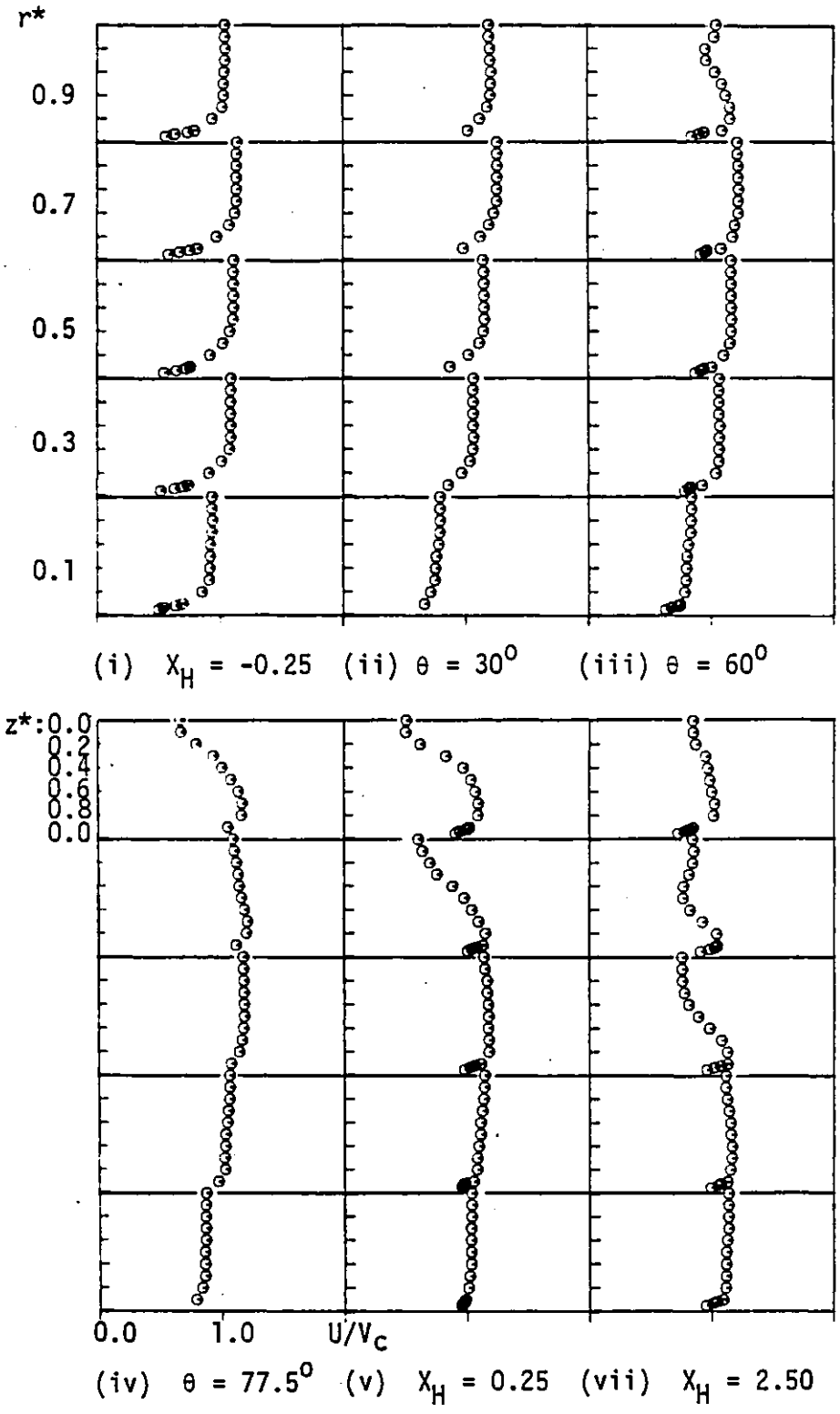


Figure 3.13 Turbulent flow: profiles of U/V_c

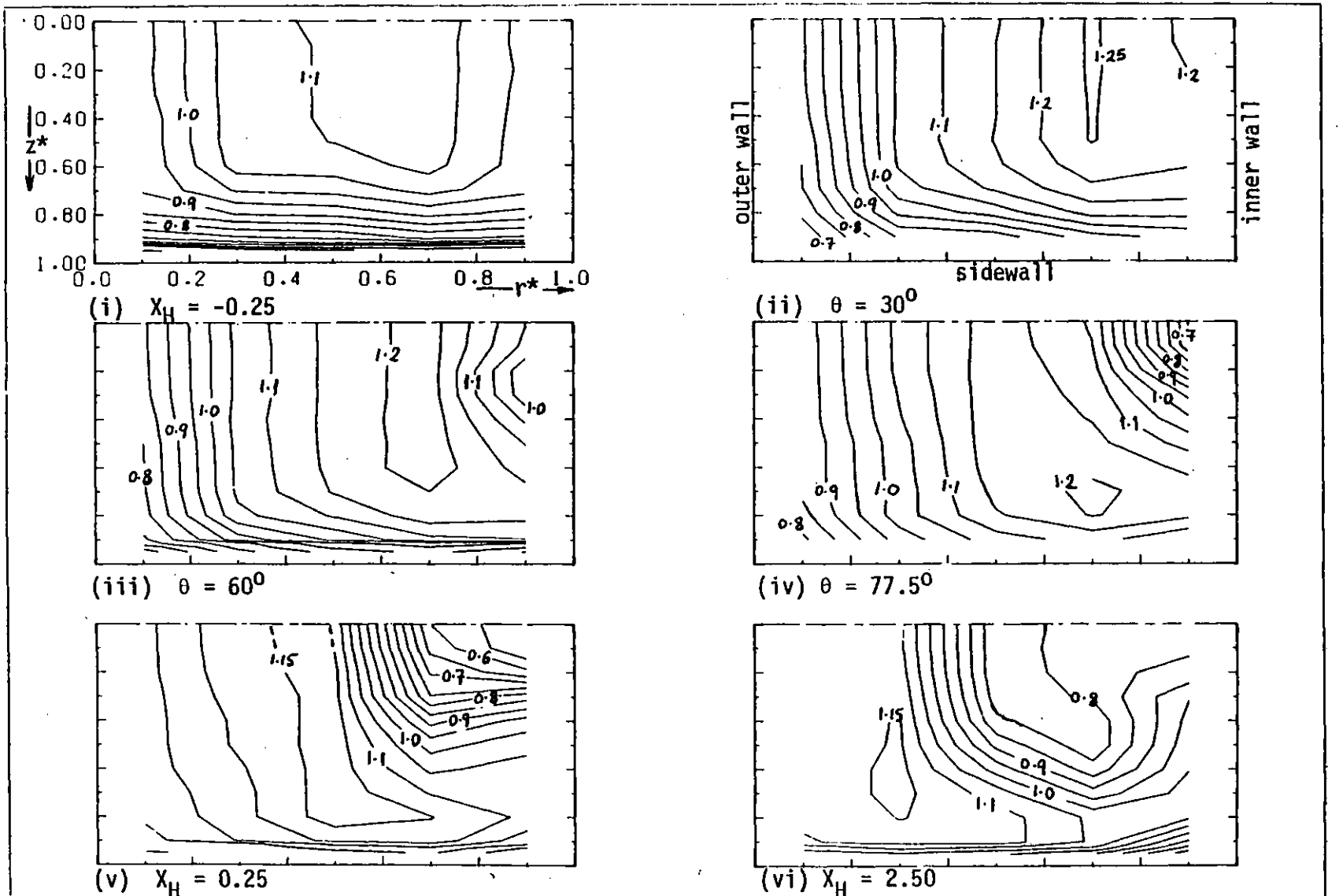


Figure 3.14 Turbulent flow: isotachs of U/V_c

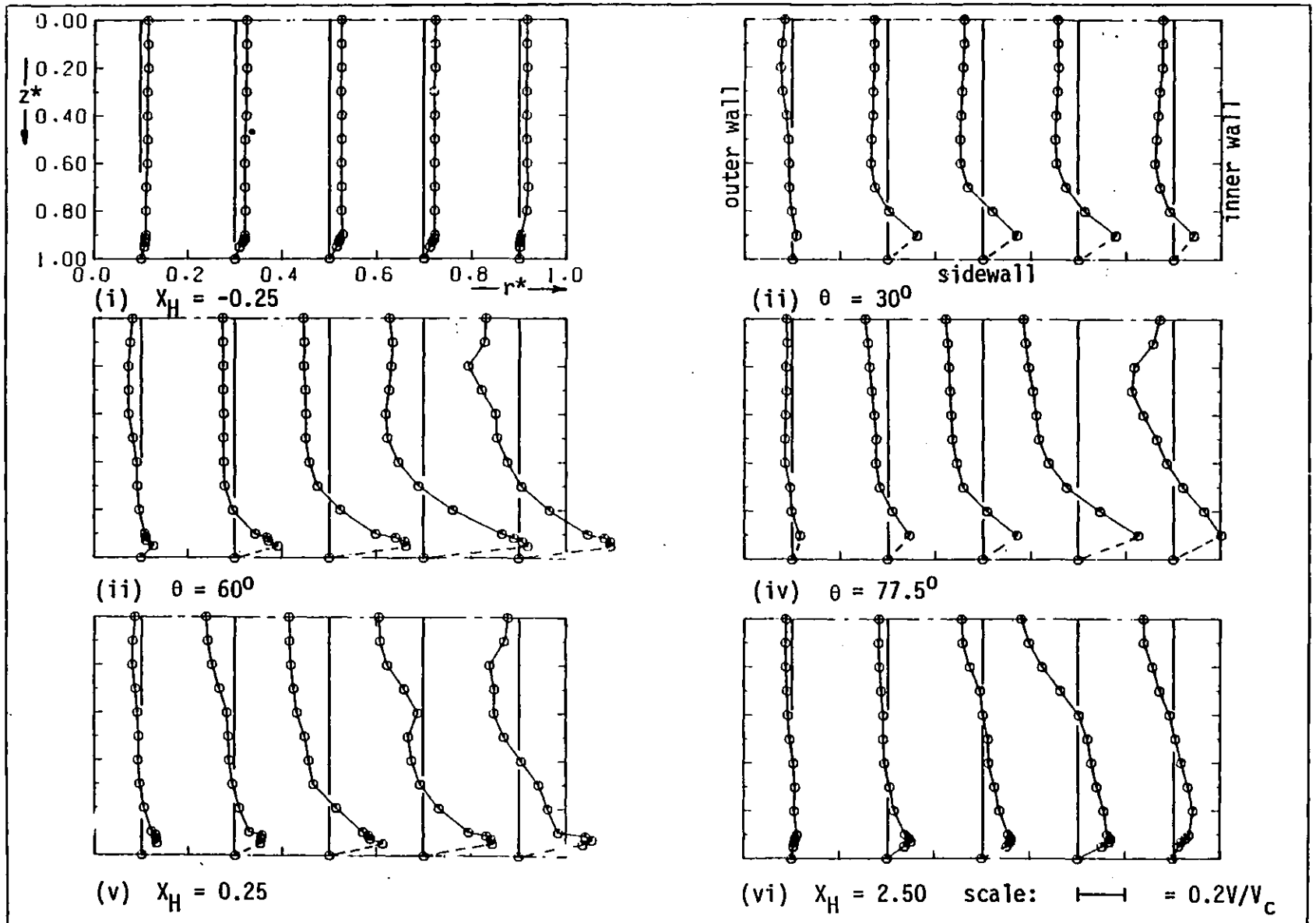


Figure 3.15 Turbulent flow: profiles of V/V_c

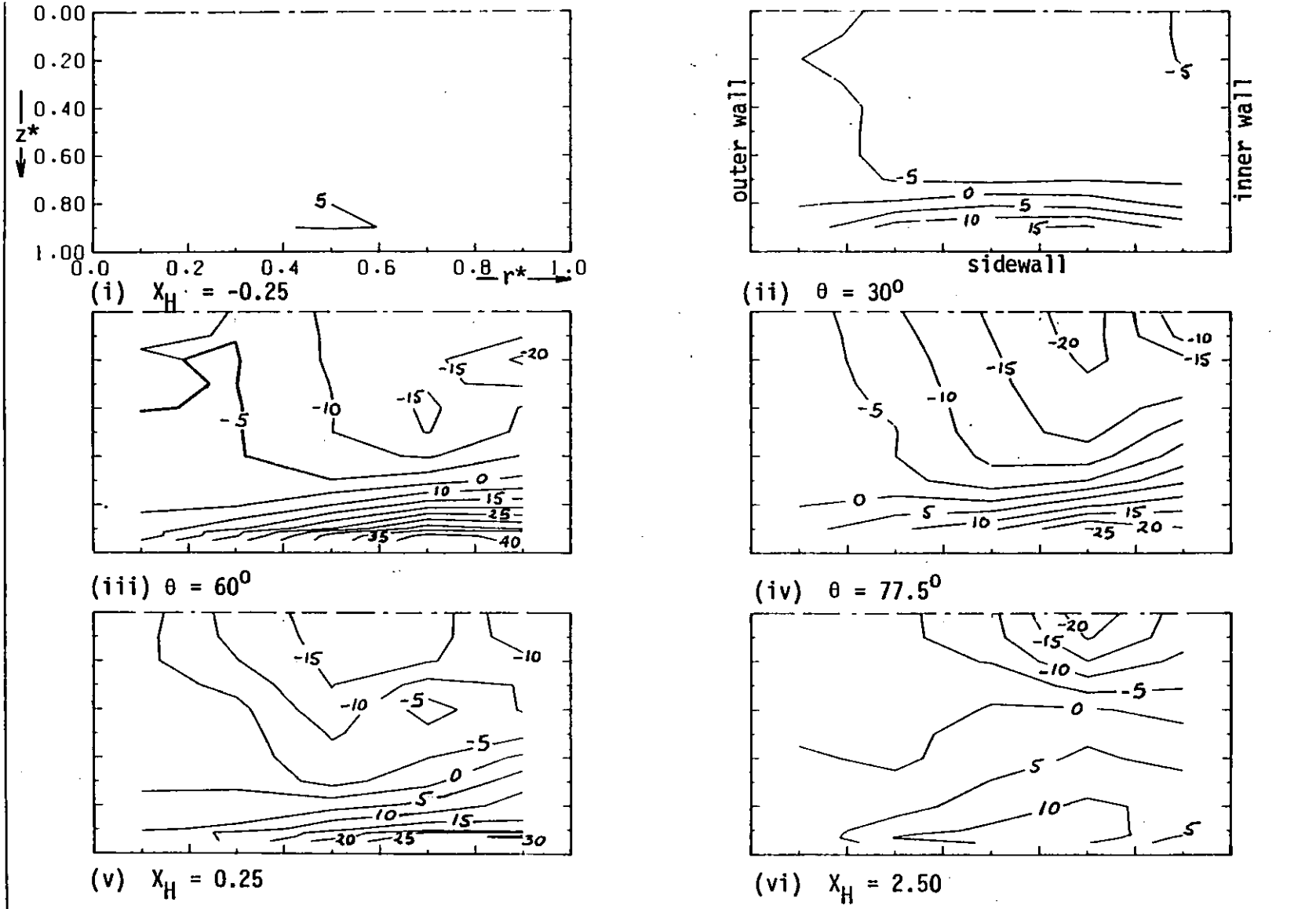
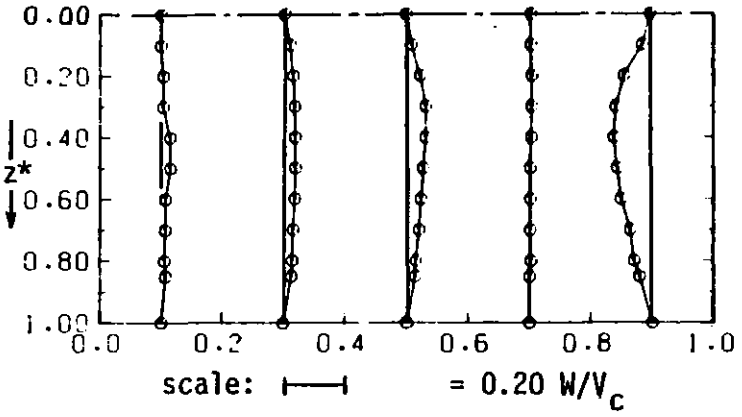


Figure 3.16 Turbulent flow: isotachs of V/V_c



: direction of positive W

Figure 3.17 Turbulent flow: profiles of W/V_c at $X_H = 2.50$.

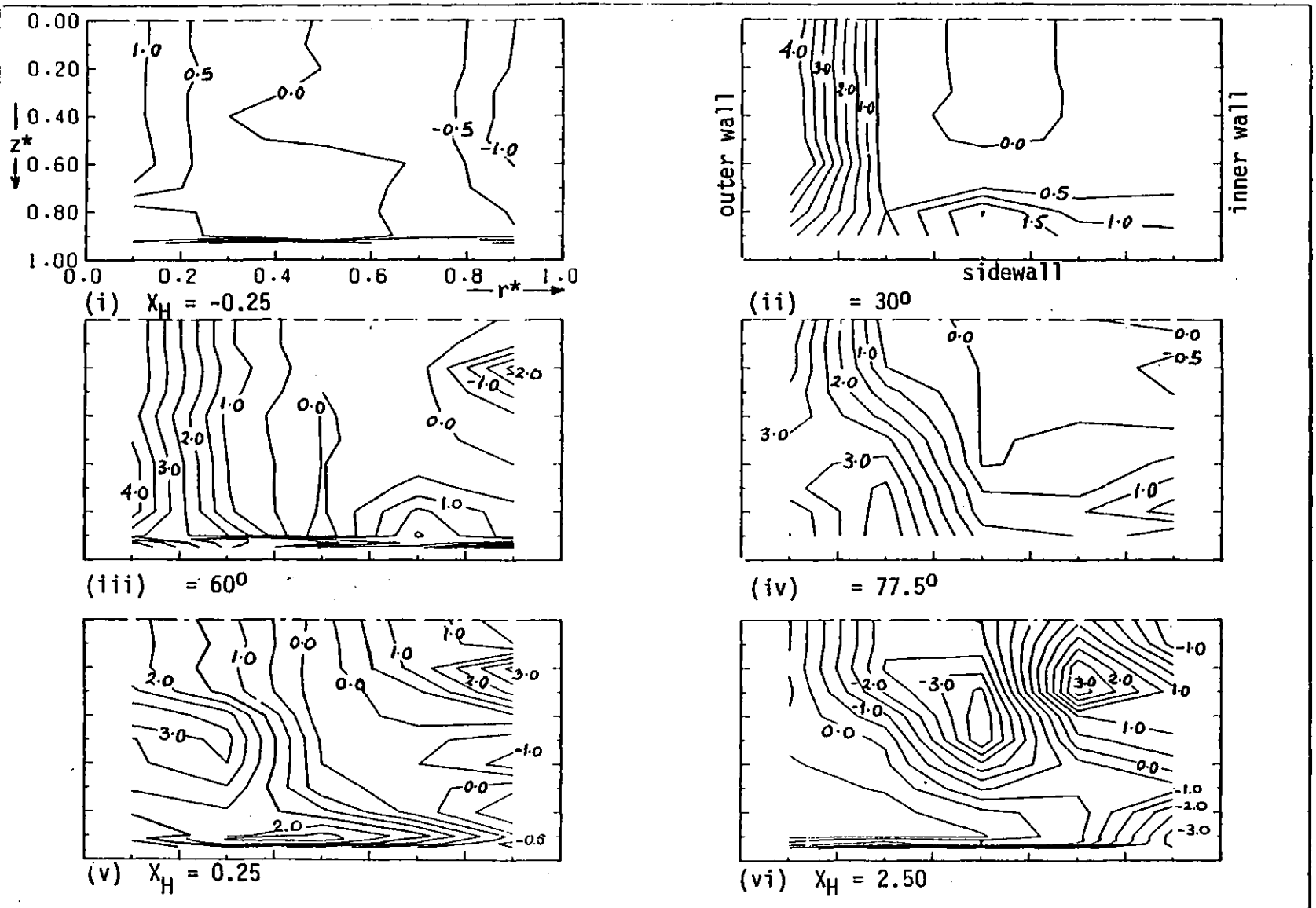


Figure 3.18 Turbulent flow: contours of $-\overline{uv}/V_c^2$(x1000)

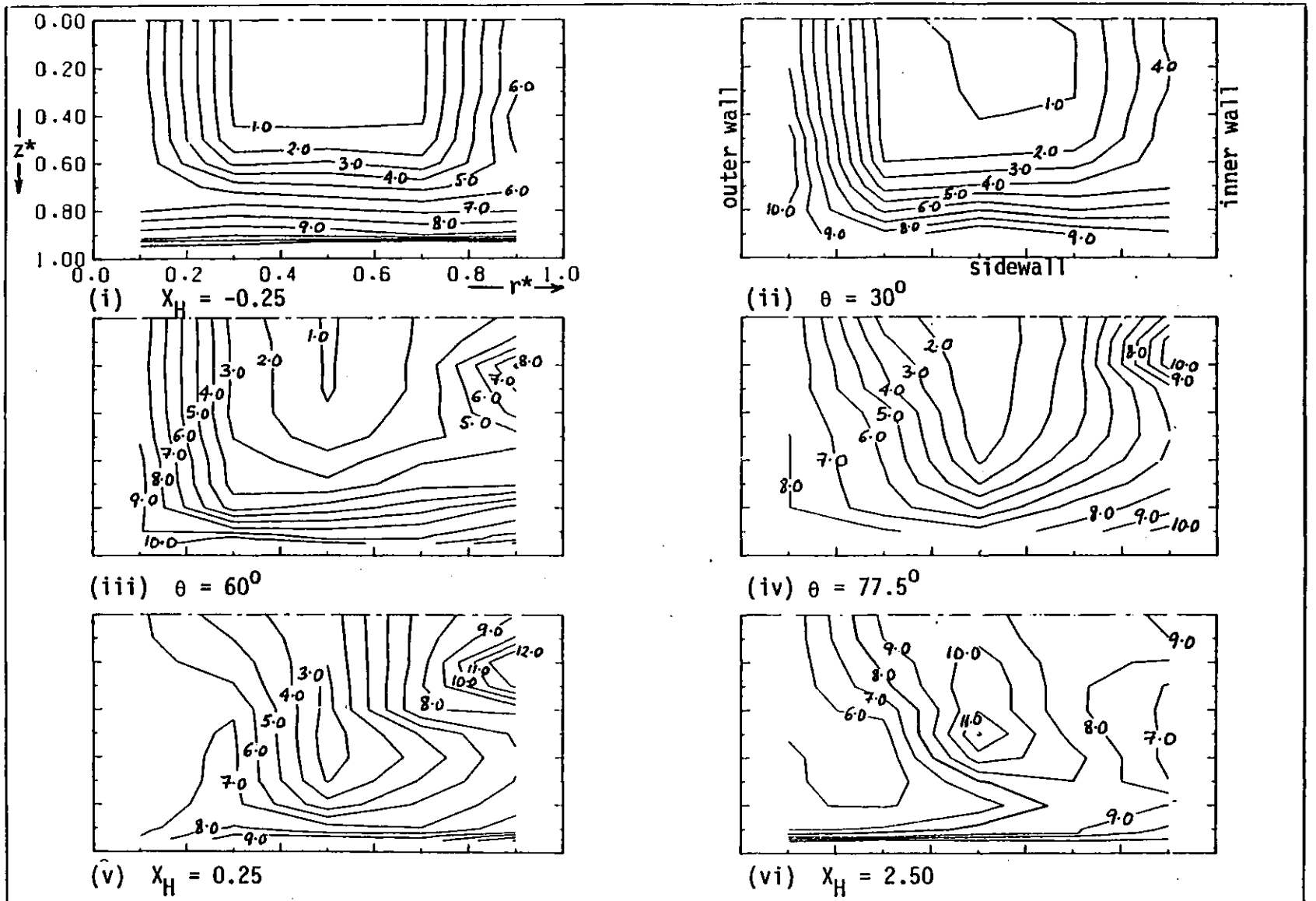


Figure 3.19 Turbulent flow: contours of $\tilde{u}/V_c$(x100)

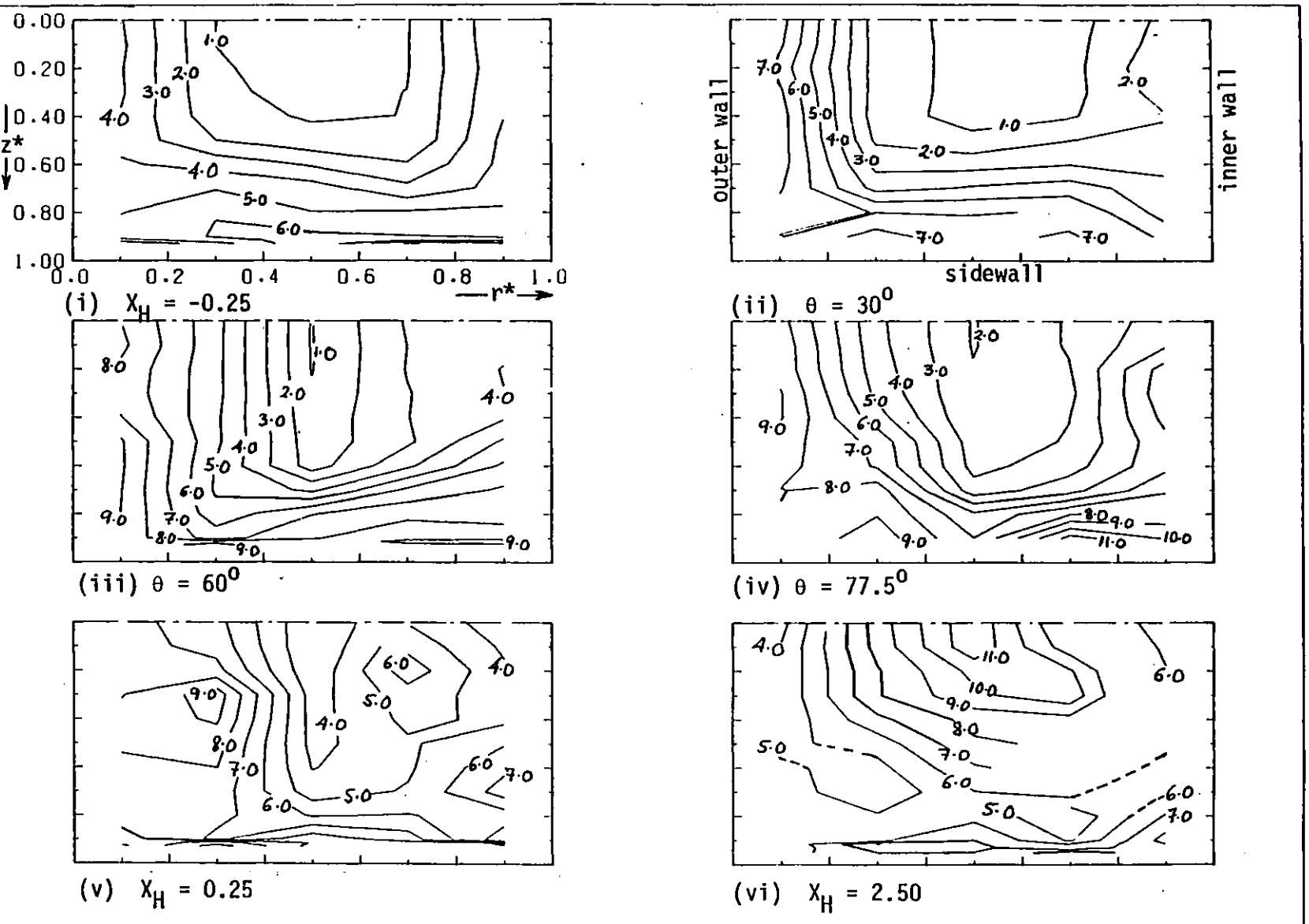


Figure 3.20 Turbulent flow: contours of $\tilde{v}/V_c$(x100)

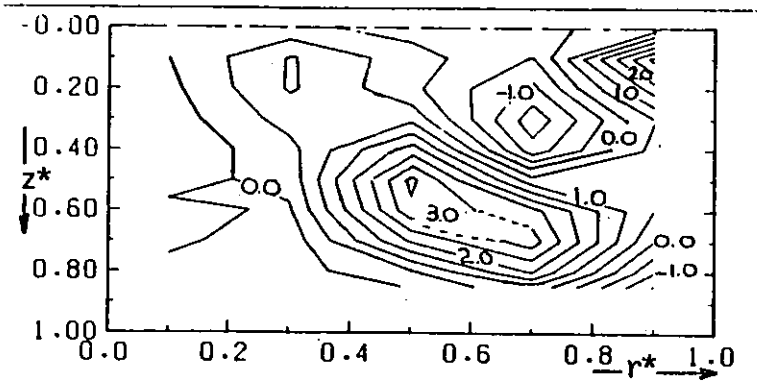


Figure 3.21 Turbulent flow: contours of $\overline{uw}/V_c^2$ (x1000) at X_H = 2.50

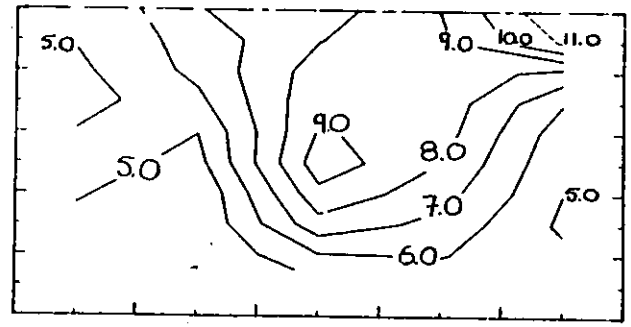


Figure 3.22 Turbulent flow: contours of $\tilde{w}/V_c^2$ (x100) at X_H = 2.50

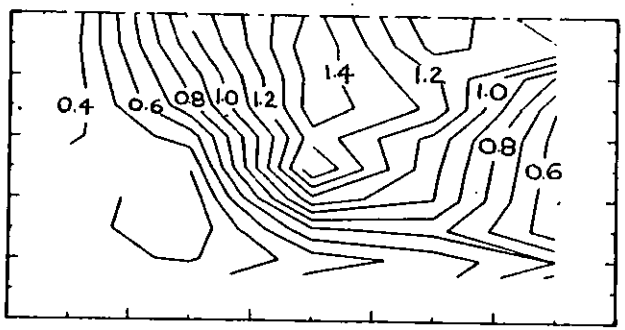


Fig. 3.23 Turbulent flow: contours of k/V_c^2 (x1000) at X_H = 2.50

CHAPTER FOUR

CONCLUDING REMARKS

At the outset of the present research, little was known of the details of the intake-generated flow in reciprocating engine cylinders or of developing bend flows. In both configurations extensive research had been carried out, as indicated in section 1.2, but with the exception of very few researchers, for example Agrawal et al (1978) and Rask (1978), difficulties stemming from instrumentation or access to the flow had limited progress. The present application of laser Doppler anemometry, following and improving those of Gosman et al (1978b) and Humphrey et al (1977, 1981) has achieved the detail and accuracy of measurement necessary to draw the conclusions of chapters two and three.

For this purpose, the measurements were primarily of the mean and variance of velocity in the turbulent flow in the cylinder of two motored model reciprocating engines and of laminar and turbulent developing flows in a strongly curved duct. Thus a description of flow processes relevant to both in-cylinder and intake passage configurations has been obtained and shows that the pressure-induced forces have a major role in the flow development over most of the flow space in both configurations.

In the reciprocated flows, the cylinder head geometry, which introduces a pressure drop to the incoming flow, is the most important factor determining the in-cylinder flow patterns during intake. With valve inlets a group of ring vortices is produced in the cylinder and is present, with some differences, even in asymmetrical configurations.

The primary ring vortex formed behind the valve recirculates most of the indrawn mass of air and its length increases with swirl. The results indicate that "rolled-up" vortices are not significant to the flow in the presence of an intake-generated flow structure.

In the bend flows, the pressure-gradient induced secondary motions dominate the flow and turbulence effects are of minor importance over most of the duct cross-section. Significant differences in the flow patterns with fully-developed flows at the bend inlet are only observed in the first 60 degrees of bend angle when the inlet boundary layer thickness is reduced to 0.15 of the duct hydraulic diameter.

It seems evident that information similar to that in the preceding chapters is required for a wider range of configurations. In engine arrangements, and following on from the present work, Bicen et al (1980) and Arcoumanis et al (1981a,b) have already extended available information to include intake-related effects not examined here, such as stroke, clearance volume and seat angle, and the influences of compression-related effects such as piston head geometry, squish and compression ratio on the flow characteristics. The present results, in conjunction with those of Arcoumanis et al and measurements in real engines (e.g. Rask, 1979 and Morse and Whitelaw, 1981), show that the main features of the flow in real engines are also found in model arrangements which are conceptually and experimentally simpler. This conclusion, already stated in sub-section 1.2.1, is important in that it provides justification for the continuing use of model engines with consequent extensive optical access and comparatively inexpensive instrumentation for the parametric investigation of relevant geometrical and flow conditions. Thus, for example, the performence of particular engine components, such as a piston-bowl or valve geometry, can

be examined in terms of air flow characteristics at less cost and with comparative ease. Measurements in real engines are, of course, required to confirm the findings and to determine the effect of combustion but can be arranged to be fewer with knowledge of the non-combusting equivalent. This approach is recommended for future work. In accordance with this method, the use of model engines could also be extended by introducing a passive scalar into the cylinder and quantifying the scalar (fuel)/air mixture density fluctuations with a non-obtrusive technique such as Rayleigh scattering.

Similarly, the investigation of duct flows in water tunnels permits the detailed examination of manifold and intake passage geometries in experimentally simple arrangements with the same Reynolds number and with a smaller scale than that obtained by air.

Useful extensions to the present work could be made in the above manner to determine the influence of bend deflection angle and cross-sectional shape on the flow characteristics. Some measurements have been made in such flows, for example in curved pipes (Enayet et al, 1981a) and in ducts with cross-sectional shape changes (Taylor et al, 1981d) but in considerably less detail than in the present flow due to problems of beam refraction at the Perspex/water non-plane surfaces.

The flow in S-shaped bends is also of practical interest and, although square-sectioned S-ducts can and have been investigated in detail (Taylor et al, 1981e), most intakes in practice employ S-shaped diffusers with cross-sectional changes which introduce the aforementioned optical problems and restrict the measurement detail. Moreover, in many curved flows in practice heat transfer processes occur, and thus it is desirable to measure in significant detail the near wall region, where heat transfer effects are predominant, in order to compare with non-

isothermal results.

It is therefore desirable to find and use a liquid of refractive index similar to that of Perspex, of low enough viscosity to enable the measurement of turbulent flow and with no unpleasant properties (i.e. non-toxic, non-volatile and non-solvent of Perspex) to facilitate future measurements in more complex bend geometries.

The detail and accuracy of the results permits the evaluation of calculation methods. Calculations of both flows to-date have shown qualitative agreement with present and related results. Quantitative agreement is restricted at present primarily due to numerical errors resulting from the lack of sufficiently refined grids to account for the steep velocity gradients present in the flows and to reduce truncation errors. In the case of in-cylinder flows, uncertainties in the specified inlet conditions are also responsible for discrepancies. Turbulence modelling errors appear to be of lesser importance at present and the use of the "k-ε" model appears to be adequate for the calculation of mean flow and turbulence properties.

The improvement of calculations is thus hindered mainly by the need for grid refinement which would increase significantly computer storage and time costs. The use of non-iterative (time-marching) techniques and improved algorithms in the numerical methods shows promise in reducing the calculation costs and thus permitting grid refinement and reduction of the numerical errors. In in-cylinder calculations it is anticipated that the extension of the calculation sufficiently upstream of the valve port, where inlet conditions can be easily specified will be necessary to remove inlet condition uncertainties.

The coordination of experimental programmes of measurements in conceptually simple arrangements as those presented in this thesis with

relevant calculations is believed to constitute an appropriate method for the improvement of the understanding of the flows concerned and should be employed for future work.

REFERENCES

AGRAWAL, Y., TALBOT, L. and GONG, K. (1978)
Laser anemometer study of flow development in curved circular pipes.
J. Fluid Mech., 85, 3, 497.

AHMADI-BEFRUI, B., GOSMAN, A.D., LOCKWOOD, F.C. and WATKINS, A.P. (1981)
Multidimensional calculation of combustion in an idealised homogenous charge engine: a progress report.
SAE paper 810151.

ALCOCK, J.F. (1934)
Air swirl in oil engines.
Proc. Instn. Mech. Engrs., 128.

ALCOCK, J.F. and SCOTT, W.M. (1962)
Some more light on Diesel combustion.
Proc. Instn. Mech. Engrs. (AD), 5.

ANNAND, W.J.D. (1969)
Engine breathing - aerodynamics of low speed flow through inlet valves and ports for reciprocating engines.
Automobile Engineer, 59.

ARCOUMANIS, C., BICEN, A.F. and WHITELAW, J.H. (1981a)
Effect of inlet parameters on the flow characteristics in a four-stroke model engine.
Imperial College, Mech. Engng. Dept., Report FS/81/12.

ARCOUMANIS, C., BICEN, A.F. and WHITELAW, J.H. (1981b)
Measurements in a motored four-stroke reciprocating model engine.
Proc. Symp. on Fluid Mech. of Comb. Systems, ASME Spring Meeting, Boulder, Colorado.

ARCOUMANIS, C., BICEN, A.F. and WHITELAW, J.H. (1981c)
Influence of compression ratio on the flow characteristics in a four-stroke model engine.
Imperial College, Mech. Engng. Dept., Report FS/81/26.

ARCOUMANIS, C., BICEN, A.F., GOSMAN, A.D., JAHANBAKSH, A. and WHITELAW, J.H. (1981d)
Calculations and measurements of the flow in a motored model engine and implications for open-chamber, direct-injection engines.
Paper to be presented at ASME Spring Meeting of Fluids Engng. Division, St. Louis, 1982.

ARCOUMANIS, C., BICEN, A.F., VLACHOS, N.S. and WHITELAW, J.H. (1982)
Effects of flow and geometry boundary conditions on fluid motion in a motored i.c. model engine.
Proc. Instn. Mech. Engrs., 196, 4.

ARCOUMANIS, C. and VLACHOS, N.S. (1980)
The influence of valve seat angle on the flow patterns in a motored piston-cylinder assembly.
Imperial College, Mech.Engng.Dept. Report, FS/80/25.

ARNOLD, M.J., TINDAL, M.J. and WILLIAMS, T.J. (1972)
Measurement of induction gas velocities in a reciprocating engine cylinder.
SAE paper 720115.

ASANUMA, T. and OBOKATA, T. (1972)
Decay of air swirl motion in an engine cylinder.
JARI Tech. Memo.,No. 10.

ASANUMA, T. and OBOKATA, T. (1973)
Decay of air swirl motion in an engine cylinder.
JARI Tech. Memo.,No. 15.

ASANUMA, T. and OBOKATA, T. (1979)
Gas velocity measurements of a motored and firing engine by laser anemometry.
SAE paper 790096.

AUSTIN, L.R. and SEADER, J.D. (1974)
Entry region for steady viscous flow in coiled circular pipes.
A.I.Ch.E. Journal, 19, 85.

BANSOD, P. and BRADSHAW, P. (1972)
The flow in S-shaped ducts.
Aeronautical Quarterly, 23, 2, 131-140.

BICEN, A.F. (1980)
Effect of a lipped cylindrical piston bowl on the flow characteristics of a motored piston-cylinder assembly.
Imperial College, Mech. Engng. Dept., Report FS/80/33.

BICEN, A.F., VLACHOS, N.S. and WHITELAW, J.H. (1980)
The creation and destruction of vortices in unsteady flows.
Lett. Heat Mass Transfer, 7, 77.

BICEN, A.F. and WHITELAW, J.H. (1981)
Refraction correction for LDA measurements in flows with curved optical boundaries.
Imperial College, Mech. Engng. Dept., Report FS/81/17.

BLUMBERG, P.N., LAVOIE, G.A. and TABACZYNSKI, R.J. (1979)
Phenomenological models for reciprocating internal combustion engines.
Prog. Energy Combust. Sci., 5, 123.

BONI, A.A., CHAPMAN, M., COOK, J.L. and SCHNEYER, G.P. (1976)
Computer simulation of combustion processes in a divided chamber stratified charge engine.
5th Int. Coll. on Gas Dynamics of Explosions and Reactive Systems, Bourges, France.

BONI, A.A. (1978)
Numerical simulation of flame propogation in internal combustion engines: a status report.
SAE paper 780316.

BRADSHAW, P. (1971)
An Introduction to Turbulence and its Measurement.
The Commonwealth and International Library, Pergamon Press, Oxford.

BRADSHAW, P. (1973)
Effects of streamline curvature on turbulent flow.
AGARDograph 169.

BRILEY, W.R. and McDONALD, H. (1977)
Solution of the multi-dimensional compressible Navier-Stokes equations by a generalized implicit method.
J. of Comp. Physics, 24, 372.

BRILEY, W.R. and McDONALD, H. (1980)
On the structure and use of linearized block ADI and related schemes.
J. of Comp. Physics, 34, 54.

BRUUN, H.H. (1979)
An experimental investigation of secondary flow losses in bends with rectangular cross-sections.
Univ. of Cambridge, Dept. of Engng. Report CUED/A-Turbo/TR 95.

BUCHHAVE, P. (1975)
Biasing errors in individual particle measurements with the LDA counter signal processor.
Proc. LDA Symp. Copenhagen, 258.

BUGGELN, R.C., BRILEY, W.R. and McDONALD, H. (1980)
Computation of the laminar and turbulent flow in curved ducts, channels, and pipes using the Navier-Stokes equations.
Science Research Associates Report R80-920006-F,prepared for the Office of Naval Research.

BUTZ, L.A. (1979)
Turbulent flow in S-shaped ducts.
M.S.A.A. Thesis, University of Purdue.

CHENG, K.C., NAKAYAMA, J. and AKIYAMA, M. (1979)
Effect of finite and infinite aspect ratios on flow patterns in curved rectangular channels.
in Flow visualization, (ed. T. Asanuma)
Hemisphere Publ. Corp. and McGraw Hill.

CHOI, U.S., TALBOT, L. and CORNET, I. (1979)
Experimental study of wall shear rates in the entry region of a curved tube.
J. Fluid Mech., 93, 465.

CHONG, M.S., MILKINS, E.E. and WATSON, H.C. (1976)
The prediction of heat and mass transfer during compression and expansion in i.c. engines.
SAE Trans. 760761.

CLAYTON, B.R. and MASSEY, B.S. (1967)
Flow visualisation in water: a review of the techniques.
J. Sci. Instrum., 44.

COLE, J.B. and SWORDS, M.D. (1979)
Optical studies of the flow field in a motored E6 engine.
Proc. Instn. Mech. Engrs., C102/79.

CRABB, D., DURAO, D.F.G., LAKER, J., MORSE, A., VLACHOS, N.S., WHITELAW, J.H. and YIANNESKIS, M. (1979)
Two signal-processing arrangements for in-cylinder velocity measurements.
Presented at Euromech 120 Conference, Copenhagen, August 1979.

CRANE, R.I. (1981)
Private communication.

CRANE, R.I. and WINOTO, S.H. (1979)
Longitudinal vortices in a concave surface boundary layer.
Proc. AGARD Conf., Lisbon.

DANESHYAR, H., FULLER, D.E. and DEKKER, B.E.L. (1973)
Vortex motion induced by the piston of an internal combustion engine.
Int. J. Mech. Sci., 15.

DAVIS, G.C. and KENT, J.C. (1979)
Comparison of model calculations and experimental measurements of the bulk cylinder flow processes in a motored PROCO engine.
SAE paper 790290.

DEMIRDZIC, I. (1981)
Private communication.

DENNISON, E.S., KUCHLER, T.C. and SMITH, D.W. (1953)
Experiments on the flow of air through engine valves.
Trans. ASME, 53.

DENT, J.C. and DERHAM, J.A. (1974)
Air motion in a four-stroke direct-injection Diesel engine.
Proc.. Instn. Mech. Engrs., 188, 00/74.

DENT, J.C. and SALAMA, N.S. (1975a)
Turbulence and structure in the spark ignition engine.
Paper no. C83/75, I. Mech. E. Conf. on Comb. in Engines, Cranfield.

DENT, J.C. and SALAMA, N.S. (1975b)
The measurement of the turbulence characteristics in an internal combustion engine cylinder.
SAE paper 750886, presented at 1975 Automot. Engng. Congress, Detroit.

DE VRIEND, H.J. (1981)
Velocity redistribution in curved rectangular channels.
J. Fluid Mech., 107, 423.

DICKSEE, C.B. (1940)
The high speed compression ignition engine.
Blackie and Son.

DIMOTAKIS, P. (1976)
Single scattering particle laser Doppler measurements of turbulence.
Paper 10, AGARD Conf. No. 193, Applications of non-intrusive instrumentation in fluid flow research.

DIWAKAR, R., ANDERSON, J.D., GRIFFIN, M.D. and JONES, E. (1976)
Inviscid solutions of the flow field in an internal combustion engine.
AIAA Journal, 14, 12.

DRAIN, L.E. (1980)
The laser Doppler technique.
John Wiley, Chichester.

DURAO, D.F.G. (1976)
The application of laser anemometry to free jets and flames with and without recirculation.
Ph.D.Thesis, University of London.

DURAO, D.F.G. and WHITELAW, J.H. (1975)
The influence of sampling procedures on velocity bias in turbulent flows.
Proc. of the LDA-Symposium Copenhagen 1975, 138.

DURAO, D.F.G. and WHITELAW, J.H. (1978)
Relationship between velocity and signal quality in laser Doppler anemometry.
J. Phys. E: Sci. Instrum., 12, 47.

DURAO, D.F.G., LAKER, J. and WHITELAW, J.H. (1980)
Bias effects in laser Doppler anemometry.
J. Phys. E: Sci. Instrum., 13, 442.

DURST, F., MELLING, A. and WHITELAW, J.H. (1976) and 2nd edition (1981)
Principles and practice of laser Doppler anemometry.
Academic Press, London.

EISEMAN, P.R., LEVY, R., McDONALD, H. and BRILEY, W.R. (1978)
Development of a three-dimensional turbulent duct flow analysis.
NASA Contractor Report 3029.

EKCHIAN, A. and HOULT, D.P. (1979)
Flow visualisation study of the intake process of an internal combustion engine.
SAE paper 790095.

EL-KHAFAJI, A.H.A., TINDAL, M.J. and WILLIAMS, T.J. (1971)
Engine cylinder gas flow measurements by hot-wire anemometry.
Proc. Symp. on Flow - Its measurement and control in science and industry, Pittsburgh.

ENAYET, M.M., GIBSON, M.M., TAYLOR, A.M.K.P. and YIANNESKIS, M. (1981a)
Laser Doppler measurements of laminar and turbulent flow in a pipe bend.
Report submitted as NASA Contractor Report. Presented at the Int. Symp. on 'Applications of Fluid Mechanics and Heat Transfer to Energy and Environmental Problems', University of Patras, Greece, June 1981.

ENAYET, M.M., GIBSON, M.M. and YIANNESKIS, M. (1981b)
Developing flow in a moderately curved duct.
Imperial College, Mech. Engng. Dept. Report FS/82/4.

ESKINAZI, S. and YEH, M. (1956)
An investigation of fully-developed turbulent flows in a curved channel.
J. Aero. Sci., 23, 23.

FITZGEORGE, D. and ALLISON, J.L. (1963)
Air swirl in a road vehicle Diesel engine.
Proc. Instn. Mech. Engrs., (AD), No. 4.

FULLER, D.E. (1975)
Mixture motion in an engine cylinder.
Ph.D.Thesis, University of Cambridge.

GANY, A., LARREA, J.J. and SIRIGNANO, W.A. (1980)
Laser Doppler velocimetry measurements in a motored i.c. engine simulator.
AIAA paper 80-0079.

GEORGE, W.K. and LUMLEY, J.L. (1973)
The laser-Doppler velocimeter and its application to the measurement of turbulence.
J. Fluid Mech., 60, 321.

GOSMAN, A.D. and JOHNS, R.J.R. (1978)
Development of a predictive tool for in-cylinder gas motion in engines.
SAE paper 780315, presented at SAE Congress, Detroit, 1978.

GOSMAN, A.D., JOHNS, R.J.R. and WATKINS, A.P. (1978a)
Assessment of a predictive method for in-cylinder processes in reciprocating engines.
Proc. General Motors Res. Labs. Symp. on Comb. Modelling in Reciprocating Engines.

GOSMAN, A.D., MELLING, A., WHITELAW, J.H. and WATKINS, A.P. (1978b)
Axisymmetric flow in a motored reciprocating engine.
Proc. Instn. Mech. Engrs., 192, 11.

GOSMAN, A.D., JOHNS, R.J.R., TIPLER, W. and WATKINS, A.P. (1979)
Computer simulation of in-cylinder flow, heat transfer and combustion: a progress report.
Proc. 13th CIMAC Conf., Vienna, 1979.

GOSMAN, A.D. and WATKINS, A.P. (1976a)
Calculations of turbulent heat transfer in a closed piston/cylinder system.
Imperial College, Mech. Engng. Dept. Report.

GOSMAN, A.D. and WATKINS, A.P. (1976b)
Simulation of flow and heat transfer during a four-stroke motored engine cycle.
Imperial College, Mech. Engng. Dept. Report.

GRIFFIN, M.D., ANDERSON, J.D. Jnr. and DIWAKAR, R. (1976)
Navier-Stokes solutions of the flow field in an internal combustion engine.
AIAA paper 76-403, 9th Fluid and Plasma Dynamics Conf., San Diego.

GRIFFIN, M.D., DIWAKAR, R., ANDERSON, J.D. and JONES, E. (1978)
Computational fluid dynamics applied to flows in an internal combustion engine.
AIAA paper 78-57, 16th Aerospace Sciences Meeting, Huntsville, Alabama.

GUPTA, H.C., STEINBERGER, R.L. and BRACCO, F.V. (1978)
Combustion in a divided-chamber stratified-charge reciprocating engine: initial comparisons of calculated and measured flame propagation.
Proc. 17th Int. Symp. on Comb.

HABIB, M.A. and WHITELAW, J.H. (1979)
Velocity characteristics of confined coaxial jets with and without swirl.
Paper 79-WA/FE-21, presented at the ASME WAM, New York, Dec. 1979.

HIRT, C.W., AMSDEN, A.A. and COOK, J.L. (1974)
An arbitrary Langrangian-Eulerian computing method for all flow speeds.
J. Comp. Phys., 14, no. 3.

HOESEL, H. and RODI, W. (1977)
New biasing elimination method for laser Doppler velocimeter counter processing.
Rev. Sci. Instrum., 48, 910.

HOFFMANN, P.H. and BRADSHAW, P. (1978)
Turbulent boundary layers on surfaces of mild longitudinal curvature.
Imperial College, Aeron. Dept. Rept. 78-04.

HORVATIN, M. and HUSSMANN, A.W. (1969)
Measurement of air movement in internal combustion engine cylinders.
DISA Information, 8.

HOULT, D.P. and WONG, V.W. (1978)
The generation of turbulence in an internal combustion engine.
Presented at the 1978 GM Research Symposium on Comb. Modelling in Reciprocating Engines.

HUEBNER, K.H. and McDONALD, A.T. (1972)
Experimental determination of airflow patterns in piston engines with induction swirl.
SAE paper 720026.

HUMPHREY, J.A.C. (1977)
Flow in ducts with curvature and roughness.
Ph.D.Thesis, University of London.

HUMPHREY, J.A.C. (1978)
Numerical calculation of developing laminar flow in pipes of arbitrary curvature radius.
The Canadian Journal of Chemical Engineering, 56, 151.

HUMPHREY, J.A.C., and POURAHMADI, F. (1981)
A generalised algebraic relation for predicting developing curved channel flow with a k-ε model of turbulence.
Presented at 3rd Symp. on Turbulent Shear Flows, University of California, Davis, September 1981.

HUMPHREY, J.A.C., TAYLOR, A.M.K. and WHITELAW, J.H. (1977)
Laminar flow in a square duct of strong curvature.
J. Fluid Mech., 83, 509.

HUMPHREY, J.A.C., WHITELAW, J.H. and YEE, G. (1981)
Turbulent flow in a square duct with strong curvature.
J. Fluid Mech., 103, 443.

HUNT, I.A. and JOUBERT, P.N. (1979)
Effects of small streamline curvature on turbulent duct flow.
J. Fluid Mech., 91, 633.

ISHIKAWA, N. and DAILY, J.W. (1978)
Observations of flow characteristics in a model i.c. engine cylinder.
SAE paper 780230.

ITO, H. (1959)
Friction factors for turbulent flow in curved pipes.
J. Basic Engng., 11, 123.

JAMES, E.H. (1972)
Investigations of turbulent flow in the combustion chamber of a spark-ignition engine.
Ph.D.Thesis, Loughborough University of Technology.

JAMES, E.J. and LUCAS, G.G. (1975)
Turbulent flow in spark ignition engine combustion chambers.
SAE paper 750886, presented at 1975 Automot. Engng. Congress, Detroit.

JOHNS, R.J.R. (1980)
Prediction of flow in Diesel engine cylinders.
Ph.D. Thesis, University of London.

JONES, W.P. and LAUNDER, B.E. (1972)
The prediction of laminarisation with a two-equation model of turbulence.
Int. J. Heat Mass Transfer, 15, 301.

KASTNER, L.J., WILLIAMS, T.J. and WHITE, J.B. (1963)
Poppet inlet valve characteristics and their influence on the induction process.
Proc. Instn. Mech. Engrs., 178, 955.

KHAN, I.M. and WANG, C.H.T. (1972)
Factors affecting emissions of smoked gaseous pollutants from d.i. Diesel engines.
Proc. Instn. Mech. Engrs. Conf. on air pollution control symposium, C151, 293.

LANCASTER, D.R. (1976)
Effects of engine variables on turbulence in a spark-ignition engine.
Research Publication GMR-2026R, Research Laboratories - General Motors Corp. Presented at SAE Congress and Exposition, Detroit, February 1976
SAE paper 760159.

LAUNDER, B.E., REECE, G.J. and RODI, W. (1975)
Progress in the development of a Reynolds-stress turbulence closure.
J. Fluid Mech., 68, 3.

LEE, D.W. (1939)
A study of air flow in an engine cylinder.
NACA Report 653.

LESCHZINER, M.A. and RODI, W. (1979)
Calculation of strongly curved open channel flow.
Journal of the Hydraulics Division, ASCE, 105, 1297.

LEVY, R., McDONALD, H., BRILEY, W.R. and KRESKOVSKY, J.P. (1980)
A three-dimensional turbulent compressible subsonic duct flow analysis for use with constructed coordinate systems.
AIAA Paper No. 80-1398.

LIN, J.Y. and TARBELL, J.M. (1980)
An experimental and numerical study of periodic flow in a curved tube.
J. Fluid Mech., 100, 623.

MA, T.H. (1975)
Effects of cylinder charge motion on combustion.
Proc. Instn. Mech. Engrs., C81/75.

MARTIN, M.E. and DEVERSON, E.C. (1960)
The effect of bend outlet conditions on the pressure losses in bent circular pipes.
C.P. No. 505 (19, 502), ARC Technical Report.

McDONALD, H. and BRILEY, W.R. (1975)
Three-dimensional supersonic flow of a viscous or inviscid gas.
J. Comp. Phys., 19, 150.

McLAUGHLIN, D.K. and TIEDERMAN, W.G. (1973)
Biasing correction for individual realisation of laser anemometer measurements in turbulent flows.
The Physics of Fluids, 16, 2082.

MELLING, A. (1975)
Investigation of flow in non-circular ducts and other configurations by laser Doppler anemometry.
Ph.D.Thesis, University of London.

MELLING, A. (1977)
Axisymmetric, turbulent flow in a motored reciprocating engine.
Imperial College, Mech. Engng. Dept. Report, CHT/77/4.

MELLING, A. and WHITELAW, J.H. (1973)
Seeding of gas flows for laser anemometry.
DISA Information, No. 15, 5.

MELLING, A. and WHITELAW, J.H. (1976a)
Design of laser Doppler anemometers for reciprocating engines.
Imperial College, Mech. Engng. Dept. Report CHT/76/6.

MELLING, A. and WHITELAW, J.H. (1976b)
Turbulent flow in a rectangular duct.
J. Fluid Mech., 78, 289.

MERONEY, R.N. and BRADSHAW, P. (1975)
Turbulent boundary-layer growth over a longitudinally curved surface.
AIAA Journal 13, 1448.

MILLER, D.S. (1978)
Internal flow systems
BHRA Fluid Engineering Series, 5.

MOLCHANOV, L.K. (1953)
On the problem of gas motion and combustion in a light fuel engine.
Trudy Makowkogo Automil'No-Dorozhnogo Instituta, Autatransizdat, Moscow, 17.

MOORE, J. and MOORE, J.G. (1979a)
A calculation procedure for three-dimensional, viscous, compressible duct flow. Part I. Inviscid flow calculations.
J. Fluids Engng., 101, 415.

MOORE, J. and MOORE, J.G. (1979b)
A calculation procedure for three-dimensional, viscous, compressible duct flow. Part II . Stagnation pressure losses in a rectangular elbow.
J. Fluids Engng., 101, 423.

MORSE, A. (1977)
The effect of crank-angle broadening on laser Doppler measurements in reciprocating engines.
Imperial College, Mech. Engng. Dept. Report FS/77/8.

MORSE, A.P. (1981)
Axisymmetric free turbulent shear flows with and without swirl.
Ph.D.Thesis, University of London.

MORSE, A.P. and WHITELAW, J.H. (1981)
Measurements of the in-cylinder flow of a motored four-stroke reciprocating engine.
Proc. R. Soc. Lond., A377, 309.

MORSE, A.P., WHITELAW, J.H. and YIANNESKIS, M. (1979a)
Turbulent flow measurements by laser Doppler anemometry in motored piston-cylinder assemblies.
J. Fluids Engng. 101, 208.

MORSE, A.P., WHITELAW, J.H. and YIANNESKIS, M. (1979b)
The influence of swirl on the flow characteristics of a reciprocating piston-cylinder assembly.
Atomic Energy Research Establishment, Harwell, AERE Report 9510.

MORSE, A.P., WHITELAW, J.H. and YIANNESKIS, M. (1979c)
The effect of engine speed on the flow patterns in reciprocating engines.
Imperial College, Mech. Engng. Dept. Report FS/79/12.

MORSE, A., WHITELAW, J.H. and YIANNESKIS, M. (1980a)
The flow characteristics of a piston-cylinder assembly with an off-centre open port.
Proc. Instn. Mech. Engrs., 194, 31.

MORSE, A.P., WHITELAW, J.H., and YIANNESKIS, M. (1980b)
The influence of swirl on the flow characteristics of a reciprocating piston-cylinder assembly.
J. Fluids Engng., 102, 478.

MULLIN, T. and GREATED, C.A. (1980a)
Oscillatory flow in curved pipes. Part 1. The developing flow case.
J. Fluid Mech., 98, 383.

MULLIN, T. and GREATED, C.A. (1980b)
Oscillatory flow in curved pipes. Part 2. The fully-developed case.
J. Fluid Mech., 98, 397.

NAMAZIAN, M., HANSEN, S., LYFORD-PIKE, E., SANCHEZ-BARSSE, J., HEYWOOD, J. and RIFE, J. (1980)
Schlieren visualisation of the flow and density fields in the cylinder of a spark-ignition engine.
SAE paper 800044

NIPPERT, H. (1929)
Über den Strömungsverlust in gekrümmten Kanälen.
V.D.I. - Forschungsarbeiten, 320.

OBERT, E.F. (1968)
Internal Combustion Engines.
International Textbook Co., Penn.

OHIGASHI, S., HAMAMOTO, Y. and TANABE, S. (1972)
Swirl - Its measurement and effect on combustion in a Diesel engine.
Proc. Instn. Mech. Engrs., C134, 129.

OLDENGARM, J., van KRIEKEN, A.H. and RATERNIK, H.J. (1976)
Development of a rotating grating and its use in laser velocimetry.
Bericht R117/76, ISL, St. Louis, France. Proceedings of the ISL/AGARD workshop on laser anemometry, May 5-7, 1976.

OPPENHEIM, A.K., CHONG, R.K., TEICHMAN, K., SMITH, O.T., SAWYER, R.F., HOM, K. and STEWART, H.E. (1976)
Cinematographic study of combustion in an enclosure fitted with a reciprocating piston.
Conf. on Stratified Charge Engines,Instn. Mech. Engrs., London.

PRANDTL, L. (1926)
Verhandlung des 2. internationalen Kongresses für technische Mechanik, Zürich.

PRATAP, V.S. and SPALDING, D.B. (1975)
Numerical computations of the flow in curved ducts.
Aero. Quart., 26, 219.

RAMAPRIAN, B.R. and SHIVAPRASAD, B.G. (1978)
The structure of turbulent boundary layers along mildly curved surfaces.
J. Fluid Mech., 85, 273.

RAMOS, J.I., HUMPHREY, J.A.C. and SIRIGNANO, W.A. (1979)
Numerical prediction of axisymmetric laminar and turbulent flows in motored, reciprocating internal combustion engines.
SAE paper 790356.

RAMOS, J.I. and SIRIGNANO, W.A. (1980)
Axisymmetric flow model with and without swirl in a piston-cylinder arrangement with idealised valve operation.
SAE paper 800284.

RASK, R.B. (1978)
Velocity measurements inside the cylinder of a motored internal combustion engine.
General Motors Research Publication GMR 2723, July 1978, presented at Third International Workshop on Laser Velocimetry, Purdue University, July 11-13, 1978.

RASK, R.B. (1979)
Laser Doppler anemometer measurements in an internal combustion engine.
SAE paper 790094.

RASK, R.B. (1981)
Comparison of window, smoothed-ensemble, and cycle-by-cycle data reduction techniques for laser Doppler anemometer measurements of in-cylinder velocity.
Proc. ASME Conf. on Fluid Mech. of Comb. Systems, Boulder, Colorado, June 22-23, 1981.

RENSHAW, J. (1980)
Private communication.

RENSHAW, J. and WIGLEY, G. (1979)
In-cylinder swirl measurements by laser anemometer in a production Diesel engine.
Atomic Energy Research Establishment, AERE, Harwell Report R9646.

REYNOLDS, W.C. (1978)
Modelling of fluid motions in engines - an introductory overview.
Proc. General Motors Res. Labs., Symp.on Comb. Modelling in Reciprocating Engines.

ROWE, M. (1970)
Measurements and computations of flow in pipe bends.
J. Fluid Mech., 43, 771.

SATO, H. and SAKAO, F. (1964)
An experimental investigation of the instability of a two-dimensional jet at low Reynolds numbers.
J. Fluid Mech., 20, 337

SCHLICHTING, H. (1955)
Boundary Layer Theory.
McGraw Hill, New York.

SCHRAUB, F.A., KLINE, S.J., HENRY, J., RUNSTADLER, P.W. Jnr., and LITTELL, A. (1965)
Use of hydrogen bubbles for quantitative determination of time-dependent velocity fields in low-speed water flows.
J. Basic Engng., June 1965, pp. 429-443.

SCORER, R.S. (1978)
Environmental Aerodynamics.
Ellis Horwood, Chichester.

SEMENOV, E.S. (1958)
Studies of turbulent gas flow in piston engines.
Otedelenie Technicheskikh Nauk, 8, and NACA Tech. Transl. F97, 1963.

SINGH, M.P. (1974)
Entry flow in a curved pipe.
J. Fluid Mech., 65, 517.

SINGH, M.P., SINHA, P.C. and AGGARWAL, M. (1978)
Flow in the entrance of the aorta.
J. Fluid Mech., 87, 97.

SMITH, A.M.O. (1955)
On the growth of Taylor-Görtler vortices along highly concave walls.
Quart. Appl. Math. 13, No. 3.

SO, R.M.C. and MELLOR, G.L. (1972)
An experimental investigation of turbulent boundary layers along curved surfaces.
NASA CR-1940.

SPALDING, D.B. (1972)
A novel finite difference formulation for differential expressions involving both first and second derivatives.
Int. J. for Num. Methods in Engng., 4, 551.

SPIERS, H.M. (ed.) (1962)
Technical data on fuel.
The British National Committee, World Power Conference, London.

SYED, S.A., and BRACCO, F.V. (1979)
Further comparisons of computed and measured divided-chamber engine combustion.
SAE paper 790247.

TABACZYNSKI, R.J., HOULT, D.P. and KECK, J.C. (1970)
High Reynolds number flow in a moving corner.
J. Fluid Mech., 42, 249.

TANAKA, K. (1929)
Air flow through suction valves of conical seats. Parts I and II.
Aero. Res. Inst., 4, 9.

TANI, I. (1962)
Production of longitudinal vortices in the boundary layer along a concave wall.
J. Geophys. Res., 67, 3075.

TAYLOR, G.I. (1929)
The criterion for turbulence in curved pipes.
Proc. R. Soc., A124, 243.

TAYLOR, A.M.K.P. (1981)
Confined isothermal and combusting flows behind axisymmetric baffles.
Ph.D.Thesis, University of London.

TAYLOR, A.M.K.P., WHITELAW, J.H. and YIANNESKIS, M. (1981a)
Measurements of laminar and turbulent flow in a curved duct with thin inlet boundary layers.
NASA Contractor Report 3367.

TAYLOR, A.M.K.P., WHITELAW, J.H. and YIANNESKIS, M. (1981b)
Measurements in ducted flows by laser Doppler anemometry.
Proc. Symp. on Numerical and Physical Aspects of Aerodynamic Flows, California State University, January 1981. To be published by Springer-Verlag.

TAYLOR, A.M.K.P., WHITELAW, J.H. and YIANNESKIS, M. (1981c)
Curved ducts with strong secondary motion: Velocity measurements of developing laminar and turbulent flow.
Imperial College, Mech. Engng. Dept. Report, FS/81/20. To be published in J. Fluids Engng.

TAYLOR, A.M.K.P., WHITELAW, J.H. and YIANNESKIS, M. (1981d)
Turbulent flow in a square-to-round transition.
NASA Contractor Report 3447.

TAYLOR, A.M.K.P., WHITELAW, J.H. and YIANNESKIS, M. (1981e)
Developing flow in S-shaped ducts.
Imperial College, Mech. Engng. Dept. Report FS/81/22. Submitted as NASA Contractor Report.

TENNEKES, H. and LUMLEY, J.L. (1972)
A first course in turbulence.
MIT Press, London/New York.

TINDAL, M.J., WILLIAMS, T.J. and EL-KHAFAJI, A.H.A. (1974)
Gas flow measurements in engine cylinders.
SAE Trans., paper 740719.

TOWNE, C.E. and ANDERSON, B.H. (1981)
Numerical simulation of flows in curved diffusers with cross-sectional transitioning using a three-dimensional viscous analysis.
NASA Technical Memorandum 81672.

VLACHOS, N.S. (1977)
Blood flow in small diameter ducts; particularly in venules.
Ph.D. Thesis, University of London.

WAKISAKA, T., HAMAMOTO, Y., OHIGASHI, S. and HASHIMOTO, M. (1979)
Measurements of air swirl and its turbulence characteristics in the cylinder of an internal combustion engine.
Proc. Instn. Mech. Engrs., C91/79.

WARD-SMITH, A.J. (1971)
Pressure losses in ducted flows.
Butterworths, London.

WATKINS, A.P. (1973)
Calculation of flow and heat transfer in the combustion chamber of a reciprocating engine.
M.Sc.Thesis, University of London.

WATKINS, A.P. (1977)
Flow and heat transfer in piston/cylinder assemblies.
Ph.D.Thesis, University of London.

WHITE, C.M. (1929)
Streamline flow through curved pipes.
Proc. R. Soc., A123, 645.

WIGLEY, G. and HAWKINS, M.G. (1978)
Three-dimensional velocity measurements by laser anemometry in a Diesel engine under steady state inlet flow conditions.
SAE paper 780060.

WIGLEY, G. PATTERSON, A.C. and RENSHAW, J. (1981)
Swirl velocity measurements in a firing production Diesel engine by laser anemometry.
Proc. ASME Conf. on Fluid Mechs. of Comb. Systems, Boulder, Colorado, June 22-23, 1981.

WILLIAMS, T.J. and TINDAL, M.J. (1980)
Gas flow studies in direct injection Diesel engines with re-entrant combustion chambers.
SAE paper 800027.

WILLIS, D.A., MEYER, W.E. and BIRNIE, C.,Jnr. (1966)
Mapping of airflow patterns in engines with induction swirl.
SAE paper 660093.

WILSON, N.M. (1978)
Digital signal-processing techniques for laser Doppler velocimetry.
J. Phys. E: Sci. Instrum., 11, 555.

WITZE, P.O. (1976a)
Hot-wire measurements of the turbulence structure in a motored spark-ignition engine.
AIAA Paper No. 76-37, 14th Aerospace Sciences Meeting, Washington.

WITZE, P.O. (1976b)
Revised figures for AIAA paper no. 76-37.

WITZE, P.O. (1976c)
Preliminary hot-wire measurements in a motored engine with an axisymmetric cylinder geometry.
Sandia Laboratories Report, Livermore, July 1976.

WITZE, P.O. (1977)
Measurements of the spatial distribution and engine speed dependence of turbulent air motion in an i.c. engine.
SAE paper 770220, presented at 1977 Automot. Engng. Congress, Detroit.

WITZE, P.O. (1978)
Application of laser velocimetry to a motored internal combustion engine.
Third Int. Workshop on Laser Velocimetry, Purdue University, July 1978.

WITZE, P.O. (1980)
A critical comparison of hot-wire anemometry and laser Doppler velocimetry for i.c. engine applications.
Sandia Report SAND79-8685, presented at 1980 SAE Automot. Engng. Contress and Exposition, Detroit, February 25-29.

WOODS, W.A. and GHIRLANDO, R. (1975)
Radial flow in an engine cylinder near the end of compression.
Proc. Instn. Mech. Engrs., C82/75.

WOOD, G.B., HUNTER, D.U., TAYLOR, E.S. and TAYLOR, E.F. (1942)
Air flow through intake valves.
Trans. SAE, 50, No. 6.

YAO, L.S. and BERGER, S.A. (1978)
Flow in heated curved pipes.
J. Fluid Mech., 88, 339.

YEE, G. and HUMPHREY, J.A.C. (1979)
Developing laminar flow and heat transfer in strongly curved ducts of rectangular cross-section.
ASME Paper 79WA/HT-15.

YIANNESKIS, M. (1977)
Flow patterns in internal combustion engines.
M.Sc. Thesis, University of London.